Netherlands Enterprise Agency

Metocean Assessment Analysis Report

IJmuiden Ver Wind Farm Zone

>> *Sustainable. Agricultural. Innovative. International.*

Netherlands Enterprise Agency

RVO Approval for Publication

Document Characteristics

Version	Title	Date of Publication	Reference Contractor	Reference RVO
1.0	Metocean Assessment Analysis report IJmuiden Ver Wind Farm Zone	December 22nd , 2023	11827690	WOZ2220015

Approval

Approval for public disclosure	Position
Daniëlle Gerritsma	Project Manager RVO Offshore Wind Energy
Joep Bronkhorst	Senior Project Manager RVO Offshore Wind Energy

Statement RVO

The underlying report presents normal- and extreme design values for wind, waves, water levels and currents as derived by DHI using proprietary methods at one analysis location in the IJmuiden Ver Beta wind farm zone. DHI have stated that the presented values represent their most accurate estimates based on the most advanced methods known and available to them during the study and that during the estimation process no choices were made that lead to conservatism.

These results are updates to RVO's previously published precedents. Users should make their own decisions on what values to use for preliminary and/or detailed engineering design. RVO has decided in discussion with DHI to publish a non-certified, concise metocean assessment report due to time constraint related to the permit tender. A complete and final certified report pertaining to more analysis locations and maps of normal and extreme conditions will follow in 2024, after the IJmuiden Ver Alpha and Beta permit tender.

IJmuiden Ver Wind Farm Zone

Part B: Metocean Data Analysis

Rijksdienst voor Ondernemend Nederland

20.12.2023

Prepared for Rijksdienst voor Ondernemend Nederland (RVO)

The expert in **WATER ENVIRONMENTS**

IJmuiden Ver Wind Farm Zone

Part B: Metocean Data Analysis

Prepared for: Rijksdienst voor Ondernemend Nederland (RVO)
Represented by Ms. Danielle Gerritsma

Contact person:	Ameya Sathe, amsa@dhigroup.com
Project Manager:	Ameya Sathe
Quality Supervisor:	Jacob Berg Jørgensen, Ameya Sathe, Daniel Caichac, Verena Schrameyer, Sarah Lumban-Tobing
Author:	Eloise Merlaud, Joana Mendes, Helene Syneva Wellm Resende de Paiva, Sara Jackson, Cecilie Borch Devantier
Project No.:	11827690
Approved by:	Jesper Ulrik Fuchs
Approval date:	20.12.2023
Revision:	Final 1.0
Classification:	**Open:** This document may be shared inside and outside the DHI Group entities without the client's prior approval.
File name:	11827690_IJV_DHI_Metocean_Data_Analysis_clean_version_1.0.docx

Contents

Figures

Tables

Appendices

Revision History

Revision	Date	Reviewer	Approver	Comments
Draft 0.1	03-12-2023	Ameya Sathe	Jesper Ulrik Fuchs	First draft
Draft 0.2	15-12-2023	Ameya Sathe	Jesper Ulrik Fuchs	Second draft incorporating RVO comments
Final 1.0	20-12-2023	Ameya Sathe	Jesper Ulrik Fuchs	Final revision incorporating revised RVO comments

Nomenclature

Abbreviations	
DA	Data Assimilation
DWF	Dutch Wind Farm
ECMWF	European Centre for Medium-Range Weather Forecasts
ERA5	ECMWF Reanalysis 5
FM	Flexible Mesh
HD	Hydrodynamic
HKN	Hollandse Kust (noord)
HKW	Hollandse Kust (west)
HKZ	Hollandse Kust (zuid)
IJV	IJmuiden Ver
IJVWFZ	IJmuiden Ver Wind Farm Zone
IOS	Institute of Oceanographic Sciences
KNMI	Royal Netherlands Meteorological Institute
LAT	Lowest Astronomical Tide
MOOD	DHI's Metocean-On-Demand Portal
MSL	Mean Sea Level
NE	North Europe
NL	The Netherlands
OWF	Offshore Wind Farm
RVO	Rijksdienst voor Ondernemend Nederland
RWS	Rijkswaterstaat
SW	Spectral Wave
TNW	Ten noorden van de Waddeneilanden
UTC	Coordinated Universal Time (Universal Time Coordinated)
UTM	Universal Transverse Mercator
WFZ	Wind Farm Zone
WGS84	World Geodetic System 1984
WL	Water Level
WRF	Weather Research & Forecasting Model

Subscripts	
2DH	2D Depth-averaged
Total-Dep	Depth-averaged total current speed
Tide-Dep	Depth-averaged tidal current speed
Residual-Dep	Depth-averaged residual current speed
Total-Surf	Surface total current speed
Tide-Surf	Surface tidal current speed
Residual-Surf	Surface residual current speed
Residual,near-seabed	Near-seabed residual current speed
NE	North Europe
DA	Data Assimilation
Total or tot	Total signal of a parameters, e.g., WL, CS, CD, H_{m0} etc.
Tide	Tidal component of WL, CS and CD
Residual or Res	Residual component of WL, CS and CD
z	WS, WD, CS and CD at specific vertical level z
Sea	Wind-sea component of wave spectrum
Swell	Swell component of wave spectrum

Definitions	
Time	Times are relative to UTC
Level	Levels are relative to MSL (if not specified otherwise)
Coordinate System	Project coordinate system is ETRS 89 UTM 31N (EPSG:25831) Numerical models are set up in Lon/Lat WGS84 (EPSG:4326)
Direction	Directions are 30 bins relative to true north, i.e., 12 bins covering: 360°: 0° = ÷15° -15°N, 30° = 15°-45°N, etc. Clockwise from North Wind and Waves: °N coming from Current: °N going to Nautical convention was used
Time averaging	All time averages are based on a central window rolling averaging
MEAN, MIN, MAX, STD	Average, minimum, maximum, standard deviation calculated for a parameter
P5, P50, P95	$5^{th,}$ $50^{th,}$ 95^{th} percentile of data

Symbols		Units
CD	Current Direction	°N (going to)
CS	Current Speed	m/s
WL	Water Level	m
WS_{10}	Wind Speed at 10 mMSL	m/s
WD_{10}	Wind Direction at 10 mMSL	°N (coming from)
WS_{160}	Wind Speed at 160 mMSL	m/s
WD_{160}	Wind Direction at 160 mMSL	°N (coming from)
α	Shear Coefficient for Wind Speed or Current Speed	-
DSD	Direction Standard Deviation	°
H_{m0}	Spectral Significant Wave Height	m
MSLP	Mean Sea Level Pressure	hPa
MWD	Mean Wave Direction	°N (coming from)
N	Sample Count	-
PBL height	Planetary Boundary Layer Height	mMSL
Px	x% Percentiles	-
PWD	Peak Wave Direction	°N (coming from)
RH_z	Relative Humidity @ z mMSL	
σ	Spectral Width Parameter	-
SST	Sea Surface Temperature	°C
SWSR	Short Wave Solar Radiation	W/m^2
H_{m0}	Significant Wave Height	m
$H_{m0,p,eq}$	Characteristic Significant Wave Height used in J-EVA	m
H_{max}	Maximum Wave Height	m
$C_{max,\ SWL}$	Maximum Crest Height Relative to Still Water Level	m
$C_{max,\ MSL}$	Maximum Crest Height Relative to Mean Sea Level	m
T_{01}	Spectral Equivalent of Mean Wave Period	s
T_{02}	Spectral Equivalent of Mean Zero-down-crossing Wave Period	s
T_{airz}	Air Temperature @ z mMSL	°C

Symbols		Units
T_p	Associated Peak Wave Period to H_{m0}	s
T_{Hmax}	Associated Period to H_{max}	s
P_{break}	Wave Breaking Probability	-
N, E, S, W	North, East, South and West	-
z	Vertical Coordinate, Positive Up	mMSL
d	Water Depth	mMSL

Executive Summary

In English

This report provides detailed information on the metocean analysis for the IJmuiden Ver offshore wind farm area.

Under contract with Rijksdienst voor Ondernemend Nederland (RVO), DHI A/S (DHI) established dedicated high-resolution (~400 m) hydrodynamic and spectral wave state-of-the-art numerical models (based on MIKE Powered by DHI software package) covering the 44-year period from 1979 to 2022 to provide metocean conditions in the IJmuiden Ver (IJV) Offshore Wind Farm Zone (IJVWFZ). The models were forced with wind/pressure fields data from a dedicated Weather Research Forecasting (WRF) model, which was developed specifically for this project, downscaled from the ERA5 dataset, established by the European Centre for Medium-Range Weather Forecasts (ECMWF).

A local hindcast 2D hydrodynamic model was set up to simulate water levels and currents using the MIKE 21 HD model. The model domain covers not only the IJV Offshore Wind Farm Zone, but also most of the Dutch Exclusive Economic Zone of the North Sea, thus comprising all the offshore wind farm search areas within Dutch maritime boundaries.

The waves were likewise simulated using the MIKE 21 SW spectral wave model, covering the same domain as the hydrodynamic model.

Extensive validation of the models was conducted using a comprehensive set of wind, water level, current, and wave measurement data. The validation showed very good model performance and thus ensured accurate high-quality metocean conditions not only at IJVWFZ but also across the whole feasibility domain area.

A comprehensive web-based digital database is provided, which enables users to access the modelling data and the analysis results through a user-friendly web interface called MOOD[1]. Users can also download the data using an API[2].

Normal and extreme metocean conditions analyzed at one analysis location IJV1 (see Table 2.1 and Figure 2.1) are described in detail in this report.

Normal Conditions

At IJV1 (see Table 2.1 and Figure 2.1), the mean wind speed at 160 m height is 10.33 m/s, and the mean significant wave height is 1.47 m with peak wave periods most frequently between 4 s and 8 s. The wave conditions are characterized by a mix of swell from the North Atlantic and local wind-sea with a dominance of extremes from the north and north-west.

The tides are moderate with HAT = +0.89 mMSL and LAT = -0.9 mMSL, giving a total tidal envelope of 1.79 m. The highest and lowest total water levels in the hindcast period (1979 to 2022) is +2.29 mMSL and -1.72 mMSL and occur during winter (Nov. – Feb.). The mean total depth-averaged current speed is 0.44±0.14 m/s dominated by the tidal component.

[1] https://www.metocean-on-demand.com/
[2] https://www.metocean-on-demand.com/features#api

Extreme Conditions

Extreme metocean conditions were established using DHI's state-of-the-art Joint Extreme Value Analysis (J-EVA) analysis toolbox. Extreme values were established for return periods up to 10000 years for wind, waves (significant wave height, maximum individual wave and crest height based on Forristall short-term distribution), water levels, and currents. Joint probability of metocean conditions is also provided.

The annual, omni-directional extreme value estimates at the analysis point IJV1 (see Table 2.1 and Figure 2.1) are presented in the table below.

Variable	Extreme value (omni) - Return period [year]							
	1	2	5	10	50	100	1000	10000
Extreme Wind Speed, WS [m/s], 160m, 10 min	31.8	33.3	35.1	36.3	39.0	40.2	43.8	47.7
Extreme Wind Speed, WS [m/s], 160m, 10 min, adjusted by 7 %	34.0	35.6	37.6	38.8	41.7	43.0	46.9	51.0
High Water Level, Total, HWL_{tot} [mMSL]	1.6	1.7	1.9	2.0	2.3	2.4	2.9	3.3
Low Water Level, Total, LWL_{tot} [mMSL]	-1.2	-1.3	-1.4	-1.5	-1.7	-1.7	-2.0	-2.2
High Water Level, Residual, HWL_{res} [m]	1.2	1.4	1.6	1.7	2.0	2.2	2.6	3.1
Low Water Level, Residual, LWL_{res} [m]	-0.8	-0.9	-1.0	-1.1	-1.3	-1.4	-1.7	-2.0
Current Speed, Total, Depth-averaged, CS_{tot} [m/s]	0.6	0.6	0.7	0.8	0.9	0.9	1.1	1.3
Significant Wave Height, 3hr, H_{m0} [m]	5.9	6.2	6.7	7.0	7.6	7.9	8.7	9.5
Peak Wave Period, Assoc. with H_{m0}, $T_p\|H_{m0}$ [s]	10.4	10.8	11.4	11.7	12.6	12.9	13.9	14.8
Mean Zero-crossing Period, Assoc. with H_{m0}, $T_{02}\|H_{m0}$ [s]	6.8	7.1	7.5	7.7	8.2	8.4	9.0	9.5
Maximum Wave Height, H_{max} [m]	11.0	11.7	12.6	13.2	14.6	15.2	17.0	18.6
Wave Period Assoc. with H_{max}, T_{Hmax} [s]	9.2	9.5	9.8	10.0	10.5	10.7	11.3	11.9
Maximum Crest Level with Respect to SWL, $C_{max,SWL}$	7.1	7.6	8.2	8.6	9.6	10.1	11.5	12.8
Maximum Crest Level with Respect to MSL, $C_{max,MSL}$	7.9	8.5	9.2	9.8	11.0	11.5	13.0	14.4

In Dutch

Samenvatting

Dit rapport biedt gedetailleerde informatie over de metocean-analyse (meteorologisch-oceanografisch) voor het offshore windparkgebied IJmuiden Ver (IJV).

In opdracht van de Rijksdienst voor Ondernemend Nederland (RVO) heeft DHIA/S (DHI) hoge resolutie (~400 m), state-of-the-art, hydrodynamische en spectrale numerieke golfmodellen ontwikkeld (gebaseerd op DHI's MIKE21-softwarepakket). De modellen bestrijken een periode van 44 jaar (van 1979 tot en met 2022), met als doel de oceanografische en meteorologische omstandigheden in de IJmuiden Ver (IJV) Offshore Windparkzone (IJVWFZ) vast te stellen. De modellen zijn aangedreven door wind- en luchtdrukgegevens die afkomstig zijn van een speciale versie van het Weather Research Forecasting (WRF) model, afgeleid van een gedownscalede ERA5 dataset, opgezet door het European Centre for Medium-Range Weather Forecasts (ECMWF).

Een lokaal 2D hydrodynamisch hindcastmodel (een model met historische simulaties) is opgezet om waterniveaus en zeestromingen te simuleren met behulp van het MIKE 21 HD-model. Het modeldomein bestrijkt niet alleen de IJV Offshore Windparkzone, maar ook het grootste deel van de Nederlandse Exclusieve Economische Zone van de Noordzee en omvat derhalve alle zoekgebieden voor offshore windparken binnen de Nederlandse maritieme grenzen.

De golven zijn gesimuleerd met behulp van het MIKE 21SW spectrale golfmodel, dat hetzelfde domein bestrijkt als het hydrodynamische model.

De modellen zijn uitgebreid gevalideerd met behulp van een omvangrijke reeks aan wind-, waterniveau-, stromings-en golfmeetgegevens. De validatie laat een zeer goede prestatie van het model zien, wat de beschikbaarheid van accurate, kwalitatief hoge metocean gegevens garandeert, in zowel de IJV Offshore Windparkzone als het hele haalbaarheidsdomein.

Via de gebruiksvriendelijke webinterface genaamd MOOD1, hebben gebruikerstoegang tot een uitgebreide digitale database waar de modelleringsgegevens en de analyseresultaten in te vinden zijn. Gebruikers kunnen de gegevens ook downloaden via een API[3].

Normale en extreme metocean condities, geanalyseerd voor de analyselocatie IJV1 (zie Table 2.1 en Figure 2.1) worden gedetailleerd beschreven in dit rapport.

Normale Omstandigheden

Bij IJV1 (zie Table 2.1 en Figure 2.1) bedraagt de gemiddelde windsnelheid 10,33 m/sop 160 m hoogte en de gemiddelde significante golfhoogte 1,47 m, waarbij piekgolfperioden veelal tussen 4 en 8 s liggen. De golfomstandigheden worden gekenmerkt door een combinatie deining uit de Noord-Atlantische Oceaan en door lokale wind gedreven golven, met een dominantie van extremen uit het noorden en noordwesten.

[3] https://www.metocean-on-demand.com/features#api

De getijden zijn gematigd met HAT = +0,89 mMSL en LAT = -0,9 mMSL, wat een totale getijdenbereik van 1,79 m oplevert. De hoogste en laagste totale waterstanden in de gesimuleerde periode (1979 tot en met 2022) bedragen +2,29 mMSL en -1,72 mMSL en komen voor tijdens de winter (november–februari). De gemiddelde totale diepte-gemiddelde stroomsnelheid bedraagt 0,44 ± 0,14 m/s, gedomineerd door de getijdencomponent.

Extreme Omstandigheden

Extreme condities zijn bepaald met behulp van DHI's Joint Extreme Value Analysis (J-EVA) analysetoolbox. Er zijn extreme waarden bepaald voor terugkeerperioden tot 10.000 jaar voorwind, golven (significante golfhoogte en maximale individuele golf-en tophoogte gebaseerd op Forristall), waterstanden en stromingen.

De jaarlijkse, omnidirectionele schattingen van de extreme waarden op het analysepunt IJV1 (zie Table 2.1 en Figure 2.1) worden weergegeven in de onderstaande tabel.

Variable	Extreme value (omni) - Return period [year]							
	1	2	5	10	50	100	1000	10000
Extreme Wind Speed, WS [m/s], 160m, 10 min	31.8	33.3	35.1	36.3	39.0	40.2	43.8	47.7
Extreme Wind Speed, WS [m/s], 160m, 10 min, adjusted by 7 %	34.0	35.6	37.6	38.8	41.7	43.0	46.9	51.0
High Water Level, Total, HWL_{tot} [mMSL]	1.6	1.7	1.9	2.0	2.3	2.4	2.9	3.3
Low Water Level, Total, LWL_{tot} [mMSL]	-1.2	-1.3	-1.4	-1.5	-1.7	-1.7	-2.0	-2.2
High Water Level, Residual, HWL_{res} [m]	1.2	1.4	1.6	1.7	2.0	2.2	2.6	3.1
Low Water Level, Residual, LWL_{res} [m]	-0.8	-0.9	-1.0	-1.1	-1.3	-1.4	-1.7	-2.0
Current Speed, Total, Depth-averaged, CS_{tot} [m/s]	0.6	0.6	0.7	0.8	0.9	0.9	1.1	1.3
Significant Wave Height, 3hr, H_{m0} [m]	5.9	6.2	6.7	7.0	7.6	7.9	8.7	9.5
Peak Wave Period, Assoc. with H_{m0}, $T_p\|H_{m0}$ [s]	10.4	10.8	11.4	11.7	12.6	12.9	13.9	14.8
Mean Zero-crossing Period, Assoc. with H_{m0}, $T_{02}\|H_{m0}$ [s]	6.8	7.1	7.5	7.7	8.2	8.4	9.0	9.5
Maximum Wave Height, H_{max} [m]	11.0	11.7	12.6	13.2	14.6	15.2	17.0	18.6
Wave Period Assoc. with H_{max}, T_{Hmax} [s]	9.2	9.5	9.8	10.0	10.5	10.7	11.3	11.9
Maximum Crest Level with Respect to SWL, $C_{max,SWL}$	7.1	7.6	8.2	8.6	9.6	10.1	11.5	12.8
Maximum Crest Level with Respect to MSL, $C_{max,MSL}$	7.9	8.5	9.2	9.8	11.0	11.5	13.0	14.4

1 Introduction

This study has been developed as a part of the metocean assessment for Dutch Wind Farm Zones. The assessment includes detailed modelling of the metocean conditions in the wind farm zones together with a comprehensive metocean analysis using the state-of-the-art modelling and analysis methods. This report presents detailed metocean analyses in the IJmuiden Ver Wind Farm Zone.

The Dutch government has developed a Routekaart Wind op Zee[4], which sets out the development of offshore wind energy up to a total capacity of approximately 21 GW by 2030, enough to supply 8.5% of all the energy in the Netherlands.

The IJmuiden Ver (IJV) Wind Farm Zone (WFZ, together IJVWFZ, Project sites) has been identified by Rijksdienst voor Ondernemend Nederland (RVO) as an area of potential wind energy development. The Project site is in the Dutch Exclusive Economic Zone on the Dutch shelf in the North Sea. It lies approximately 62 km from the west mainland coast of the Netherlands.

Within the IJVWFZ, the Dutch Ministry of Economic Affairs and Climate Policy has identified three offshore wind farm sites (OWF) for development, labelled IJV Alpha OWF, IJV Beta OWF and IJV Gamma OWF. Two additional OWF zones have also been identified by RVO, namely Nederwiek and Doordewind, in the vicinity of IJVWFZ. Exact information on the location and shape of the project sites can be found through the online portal of RVO [1]. The locations of the project sites are presented in Figure 1.1.

RVO plays a central role in the tendering process for Dutch Offshore Wind Farm Zones. Preliminary investigations are carried out for suitable sites, and their results are published as part of the tendering process. As part of the bid calculation, the bidder needs as detailed information as possible to estimate the metocean conditions in the area. To address this requirement, DHI has carried out comprehensive metocean modelling and analyses. The results produced by DHI aim to provide the input required for the bidders to use in their preliminary front-end engineering design (Pre-FEED) and arrive at an optimal bid. The modelling is carried out for the feasibility domain. The analysis is carried out at one location (named IJV1) in IJVWFZ, as indicated in Figure 1.1. Analysis in the entire domain as well as certification of the study will be carried out at later stage and will be available in the year 2024.

One of the main requirements of RVO in this study was to align between the wind resource assessment (WRA) and the metocean analysis. To address this requirement, DHI A/S (DHI) formed and led a consortium with partners OWC and C2 Wind Aps. OWC, together with its partners ProPlanEn, ArcVera and Innosea, were responsible for the development of the mesoscale modelling and wind resource assessment [2]. DHI is overall responsible for all the deliveries in the project. DHI carried out the modelling of water levels, currents, and waves that is presented in [3]. In this report, comprehensive metocean analysis using the models in [3] is presented.

[4] https://windopzee.nl/onderwerpen/wind-zee/wanneer-hoeveel/wind-zee-rond-2030/

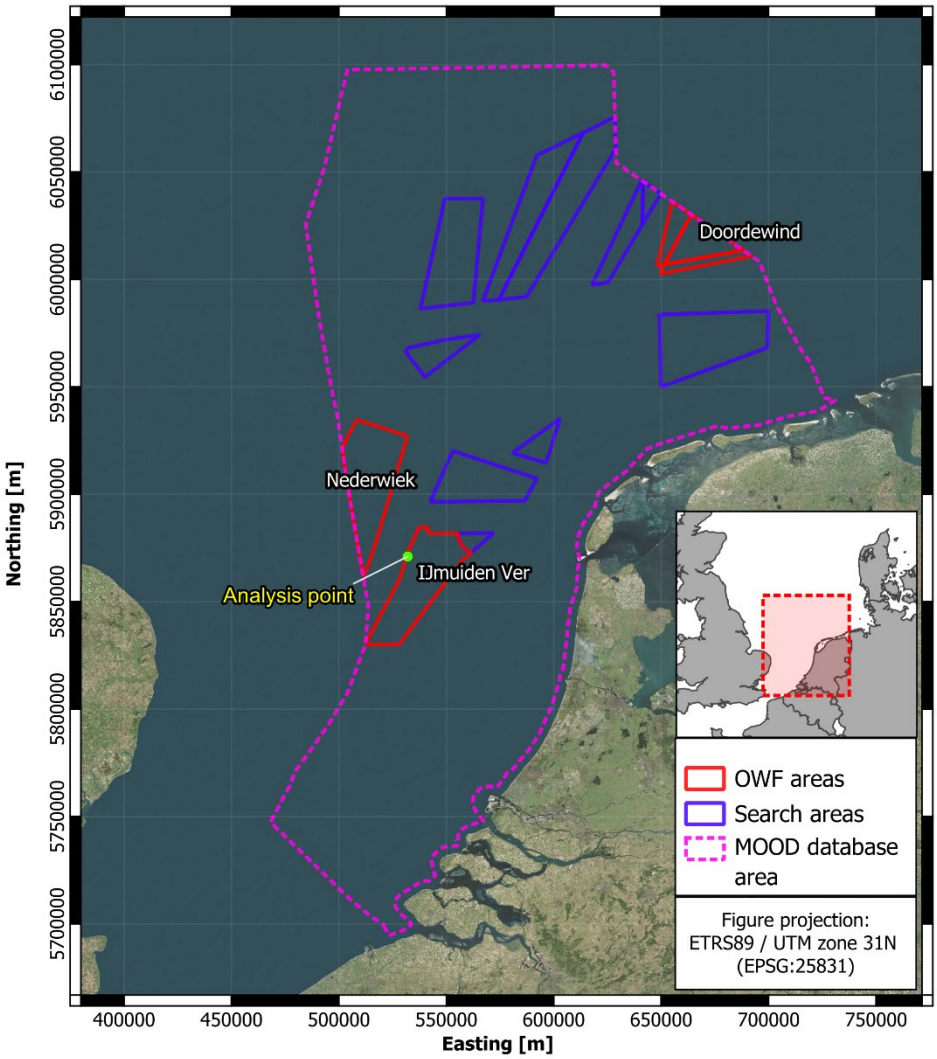

Figure 1.1 Area of coverage of the study shown in magenta called as feasibility domain.
The modelling is carried out for the feasibility domain. The analysis is carried out at one location in the IJVWFZ.

1.1 Scope of the study and reports

The scope of the study is two-fold:

1. To perform comprehensive metocean modelling across the feasibility domain (see Figure 1.1) containing the IJVWFZ.
2. To perform detailed metocean analyses at one location in the IJVWFZ (see Figure 1.1 and Figure 1.2).

The study is presented in two separate reports tackling each scope. This report presents the comprehensive metocean data analysis, whereas [3] provides background information on the models and methods used to produce the data analysed in the underlying report.

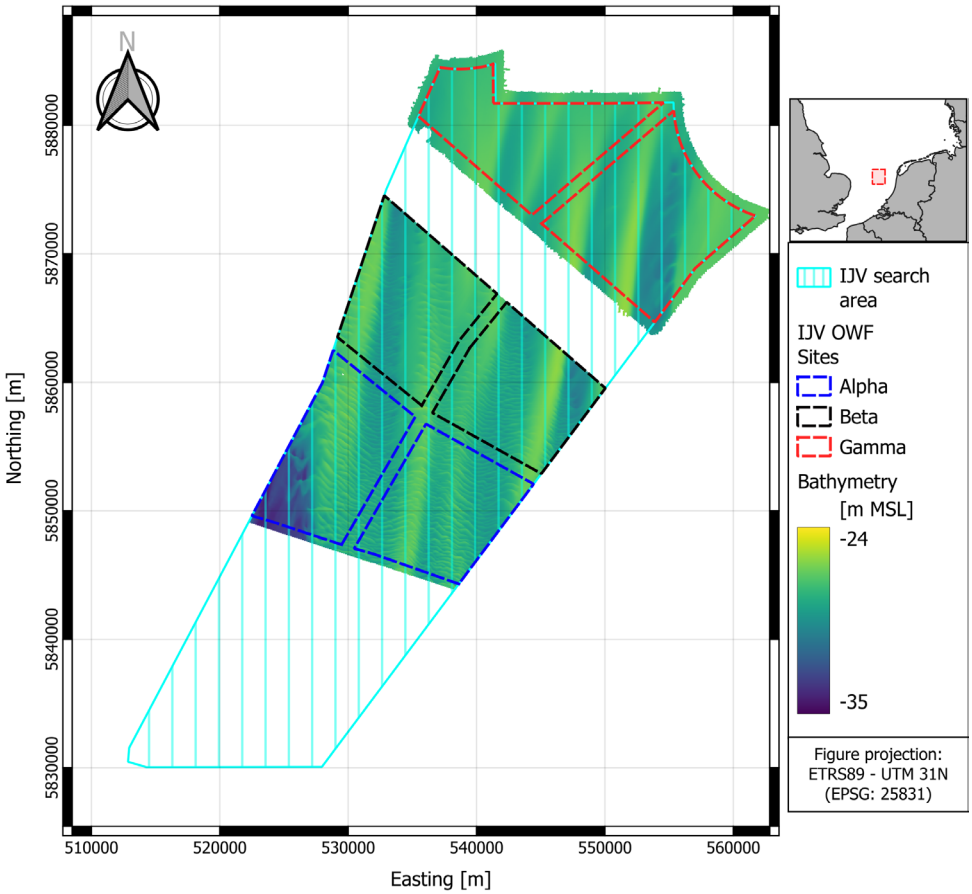

Figure 1.2 IJV Ver OWF zone comprising of three sub zones, namely, Alpha, Beta, and Gamma.
The three sub zones are Alpha (dark blue), Beta (black) and Gamma (red).

1.2 Conventions

Unless noted otherwise, the following conventions are used throughout the report (see Figure 1.3).

1. Elevations are given as distance above MSL.
2. Nautical convention was used.
3. Directions are relative to North (0°) with clockwise direction as positive (e.g., East is 90°).
4. Wind and wave directions are designated by the direction they come from.
5. Current directions are designated by the direction it is heading.
6. Directions stated in different tables correspond to the centre of the bin. For example, 0° direction lies between -15° - 15°, 30° lies between 15° - 45° and so on.
7. The reference coordinate system is ETRS 89 UTM 31N with the EPSG Code 25831.

8. English Style Guide of the European Commission [4] is applicable throughout the document. Point is used as a decimal separator in this study. It is noted that no thousand grouping was used in this study deviating from the same guideline.

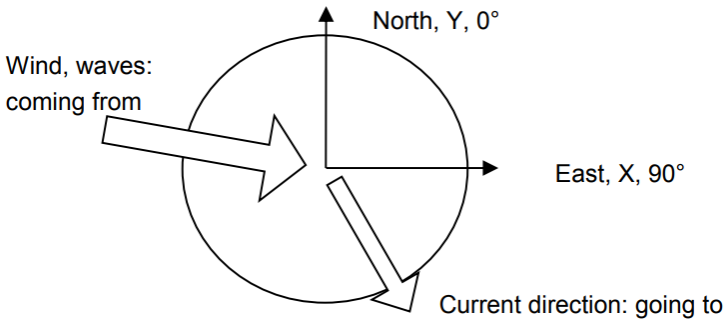

Figure 1.3 Conventions of direction

1.3 Report structure

This report is arranged as follows:

- Section 2 presents the motivation behind the selection of the analysis point within the IJV Ver OWF area.
- Section 3 presents the normal conditions analyses for wind, water levels, currents, waves, and other metocean parameters.
- Section 4 presents the extreme conditions analyses for wind, water levels, currents, waves, and other metocean parameters using the J-EVA method.
- Section 5 presents a brief comparison of the normal and extreme conditions with the previous analysis carried out in the IJVWFZ.
- Section 6 briefly describes the web-based database for IJmuiden Ver.
- Section 7 presents the list of references that were used in this study.
- Appendices supporting the analysis in the main body of the report are provided in the end.

2 Analysis Point

This section discusses the selected analysis point, IJV1, for this study. The specifications of the delivered time series data are also provided herein.

Figure 2.1 shows a map of the IJVWFZ together with the analysis location IJV1, and Table 2.1 presents the coordinates and water depth of the point.

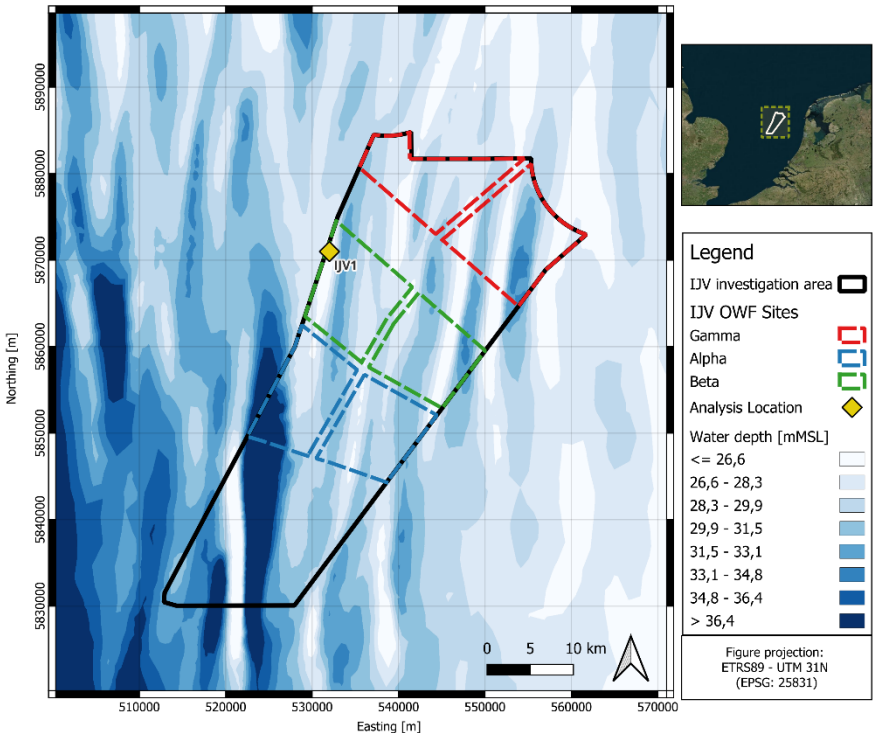

Figure 2.1 Map of the IJmuiden Ver OWF Zone (IJVWFZ) and the analysis point IJV1.
The figure shows the three subzones, namely Alpha (blue), Beta (green) and Gamma (red).

Table 2.1 Metocean analysis point applied in this study.
The present study assesses one (1) analysis point, IJV1, and delivers data at the same spectral point (IJV1). The table states the analysis location, coordinates as the approximate water depth in the different models as well as survey.

Analysis Location	Longitude [°E]	Latitude [°N]	UTM 31N coordinates [m]	Water depth SW_{DWF23} [mMSL]	Water depth HD_{DWF23} [mMSL]	Water depth Survey [mMSL]
IJV1	3.47669	52.98762	Easting: 532000 Northing: 5871000	25.81	25.84	25.87

2.1 Selection of analysis point

Within the IJVWFZ, the selection of the analysis location, IJV1, was based on the maps of extreme significant wave height and statistics of the depth-

averaged current speed. Figure 2.2 shows the map of the 50-year extreme significant wave height (H_{m0}), and Figure 2.3 illustrates the mean of yearly maxima of total depth-averaged current speeds.

The extreme map of H_{m0} shows two main areas with large values (larger than 7.5m); one in the Beta site (green), and another in the Gamma site (red). The Beta site was preferred for the analysis location, as the extremes were slightly higher in the Beta site. Moreover, it was confirmed by RVO that the Beta site will be available for tendering of the development of OWF, which further added a justification for selecting an analysis point inside the Beta site.

Additionally, a map of the mean of the annual current speed maxima (Figure 2.3) was created, which shows higher values in the Beta site, thereby further justifying the selection of an analysis location in the Beta site. Therefore, the location IJV1 was selected in the northwest part of the Beta site with the most severe wave conditions and to match a wave spectra location.

Note that the extremes map presented in Figure 2.2 was derived using a traditional extreme value analysis (see Appendix C), since the goal of this exercise was to arrive at a reasonable analysis location for performing a more comprehensive extreme value analysis using the J-EVA method (see Appendix D - Appendix F).

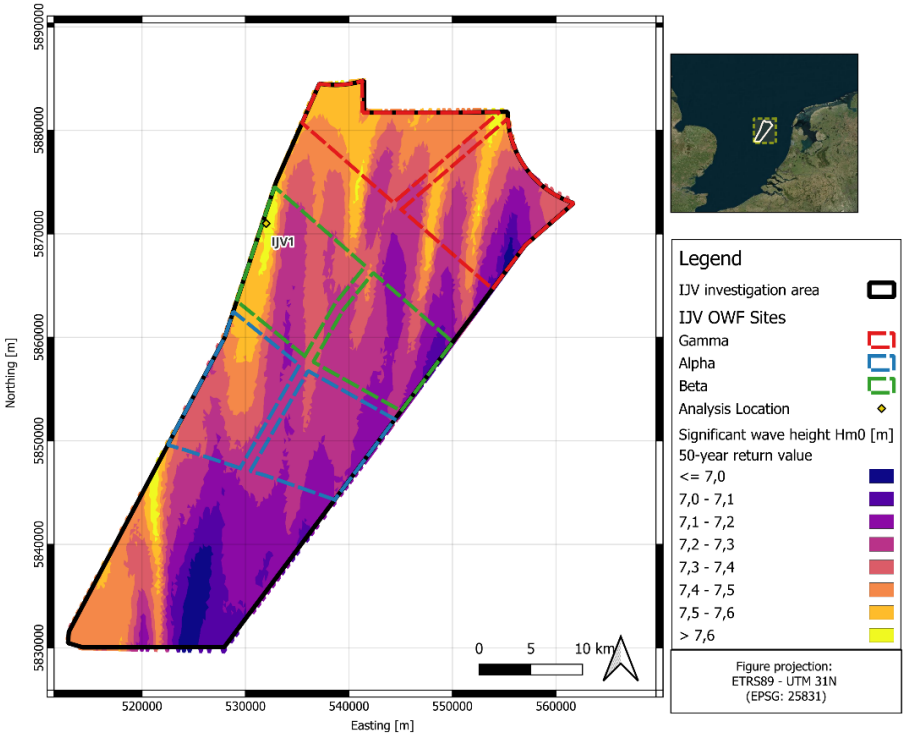

Figure 2.2 Map of extreme significant wave height at the IJVWFZ.
Extreme H_{m0} for the 50-year return period. The input data was taken from the SW_{DWF23} model from 1979-01-15 to 2022-12-31 (inclusive). The extreme values are computed using the traditional extreme value analysis.

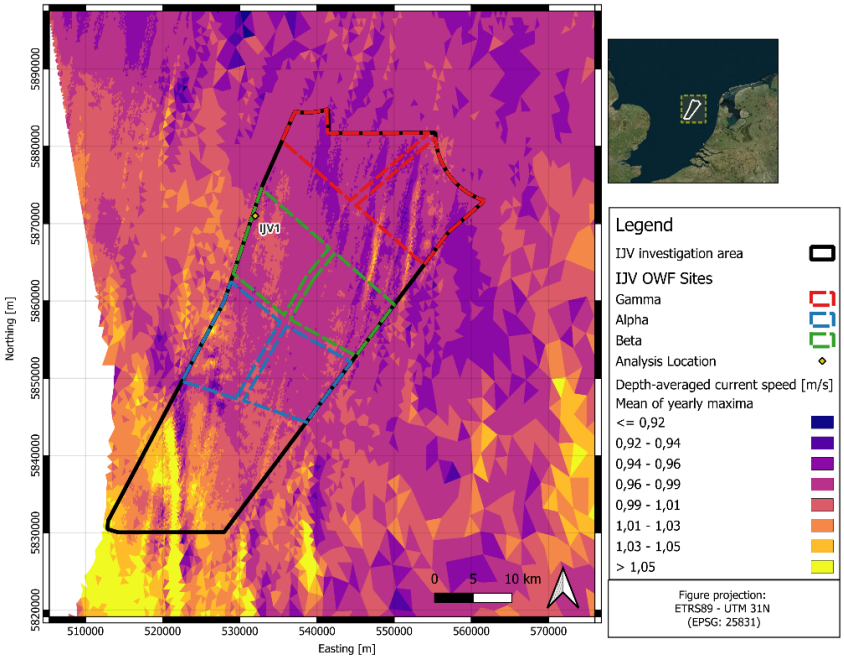

Figure 2.3 Map of mean of annual maxima of total current speed at the IJVWFZ.
Mean of annual maxima of depth-averaged total current speed [m/s] at the IJVWFZ. The input data is taken from the HD_{DWF23} model from 1979 to 2022 (inclusive).

2.2 Data sources

All the analyses performed in this report used the data source provided in Table 2.2.

Table 2.2 Data sources used for analysis parameters in this study.

Parameter	Source
Waves	SW_{DWF23}
Water Level and Depth-averaged Currents	HD_{DWF23}
Sea Salinity and Sea Water Temperature	HD_{UKNS}
Ice Conditions	ERA5
Lightning	NASA's GHRC
Wind and Other Atmospheric Parameters at Multiple Heights	WRF Set-up Specifically for the Dutch Offshore Wind Farms Area

Further details and validation of the SW_{DWF23}, HD_{DWF23}, WRF, and HD_{UKNS} models are presented in the modelling report [3].

2.3 Delivery of time series and statistics

The time series deliverables are delivered through the web-based database MOOD[5]. The details of the deliverables are provided in [3]. Furthermore, statistics of the normal and extreme conditions at IJV1 are uploaded to MOOD database as Excel files.

[5] https://www.metocean-on-demand.com

3 Normal Conditions Analyses

The normal metocean condition analyses are based on the output from the WRF high resolution atmospheric model (wind), DHI's 2D HD_{DWF23} hydrodynamic model (water level and currents), and DHI's SW_{DWF23} spectral wave model datasets (waves). The model datasets are available for 44 years (1979-01-15 to 2022-12-31) considering winds, water levels, depth-averaged currents, and waves. The surface currents have been derived through a theoretical vertical profile. The analyses presented were based on data extracted from the models at one (1) specified location, namely IJV1, in this report and delivered as accompanying digital appendices.

The normal metocean conditions analyses are summarised in the following sections:

- Wind: Section 3.1
- Water Level: Section 3.2
- Current: Section 3.3
- Wave: Section 3.4
- JPA (Wind-Wave): Section 3.5
- Other Metocean Parameters: Section 3.6

It is noted that for the first year of data (1979), a period of about 14 days has been removed from the beginning of the wind, water levels and waves datasets to remove any effect of the spin-up of the hydrodynamic and wave model. Furthermore, the results of the analysis of some parameters in this study, e.g., wind speed will not match the corresponding analysis carried out in [2], primarily due to different duration of the input time series used. In this study approximately 44 years of input data is used, whereas in [2], 13 years of input data is used.

The analyses are performed at a single location (IJV1), and the directional results are presented at 12 bins (30 degree centered at 0°N, 30°N, …). Details on the normal metocean condition analyses are summarised in Table 3.1.

Table 3.1 Normal metocean conditions analyses.
The normal conditions are delivered at **one (1) analysis location, IJV1,** as presented in this report, and the full set of results are provided as figures and Excel (.xlsx) tables in a digital appendix.

Category	Analysis	Variables	Unit	Type	Comments	
Wind	Rose Plot	WS_{10} WD_{10} WS_{160} WD_{160}	m/s °N-from	Omni	Heights: 10 m and 160 m	
	Weibull Parameters (Shape + Scale)	WS_{10} WS_{160}	m/s	Omni	Heights: 10 m and 160 m	
				Directional		
	Persistence	WS_{10}	m/s	Omni	Heights (mMSL)	10 m
					Thresholds (m/s)	2, 4, 6, 8, 9, 10, 11, 12, 15, 20 and 25
					Exceedance Probability (%)	20, 50, 80
					Time Window (1h)	1, 2, 4, 6, 12, 24, 48, 72
	Characteristic Profile	WS	m/s	Omni	From 10mMSL to 300mMSL	
	Turbulence Intensity	TI	-	Omni	Heights: 100 and 200 mMSL	
Water Level	Astronomical tidal levels	-	mMSL	N.A.	Levels: LAT, MLWS, MLWN, MSL, MHWN, MHWS, HAT	
Current	Rose Plot	$CS_{Total-Dep}$ $CS_{Tidal-Dep}$ $CS_{Residual-Dep}$ $CD_{Total-Dep}$ $CD_{Tidal-Dep}$ $CD_{Residual-Dep}$ $CS_{Total-Surf}$ $CS_{Tidal-Surf}$ $CS_{Residual-Surf}$ $CD_{Total-Surf}$ $CD_{Tidal-Surf}$ $CD_{Residual-Surf}$	m/s °N-to	Omni	Surface and Depth-averaged	
	Characteristic Profile	$CS_{Total-Dep}$ $CS_{Tidal-Dep}$ $CS_{Residual-Dep}$	m/s	Omni	From Mean Water Level to Seabed	

Category	Analysis	Variables	Unit	Type	Comments	
Waves	Rose Plot	$H_{m0\text{-}Total}$ + $T_{p\text{-}Total}$ PWD_{Total}	m s °N-from	Omni	For Total Components	
	Scatter Table	$H_{m0\text{-}Total}$ – $T_{p\text{-}Total}$, PWD_{Total}		Omni		
		$H_{m0\text{-}Total}$ – $T_{02\text{-}Total}$, PWD_{Total}		Directional		
	H–T scatter table	H, T	m, s	Omni		
	Normal Sea State Tables	WS_{160} – $H_{m0\text{-}Total}$, PWD_{Total}	m/s, m	Omni		
		$H_{m0\text{-}Total}$ - $T_{p\text{-}Total}$, PWD_{Total}	m, s	Directional		
	Persistence	$H_{m0\text{-}Total}$ $H_{m0\text{-}Sea}$ $H_{m0\text{-}Swell}$	m	Omni	Threshold (m)	0.25, 0.50, 0.75, 1.00, 1.25, 1.50, 1.75, 2.00, 2.25, 2.75, 3.00, 3.50, 4.00, 4.50, 5.00
					Exceedance Probability (%)	20, 50, and 80
					Time Window	1, 2, 4, 6, 12, 24, 48, 72
	Wave Spectrum	γ	-	Omni	Sea and Swell Components if Applicable	
Joint probability Wind-Wave	Misalignment Tables	WD_{160} – MWD_{Total}		Omni	Heights: Hub Height	
		$H_{m0\text{-}Total}$ – WD_{160}		Directional		
	Persistence	$H_{m0\text{-}Total}$ – WS_{10}		Omni	Wind Thresholds (m/s)	2, 4, 6, 8, 9, 10, 11, 12, 15, 20, 25
					Wave Thresholds (m)	0.25, 0.50, 0.75, 1.00, 1.25, 1.50, 1.75, 2.00, 2.25, 2.75, 3.00, 3.50, 4.00, 4.50, 5.00
					Exceedance Probability (%)	20, 50, and 80
					Time Window	1, 2, 4, 6, 12, 24, 48 and 72
Other metocean parameters	Statistics	Visibility Lightning		Omni		
		Rainfall Snow Ice accretion Sea Ice Marine Growth		Omni		

Category	Analysis	Variables	Unit	Type	Comments
Other metocean parameters (continued)	Statistics	T_{Sea} Salinity ρ_{sea}		Omni	Sea Surface
	Statistics	ρ_{air}	kg/m^3	Omni	Heights: Hub Height
		P_{air}	pa		
		RH	%		
		T_{air}	° C		

3.1 Wind

Presented in this section are the analyses conducted on the 10 mMSL and 160 mMSL wind speed (WS_{10} and WS_{160}) and wind direction (WD_{10} and WD_{160}) time series data for IJV1 for the period of 1979-01-15 to 2022-12-31 extracted from the WRF model datasets.

Results are presented showing time series plots, seasonal statistics, wind roses, and probability exceedance.

3.1.1 Time series and annual statistics

The WS_{10} and WS_{160} time series at IJV1 are presented in Figure 3.1. The average wind speed of WS_{10} and WS_{160} is 8.1 m/s and 10.3 m/s, respectively.

The maximum modelled wind speed values (30.2 m/s for WS_{10} and 39.5 m/s for WS_{160}) occurred during the "Great Storm" in 1987, which impacted the North Sea from 1987-10-15 to 1987-10-16. The annual statistics of WS_{10} and WS_{160} can be seen in Table 3.20.

Table 3.2 Annual statistics of WS [m/s] at IJV1.
Statistical analyses include the number of data points, mean, min, max and STD of wind speed at 10 mMSL.

Parameter	Number of data points	Mean [m/s]	Min [m/s]	Max [m/s]	STD [m/s]
WS_{10}	2,312,203	8.1	0.02	30.2	3.88
WS_{160}	2,312,203	10.3	0.03	39.5	5.21

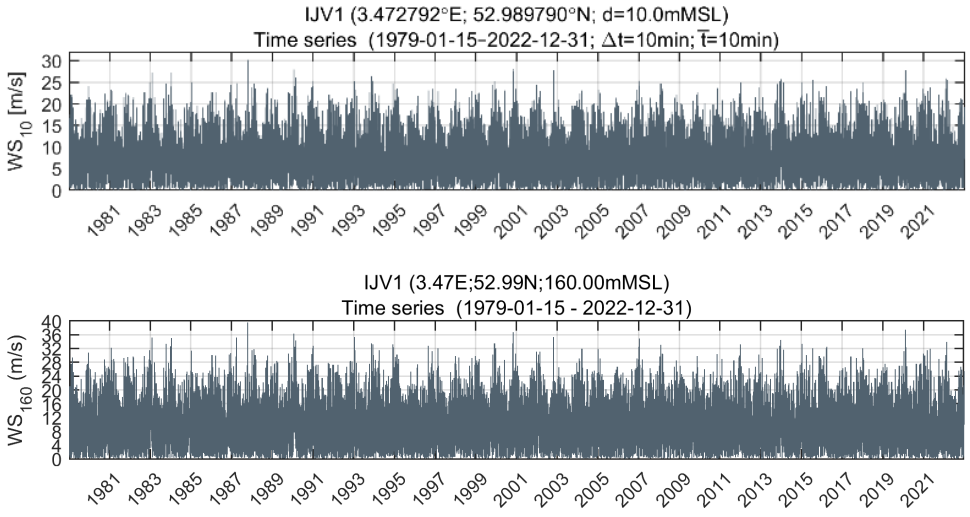

Figure 3.1 Time series of wind speed at 10 mMSL (WS_{10}) and 160 mMSL (WS_{160}) [m/s] at IJV1.
Time series of WS_{10} (top panel) and WS_{160} (bottom panel) values shown for the full period of analysis (1979-01-15 to 2022-12-31) for IJV1.

3.1.2 Wind Rose

Rose plots showing wind speeds (WS_{10} and WS_{160}) for the corresponding wind directions (WD_{10} and WD_{160}) at IJV1 are presented in Figure 3.2. The rose plots for IJV1 indicate that the wind is dominated by south-westerly winds (> 10% of the time), followed by westerly winds (~ 10% of the time). More detailed information on the occurrence frequency can be found in Table 3.3 and Table 3.4, for WS_{10} and WS_{160}, respectively.

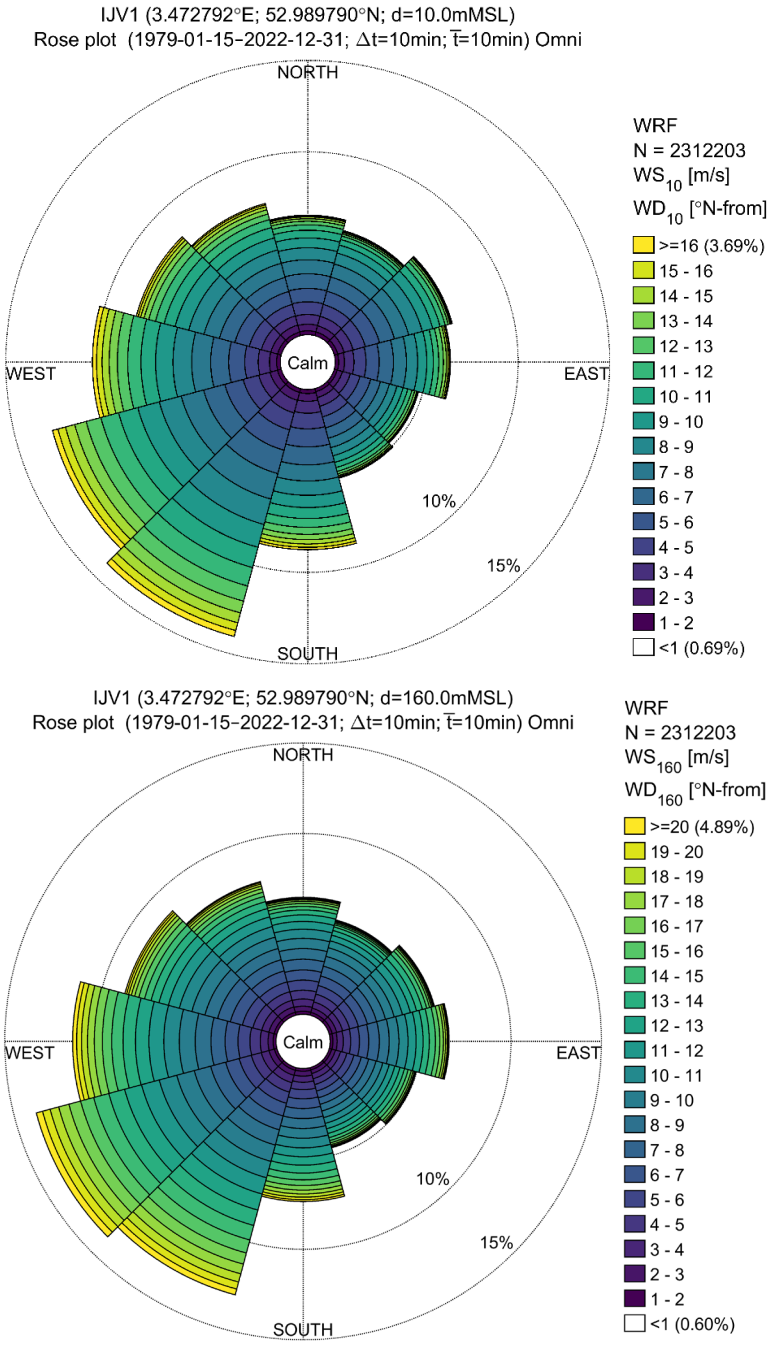

Figure 3.2 Wind rose plots of WS_{10} – WD_{10} and WS_{160} – WD_{160} [m/s] at IJV1. Wind roses at IJV1 are shown (WS_{10}-WD_{10} – top panel and WS_{160}-WD_{160} – bottom panel), where the analysis period covers 1979-01-15 to 2022-12-31. Directions are 'coming from'. The values represent 10-min average wind speed.

Table 3.3 Frequency of occurrence for WS_{10} [m/s] and WD_{10} [deg] at IJV1.
Table presents the directional results at each 1 m/s bin of WS_{10}.

WS_{10}\WD_{10}	[-15;15[	[15;45[	[45;75[	[75;105[	[105;135[	[135;165[	[165;195[	[195;225[	[225;255[	[255;285[	[285;315[	[315;345[	Total
[0-1[	0.06	0.06	0.06	0.06	0.05	0.05	0.06	0.06	0.06	0.06	0.06	0.06	0.69
[1-2[	0.21	0.21	0.20	0.19	0.16	0.18	0.22	0.22	0.21	0.20	0.21	0.20	2.39
[2-3[	0.36	0.35	0.36	0.32	0.30	0.33	0.42	0.45	0.42	0.39	0.38	0.40	4.48
[3-4[	0.53	0.53	0.51	0.52	0.45	0.49	0.65	0.71	0.64	0.62	0.54	0.52	6.71
[4-5[	0.69	0.67	0.69	0.66	0.55	0.60	0.86	0.96	0.88	0.74	0.69	0.65	8.64
[5-6[	0.73	0.75	0.81	0.72	0.60	0.62	0.99	1.15	1.04	0.88	0.81	0.73	9.84
[6-7[	0.80	0.80	0.84	0.78	0.55	0.59	0.98	1.32	1.20	0.98	0.87	0.80	10.51
[7-8[	0.77	0.74	0.81	0.71	0.51	0.54	0.88	1.44	1.27	1.04	0.87	0.80	10.37
[8-9[	0.66	0.62	0.77	0.61	0.43	0.46	0.78	1.44	1.24	1.02	0.87	0.76	9.66
[9-10[	0.54	0.45	0.59	0.50	0.35	0.37	0.67	1.29	1.22	0.95	0.77	0.68	8.38
[10-11[	0.42	0.31	0.42	0.36	0.27	0.29	0.60	1.15	1.09	0.80	0.62	0.59	6.90
[11-12[	0.29	0.20	0.29	0.30	0.24	0.22	0.48	1.05	1.01	0.72	0.49	0.45	5.72
[12-13[	0.19	0.12	0.18	0.25	0.16	0.14	0.39	0.86	0.83	0.57	0.38	0.32	4.37
[13-14[	0.14	0.08	0.10	0.17	0.11	0.10	0.29	0.66	0.65	0.45	0.27	0.24	3.25
[14-15[	0.10	0.06	0.05	0.10	0.05	0.07	0.24	0.56	0.53	0.39	0.19	0.17	2.51
[15-16[	0.06	0.03	0.04	0.07	0.03	0.05	0.18	0.44	0.43	0.30	0.14	0.11	1.88
[16-17[	0.04	0.02	0.03	0.05	0.02	0.03	0.13	0.34	0.30	0.22	0.11	0.08	1.36
[17-18[	0.02	0.01	0.02	0.03	0.01	0.02	0.09	0.24	0.20	0.18	0.07	0.05	0.93
[18-19[	0.01	0.01	0.01	0.01	0.01	0.01	0.06	0.15	0.14	0.12	0.05	0.04	0.60
[19-20[	0.01	0.00	0.01	0.01	0.00	0.00	0.04	0.08	0.07	0.08	0.03	0.02	0.35
[20-21[	0.00	0.00	0.00	0.00	0.00	0.00	0.02	0.05	0.04	0.05	0.02	0.01	0.20
[21-22[	0.00	0.00	0.00	0.00	0.00	0.00	0.01	0.03	0.02	0.03	0.01	0.00	0.11
[22-23[	0.00	0.00	0.00	0.00	0.00	0.00	0.01	0.02	0.01	0.02	0.01	0.00	0.06
[23-24[	0.00	0.00	0.00	0.00	0.00	0.00	0.00	0.01	0.01	0.01	0.00	0.00	0.04
[24-25[	0.00	0.00	0.00	0.00	0.00	0.00	0.00	0.00	0.01	0.01	0.00	0.00	0.02
[25-26[	0.00	0.00	0.00	0.00	0.00	0.00	0.00	0.00	0.00	0.00	0.00	0.00	0.01
Total	6.64	6.03	6.78	6.41	4.84	5.15	9.06	14.68	13.49	10.82	8.44	7.67	100.00

Table 3.4 Frequency of occurrence for WS_{160} [m/s] and WD_{160} [deg] at IJV1.
Table presents the directional results at each 1 m/s bin of WS_{160}.

WS_{160}\WD_{160}	[-15;15[	[15;45[	[45;75[	[75;105[	[105;135[	[135;165[	[165;195[	[195;225[	[225;255[	[255;285[	[285;315[	[315;345[	Total
[0-1[	0.05	0.05	0.05	0.05	0.04	0.04	0.05	0.05	0.05	0.05	0.05	0.06	0.60
[1-2[	0.17	0.16	0.17	0.15	0.14	0.13	0.15	0.15	0.15	0.16	0.16	0.17	1.85
[2-3[	0.28	0.25	0.26	0.24	0.21	0.21	0.27	0.29	0.31	0.28	0.30	0.30	3.19
[3-4[	0.40	0.35	0.34	0.34	0.29	0.30	0.34	0.42	0.44	0.43	0.41	0.38	4.43
[4-5[	0.49	0.45	0.41	0.41	0.37	0.34	0.41	0.54	0.57	0.57	0.51	0.49	5.55
[5-6[	0.56	0.49	0.50	0.48	0.40	0.37	0.51	0.64	0.70	0.66	0.60	0.57	6.47
[6-7[	0.56	0.54	0.52	0.51	0.42	0.38	0.54	0.72	0.77	0.72	0.69	0.63	7.01
[7-8[	0.60	0.56	0.53	0.58	0.42	0.37	0.56	0.80	0.86	0.78	0.73	0.64	7.42
[8-9[	0.59	0.56	0.51	0.55	0.42	0.39	0.55	0.87	0.94	0.87	0.73	0.64	7.62
[9-10[	0.56	0.49	0.50	0.54	0.39	0.38	0.54	0.93	1.00	0.88	0.75	0.65	7.61
[10-11[	0.51	0.39	0.48	0.51	0.37	0.33	0.53	0.94	1.01	0.86	0.71	0.61	7.23
[11-12[	0.43	0.33	0.45	0.45	0.32	0.31	0.49	0.93	1.01	0.82	0.63	0.56	6.72
[12-13[	0.36	0.27	0.36	0.38	0.30	0.27	0.46	0.92	0.97	0.75	0.54	0.48	6.05
[13-14[	0.28	0.21	0.34	0.35	0.26	0.24	0.44	0.88	0.91	0.69	0.45	0.40	5.42
[14-15[	0.20	0.12	0.25	0.33	0.21	0.17	0.38	0.83	0.87	0.62	0.37	0.30	4.65
[15-16[	0.16	0.09	0.17	0.24	0.18	0.13	0.31	0.75	0.75	0.52	0.33	0.24	3.85
[16-17[	0.12	0.07	0.10	0.20	0.11	0.11	0.25	0.64	0.67	0.45	0.25	0.20	3.15
[17-18[	0.09	0.05	0.07	0.13	0.08	0.07	0.21	0.56	0.59	0.38	0.19	0.15	2.55
[18-19[	0.06	0.04	0.05	0.09	0.05	0.05	0.18	0.47	0.49	0.33	0.16	0.11	2.07
[19-20[	0.05	0.02	0.04	0.06	0.03	0.04	0.14	0.40	0.43	0.27	0.12	0.08	1.66
[20-21[	0.03	0.02	0.02	0.04	0.02	0.02	0.11	0.33	0.36	0.22	0.10	0.06	1.32
[21-22[	0.02	0.01	0.02	0.02	0.01	0.02	0.08	0.29	0.29	0.18	0.07	0.05	1.03
[22-23[	0.01	0.00	0.01	0.01	0.01	0.01	0.06	0.23	0.23	0.13	0.05	0.04	0.78
[23-24[	0.01	0.00	0.00	0.01	0.00	0.00	0.04	0.17	0.18	0.11	0.04	0.02	0.59
[24-25[	0.00	0.00	0.01	0.00	0.00	0.00	0.03	0.13	0.12	0.08	0.02	0.02	0.42
[25-26[	0.00	0.00	0.00	0.00	0.00	0.00	0.02	0.09	0.07	0.05	0.02	0.01	0.26
[26-27[	0.00	0.00	0.00	0.00	0.00	0.00	0.02	0.06	0.04	0.03	0.01	0.01	0.16
[27-28[	0.00	0.00	0.00	0.00	0.00	0.00	0.01	0.04	0.03	0.02	0.01	0.00	0.11
[28-29[	0.00	0.00	0.00	0.00	0.00	0.00	0.01	0.02	0.02	0.02	0.01	0.00	0.07
[29-30[	0.00	0.00	0.00	0.00	0.00	0.00	0.00	0.02	0.01	0.01	0.00	0.00	0.05
[30-31[	0.00	0.00	0.00	0.00	0.00	0.00	0.00	0.01	0.01	0.01	0.00	0.00	0.04
[31-32[	0.00	0.00	0.00	0.00	0.00	0.00	0.00	0.01	0.01	0.00	0.00	0.00	0.03
[32-33[	0.00	0.00	0.00	0.00	0.00	0.00	0.00	0.01	0.00	0.00	0.00	0.00	0.01
[33-34[	0.00	0.00	0.00	0.00	0.00	0.00	0.00	0.00	0.00	0.00	0.00	0.00	0.01
Total	6.57	5.53	6.11	6.67	5.04	4.67	7.67	14.13	14.84	11.94	8.99	7.85	100.00

3.1.3 Histogram

The probability of occurrence of the WS_{10} and WS_{160} can be seen in Figure 3.3, with data binned per 1 m/s, and respective Weibull parameters (scale, shape, and frequency). The majority of data occurrence (frequency of 10%) are in the bin of 6-7 m/s and 7-8 m/s for WS_{10}, while the highest occurrence (frequency of 7%) for WS_{160} is within 7-10 m/s bins. The statistics including mean (m), scale (A), shape (k), and frequency and can be consulted in Table 3.5 and Table 3.6.

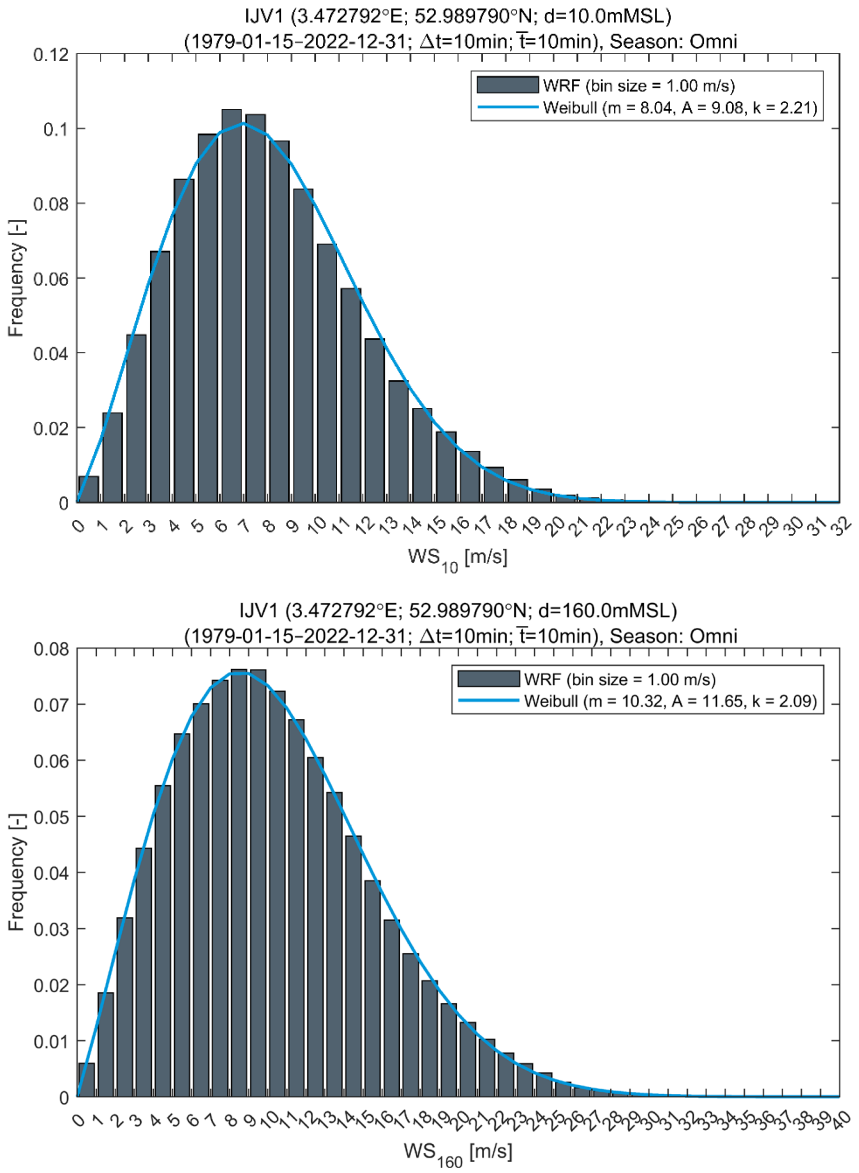

Figure 3.3 Probability WS_{10} and WS_{160} [m/s] at IJV1.
Wind probability (WS_{10} and WS_{160}) at IJV1 is shown where the analysis period covers 1979-01-15 to 2022-12-31. Data binned by 1 m/s.

Table 3.5 Weibull statistics for WS_{10}.
The Weibull statistics include mean, scale, shape, and frequency per directional bin.

Directions	Mean [m/s]	Scale, A [m/s]	Shape, k [-]	Frequency, f [-]
Omni	8.04	9.08	2.21	1.00
0	7.17	8.09	2.30	0.07
30	6.73	7.60	2.41	0.06
60	7.09	7.99	2.47	0.07
90	7.30	8.25	2.25	0.06
120	6.92	7.82	2.19	0.05
150	6.88	7.77	2.17	0.05
180	7.94	8.96	2.11	0.09
210	9.09	10.26	2.36	0.15
240	9.15	10.32	2.37	0.13
270	8.92	10.07	2.23	0.11
300	8.06	9.10	2.29	0.08
330	7.89	8.91	2.26	0.08

Table 3.6 Weibull statistics for WS_{160}.
The Weibull statistics include mean, scale, shape, and frequency per directional bin.

Directions	Mean [m/s]	Scale, A [m/s]	Shape, k [-]	Frequency, f [-]
Omni	10.32	11.65	2.09	1.00
0	8.69	9.81	2.15	0.07
30	8.13	9.18	2.23	0.06
60	8.90	10.05	2.20	0.06
90	9.46	10.68	2.18	0.07
120	8.95	10.10	2.11	0.05
150	8.89	10.04	2.07	0.05
180	10.42	11.76	2.05	0.08
210	12.20	13.78	2.25	0.14
240	12.07	13.63	2.27	0.15
270	11.22	12.67	2.16	0.12
300	9.88	11.16	2.16	0.09
330	9.49	10.71	2.14	0.08

3.1.4 Persistence/Weather Windows

The persistence of wind parameters is reported in this section. A description of persistence analyses is provided in Appendix B.

Workability tables for different parameters for offshore operations are supplied as digital appendices regarding the parameters of $WS_{10,}$ considering different time windows, threshold values and quantiles. Table 3.7 summarises the workability tables provided at IJV1. Tables are delivered as digital appendices and an example table for IJV1 is provided in this section.

Table 3.7 Workability (weather-windows) tables for WS_{10}.
The criteria for the workability analyses are specified in the table (parameter, time windows, threshold values and percentiles) for IJV1.

Parameter	Time Windows [h]	Threshold [m/s]	Percentiles
WS_{10} [m/s]	1, 2, 4, 6, 12, 24, 48, 72	2, 4, 6, 8, 9, 10, 11, 12, 15, 20 and 25	P20, P50 and P80

Examples of WS_{10} weather windows with a duration of 24 hours (non-overlapping) and with 50 % probability of exceedance estimates at IJV1 are presented in Figure 3.4. The corresponding table is shown in Table 3.8. The horizontal bars in the figures indicate the plus/minus one (1) standard deviation for each threshold, which are also designated by the numbers in the parentheses in Table 3.8. The standard deviations in these figures describe how much the data varies from the mean due to the interannual variability of the analysed period.

The example at IJV1 with 50 % percentile (Figure 3.4 and Table 3.8) shows that for a typical month of June, there is a 98.3 % chance of wind speeds below 15 m/s for a 24 hour period and a 1.7 % chance of wind speeds above 15 m/s during a 24 hours period. For winds below 15 m/s in December, the chance decreases to 75.6 % and 24.4 % probability of winds above 15 m/s.

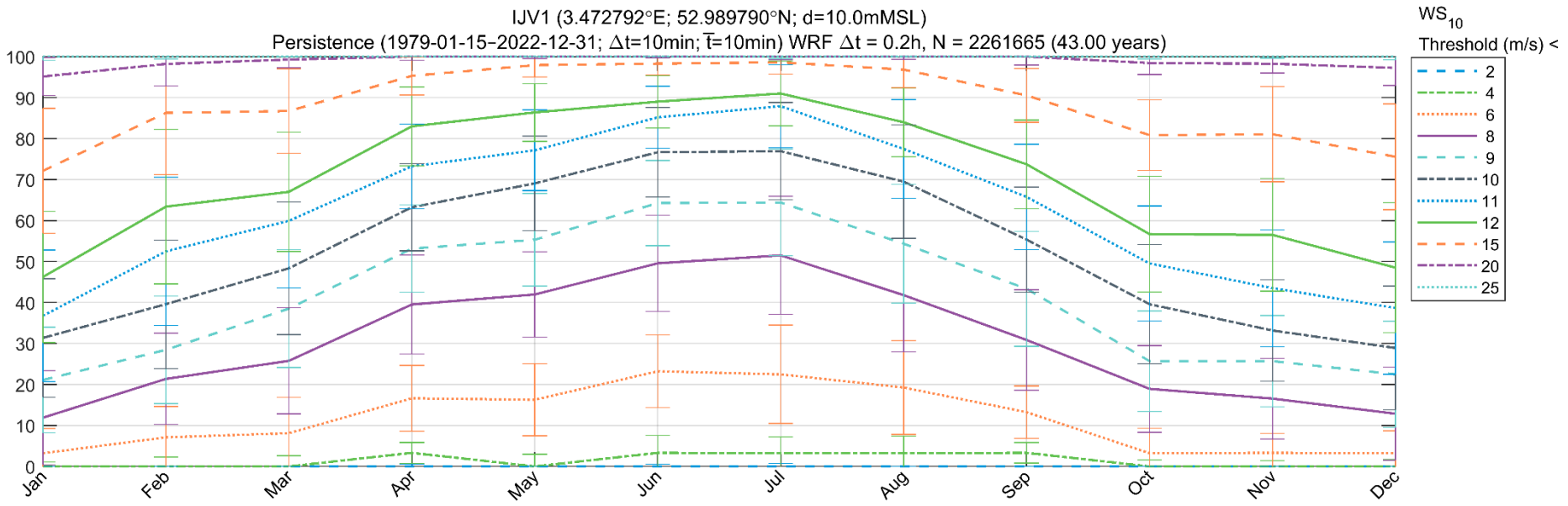

Figure 3.4 **Example of persistence (weather-window) analysis of wind speed (WS_{10}) [m/s] at IJV1.**
The analysis considers a duration of at least 24 hours (non-overlapping) and P=50% from 1979-01-15 to 2022-12-31 with thresholds varying between 2 m/s and 25 m/s.

Table 3.8 **Example table of persistence (weather-window) analysis table of wind speed (WS_{10}) [m/s] at IJV1.**
Considering a duration of at least 24-hours (non-overlapping) and P=50% the values correspond to the lines shown in Figure 3.4 while the values in parenthesis are one (1) plus/minus standard deviation representing the interannual variability of the period spanning from 1979-01-15 to 2022-12-31.

IJV1 (3.472792°E; 52.989790°N; d=10.0mMSL)
Persistence (1979-01-15–2022-12-31; Δt=10min; $\bar{t}$=10min) WRF Δt = 0.2h, N = 2261665 (43.00 years)
Weather Windows$_{P=50\%} \geq$ 24h (Non-Overlapping) [%]

WS_{10} Threshold (m/s) <	Jan	Feb	Mar	Apr	May	Jun	Jul	Aug	Sep	Oct	Nov	Dec
2	0.0 (0.0)	0.0 (0.0)	0.0 (0.0)	0.0 (0.5)	0.0 (0.0)	0.0 (0.5)	0.0 (0.7)	0.0 (0.0)	0.0 (0.0)	0.0 (0.0)	0.0 (0.0)	0.0 (0.0)
4	0.0 (1.0)	0.0 (2.3)	0.0 (2.6)	3.3 (2.5)	0.0 (3.0)	3.3 (4.2)	3.2 (4.0)	3.2 (4.2)	3.3 (2.5)	0.0 (1.6)	0.0 (1.4)	0.0 (1.7)
6	3.2 (6.1)	7.1 (7.5)	8.1 (8.8)	16.6 (8.0)	16.3 (8.8)	23.2 (8.9)	22.5 (12.0)	19.2 (11.5)	13.2 (6.4)	3.2 (6.1)	3.3 (4.7)	3.2 (5.5)
8	11.9 (11.5)	21.4 (11.2)	25.8 (12.9)	39.5 (12.0)	42.0 (10.4)	49.6 (11.8)	51.5 (14.4)	41.8 (13.8)	30.9 (12.3)	18.9 (10.6)	16.6 (9.9)	12.9 (11.3)
9	21.1 (12.9)	28.4 (13.1)	38.5 (14.4)	53.1 (10.6)	55.3 (11.3)	64.3 (10.4)	64.4 (13.0)	54.3 (14.5)	43.3 (14.0)	25.7 (12.3)	25.7 (11.1)	22.5 (12.9)
10	31.4 (14.5)	39.6 (15.7)	48.3 (16.2)	63.2 (10.7)	69.1 (11.5)	76.7 (10.9)	76.9 (11.9)	69.5 (13.8)	55.3 (12.9)	39.6 (14.5)	33.2 (12.4)	28.9 (15.1)
11	36.8 (16.1)	52.5 (18.1)	59.9 (16.4)	73.2 (10.3)	77.1 (9.9)	85.2 (7.6)	87.9 (10.2)	77.5 (12.0)	65.8 (12.8)	49.5 (14.0)	43.5 (14.3)	38.6 (16.2)
12	46.2 (16.0)	63.4 (18.8)	67.0 (14.5)	83.0 (9.6)	86.4 (7.0)	89.0 (6.4)	91.0 (7.9)	84.0 (8.4)	73.7 (10.8)	56.7 (14.1)	56.5 (13.8)	48.5 (15.9)
15	72.1 (15.2)	86.3 (15.1)	86.7 (10.3)	95.3 (4.7)	97.9 (2.8)	98.3 (2.8)	98.6 (2.9)	96.8 (4.4)	90.5 (6.6)	80.8 (8.6)	81.1 (11.6)	75.6 (12.9)
20	95.1 (4.7)	98.2 (5.4)	99.3 (2.0)	100.0 (0.9)	100.0 (0.5)	100.0 (0.3)	100.0 (0.8)	100.0 (0.7)	100.0 (2.0)	98.4 (2.8)	98.3 (2.3)	97.2 (4.3)
25	100.0 (0.9)	100.0 (0.6)	100.0 (0.0)	100.0 (0.0)	100.0 (0.0)	100.0 (0.0)	100.0 (0.5)	100.0 (0.0)	100.0 (0.0)	100.0 (0.6)	100.0 (0.4)	100.0 (0.7)

3.1.5 Wind shear

The wind shear is presented in Section 3.3.2 and 3.3.4 of WRA [2]. The vertical wind shear profile is characterized by a power law given by

$$\mathrm{WS}_{z_2} = \mathrm{WS}_{z_1} \times \left(\frac{z_2}{z_1}\right)^{\alpha} \quad \textbf{(3.1)}$$

Where WS_z is the wind speed at height z, and α is the wind shear coefficient. The overall wind shear coefficient of $\alpha = 0.07$ can be used at IJV1.

3.1.6 Turbulence intensity

The turbulence intensity is presented in section 6.6 of WRA [2], where the analyses are provided at 92 mMSL. Table 3.9 provides the mean ambient TI (taken from [2]) for a typical range between the cut-in and cut-out wind speeds estimated at using the MMIJ measurements.

Table 3.9 Mean ambient TI (%) at 92 m estimated at MMIJ

Mean wind speed (m/s)	Mean ambient TI (%)
3	9.1
4	7.7
5	6.7
6	6.2
7	5.7
8	5.4
9	5.3
10	5.3
11	5.2
12	5.1
13	5.2
14	5.3
15	5.5
16	5.6
17	5.8
18	6.0
19	6.4
20	6.6
21	6.7
22	6.8
23	7.1
24	7.4
25	7.6

The present report considers a hub height of 160 mMSL. Because there are no reliable TI measurements at 160 mMSL, and considering that turbulence decreases with increasing height [5], the TI estimates provided in Table 3.9 can be used at 160 mMSL as a conservative estimate.

3.2 Water levels

Presented in this section are the analyses conducted on the total, tidal and residual water level (WL_{Total}, WL_{Tide} and $WL_{Residual}$) time series data for IJV1. Results are displayed, featuring time series plots, seasonal statistics, and tidal datums, with a temporal resolution of 30 minutes.

Absolute values are reported relative to mean sea level (MSL) and to lowest astronomical tide (LAT); however, all graphs present the results referenced to MSL only. The distance MSL-LAT extracted from the model results was applied afterwards to convert levels relative to MSL at equivalent levels referenced to LAT.

3.2.1 Tidal levels

The astronomical tidal water level variations were calculated using harmonic analysis. Parameters including HAT and LAT values, are defined.

Modelled water levels were subjected to a harmonic tidal analysis to separate the tidal and non-tidal (residual) components. The harmonic analysis was conducted using the U-tide toolbox, see[6], which is based on the IOS tidal analysis method described by [7] and integrates the approaches in [8] and[9]. The analysis considered 68 constituents. The astronomical tide levels were derived by decomposing the total water levels into predicted tidal level and the residual component (total minus tidal component). The tidal constituents (phase and amplitude) used in the tidal analysis of water level at IJV1 are shown in Figure 3.5.

The astronomical values of WL_{Tide} that will be derived from the modelled tidal water levels (WL_{Total}) time series are as follows:

- Highest Astronomical Tide (HAT): the maximum predicted $WL_{Tide.}$
- Mean High-Water Spring (MHWS): the average of the two successive high waters reached during the 24-hours when the tidal range is at its greatest (i.e., spring tides).
- Mean Sea Level (MSL): the mean (average) of the predicted $WL_{Tide.}$
- Mean Low-Water Springs (MLWS): the average of the two successive low waters reached during the 24 hours when the tidal range is at its greatest (spring tide).
- Lowest Astronomical Tide (LAT): the minimum predicted WL_{Tide}.

Table 3.10 summarises the tidal levels based on WL_{Tide} at IJV1.

Table 3.10 Tidal levels at IJV1 [mMSL].
Tidal levels were processed from the WL_{Tide} time series data for the tidal levels between 1979-01-15 and 2022-12-31.

Tidal levels	IJV1 [mMSL]
HAT	0.89
MHWS	0.52
MHWN	0.22
MSL	0.00
MLWN	-0.31
MLWS	-0.66
LAT	-0.90

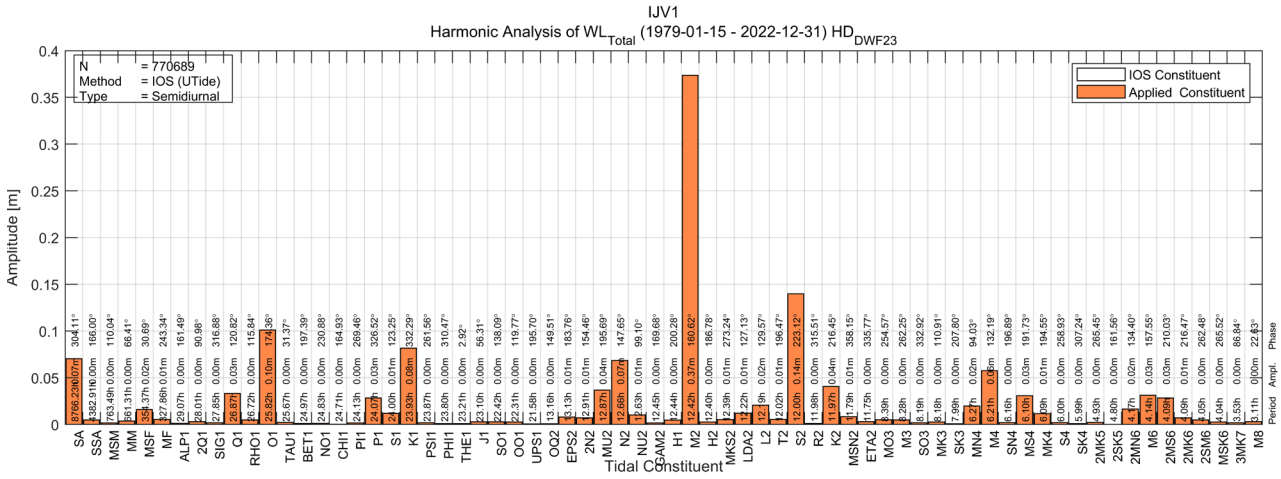

Figure 3.5 Tidal constituents (phase and amplitude) at IJV1.
Tidal constituents applied in the harmonic analysis of water level.

3.2.2 Time series and annual statistics

The WL_{Total}, WL_{Tide} and $WL_{Residual}$ time series at IJV1 are presented in Figure 3.6. The maximum total WL_{Total} and residual $WL_{Residual}$ water level is 2.29 mMSL and 2.10 mMSL, respectively. Analysing Figure 3.6 one can see that both the tidal component (blue line) and residual component (green line) will contribute to the total component IJV1 site. However, during normal conditions, the tide is the main driver of the flow.

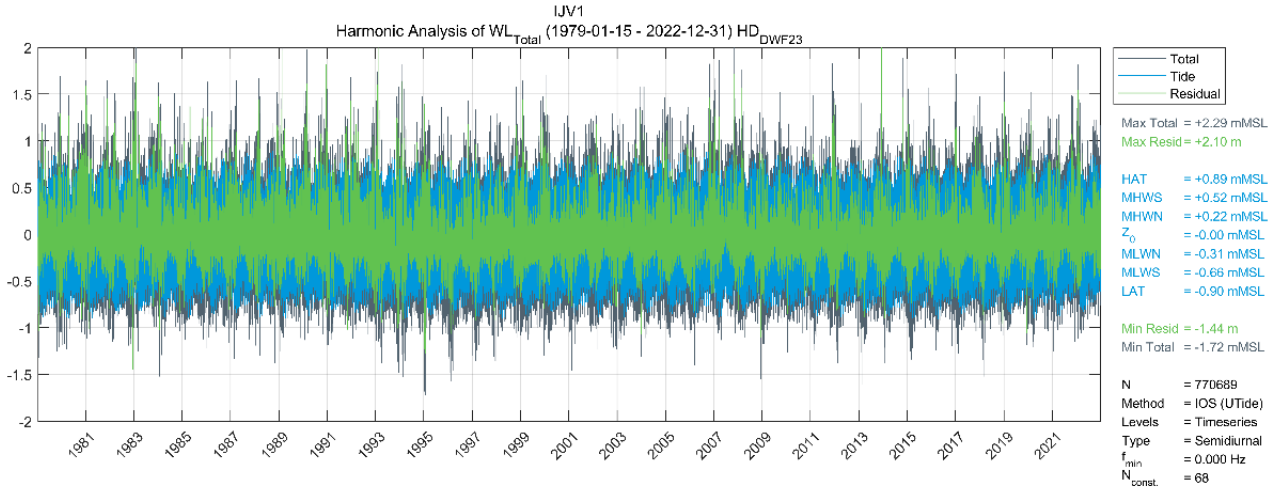

Figure 3.6 Time series of WL_{Total}, WL_{Tide} and $WL_{Residual}$ (mMSL) at IJV1.
Time series of WL_{Total}, WL_{Tide} and $WL_{Residual}$ (values shown for the full period of analysis (1979-01-15 to 2022-12-31) for IJV1.

Table 3.11 Annual statistics of WL_{Total} [m], WL_{Tide} [m], $WL_{Residual}$ [m] at IJV1.
Statistical analyses include the number of data points, mean, min, max and STD of WL_{Total}, WL_{Tide}, and $WL_{Residual}$ at IJV1.

Parameter	Number of data points	Mean	Min	Max	STD
WL_{Total} [mMSL]	770689	0.00	-1.72	2.29	0.39
WL_{Total} [mLAT]	770689	0.00	-2.62	1.39	0.39
WL_{Tide} [mMSL]	770689	0.00	-0.90	0.89	0.32
WL_{Tide} [mLAT]	770689	0.00	0.00	1.79	0.32
$WL_{Residual}$ [m]	770689	0.00	-1.44	2.10	0.22

3.3 Currents

Presented in this section are the analyses conducted on the total, tidal and residual current speeds for the depth-averaged ($CS_{Total-Dep}$, $CS_{Tide-Dep}$, and $CS_{Residual-Dep}$) and for surface ($CS_{Total-Surf}$, $CS_{Tide-Surf}$ and $CS_{Residual-Surf}$) time series data for IJV1. Results are presented by time series plots, annual statistics, current roses, and the current characteristic profile to obtain the current values at surface.

3.3.1 Characteristic current profile

Current profiles under normal conditions are analysed using the following approach.

1. Guidelines from the IEC [10] and DNV [11] standards are used to establish a current profile.

2. Data from four (4) measuring stations, namely IJVA, IJVB, NWA and NWB, are used in combination with the design standards [10, 11].
3. A power law coefficient α is recommended to derive current profiles under normal conditions at IJV1.

3.3.1.1 Guidelines from the standards

The IEC [10] and DNV [11] standards recommend using a power law profile (see Section 4.1.4.2 in [11]), as given by Eq. (3.2):

$$\mathrm{CS}_{\mathrm{tide}}(\mathrm{z}) = \mathrm{CS}_{\mathrm{tide}}(0) \times \left(\frac{d+z}{d}\right)^{\alpha} \quad for\ z \leq 0 \tag{3.2}$$

where z is the distance from still water level, positive upwards, and d is the water depth to still water level (taken positive). It is noted that Eq. (3.2) is applicable to tidal component of the current speed. As noted in section 3.3.2.1, under normal conditions, the tidal component is dominant in comparison to the residual component. Therefore, Eq. (3.2) can be applied to CS_{Tide} and CS_{Total}. The current profile is therefore dependent on the value of α, which is estimated using measurements in the vicinity of IJV1.

3.3.1.2 Analysis of measurements

Figure 3.7 shows the locations of four measurement stations, IJVA, IJVB, NWA, and NWB, relative to IJV1. It is noted that the surface and near-seabed measurements have been previously discarded as explained in the modelling report [3]. Extension of the theoretical profile given in Eq. (3.2) is applied to obtain the surface and near-seabed current speeds.

Figure 3.8 shows the current profiles (using all data) at the four locations as well as the mean and 50 % of the measurements. Theoretical profile is plotted using Eq. (3.1) and a typical value of $\alpha = 1/7$ is used. From Figure 3.8, it is not apparent whether $\alpha = 1/7$ provides the best fit at all locations. Therefore, further investigation is carried out to find the best α fit at the four measurement stations.

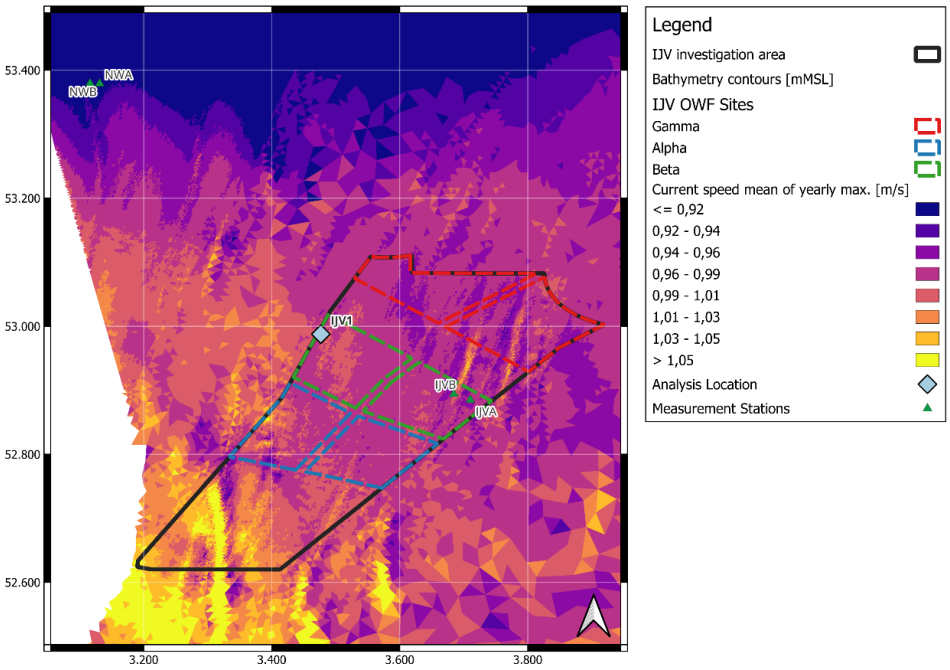

Figure 3.7 Current speed spatial map [m/s] at IJVWFZ and measuring stations (IJVA, IJVB, NWA and NWB).
The maps show the mean of the yearly maxima of current speeds at the IJVWFZ. IJV1 can be seen as a blue rhombus and measurements stations as green triangles.

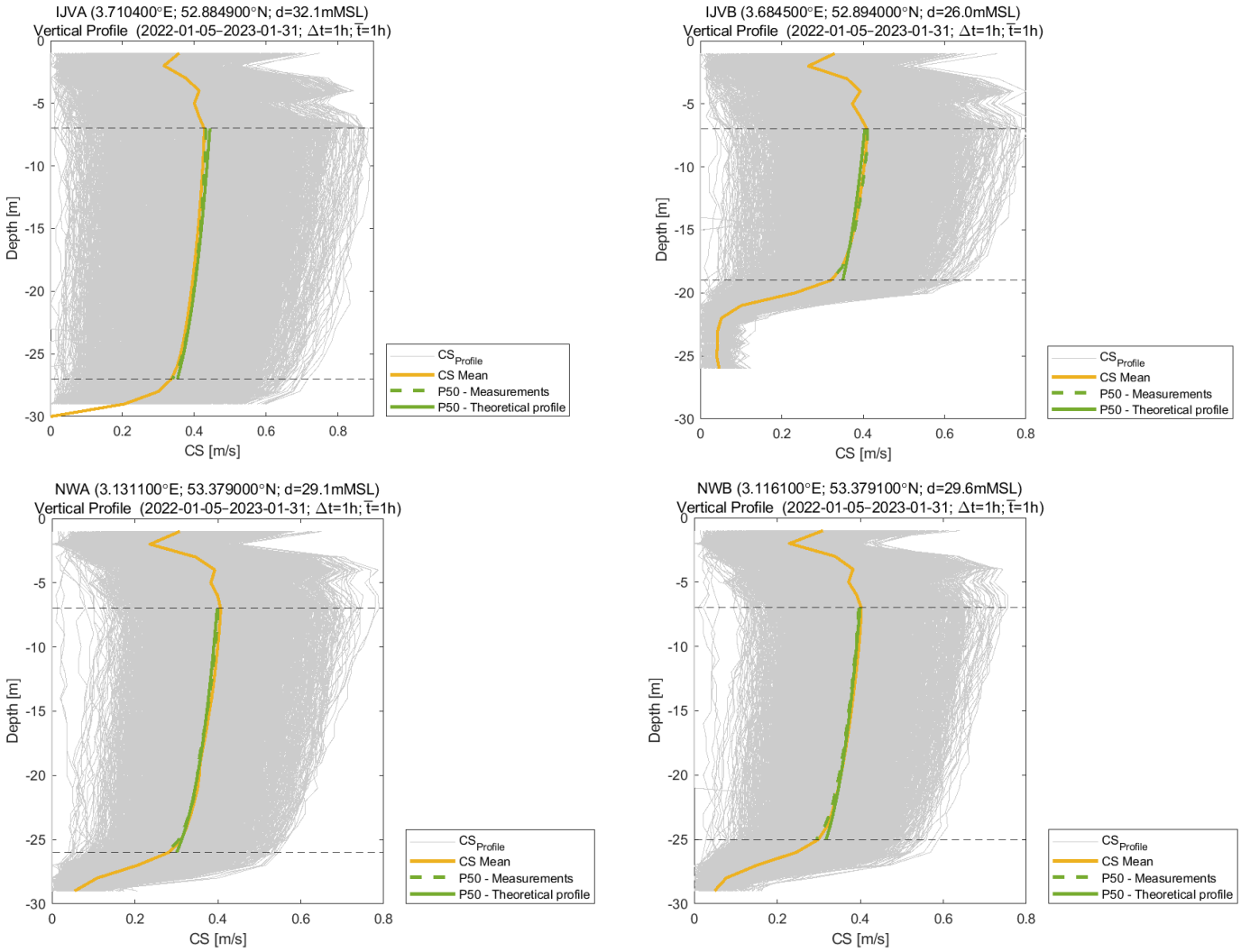

Figure 3.8 **Measured and fitted current profiles at IJVA (top left), IJVB (top right), NWA (bottom left), and NWB (bottom right).**
Theoretical profile is obtained using $\alpha = 1/7$ at all stations. The mean and 50% profiles are also shown.

Figure 3.9 - Figure 3.12 show the variation in the fitted current profile using Eq. (3.2) for different values of α at the four measurement stations. The measurements correspond to the 50% percentile of the measurements at each depth bin. For normal conditions, using the 50% is considered an adequate representation. The measurements and theoretical profile have been normalized by the depth-averaged value at each station. The current speed at 2/5th depth is considered as depth average current speed.

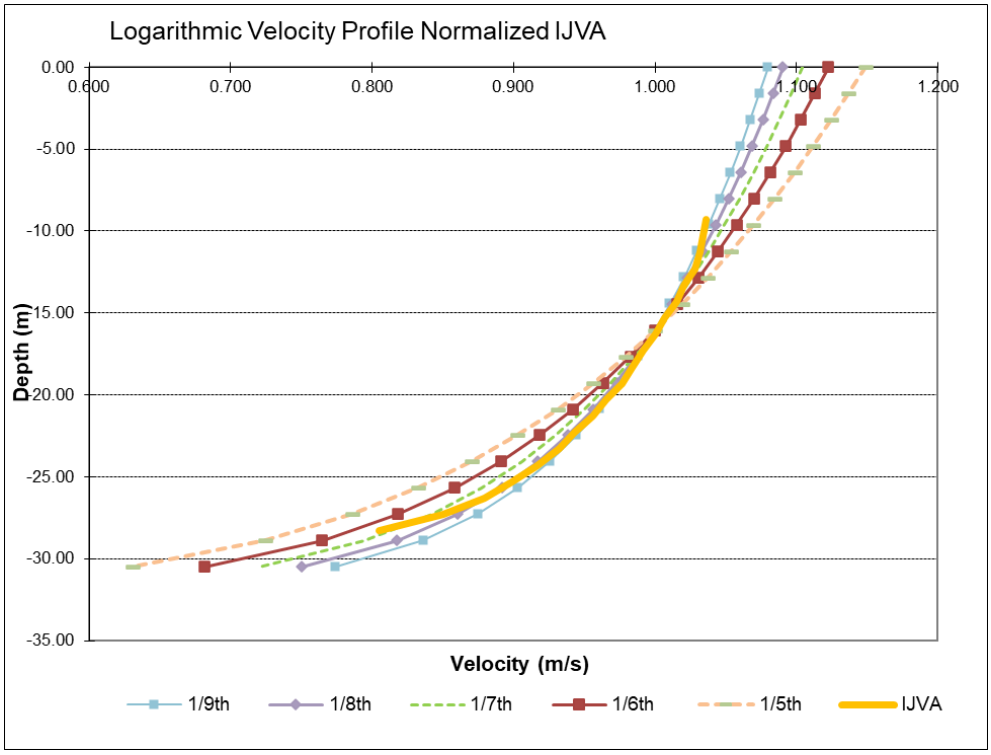

Figure 3.9 Normalized current profile of IJVA for normal conditions. The data show several profiles with distinct α values for the period of analyses (2022-05-01 to 2023-01-31). Measured profile (50%) is shown as solid yellow line.

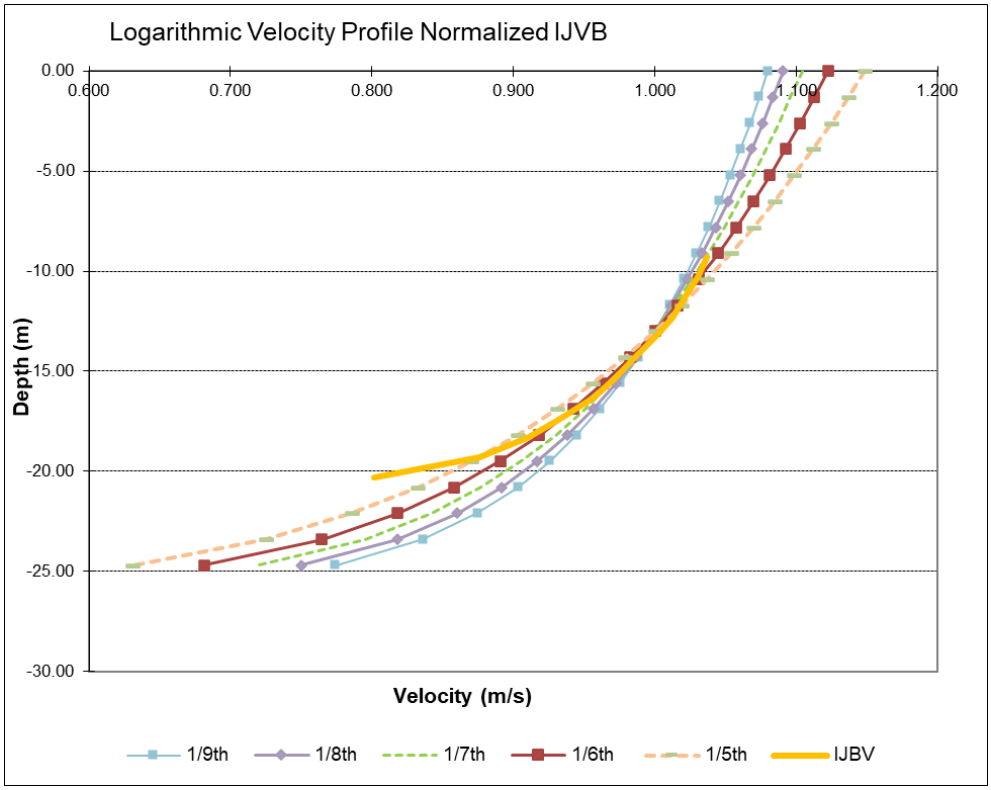

Figure 3.10 Normalized current profile of IJVB for normal conditions. The data show several profiles with distinct α values for the period of analyses (2022-05-01 to 2023-01-31). Measured profile (50%) is shown as solid yellow line.

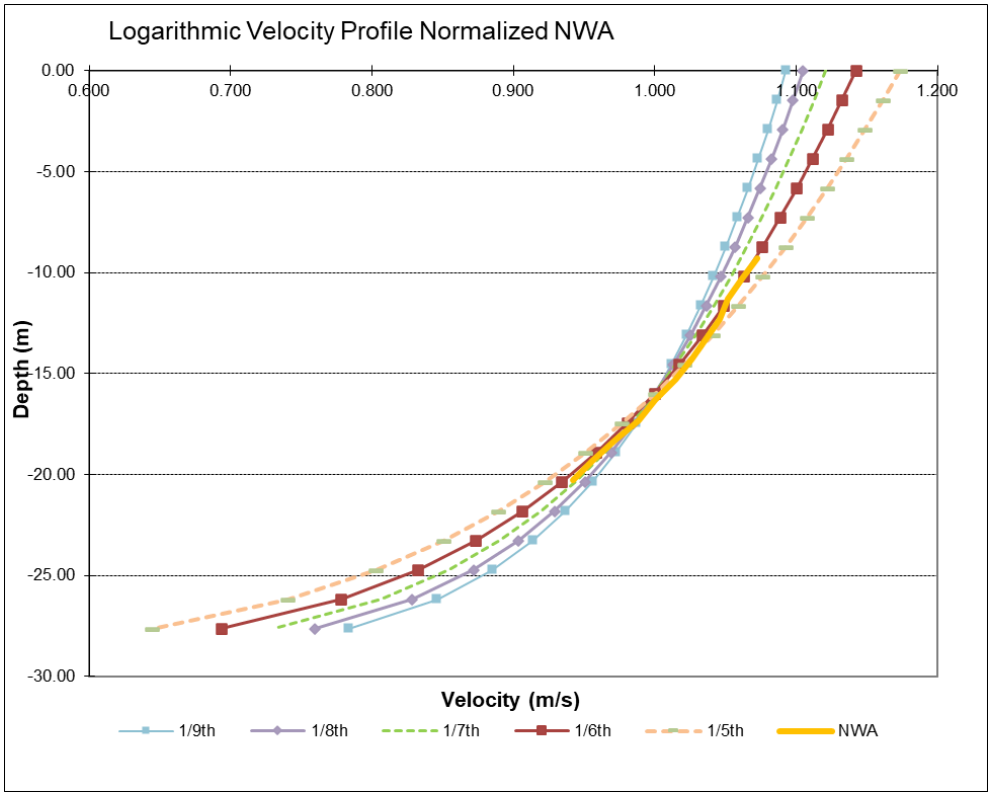

Figure 3.11 Normalized current profile of NWA for normal conditions. The data show several profiles with distinct α values for the period of analyses (2022-05-01 to 2023-01-31). Measured profile (50%) is shown as solid yellow line.

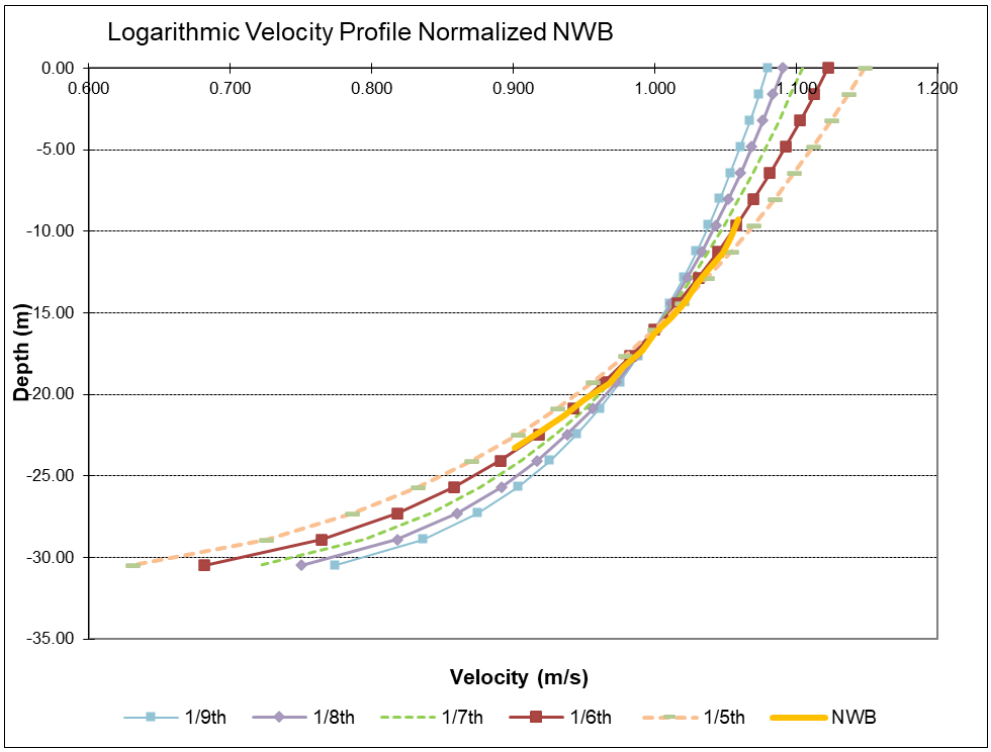

Figure 3.12 Normalized current profile of NWB for normal conditions. The data show several profiles with distinct α values for the period of analyses (2022-05-01 to 2023-01-31). Measured profile (50%) is shown as solid yellow line.

At IJVA (Figure 3.9), the best fit for surface currents is closer to $\alpha = 1/9$, whilst for the bottom currents appears to be $\alpha = 1/8$. At IJVB, as seen in Figure 3.10, a value of $\alpha = 1/6$ seems to be the most appropriate up to a depth of 18 m. Below 18 m, the profile with $\alpha = 1/6$ slightly overestimates the currents near the seabed. For both NWA and NWB (Figure 3.11 and Figure 3.12), a value of $\alpha = 1/6$ shows to be the best fit over all water column.

It is interesting to note that despite the measurement stations IJVA and IJVB being separated by only 1 km from each other, they show different behaviour of the current profile. A closer inspection of the bathymetric features is provided in Figure 3.13, which shows that IJVA is at the trough of the sand wave, whereas IJVB is at the crest of the sand wave.

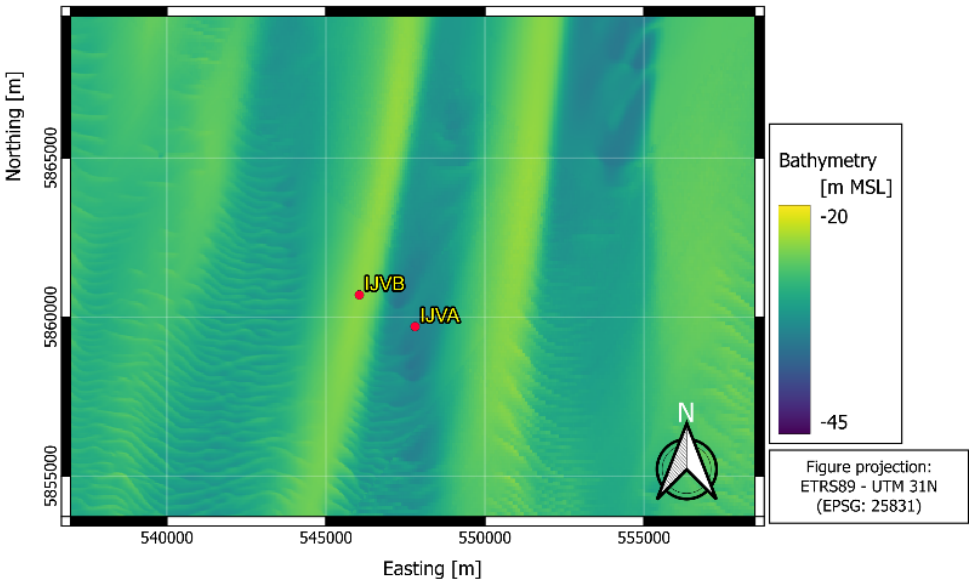

Figure 3.13 Bathymetric features of IJVA and IJVB at IJV area.
The map shows the high resolution of IJVA and IJVB at IJV area. IJVA is in the trough of the sand wave while IJVB stands at a crest of the sand wave.

Variation of the vertical profiles during the flood and the ebb moments (for a single time step) is shown in Figure 3.14 and Figure 3.15. For both, the flood and the ebb moments, the current profiles behave differently at IJVA and IJVB, such that during both conditions, i.e., flood and ebb, generally IJVA measurements show larger magnitudes of current speeds compared to IJVB. This confirms the observed differences between IJVA and IJVB current profiles.

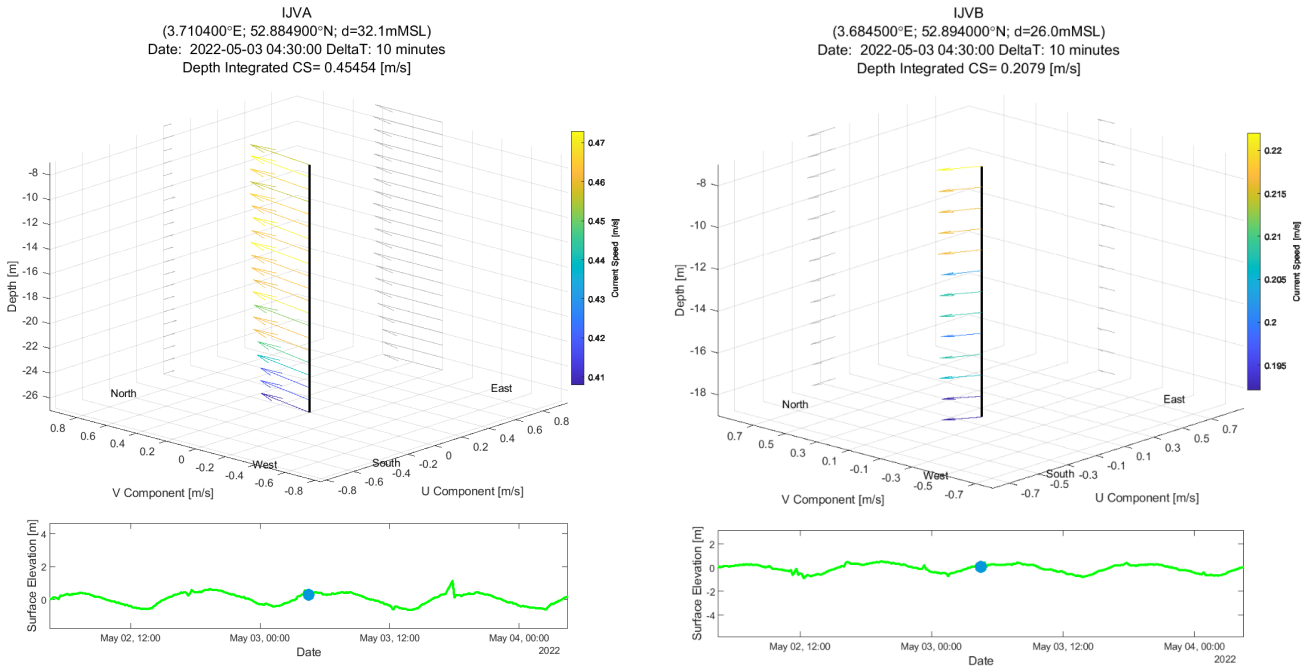

Figure 3.14 Vertical profile of IJVA (left) and IJVB (right) during flood at a single timestep.
The graphic shows a measured vertical profile during flood at 2022-05-03 at 04:30:00 at both stations.

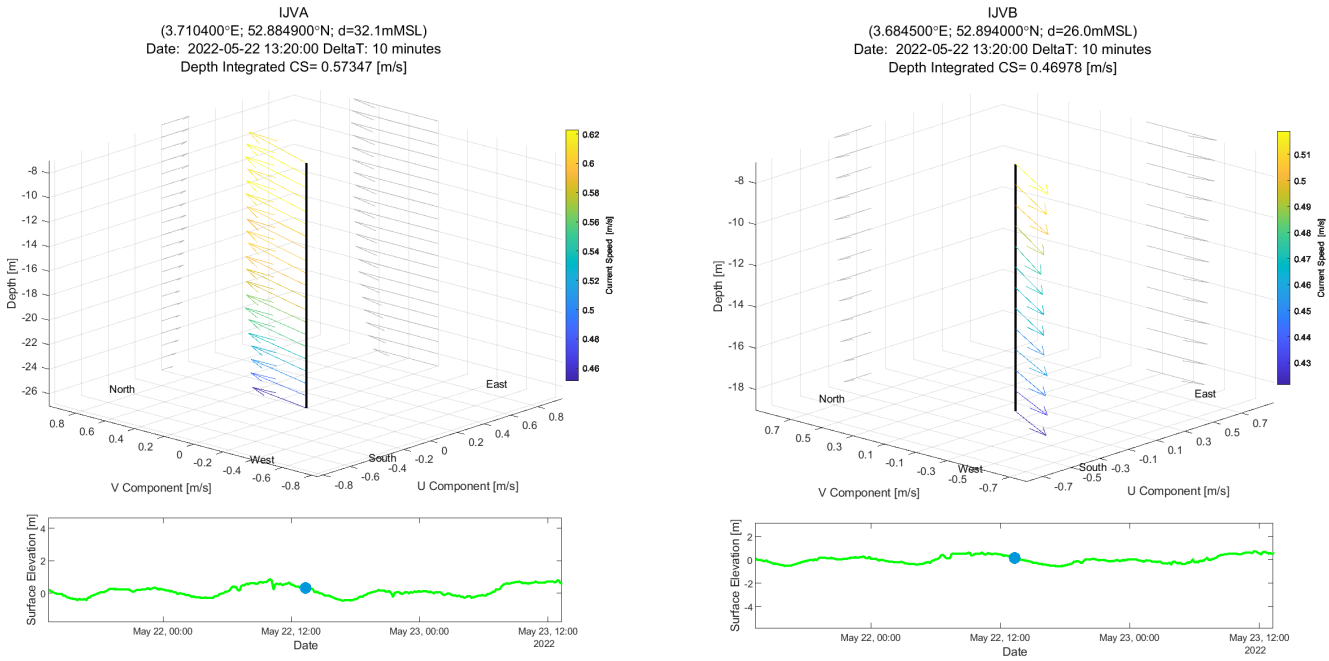

Figure 3.15 Vertical profile of IJVA (left) and IJVB (right) during ebb at a single timestep.
The graphic shows a measured vertical profile during ebb at 2022-05-22 at 13:20:00 at both stations.

3.3.1.3 Recommended design current profile

Except at IJVA, $\alpha = 1/6$ gives the best fit at the three stations, i.e., IJVB, NWA, and NWB. From Figure 3.9, it is seen that at IJVA, using $\alpha = 1/6$, the current speeds will be slightly conservative near the surface, whereas they will be slightly less conservative near the seabed.

Given all considerations, it is **recommended** to use $\alpha = 1/6$ **for normal design conditions**. Assuming the current speed at 2/5th depth to be representative of the depth average current speed, we get $CS_{\{Tide-Surf\}} = \frac{7}{6}\ CS_{\{Tide-Dep\}}$.

3.3.2 Time series and annual statistics

3.3.2.1 Depth-averaged currents

The $CS_{Total\text{-}Dep}$, $CS_{Tide\text{-}Dep}$ and $CS_{Residual\text{-}Dep}$ time series at IJV1 are presented in Figure 3.16. The maximum depth-averaged total $CS_{Total\text{-}Dep}$, tidal $CS_{Tide\text{-}Dep}$ and residual $CS_{Residual\text{-}Dep}$ current speed is 1.10 m/s, 0.87 m/s and 0.94 m/s, respectively. The mean values for $CS_{Total\text{-}Dep}$, $CS_{Tide\text{-}Dep}$ and $CS_{Residual\text{-}Dep}$ are 0.44 m/s, 0.43 m/s and 0.08 m/s. The annual statistics of $CS_{Total\text{-}Dep}$, $CS_{Tide\text{-}Dep}$ and $CS_{Residual\text{-}Dep}$ can be seen in Table 3.12.

The detiding of currents, to obtain the tidal and residual components, followed the same procedure as tidal levels, described in Section 3.2.1.

Analysing Figure 3.16 and the previous stated statistics (previous paragraph), one can see that mainly the tidal component (blue line) is predominant when considering the normal conditions for the total component. However, when analysing maximum values, the residual component has the same magnitude order as the tidal component. The highest current speeds modelled for the analyses period, namely 1.1 m/s at IJV1, was obtained during storm Ciara that affected the UK and the North Sea on 20th of February 2020.

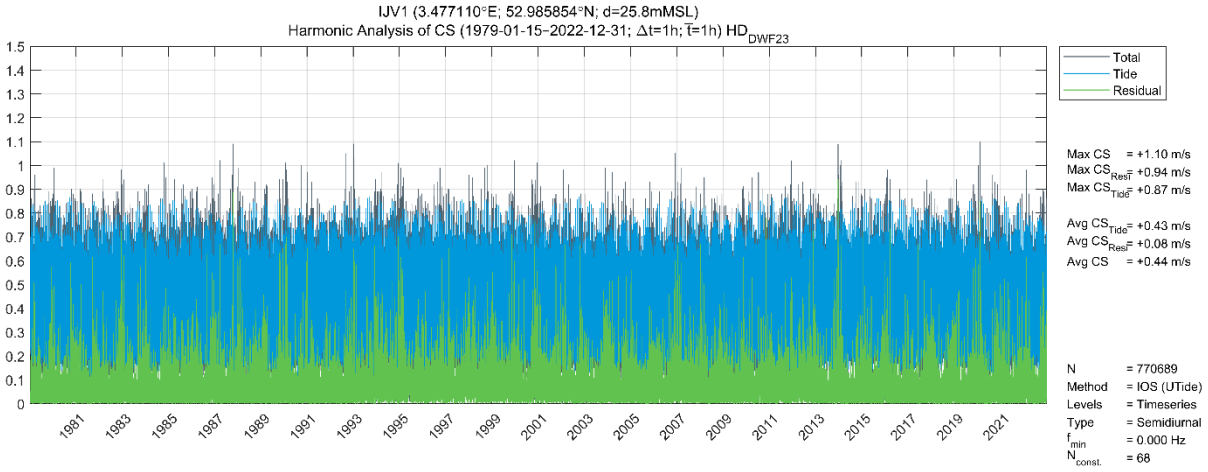

Figure 3.16 Time series of $CS_{Total\text{-}Dep}$, $CS_{Tide\text{-}Dep}$ and $CS_{Residual\text{-}Dep}$ [m/s] at IJV1.
Time series of $CS_{Total\text{-}Dep}$, $CS_{Tide\text{-}Dep}$ and $CS_{Residual\text{-}Dep}$ (values shown for the full period of analysis (1979-01-15 to 2022-12-31) for IJV1.

Table 3.12 Annual statistics of $CS_{Total-Dep}$, $CS_{Tide-Dep}$ and $CS_{Residual-Dep}$ [m/s] at IJV1.
Statistical analyses include the number of data points, mean, min, max and STD of current speed.

Parameter	Number of data points	Mean [m/s]	Min [m/s]	Max [m/s]	STD [m/s]
$CS_{Total-Dep}$	770689	0.44	0.00	1.10	0.14
$CS_{Tide-Dep}$	770689	0.43	0.08	0.87	0.14
$CS_{Residual-Dep}$	770689	0.08	0.00	0.94	0.06

The tidal constituents (phase and amplitude) used in the tidal analysis of current speed at IJV1 are shown in Figure 3.17.

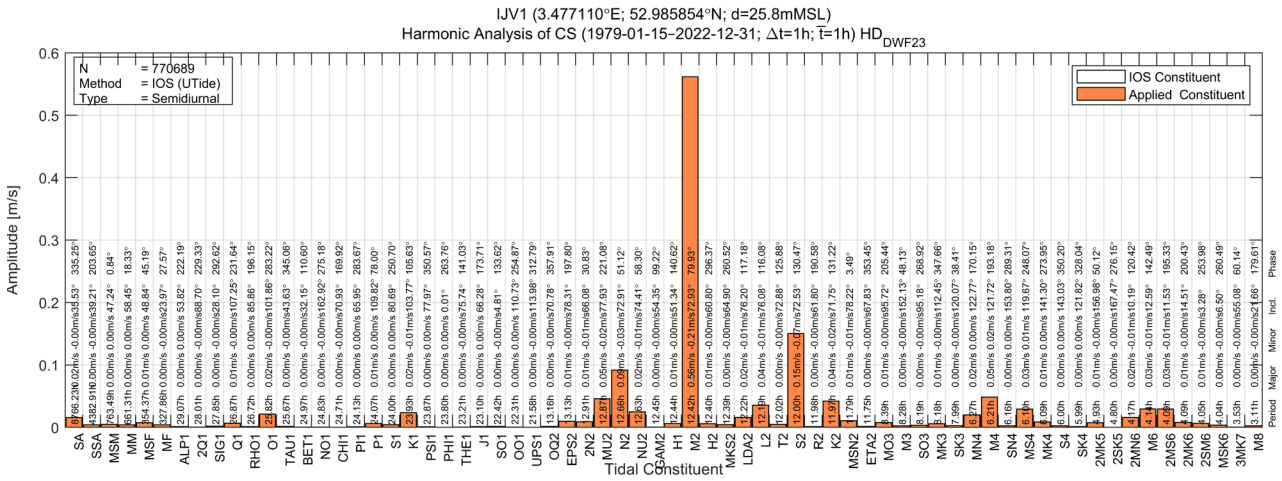

Figure 3.17 Tidal constituents (phase and amplitude) at IJV1.
Tidal constituents applied in the harmonic analysis of current speed.

3.3.2.2 Surface currents

The $CS_{Total-Surf}$, $CS_{Tide-Surf}$ and $CS_{Residual-Surf}$ time series at IJV1 are presented in Figure 3.18. The maximum current speed value considering $CS_{Total-Surf}$, $CS_{Tide-Surf}$ and $CS_{Residual-Surf}$ is 1.28 m/s, 1.10 m/s and 1.01 m/s. The mean values for $CS_{Total-Surf}$, $CS_{Tide-Surf}$ and $CS_{Residual-Surf}$ are 0.44 m/s, 0.43 m/s and 0.08 m/s. The annual statistics of $CS_{Total-Surf}$, $CS_{Tide-Surf}$ and $CS_{Residual-Surf}$ can be seen in Table 3.14.

Like the depth-averaged currents, the tidal component (blue line) is predominant component of the total component for normal conditions. However, when analysing maximum values, the residual component has the same magnitude order as the tidal component. The highest current speed modelled for the analysis period, namely 1.3 m/s at IJV1, was obtained during storm Ciara that affected the UK and the North Sea on 20th February 2020.

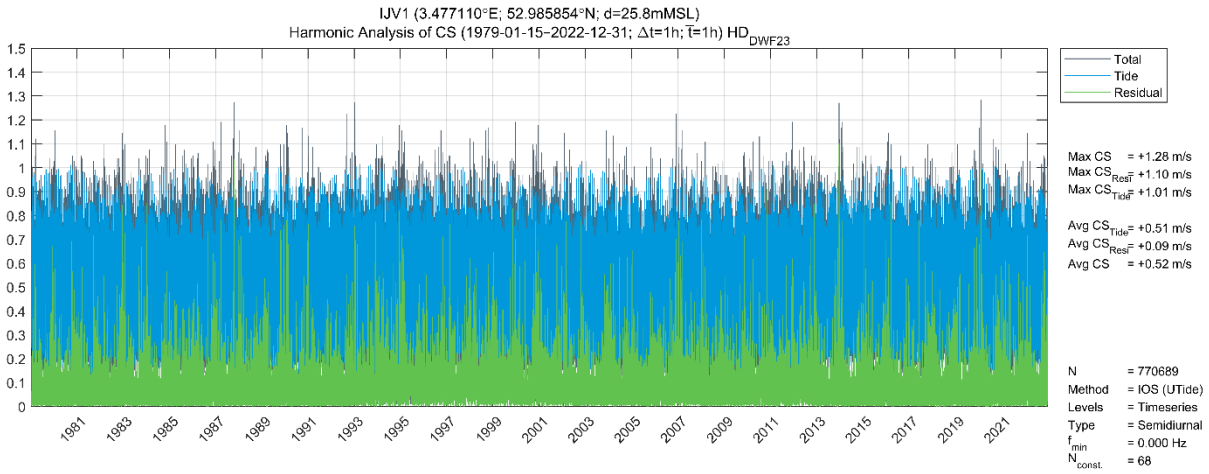

Figure 3.18 Time series of $CS_{Total-Surf}$, $CS_{Tide-Surf}$ and $CS_{Residual-Surf}$ [m/s] at IJV1
Time series of $CS_{Total-Surf}$, $CS_{Tide-Surf}$ and $CS_{Residual-Surf}$ (values shown for the full period of analysis (1979-01-15 to 2022-12-31) for IJV1.

Table 3.13 Annual statistics of $CS_{Total-Surf}$, $CS_{Tide-Surf}$ and $CS_{Residual-Surf}$ [m/s] at IJV1.
Statistical analyses include the number of data points, mean, min, max and STD of current speed.

Parameter	Number of data points	Mean [m/s]	Min [m/s]	Max [m/s]	STD [m/s]
$CS_{Total-Surf}$	770689	0.52	0.00	1.28	0.17
$CS_{Tide-Surf}$	770689	0.51	0.10	1.01	0.16
$CS_{Residual-Surf}$	770689	0.09	0.00	1.10	0.07

3.3.3 Current rose

3.3.3.1 Depth-averaged currents

Rose plot showing total depth-averaged current speeds ($CS_{Total-Dep}$) for the corresponding direction ($CD_{Total-Dep}$) at IJV1 is presented in Figure 3.19. The rose plots for IJV1 indicate that the current mainly flows to northeast (> 20% of the time), followed by southwest (> 15% of the time). Higher current speed magnitudes can be found both in northeast (30°N) and southwest (180°N).

Considering the tidal depth-averaged current speeds and directions ($CS_{Tide-Dep}$ and $CD_{Tide-Dep}$), the results are shown in Figure 3.20. The most prominent directions are currents flowing to southeast (> 17% of the time) followed by northeast (> 15% of the time) and north (> 15% of the time). The northeast bin presents the highest $CS_{Tide-Dep}$ magnitude values.

The residual component of the depth-averaged current speed ($CS_{Residual-Dep}$ and $CD_{Residual-Dep}$) can be assessed in Figure 3.21. Approximately 20% of the time the currents are flowing to northeast, followed by east direction. Only 1.4% of the time the $CS_{Residual-Dep}$ speeds are above 0.28 m/s.

Since the residual component is mainly wind driven (see Figure 3.2 - most of wind directions coming from southwest), the $CS_{Residual-Dep}$ appear to be aligned with most events (> 20% of the time) going to northeast.

It is worth mentioning that due to the different magnitudes the colour scale of the current roses is not the same (e.g., Figure 3.19 ranges from

0.05 – 0.95 m/s whilst Figure 3.21 ranges between speed magnitudes of 0.02 – 0.28 m/s).

More detailed information on the occurrence frequency and respective current bins can be found in Table 3.14, Table 3.15 and Table 3.16 for $CS_{Total\text{-}Dep}$, $CS_{Tide\text{-}Dep}$ and $CS_{Residual\text{-}Dep}$, respectively.

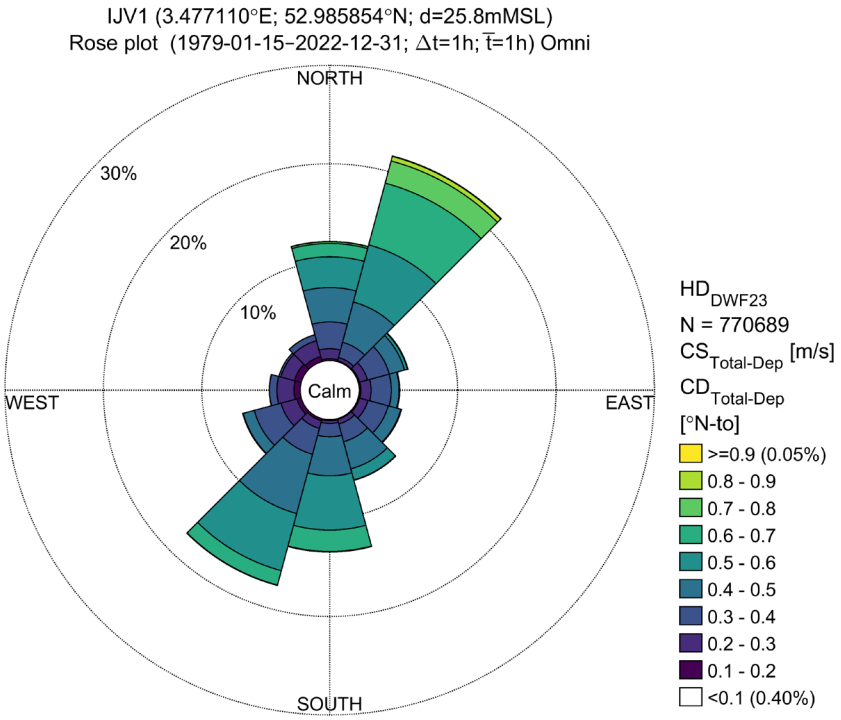

Figure 3.19 Current rose plots of $CS_{Total\text{-}Dep}$ – $CD_{Total\text{-}Dep}$ [m/s] at IJV1. Current roses at IJV1 are shown ($CS_{Total\text{-}Dep}$ – $CD_{Total\text{-}Dep}$), where the analysis period covers 1979-01-15 to 2022-12-31. Directions are 'going to'.

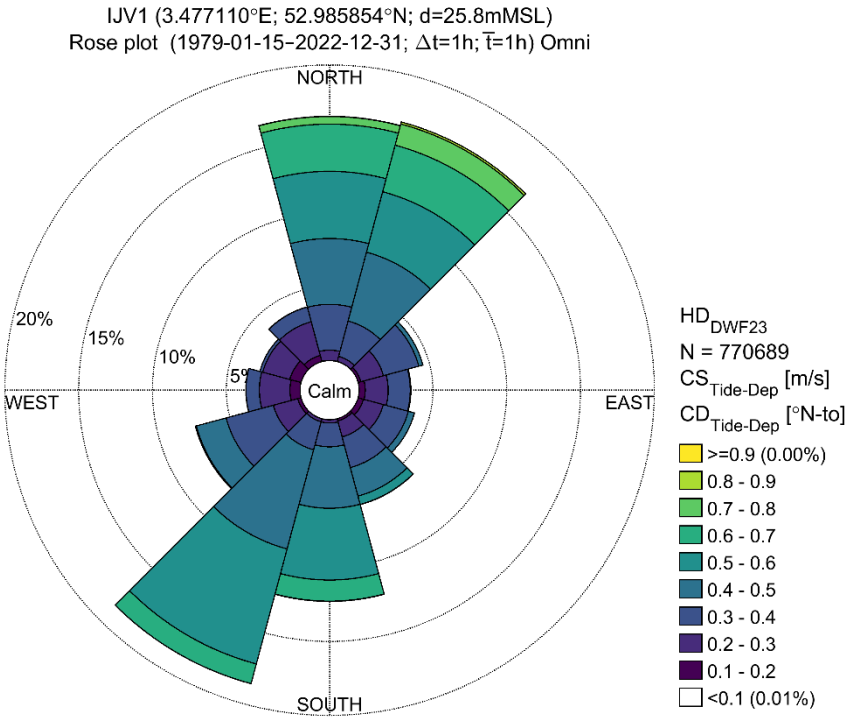

Figure 3.20 Current rose plots of $CS_{Tide\text{-}Dep}$ – $CD_{Tide\text{-}Dep}$ [m/s] at IJV1. Current roses at IJV1 are shown ($CS_{Tide\text{-}Dep}$ – $CD_{Tide\text{-}Dep}$), where the analysis period covers 1979-01-15 to 2022-12-31. Directions are 'going to'.

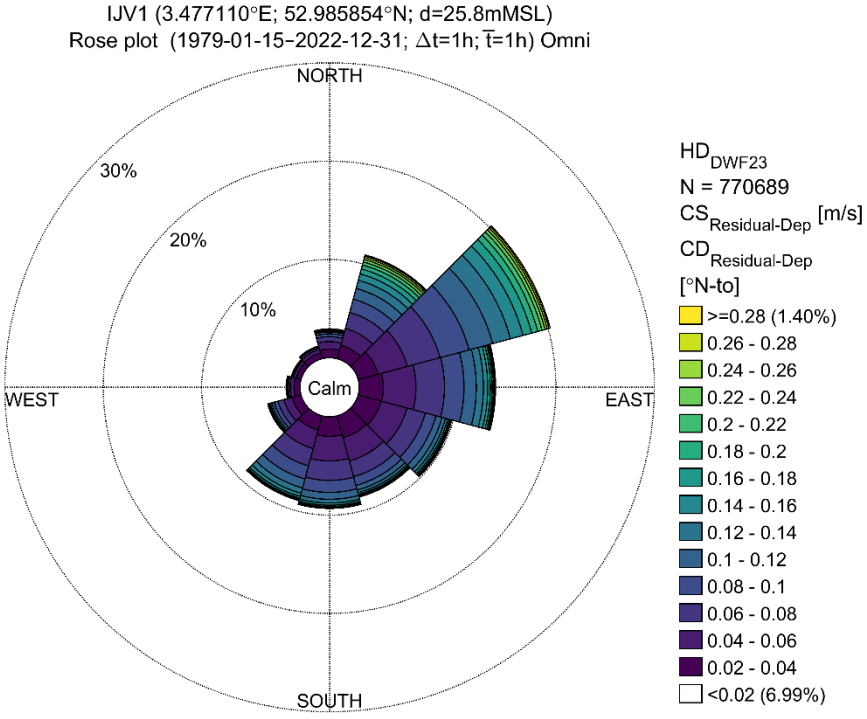

Figure 3.21 Current rose plots of $CS_{Residual\text{-}Dep}$ – $CD_{Residual\text{-}Dep}$ [m/s] at IJV1. Current roses at IJV1 are shown ($CS_{Residual\text{-}Dep}$ – $CD_{Residual\text{-}Dep}$), where the analysis period covers 1979-01-15 to 2022-12-31. Directions are 'going to'.

Table 3.14 Frequency of occurrence for $CS_{Total-Dep}$ [m/s] and $CD_{Total-Dep}$ [deg] at IJV1.
Table presents the directional results at each 1 m/s bin of $CS_{Total-Dep}$.

IJV1 (3.477110°E; 52.985854°N; d=25.8mMSL)
Frequency of Occurrence [%] (1979-01-15-2022-12-31; Δt=1h; $\bar{t}$=1h) Omni
$CS_{Total-Dep}$ [m/s] - HD_{DWF23}

$CD_{Total-Dep}$ [°N-to] - HD_{DWF23}	[0-0.1[	[0.1-0.2[	[0.2-0.3[	[0.3-0.4[	[0.4-0.5[	[0.5-0.6[	[0.6-0.7[	[0.7-0.8[	[0.8-0.9[	[0.9-1[	Total	Accum
[315-345[	0.050	0.524	1.668	0.627	0.013	0.001	-	-	-	-	2.881	99.993
[285-315[	0.062	0.706	1.426	0.211	0.001	-	-	-	-	-	2.407	97.112
[255-285[	0.065	0.631	1.733	0.761	0.018	0.001	-	-	-	-	3.209	94.704
[225-255[	0.051	0.446	1.672	2.819	1.157	0.057	0.004	-	-	-	6.206	91.495
[195-225[	0.033	0.213	0.809	2.721	6.235	6.013	1.514	0.038	0.002	-	17.579	85.289
[165-195[	0.023	0.090	0.295	1.358	3.963	5.508	2.179	0.053	0.002	-	13.470	67.710
[135-165[	0.017	0.077	0.489	1.858	2.854	1.163	0.044	0.001	-	-	6.503	54.240
[105-135[	0.015	0.124	0.899	2.131	1.332	0.070	0.003	-	-	-	4.575	47.737
[75-105[	0.015	0.153	1.048	2.057	0.781	0.062	0.006	0.001	-	-	4.123	43.162
[45-75[	0.018	0.119	0.850	2.298	1.595	0.318	0.049	0.006	0.002	-	5.255	39.038
[15-45[	0.022	0.075	0.353	1.602	4.236	6.014	6.491	2.333	0.481	0.043	21.651	33.784
[-15-15[	0.030	0.189	1.022	2.718	3.491	3.123	1.352	0.179	0.024	0.002	12.132	12.132
Total	0.400	3.348	12.266	21.164	25.676	22.328	11.642	2.611	0.511	0.046	99.993	-
Accum	0.400	3.748	16.014	37.178	62.854	85.183	96.825	99.436	99.947	99.993	-	-

Table 3.15 Frequency of occurrence for $CS_{Tide-Dep}$ [m/s] and $CD_{Tide-Dep}$ [deg] at IJV1.
Table presents the directional results at each 1 m/s bin of $CS_{Tide-Dep}$.

IJV1 (3.477110°E; 52.985854°N; d=25.8mMSL)
Frequency of Occurrence [%] (1979-01-15-2022-12-31; Δt=1h; $\bar{t}$=1h) Omni
$CS_{Tide-Dep}$ [m/s] - HD_{DWF23}

$CD_{Tide-Dep}$ [°N-to] - HD_{DWF23}	[0-0.1[	[0.1-0.2[	[0.2-0.3[	[0.3-0.4[	[0.4-0.5[	[0.5-0.6[	[0.6-0.7[	[0.7-0.8[	[0.8-0.9[	[0.9-1[	Total	Accum
[315-345[	-	0.434	2.359	1.027	0.011	-	-	-	-	-	3.831	100.000
[285-315[	0.001	0.790	1.896	0.203	-	-	-	-	-	-	2.890	96.169
[255-285[	0.001	0.685	2.071	0.909	0.010	-	-	-	-	-	3.675	93.279
[225-255[	-	0.231	1.713	3.312	2.091	0.070	-	-	-	-	7.417	89.604
[195-225[	-	0.001	0.209	1.966	6.946	8.054	1.375	0.006	-	-	18.557	82.187
[165-195[	-	0.004	0.222	1.605	4.159	4.854	1.430	0.019	-	-	12.293	63.630
[135-165[	-	0.154	1.118	2.150	1.998	0.582	0.016	-	-	-	6.018	51.337
[105-135[	0.001	0.370	1.398	1.757	0.426	0.001	-	-	-	-	3.954	45.319
[75-105[	0.003	0.415	1.555	1.496	0.043	-	-	-	-	-	3.512	41.365
[45-75[	-	0.189	1.584	2.483	0.288	-	-	-	-	-	4.545	37.853
[15-45[	-	0.008	0.358	2.476	4.820	4.235	3.260	1.482	0.144	-	16.783	33.308
[-15-15[	-	0.009	0.695	3.100	4.453	4.548	3.192	0.514	0.014	-	16.526	16.526
Total	0.006	3.291	15.178	22.483	25.245	22.343	9.273	2.021	0.158	-	100.000	-
Accum	0.006	3.298	18.476	40.959	66.204	88.548	97.821	99.842	100.000	100.000	-	-

Table 3.16 Frequency of occurrence for $CS_{Residual-Dep}$ [m/s] and $CD_{Residual-Dep}$ [deg] at IJV1.
Table presents the directional results at each 1 m/s bin of $CS_{Residual-Dep}$.

IJV1 (3.477110°E; 52.985854°N; d=25.8mMSL)
Frequency of Occurrence [%] (1979-01-15–2022-12-31; Δt=1h; $\bar{t}$=1h) Omni
$CS_{Residual-Dep}$ [m/s] - HD_{DWF23}

$CD_{Residual-Dep}$ [°N-to] - HD_{DWF23}

	[0-0.1[	[0.1-0.2[	[0.2-0.3[	[0.3-0.4[	[0.4-0.5[	[0.5-0.6[	[0.6-0.7[	[0.7-0.8[	[0.8-0.9[	[0.9-1[	Total	Accum
[315-345[	1.660	0.078	0.003	0.001	-	-	-	-	-	-	1.742	100.000
[285-315[	1.371	0.043	0.001	-	-	-	-	-	-	-	1.415	98.258
[255-285[	1.699	0.112	0.013	0.002	-	-	-	-	-	-	1.826	96.843
[225-255[	3.306	0.602	0.078	0.008	-	-	-	-	-	-	3.994	95.017
[195-225[	7.236	2.126	0.157	0.012	0.001	-	-	-	-	-	9.532	91.022
[165-195[	8.366	1.519	0.116	0.015	0.003	0.001	-	-	-	-	10.020	81.490
[135-165[	8.090	1.123	0.102	0.015	0.003	0.001	-	-	-	-	9.334	71.470
[105-135[	8.986	1.489	0.184	0.033	0.008	0.002	0.001	-	-	-	10.703	62.136
[75-105[	11.432	2.857	0.354	0.062	0.015	0.005	0.003	-	-	-	14.727	51.434
[45-75[	12.365	7.228	1.311	0.290	0.075	0.022	0.009	-	-	-	21.300	36.706
[15-45[	6.851	3.597	1.058	0.323	0.094	0.033	0.010	0.004	0.001	-	11.972	15.406
[-15-15[	2.912	0.453	0.056	0.011	0.002	-	-	-	-	-	3.434	3.434
Total	74.274	21.228	3.433	0.771	0.201	0.064	0.023	0.004	0.001	-	100.000	-
Accum	74.274	95.502	98.935	99.706	99.907	99.971	99.994	99.998	100.000	100.000	-	-

3.3.3.2 Surface currents

Rose plot showing total surface current speeds ($CS_{Total-Surf}$) for the corresponding direction ($CD_{Total-Surf}$) at IJV1 is presented in Figure 3.22. The rose plots for IJV1 indicate that the current mainly flows to northeast (> 20% of the time), followed by southwest (> 17% of the time). Higher current speed magnitudes can be found both in northeast (30°N) and currents above 0.95 m/s occur 0.37% of the time.

Considering the tidal surface current speeds and directions ($CS_{Tide-Surf}$ and $CD_{Tide-Surf}$), the results are shown in Figure 3.23. The most prominent directions are currents flowing to southeast (> 17% of the time) followed by northeast (> 16% of the time) and north (> 16% of the time). North, northeast and southwest bins present the highest $CS_{Tide-Surf}$ magnitude values with 0.9 m/s occurring 0.41% of the time.

The residual component of the surface current speed ($CS_{Residual-Surf}$ and $CD_{Residual-Surf}$) can be assessed in Figure 3.24. Approximately 20% of the time the currents are flowing to northeast, followed by east direction. Only 2.5% of the time the $CS_{Residual-Surf}$ speeds are above 0.28 m/s. Since the residual component is mainly wind driven (see Figure 3.2 - most of wind directions coming from southwest), the $CS_{Residual-Dep}$ appear to be aligned with many events (20% of the time) going to northeast.

More detailed information on the occurrence frequency and respective current bins can be found in Table 3.17, Table 3.18 and Table 3.19 for $CS_{Total-Surf}$, $CS_{Tide-Surf}$ and $CS_{Residual-Surf}$, respectively.

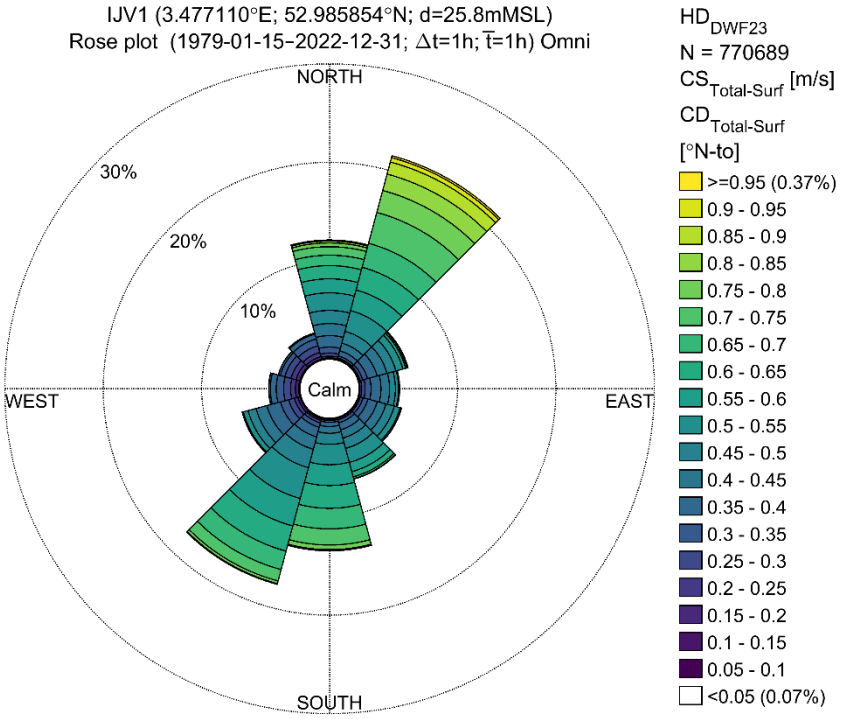

Figure 3.22 Current rose plots of $CS_{Total\text{-}Surf}$ – $CD_{Total\text{-}Surf}$ [m/s] at IJV1. Current roses at IJV1 are shown ($CS_{Total\text{-}Surf}$ – $CD_{Total\text{-}Surf}$), where the analysis period covers 1979-01-15 to 2022-12-31. Directions are 'going to'.

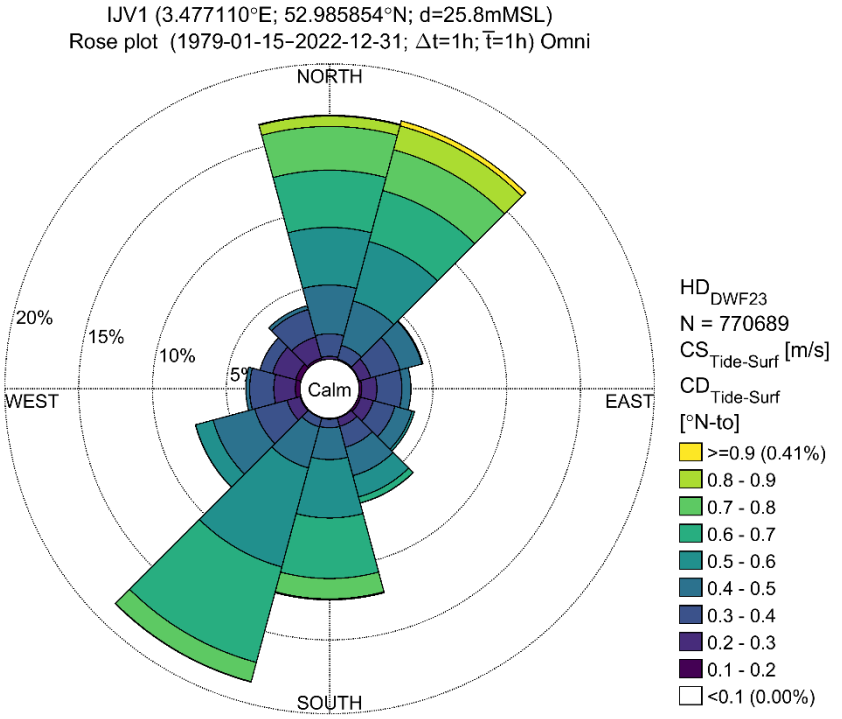

Figure 3.23 Current rose plots of $CS_{Tide\text{-}Surf}$ – $CD_{Tide\text{-}Surf}$ [m/s] at IJV1. Current roses at IJV1 are shown ($CS_{Tide\text{-}Surf}$ – $CD_{Tide\text{-}Surf}$), where the analysis period covers 1979-01-15 to 2022-12-31. Directions are 'going to'.

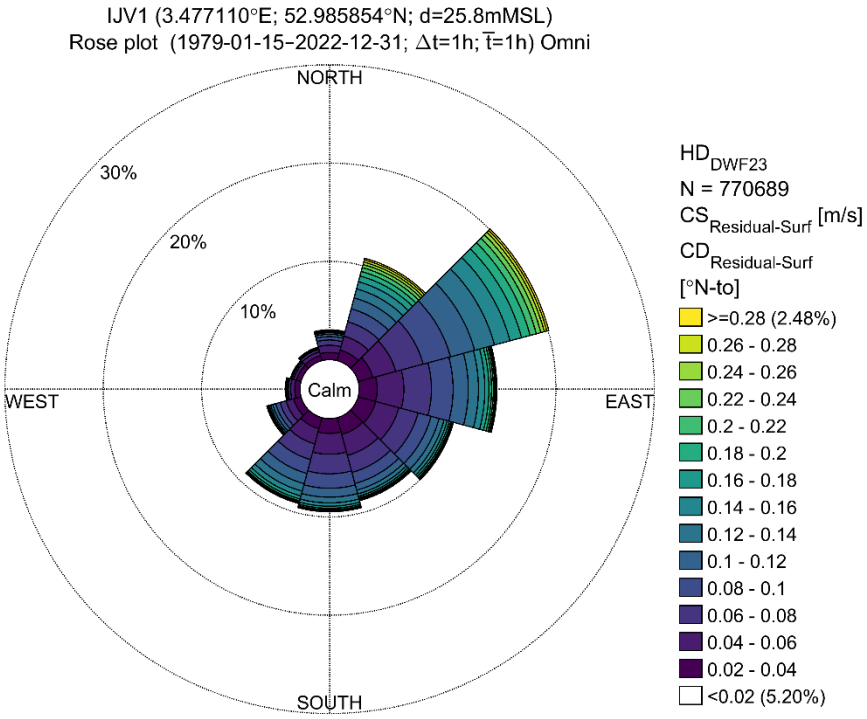

Figure 3.24 Current rose plots of $CS_{Residual-Surf}$ – $CD_{Residual-Surf}$ [m/s] at IJV1. Current roses at IJV1 are shown ($CS_{Residual-Surf}$ – $CD_{Residual-Surf}$), where the analysis period covers 1979-01-15 to 2022-12-31. Directions are 'going to'.

Table 3.17 Frequency of occurrence for $CS_{Total-Surf}$ [m/s] and $CD_{Total-Surf}$ [deg] at IJV1. Table presents the directional results at each 1 m/s bin of $CS_{Total-Surf}$.

IJV1 (3.477110°E; 52.985854°N; d=25.8mMSL)
Frequency of Occurrence [%] (1979-01-15-2022-12-31; Δt=1h; t̄=1h) Omni
$CS_{Total-Surf}$ [m/s] - HD_{DWF23}

$CD_{Total-Surf}$ [°N-to] - HD_{DWF23}

	[0-0.1[	[0.1-0.2[	[0.2-0.3[	[0.3-0.4[	[0.4-0.5[	[0.5-0.6[	[0.6-0.7[	[0.7-0.8[	[0.8-0.9[	[0.9-1[	Total	Accum
[315-345[	0.034	0.346	1.147	1.222	0.129	0.003	-	-	-	-	2.881	99.840
[285-315[	0.042	0.488	1.182	0.683	0.011	0.001	-	-	-	-	2.407	96.959
[255-285[	0.048	0.430	1.203	1.350	0.172	0.006	0.001	-	-	-	3.209	94.552
[225-255[	0.037	0.304	0.962	2.296	1.981	0.593	0.028	0.004	-	-	6.206	91.342
[195-225[	0.024	0.155	0.425	1.453	3.249	6.132	4.587	1.471	0.079	0.004	17.578	85.136
[165-195[	0.019	0.065	0.151	0.609	1.811	4.181	4.402	2.108	0.121	0.004	13.470	67.558
[135-165[	0.014	0.055	0.206	1.043	1.960	2.444	0.737	0.043	0.002	-	6.503	54.088
[105-135[	0.013	0.073	0.432	1.498	1.799	0.728	0.030	0.003	-	-	4.575	47.585
[75-105[	0.012	0.092	0.518	1.607	1.466	0.390	0.033	0.006	0.001	-	4.123	43.009
[45-75[	0.014	0.071	0.391	1.532	1.971	1.020	0.198	0.044	0.010	0.002	5.254	38.886
[15-45[	0.018	0.054	0.165	0.754	2.049	4.352	4.911	5.553	2.997	0.656	21.508	33.632
[-15-15[	0.024	0.130	0.485	1.765	2.562	3.206	2.402	1.240	0.278	0.032	12.124	12.124
Total	0.298	2.263	7.266	15.812	19.161	23.055	17.328	10.473	3.487	0.698	99.840	-
Accum	0.298	2.561	9.827	25.639	44.800	67.854	85.183	95.655	99.142	99.840	-	-

Table 3.18 Frequency of occurrence for $CS_{Tide-Surf}$ [m/s] and $CD_{Tide-Surf}$ [deg] at IJV1.
Table presents the directional results at each 1 m/s bin of $CS_{Tide-Surf}$.

IJV1 (3.477110°E; 52.985854°N; d=25.8mMSL)
Frequency of Occurrence [%] (1979-01-15–2022-12-31; Δt=1h; t̄=1h) Omni
$CS_{Tide-Surf}$ [m/s] - HD_{DWF23}

$CD_{Tide-Surf}$ [°N-to] - HD_{DWF23}	[0-0.1[	[0.1-0.2[	[0.2-0.3[	[0.3-0.4[	[0.4-0.5[	[0.5-0.6[	[0.6-0.7[	[0.7-0.8[	[0.8-0.9[	[0.9-1[	Total	Accum
[315-345[	-	0.146	1.486	1.927	0.272	-	-	-	-	-	3.831	99.998
[285-315[	-	0.375	1.623	0.886	0.006	-	-	-	-	-	2.890	96.167
[255-285[	-	0.317	1.462	1.637	0.259	-	-	-	-	-	3.675	93.277
[225-255[	-	0.071	0.910	2.260	2.922	1.235	0.019	-	-	-	7.417	89.601
[195-225[	-	-	0.045	0.620	2.880	6.942	6.688	1.353	0.028	-	18.557	82.184
[165-195[	-	-	0.060	0.578	2.150	3.955	4.100	1.380	0.068	-	12.293	63.628
[135-165[	-	0.052	0.578	1.468	1.989	1.492	0.424	0.016	-	-	6.018	51.335
[105-135[	-	0.163	0.906	1.509	1.200	0.176	-	-	-	-	3.954	45.317
[75-105[	-	0.179	1.026	1.698	0.608	-	-	-	-	-	3.512	41.362
[45-75[	-	0.059	0.820	2.052	1.553	0.061	-	-	-	-	4.545	37.851
[15-45[	-	0.001	0.087	0.954	3.112	4.173	3.571	2.861	1.674	0.348	16.780	33.306
[-15-15[	-	-	0.198	1.525	3.306	3.899	3.877	2.960	0.704	0.056	16.526	16.526
Total	-	1.364	9.199	17.115	20.258	21.934	18.677	8.570	2.475	0.405	99.998	-
Accum	-	1.365	10.564	27.679	47.936	69.870	88.548	97.118	99.593	99.998	-	-

Table 3.19 Frequency of occurrence for $CS_{Residual-Surf}$ [m/s] and $CD_{Residual-Surf}$ [deg] at IJV1.
Table presents the directional results at each 1 m/s bin of $CS_{Residual-Surf}$.

IJV1 (3.477110°E; 52.985854°N; d=25.8mMSL)
Frequency of Occurrence [%] (1979-01-15–2022-12-31; Δt=1h; t̄=1h) Omni
$CS_{Residual-Surf}$ [m/s] - HD_{DWF23}

$CD_{Residual-Surf}$ [°N-to] - HD_{DWF23}	[0-0.1[	[0.1-0.2[	[0.2-0.3[	[0.3-0.4[	[0.4-0.5[	[0.5-0.6[	[0.6-0.7[	[0.7-0.8[	[0.8-0.9[	[0.9-1[	Total	Accum
[315-345[	1.606	0.128	0.007	-	0.001	-	-	-	-	-	1.742	99.999
[285-315[	1.334	0.078	0.003	-	-	-	-	-	-	-	1.415	98.257
[255-285[	1.636	0.163	0.022	0.003	0.001	-	-	-	-	-	1.826	96.841
[225-255[	3.023	0.824	0.121	0.024	0.003	-	-	-	-	-	3.994	95.015
[195-225[	6.308	2.891	0.292	0.037	0.004	-	-	-	-	-	9.532	91.021
[165-195[	7.579	2.175	0.223	0.035	0.005	0.002	0.001	-	-	-	10.020	81.489
[135-165[	7.484	1.620	0.191	0.031	0.006	0.002	0.001	-	-	-	9.334	71.469
[105-135[	8.254	2.077	0.280	0.067	0.017	0.004	0.001	0.001	0.001	-	10.703	62.135
[75-105[	10.101	3.908	0.547	0.125	0.030	0.008	0.004	0.002	-	-	14.727	51.433
[45-75[	10.224	8.377	1.967	0.512	0.144	0.050	0.017	0.009	0.001	-	21.300	36.705
[15-45[	5.882	3.934	1.387	0.487	0.173	0.065	0.027	0.009	0.004	0.002	11.971	15.405
[-15-15[	2.716	0.600	0.095	0.018	0.004	0.001	-	-	-	-	3.434	3.434
Total	66.147	26.776	5.135	1.341	0.388	0.132	0.051	0.022	0.005	0.002	99.999	-
Accum	66.147	92.923	98.058	99.399	99.788	99.920	99.971	99.992	99.997	99.999	-	-

3.4 Waves

This section presents the analyses conducted on the spectral wave parameters ($H_{m0-Total}$, H_{m0-Sea}, $H_{m0-Swell}$, $T_{p-Total}$, T_{p-Sea}, $T_{p-Swell}$) time series data for IJV1. Results are presented as time series and annual statistics, wave roses, wave-wind and wave-period scatter plots, HT scatter table, and wave spectra.

The sea and swell partition were obtained by means of the wave age criterion as stated in Section 4.3.10 of the modelling report [3].

3.4.1 Time series and annual statistics

The timeseries for the total components of significant wave height ($H_{m0\text{-}Total}$), peak period ($T_{p\text{-}Total}$), averaged wave period ($T_{01\text{-}Total}$), and zero-crossing wave period ($T_{02\text{-}Total}$) can be seen in Figure 3.25. The annual statistics (mean, minimum, maximum and STD) can be seen in

Table 3.20 considering total, sea, and swell components.

The mean $H_{m0\text{-}Total}$ value was 1.47 m, and the maximum value (7.88 m) occurred in 1990-12-12 during a storm, with periods ($T_{p\text{-}Total}$) up to 14 s.

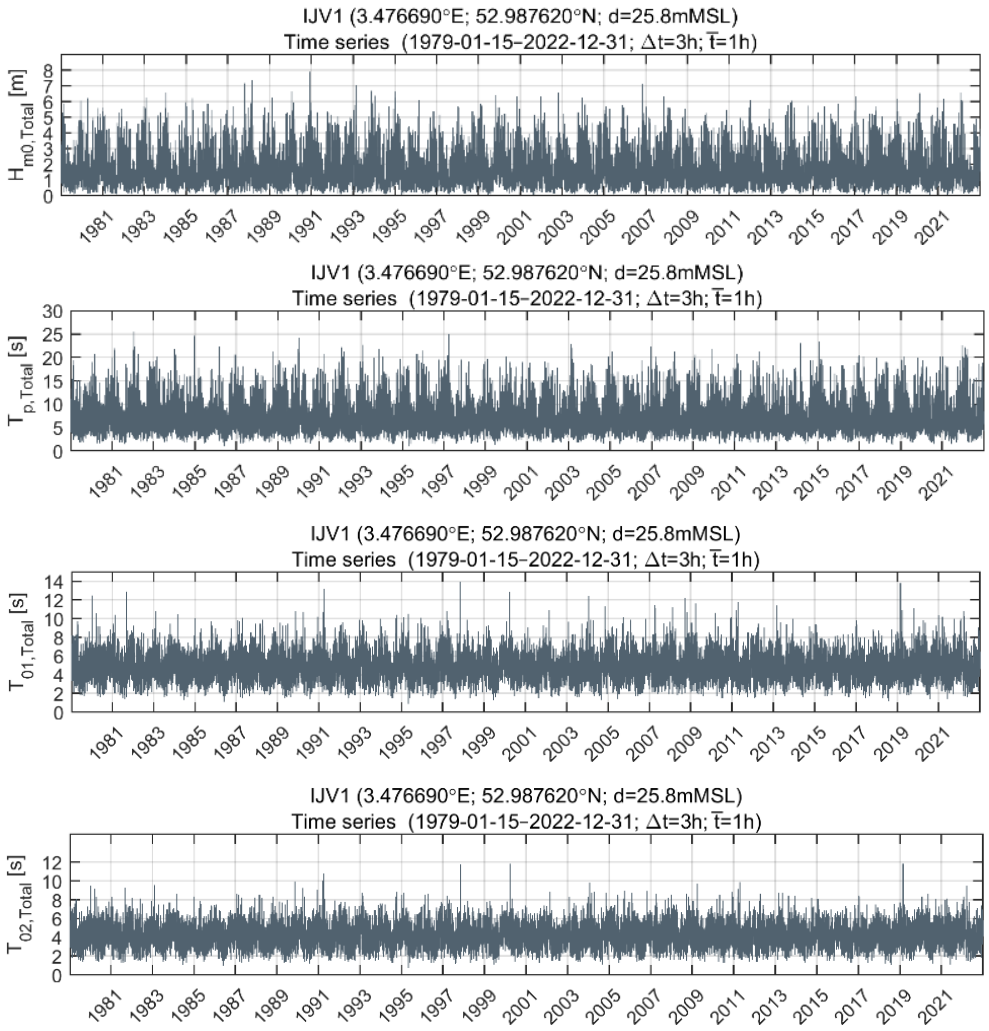

Figure 3.25 Time series of $H_{m0\text{-}Total}$ [m] and $T_{p\text{-}Total}$, $T_{01\text{-}Total}$ and $T_{02\text{-}Total}$ [s] at IJV1.

Time series of $H_{m0\text{-}Total}$ (top panel), $T_{p\text{-}Total}$ (2nd panel), $T_{01\text{-}Total}$ (3rd panel) and $T_{02\text{-}Total}$ (bottom panel) values shown for the full period of analysis (1979-01-15 to 2022-12-31) for IJV1.

Table 3.20 Annual statistics of $H_{m0\text{-}Total}$ [m], $H_{m0\text{-}Sea}$ [m], $H_{m0\text{-}Swell}$ [m], $T_{p\text{-}Total}$ [s], $T_{p\text{-}Sea}$ [s] and $T_{p\text{-}Swell}$ [s] and $T_{01\text{-}Total}$ [s], $T_{01\text{-}Sea}$ [s] and $T_{01\text{-}Swell}$ [s] and $T_{02\text{-}Total}$ [s], $T_{02\text{-}Sea}$ [s] and $T_{02\text{-}Swell}$ [s] at IJV1.
Statistical analyses include the number of data points, mean, min, max, and STD of $H_{m0\text{-}Total}$, $H_{m0\text{-}Sea}$, $H_{m0\text{-}Swell}$ and $T_{p\text{-}Total}$, $T_{p\text{-}Sea}$ and $T_{p\text{-}Swell}$ and $T_{01\text{-}Total}$, $T_{01\text{-}Sea}$ and $T_{01\text{-}Swell}$ and $T_{02\text{-}Total}$, $T_{02\text{-}Sea}$ and $T_{02\text{-}Swell}$ at IJV1.

Parameter	Number of data points	Mean	Min	Max	STD
$H_{m0\text{-}Total}$ [m]	385368	1.47	0.02	7.88	0.94
$H_{m0\text{-}Sea}$ [m]	385368	1.19	0.00	7.87	1.03
$H_{m0\text{-}Swell}$ [m]	385368	0.63	0.02	3.77	0.39
$T_{p\text{-}Total}$ [s]	385368	7.18	1.02	25.60	2.70
$T_{p\text{-}Sea}$ [s]	379726	4.77	0.79	17.71	1.98
$T_{p\text{-}Swell}$ [s]	385368	8.80	1.52	26.72	3.12
$T_{01\text{-}Total}$ [s]	385368	4.72	0.87	13.96	1.25
$T_{01\text{-}Sea}$ [s]	379726	3.52	0.64	10.58	1.49
$T_{01\text{-}Swell}$ [s]	385368	6.56	1.37	18.15	1.87
$T_{02\text{-}Total}$ [s]	385368	4.09	0.73	11.86	1.08
$T_{02\text{-}Sea}$ [s]	379726	3.19	0.60	9.12	1.35
$T_{02\text{-}Swell}$ [s]	385368	5.83	1.20	15.28	1.72

3.4.2 Wave rose

Wave roses of $H_{m0\text{-}Total}$, and their respective direction (PWD_{Total}) can be observed in Figure 3.26. Results show that the most predominant direction is from the south-west (~ 25% of the time and larger waves) for the total component, followed by north direction. The waves from the southwest directions are generally small as only 0.95% of the time the waves are larger than 4.5 m in the southwest direction.

For more detailed information on the specific bins Table 3.21 and Table 3.22 shows the wave rose frequency of occurrence for $H_{m0\text{-}Total}$-PWD_{Total} and $T_{p\text{-}Total}$-PWD_{Total}, respectively.

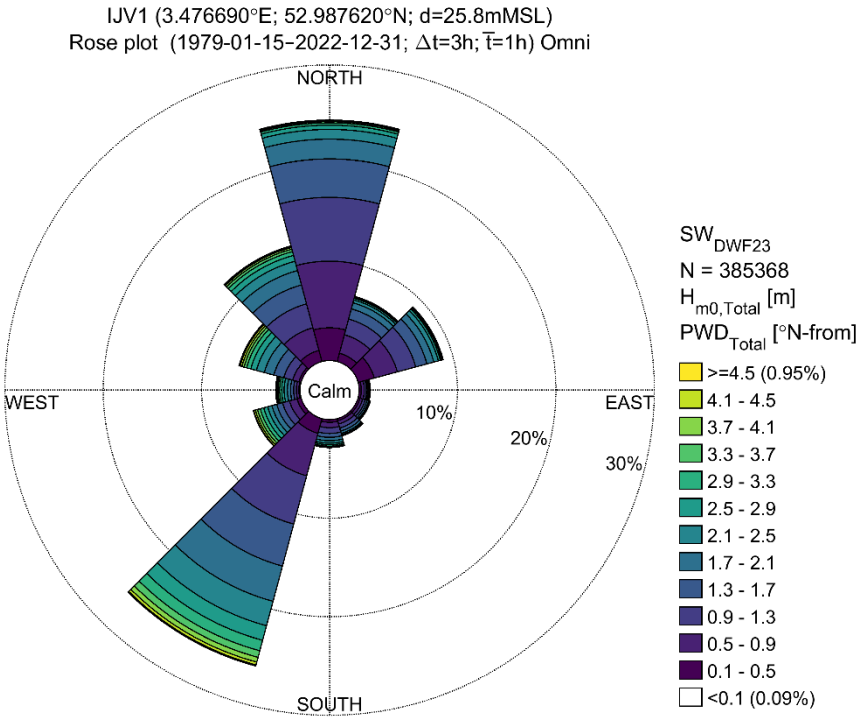

Figure 3.26 Wave rose of $H_{m0\text{-}Total}$ [m] at IJV1.
Wave rose of $H_{m0\text{-}Total}$ values shown for the full period of analysis (1979-01-15 to 2022-12-31) for IJV1. Directions are 'coming from'.

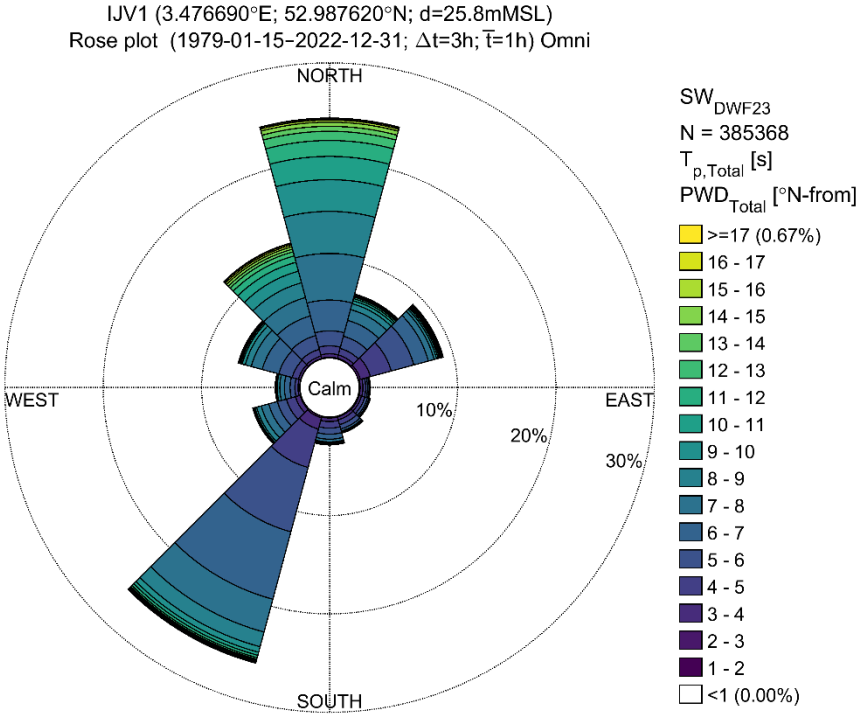

Figure 3.27 Wave rose of $T_{p\text{-}Total}$ [m] at IJV1.
Wave rose of $T_{p\text{-}Total}$ values shown for the full period of analysis (1979-01-15 to 2022-12-31) for IJV1. Directions are 'coming from'.

Table 3.21 Frequency of occurrence of $H_{m0\text{-}Total}$ against PWD_{Total} at IJV1.
Frequency of occurrence values shown for the full period of analysis (1979-01-15 to 2022-12-31) for IJV1.

IJV1 (3.476690°E; 52.987620°N; d=25.8mMSL)
Frequency of Occurrence [%] (1979-01-15–2022-12-31; Δt=3h; $\bar{t}$=1h) Omni
$H_{m0,Total}$ [m] - SW_{DWF23}

PWD_{Total} [°N-from] - SW_{DWF23}	[0-1[	[1-2[	[2-3[	[3-4[	[4-5[	[5-6[	[6-7[	[7-8[	[8-9[	Total	Accum
[315-345[	4.151	5.088	2.051	0.667	0.216	0.091	0.023	0.004	-	12.291	100.000
[285-315[	1.075	2.544	1.793	0.759	0.376	0.078	0.011	-	-	6.635	87.709
[255-285[	0.440	0.770	0.711	0.385	0.184	0.036	0.004	-	-	2.530	81.073
[225-255[	1.403	1.535	1.082	0.735	0.285	0.052	0.003	-	-	5.095	78.543
[195-225[	7.138	11.161	5.300	1.875	0.539	0.064	0.004	-	-	26.082	73.449
[165-195[	0.953	1.100	0.543	0.211	0.028	0.001	-	-	-	2.836	47.367
[135-165[	0.662	0.839	0.256	0.046	0.001	-	-	-	-	1.804	44.531
[105-135[	0.549	0.531	0.204	0.015	-	-	-	-	-	1.299	42.727
[75-105[	0.582	0.366	0.168	0.029	0.001	-	-	-	-	1.146	41.428
[45-75[	4.655	3.176	0.878	0.225	0.033	0.003	-	-	-	8.970	40.282
[15-45[	3.216	2.822	0.634	0.141	0.031	0.011	0.001	-	-	6.856	31.312
[-15-15[	11.716	10.387	1.878	0.346	0.107	0.018	0.003	-	-	24.456	24.456
Total	36.539	40.319	15.500	5.434	1.800	0.353	0.049	0.004	-	100.000	-
Accum	36.539	76.858	92.358	97.792	99.593	99.946	99.996	100.000	100.000	-	-

Table 3.22 Frequency of occurrence of $T_{p\text{-}Total}$ against PWD_{Total} at IJV1.
Frequency of occurrence values shown for the full period of analysis (1979-01-15 to 2022-12-31) for IJV1.

IJV1 (3.476690°E; 52.987620°N; d=25.8mMSL)
Frequency of Occurrence [%] (1979-01-15–2022-12-31; Δt=3h; $\bar{t}$=1h) Omni
$T_{p,Total}$ [s] - SW_{DWF23}

PWD_{Total} [°N-from] - SW_{DWF23}	[1-3[	[3-5[	[5-7[	[7-9[	[9-11[	[11-13[	[13-15[	[15-17[	[17-19[	[19-21[	[21-23[	Total	Accum
[315-345[	0.051	0.969	3.511	3.488	2.161	1.104	0.523	0.316	0.131	0.034	0.004	12.291	99.996
[285-315[	0.037	0.892	3.154	1.794	0.460	0.120	0.072	0.053	0.042	0.008	0.002	6.635	87.705
[255-285[	0.032	0.495	1.065	0.731	0.114	0.025	0.035	0.021	0.011	0.002	-	2.530	81.069
[225-255[	0.104	1.431	1.863	1.281	0.223	0.077	0.063	0.033	0.014	0.005	0.001	5.095	78.539
[195-225[	0.179	5.230	13.858	4.999	0.899	0.406	0.227	0.143	0.085	0.043	0.009	26.076	73.444
[165-195[	0.094	1.026	1.128	0.343	0.085	0.055	0.053	0.035	0.013	0.004	0.001	2.836	47.368
[135-165[	0.092	0.805	0.673	0.060	0.052	0.034	0.042	0.026	0.011	0.007	0.002	1.804	44.532
[105-135[	0.106	0.597	0.435	0.033	0.038	0.032	0.029	0.019	0.008	0.002	0.001	1.298	42.727
[75-105[	0.109	0.559	0.338	0.054	0.032	0.017	0.019	0.014	0.003	0.001	-	1.146	41.429
[45-75[	0.228	3.256	3.905	0.874	0.286	0.150	0.147	0.096	0.021	0.004	0.003	8.970	40.283
[15-45[	0.090	1.029	2.946	1.754	0.541	0.241	0.126	0.083	0.037	0.008	0.002	6.856	31.313
[-15-15[	0.090	1.149	4.653	9.015	5.588	2.549	0.930	0.338	0.113	0.026	0.005	24.457	24.457
Total	1.212	17.438	37.528	24.425	10.479	4.809	2.267	1.177	0.489	0.143	0.029	99.996	-
Accum	1.212	18.650	56.178	80.603	91.082	95.891	98.157	99.334	99.824	99.967	99.996	-	-

3.4.3 Wave scatter tables

The joint occurrence of modelled $T_{p\text{-}Total}$-$H_{m0\text{-}Total}$, $T_{p\text{-}Sea}$-$H_{m0\text{-}Sea}$, and $T_{p\text{-}Swell}$-$H_{m0\text{-}Swell}$ scatter at IJV1 are presented in Figure 3.30, considering the omni-directional results. The directional results are delivered as digital appendices.

From Figure 3.30 the existence of a sea and swell system contribution to the total wave component is clear. The swell component is mainly attributed to the

propagation from the Atlantic Ocean through the English Channel or the North Sea.

The peak wave period associated with swell contribution to the sea state is evident in the higher $T_{p\text{-}Swell}$ associated with lower $H_{m0\text{-}Swell}$ (waves lower than 3.5 m) as can be seen in the bottom panel of Figure 3.30. On the other hand, considering the middle panel of Figure 3.30, one can conclude that the larger $T_{p\text{-}Sea}$ associated with larger $H_{m0\text{-}Sea}$ (waves up to 8 m) is seen for the wind-sea contribution to the sea state.

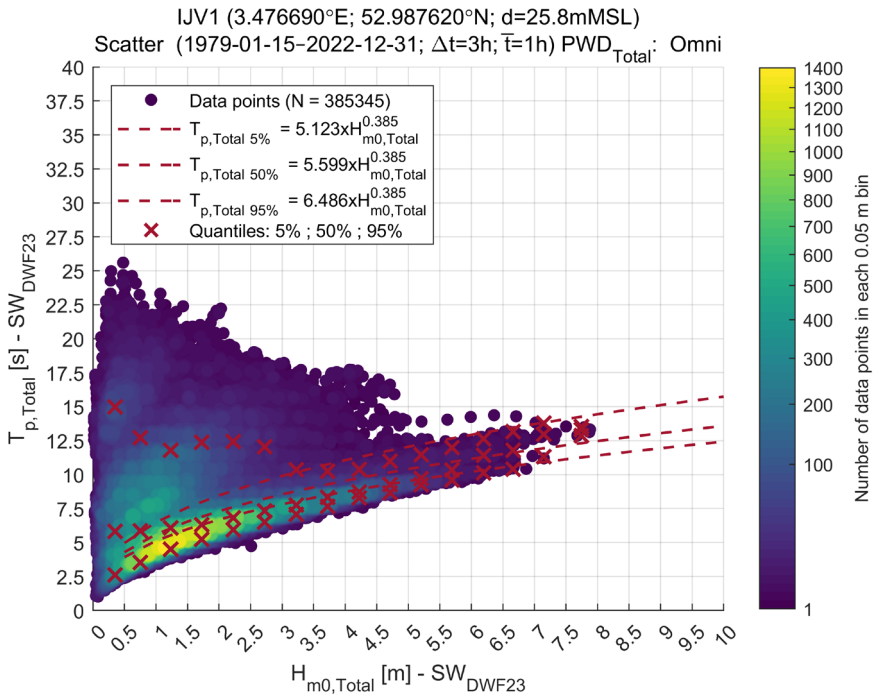

Figure 3.28 Scatter plot of $T_{p\text{-}Total}$-$H_{m0\text{-}Total}$ (top), $T_{p\text{-}Sea}$-$H_{m0\text{-}Sea}$ (middle) and $T_{p\text{-}Swell}$-$H_{m0\text{-}Swell}$ (bottom) at IJV1.
Values are shown for the full period of analysis (1979-01-15 to 2022-12-31) for IJV1.

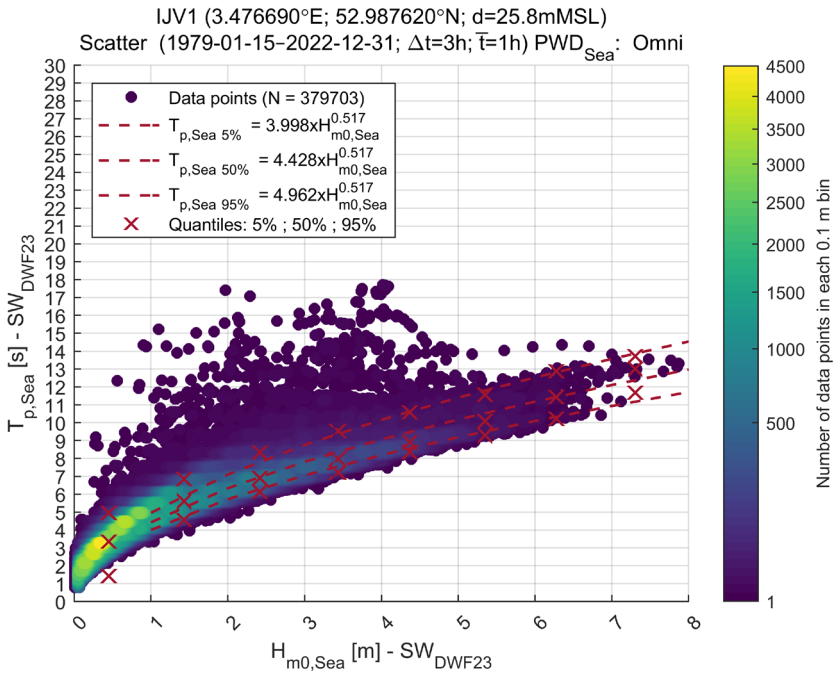

Figure 3.29 Scatter plot of $T_{p\text{-}Total}$-$H_{m0\text{-}Total}$ (top), $T_{p\text{-}Sea}$-$H_{m0\text{-}Sea}$ (middle) and $T_{p\text{-}Swell}$-$H_{m0\text{-}Swell}$ (bottom) at IJV1.
Values are shown for the full period of analysis (1979-01-15 to 2022-12-31) for IJV1.

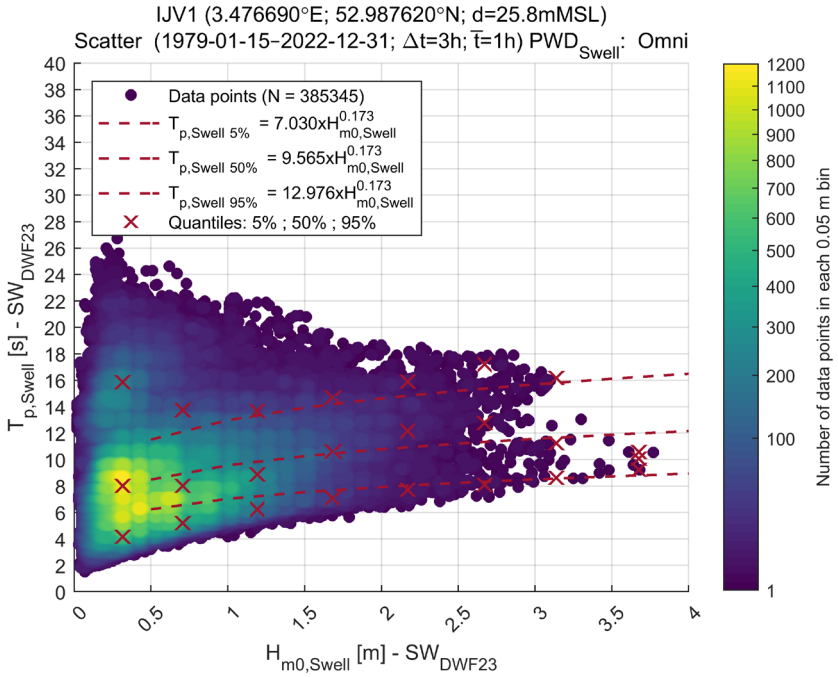

Figure 3.30 Scatter plot of $T_{p\text{-}Total}$-$H_{m0\text{-}Total}$ (top), $T_{p\text{-}Sea}$-$H_{m0\text{-}Sea}$ (middle) and $T_{p\text{-}Swell}$-$H_{m0\text{-}Swell}$ (bottom) at IJV1.
Values are shown for the full period of analysis (1979-01-15 to 2022-12-31) for IJV1.

3.4.4 H-T scatter table

A scatter table of individual wave height (H) vs. period (T), i.e., H-T scatter diagrams, were generated based on individual sea-states at IJV1. The individual wave heights and wave periods were found by performing a zero-down crossing analysis of surface elevation timeseries (generated from the SW_{DWF23} wave spectrum and assuming a Gaussian process with random phase). The H-T analysis was performed for total wave spectrum and Omni-directional wave conditions only, utilising all data covering a period of 44 years (1979-01-15 – 2022-12-31) and results are shown in Figure 3.31.

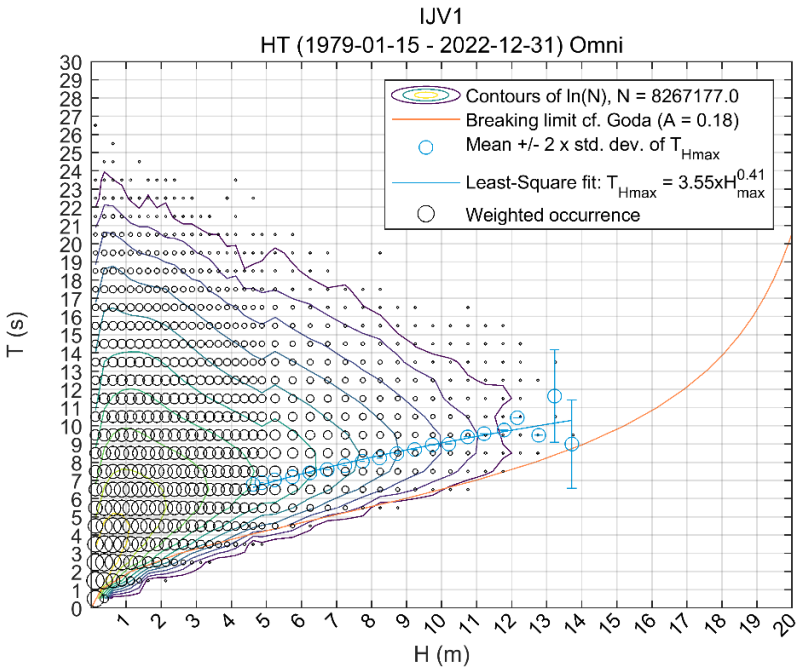

Figure 3.31 H-T scatter plot at IJV1.
Omni-directional number of waves per year (contours) for bins of H x-axis) and T (y-axis) at analyses location IJV1.

3.4.5 Normal sea states conditions

The normal sea states table (NSS) for the IJV1, considering 44 years of data is provided in this section. The NSS conditions characterise the combinations of sea-state parameters that may be used when calculating fatigue loads. In the following analysis, a series of NSS conditioned on the peak wave direction (PWD_{Total}) are considered.

The modelled WS_{160} data was used between a typical range of wind speeds. The NSS results can be seen in Table 3.23 and the directional results are delivered as digital appendices.

The methodology applied to derive the NSS parameters was as follows:

- For each wind speed ($WS_{160\ data}$) bins of 1 m/s, the mean values of significant wave height ($H_{m0\text{-}Total}$) were found.
- The peak wave period ($T_{p\text{-}Total}$) associated with the $H_{m0\text{-}Total}$ values was determined. The range of $T_{p\text{-}Total}$ values was characterized by calculating the peak wave period corresponding to 5%, 50%, 95% quantiles of the data relatively to $H_{m0\text{-}Total}$ in the specific windspeed bins.
- The calculation was repeat for omni-directional and 12 directional sectors using PWD_{Total}.
- A cut-out wind speed of 30 m/s has been assumed.

Table 3.23 Normal Sea State Conditions at IJV1.
Normal Sea State Conditions on WS_{160} [m/s], WS_{10} [m/s], $H_{m0\text{-}Total}$ [m], $T_{p\text{-}Total}$ [s] for 5%, 50% and 95% at IJV1.

WS_{160} [m/s]	WS_{10} [m/s]	$H_{m0\text{-}Total}$[6] [m]	$T_{p\text{-}Total}$ 5% [s]	$T_{p\text{-}Total}$ 50% [s]	$T_{p\text{-}Total}$ 95% [s]
< 3	< 2.3	0.1	2.36	6.51	14.14
< 3	< 2.3	0.2	3.01	6.30	14.84
< 3	< 2.3	0.3	3.37	6.12	15.54
< 3	< 2.3	0.4	3.80	6.52	16.08
< 3	< 2.3	0.50	4.19	6.79	14.95
< 3	< 2.3	0.60	4.60	6.99	13.10
3	2.2	0.66	3.71	7.54	14.46
4	2.9	0.72	3.48	7.39	14.43
5	3.7	0.80	3.19	7.00	13.85
6	4.4	0.92	3.21	6.52	13.11
7	5.2	1.07	3.41	6.09	12.70
8	5.9	1.26	3.76	5.76	12.10
9	6.6	1.48	4.14	5.76	11.74
10	7.4	1.73	4.54	6.06	11.55
11	8.1	1.99	4.97	6.28	10.72
12	8.8	2.26	5.28	6.55	9.56
13	9.6	2.56	5.67	6.89	9.49
14	10.3	2.87	6.09	7.21	9.47
15	11.1	3.19	6.36	7.57	9.52
16	11.8	3.51	6.76	7.84	9.72
17	12.5	3.86	7.05	8.28	10.31
18	13.3	4.16	7.39	8.50	10.50
19	14.0	4.42	7.64	8.69	10.83
20	14.7	4.68	7.76	8.96	11.09
21	15.5	4.90	7.94	9.18	11.21
22	16.2	5.18	8.41	9.40	11.31
23	17.0	5.39	8.48	9.48	10.72
24	17.7	5.57	8.72	9.66	10.49
25	18.4	5.77	8.87	9.89	10.59
26	19.2	6.02	8.05	9.99	11.06
27	19.9	6.25	9.31	10.28	10.70
28	20.6	6.55	10.07	10.41	11.19
30	23.6	6.87	10.42	10.42	10.42

[6] Mean value per WS_{160} bin

3.4.6 Persistence/Weather Windows

The persistence of metocean parameters is reported in this section. A description of persistence analysis is provided in Appendix B.

Workability tables for different parameters for offshore operations are supplied as digital appendices regarding the parameters of $H_{m0\text{-}Total}$, $H_{m0\text{-}Sea}$, and $H_{m0\text{-}Swell}$, considering different time windows, threshold values and quantiles. Table 3.24 summarises the workability tables provided at IJV1. Tables are delivered as digital appendices and an example table for IJV1 is provided in this section.

Table 3.24 Workability (weather-windows) tables for $H_{m0\text{-}Total}$, $H_{m0\text{-}Sea}$ and $H_{m0\text{-}Swell}$.
The criteria for the workability analyses are specified in the table (parameter, time windows, threshold values and percentiles) for IJV1.

Parameter	Time Windows [h]	Threshold [m]	Percentiles
$H_{m0\text{-}Total}$ [m] $H_{m0\text{-}Sea}$ [m] $H_{m0\text{-}Swell}$ [m]	1, 2, 4, 6, 12, 24, 48, 72	0.25, 0.50, 0.75, 1.00, 1.25, 1.50, 1.75, 2.00, 2.25, 2.75, 3.00, 3.50, 4.00, 4.50, 5.00	P20, P50 and P80

Examples of $H_{m0\text{-}Total}$ weather windows with a duration of 24 hours (non-overlapping) and with 50% probability of exceedance estimates at IJV1 are presented in Figure 3.32. The corresponding table is shown in Table 3.25. The horizontal bars in the figures indicate the plus/minus one (1) standard deviation for each threshold, which are also designated by the numbers in the parentheses in Table 3.25. The standard deviations in these figures describe how much the data varies from the mean due to the interannual variability of the analysed period.

The example at IJV1 with 50% percentile (Figure 3.32 and Table 3.25) shows that for a typical month of June, there is a 82.4% probability of a 24-hour period, during which total significant wave height is below 1.75 m. A similar probability (81.3%) for December shows a of a 24-hour period, during which total significant wave height is below 3.50 m.

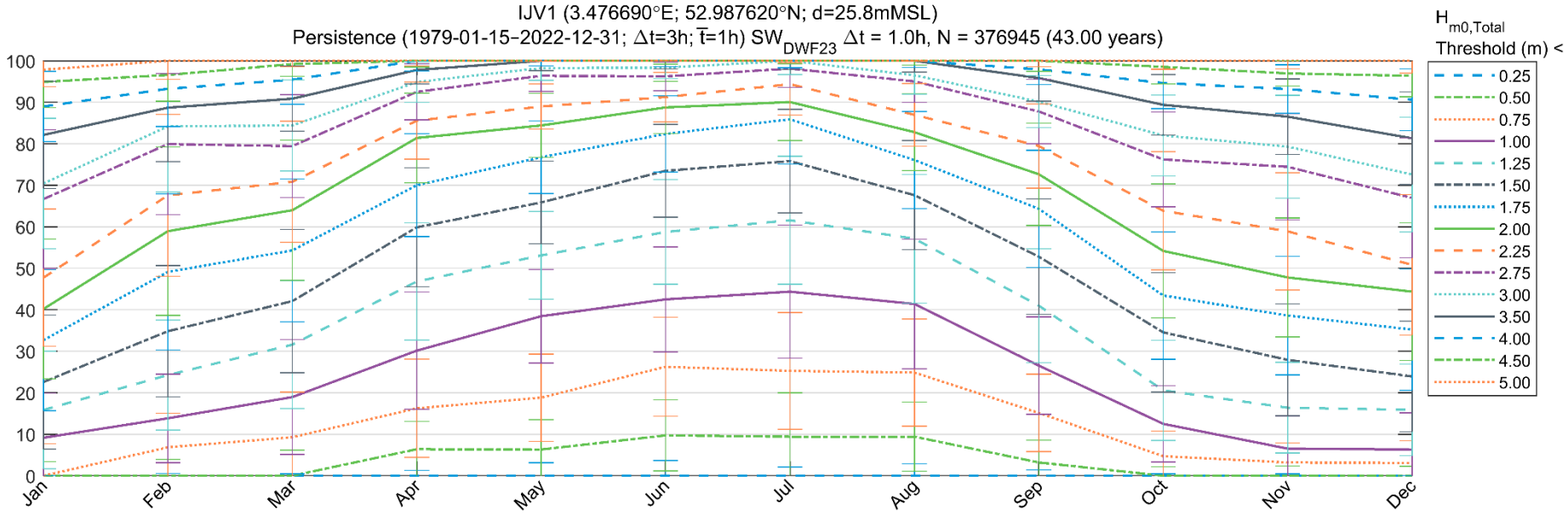

Figure 3.32 Example of persistence (weather-window) analysis of total significant wave height ($H_{m0-Total}$) [m] at IJV1.
The analysis considers a duration of at least 24 hours (non-overlapping) and P=50% from 1979-01-15 to 2022-12-31 with thresholds varying every 0.25 m from 0.5 m up to 5 m.

Table 3.25 Example table of persistence (weather-window) analysis table of total significant wave height ($H_{m0\text{-}Total}$) [m] at IJV1.
Considering a duration of at least 24-hours (non-overlapping) and P=50% the values correspond to the lines shown in Figure 3.32 while the values in parenthesis are one (1) plus/minus standard deviation representing the interannual variability of the period spanning from 1979-01-15 to 2022-12-31.

IJV1 (3.476690°E; 52.987620°N; d=25.8mMSL)
Persistence (1979-01-15–2022-12-31; Δt=3h; $\overline{t}$=1h) SW_{DWF23} Δt = 1.0h, N = 376945 (43.00 years)
Weather $Windows_{P=50\%} \geq$ 24h (Non-Overlapping) [%]

$H_{m0,Total}$ Threshold (m) <	Jan	Feb	Mar	Apr	May	Jun	Jul	Aug	Sep	Oct	Nov	Dec
0.25	0.0 (0.0)	0.0 (0.5)	0.0 (0.5)	0.0 (1.3)	0.0 (3.2)	0.0 (3.7)	0.0 (2.1)	0.0 (2.9)	0.0 (1.4)	0.0 (0.5)	0.0 (0.5)	0.0 (0.0)
0.50	0.0 (3.4)	0.0 (3.9)	0.0 (6.2)	6.4 (6.7)	6.3 (7.2)	9.7 (8.6)	9.4 (10.5)	9.4 (8.3)	3.2 (5.4)	0.0 (2.2)	0.0 (2.3)	0.0 (2.3)
0.75	0.0 (7.7)	6.8 (8.2)	9.3 (10.9)	16.3 (11.8)	18.8 (10.5)	26.3 (11.9)	25.3 (14.1)	24.9 (12.9)	15.1 (9.3)	4.7 (6.1)	3.2 (4.7)	3.1 (5.4)
1.00	9.1 (10.8)	13.8 (10.7)	19.0 (13.8)	30.1 (14.1)	38.4 (11.3)	42.5 (12.6)	44.4 (16.0)	41.4 (15.6)	26.5 (11.7)	12.5 (9.2)	6.5 (7.8)	6.3 (8.9)
1.25	15.9 (14.2)	24.3 (13.2)	31.6 (15.4)	46.8 (14.1)	53.1 (10.6)	58.8 (12.6)	61.6 (15.4)	57.1 (15.5)	41.0 (13.8)	20.6 (12.1)	16.4 (10.9)	15.9 (11.0)
1.50	22.6 (16.1)	34.8 (15.8)	42.1 (17.2)	59.9 (14.3)	65.9 (9.9)	73.5 (11.2)	75.8 (12.5)	67.6 (13.1)	52.8 (13.9)	34.5 (14.4)	27.9 (13.5)	23.9 (13.3)
1.75	32.7 (17.0)	49.1 (18.8)	54.3 (17.2)	70.0 (12.4)	76.7 (8.8)	82.4 (9.2)	85.9 (10.8)	76.1 (11.7)	64.3 (14.1)	43.4 (15.4)	38.6 (14.3)	35.2 (14.6)
2.00	40.2 (16.8)	58.9 (20.3)	64.0 (16.9)	81.4 (10.8)	84.4 (7.7)	88.8 (6.3)	90.1 (9.3)	82.8 (9.2)	72.6 (12.3)	54.2 (16.1)	47.8 (14.3)	44.4 (16.6)
2.25	47.7 (16.5)	67.6 (19.5)	70.8 (14.6)	85.6 (9.3)	89.0 (5.4)	91.3 (6.0)	94.4 (7.4)	87.0 (7.6)	79.4 (10.1)	63.8 (14.3)	58.9 (14.1)	50.8 (16.9)
2.75	66.7 (16.7)	79.9 (17.0)	79.4 (12.4)	92.5 (6.7)	96.4 (3.8)	96.3 (3.5)	98.1 (4.5)	95.0 (5.1)	87.8 (7.8)	76.2 (11.4)	74.4 (12.8)	66.9 (14.4)
3.00	70.4 (15.7)	84.2 (15.8)	84.4 (11.0)	94.9 (4.9)	98.3 (3.0)	98.3 (2.6)	100.0 (3.3)	96.5 (4.6)	90.1 (6.3)	82.0 (9.7)	79.3 (12.4)	72.6 (13.8)
3.50	82.1 (12.9)	88.7 (13.0)	90.9 (7.8)	97.8 (3.4)	100.0 (2.4)	100.0 (1.9)	100.0 (2.2)	100.0 (2.7)	95.8 (5.6)	89.4 (7.3)	86.5 (9.1)	81.3 (11.1)
4.00	89.0 (8.4)	93.2 (9.1)	95.4 (5.9)	100.0 (2.4)	100.0 (1.2)	100.0 (1.4)	100.0 (1.7)	100.0 (1.6)	97.9 (3.6)	94.6 (6.2)	93.2 (5.8)	90.6 (7.4)
4.50	94.9 (6.2)	96.6 (6.3)	99.2 (3.0)	100.0 (1.5)	100.0 (0.2)	100.0 (0.8)	100.0 (0.8)	100.0 (1.1)	100.0 (2.6)	98.5 (4.1)	96.9 (3.0)	96.4 (5.0)
5.00	97.8 (4.1)	100.0 (4.5)	100.0 (1.4)	100.0 (1.2)	100.0 (0.1)	100.0 (0.0)	100.0 (0.5)	100.0 (0.1)	100.0 (1.4)	100.0 (2.1)	100.0 (1.9)	100.0 (3.0)

3.4.7 Assessment of wave spectra

This section concerns the assessment of wave spectra, namely the applicability of theoretical spectra to describe the wave spectra for normal and extreme wave conditions. This assessment can be based on the modelled frequency spectra, which have previously been validated against measurements in Section 3.3.9 of [3].

The wave conditions in the North Sea are dominated by local wind sea, but with some contribution of North Atlantic swell system. Hence, the total sea state can, in most cases, be described adequately by a single-peaked spectrum (e.g., JONSWAP). Wave spectra with more than one peak may occur mainly during non-storm conditions, when there is comparable amount of wave energy from wind-sea and from swell partitions. Bimodal wave spectra can also occur when multiple swells are present at the same time.

3.4.7.1 The JONSWAP spectrum

The JONSWAP (J) spectrum is given by Eq. (3.3), see Section 3.5.5.2-5 in DNV RP-C205 [11].

$$S_J(\omega) = A_\gamma \cdot S_{PM}(\omega) \cdot \gamma^{\exp\left(-0.5\left(\frac{\omega-\omega_p}{\sigma\cdot\omega_p}\right)^2\right)}$$

$$\begin{aligned} &where: \\ &\gamma = \ non\ dimensional\ peak\ enhancement\ factor \\ &\sigma = \ spectral\ width\ parameter \\ &\sigma = \ \sigma_a \text{ for } \omega \ \leq \ \omega_p \\ &\sigma = \ \sigma_b \text{ for } \omega \ > \ \omega_p \\ &A\gamma \ = \frac{0.2}{0.065 \cdot \gamma^{0.803} + 0.135} \text{ is a normalizing factor} \end{aligned} \tag{3.3}$$

Average values are $\gamma = 3.3,\ \sigma_a = 0.07, \sigma_b = 0.09$. If no values are given, γ may be estimated by Eq. (3.4), i.e., defining γ for each sea state (timestep) using $T_{p\text{-}Total}$ and $H_{m0\text{-}Total}$. For $\gamma = 1.0$, the JONSWAP spectrum reduces to the Pierson-Moskowitz spectrum (see Section 3.5.5.1 in DNV RP-C205 [11]).

$$\begin{aligned} &\gamma = 5\ for\ {T_{p-Total}}\Big/{\sqrt{H_{m0-Total}}} \leq 3.6 \\ &\gamma = exp\left(5.75 - 1.15 \cdot {T_{p-Total}}\Big/{\sqrt{H_{m0-Total}}}\right)\ for\ 3.6 < {T_{p-Total}}\Big/{\sqrt{H_{m0-Total}}} \leq 5 \\ &\gamma = 1\ for\ 5 \leq {T_{p-Total}}\Big/{\sqrt{H_{m0-Total}}} \end{aligned} \tag{3.4}$$

3.4.7.2 Recommended spectrum

Figure 3.33 presents averaged modelled frequency spectra (during 1979-01-15 – 2022-12-31) of SW_{DWF23} and the corresponding mean fitted JONSWAP spectra for 1.0 m bins of $H_{m0\text{-}Total}$. The figures show that the average modelled spectra match the average JONSWAP spectra well for moderate and high sea states, $H_{m0\text{-}Total}$ > 1.5 m. Hence, when there is considerable contribution of wind-sea, the spectrum is well represented by a single JONSWAP spectrum.

For low sea states, mainly $H_{m0\text{-}Total}$ < 1.5m, the spectra are bi-modal, due to the comparable amount of wave energy in the wind-sea and the swells partitions. In such situations, there is less agreement between the averaged modelled and the average JONSWAP spectra, and the spectra should be represented by a JONSWAP fitted to each of the partitions separately, or by a proper two-peaked spectrum (such as e.g., the Torsethaugen [12] or the Ochi-Hubble spectra [13]).

In DHI's experience (from the North Sea mainly), the modelled wave spectra are not expected to inform about the peak enhancement factor (gamma) of the JONSWAP spectrum. The modelled (wind-sea) spectra are generally a bit broader, and the fitting of JONSWAP spectra to modelled spectra usually results in somewhat lower gamma values compared to the mean value of $\gamma = 3.3$ for wind-sea considered in the JONSWAP formulation following [14]. This concerns both total and the wind-sea (partitioned by wave-age) spectra. It is noted, though, that the value of gamma in [14] shows quite some spreading in the range of approximately 1 – 7 related to local conditions such as fetch and wind. The reason for the lower gamma values (compared to the mean value of 3.3) obtained by fitting of model spectra is not fully known, but it may be related to a combination of:

- Generally broader/smoother spectra of spectral models (compared to measurements).
- Too coarse discretisation of the model spectra.
- The partitioning (wave-age) not producing 'pure' wind-sea spectra.
- The fitting process not being focused enough on the peak (but rather the bulk of the spectra).

However, lower gamma values may also be due to site specific conditions. The gamma values calculated from the spectral data can be seen in Table 3.26.

Table 3.26 Mean JONSWAP peak enhancement factor (γ) per $H_{m0\text{-}Total}$ bin.

The analyses consider the full period (1979-01-15 - 2022-12-31) for 1.0 m bins (0.5 – 5.5 m) of $H_{m0\text{-}Total}$.

Location	$H_{m0\text{-}Total}$ [m]	Mean γ. Total Sea State [-]
IJV1	0.5-1.5	1.202
	1.5-2.5	1.273
	2.5-3.5	1.368
	3.5-4.5	1.384
	4.5-5.5	1.311

In conclusion, it is recommended to adopt JONSWAP spectra for normal and extreme wave conditions. For moderate and severe sea states, $H_{m0\text{-}Total}$ > 1.5 m, the spectrum is often well represented by a single JONSWAP spectrum, while for low sea states, $H_{m0\text{-}Total}$ < 1.5m, the spectra are often bi-modal, and should be represented by a JONSWAP fitted to each of the partitions separately. For information on gamma values, it is recommended to apply the guidelines in Section 3.5.5 of RP-C205 [11], i.e., defining γ based on $T_{p\text{-}Total}$

and $H_{m0\text{-}Total}$, as given in Eq. (3.4). Table 3.27 presents JONSWAP peak enhancement factor, γ, per $H_{m0\text{-}Total}$ and $T_{p\text{-}Total}$.

Table 3.27 JONSWAP peak enhancement factor, γ, per $H_{m0\text{-}Total}$ and $T_{p\text{-}Total}$ cf. Section 3.5.5.5 in DNV, [15].

γ	$T_{p\text{-}Total}$ [s]									
$H_{m0\text{-}Total}$ [m]	2	4	6	8	10	12	14	16	18	20
1	5.0	3.2	1.0	1.0	1.0	1.0	1.0	1.0	1.0	1.0
2	5.0	5.0	2.4	1.0	1.0	1.0	1.0	1.0	1.0	1.0
3	5.0	5.0	5.0	1.6	1.0	1.0	1.0	1.0	1.0	1.0
4	5.0	5.0	5.0	3.2	1.0	1.0	1.0	1.0	1.0	1.0
5	5.0	5.0	5.0	5.0	1.8	1.0	1.0	1.0	1.0	1.0
6	5.0	5.0	5.0	5.0	2.9	1.1	1.0	1.0	1.0	1.0
7	5.0	5.0	5.0	5.0	4.1	1.7	1.0	1.0	1.0	1.0
8	5.0	5.0	5.0	5.0	5.0	2.4	1.1	1.0	1.0	1.0
9	5.0	5.0	5.0	5.0	5.0	3.2	1.5	1.0	1.0	1.0
10	5.0	5.0	5.0	5.0	5.0	4.0	1.9	1.0	1.0	1.0

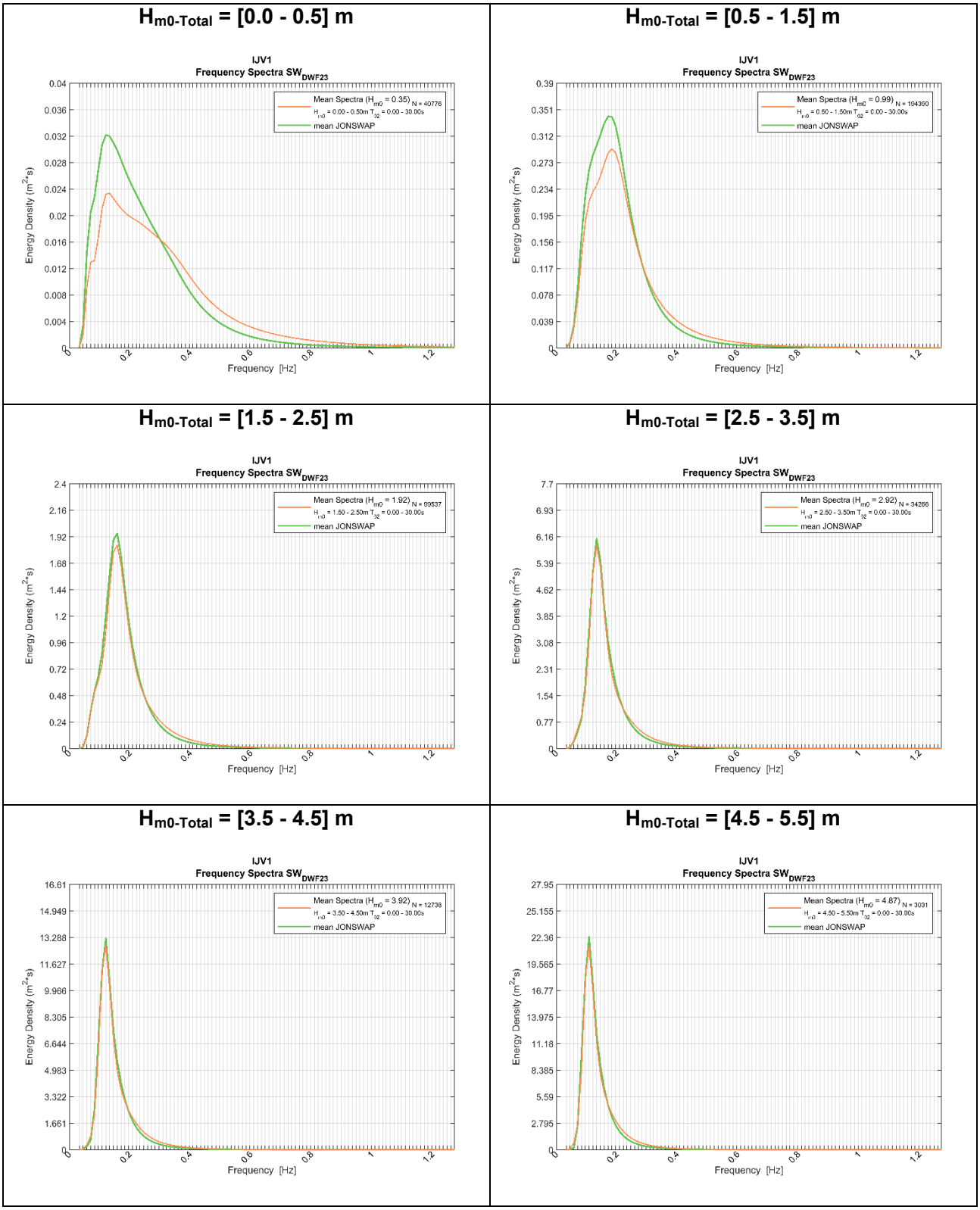

Figure 3.33 Averaged frequency spectra of SW_{SWF23} and corresponding mean JONSWAP spectrum of $H_{m0\text{-}Total}$ at IJV1.
The analyses consider the full period (1979-01-15 - 2022-12-31) for 1.0 m bins (0 – 5.5 m) of $H_{m0\text{-}Total}$ and they were calculated based on DNV [15].

3.5 Joint probability analysis (Wind-wave)

This section presents the analyses conducted on joint probability of ($H_{m0\text{-}Total}$, WS_{10}) data for IJV1. Results are presented as weather windows ($H_{m0\text{-}Total}$ – WS_{10}) and wind-wave misalignment.

3.5.1 Persistence/Weather Windows

The previous sections presented the weather results for WS_{10} (see Section 3.1.4) and for $H_{m0\text{-}Total}$ (see Section 3.4.6). The present section analyses the combined weather windows of $H_{m0\text{-}Total}$ and WS_{10}.

Table 3.28 summarises the workability tables provided at IJV1. Tables are delivered as digital appendices and an example table for IJV1 is provided in this section.

Table 3.28 Workability (weather-windows) tables for $H_{m0\text{-}Total}$ – WS_{10}. The criteria for the workability analyses are specified in the table (parameter, time windows, threshold values and percentiles) for IJV1.

Parameter	Time Window [h]	Threshold for Wave [m]	Threshold for Wind [m/s]	Percentiles
$H_{m0\text{-}Total}$ [m] WS_{10} [m/s]	1, 2, 4, 6, 12, 24, 48, 72	0.25, 0.50, 0.75, 1.00, 1.25, 1.50, 1.75, 2.00, 2.25, 2.75, 3.00, 3.50, 4.00, 4.50, 5.00	2, 4, 6, 8, 9, 10, 11, 12, 15, 20, 25	P20, P50 and P80

Examples of $H_{m0\text{-}Total}$ weather windows with a duration of 24 hours (non-overlapping) and with 50% probability of exceedance estimates at IJV1 are presented in Figure 3.34. The results consider the values of $H_{m0\text{-}Total}$ conditioned on WS_{10}, below 10 m/s for the shown example.

The corresponding table is shown in Table 3.29. The horizontal bars in the figures indicate the plus/minus one (1) standard deviation for each threshold, which are also designated by the numbers in the parentheses in Table 3.29. The standard deviations in these figures describe how much the data varies from the mean due to the interannual variability of the analysed period.

The example at IJV1 with 50% percentile (Figure 3.34 and Table 3.29) shows that for a typical month of June, there is a 59.6% probability of a 24-hours period, during which total significant wave height is below 1.75 m (with wind speeds below 10 m/s. A similar probability (64.2%) for December shows a 24-hours period, during which total significant wave height is below 4.00 m (with wind speeds below 10 m/s).

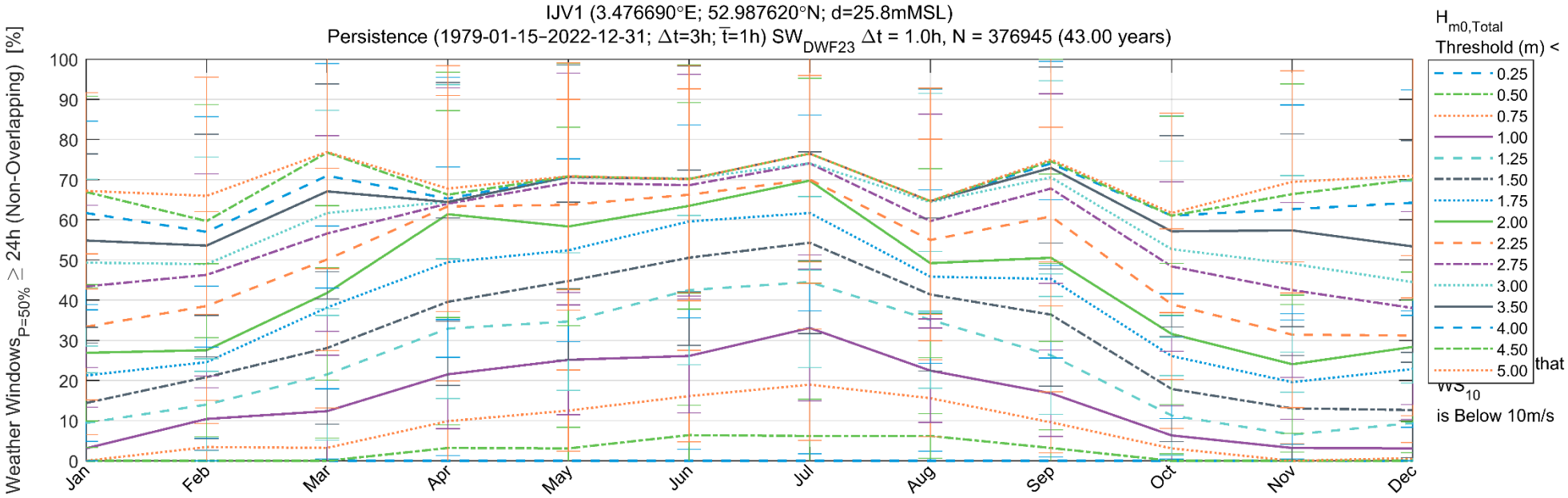

Figure 3.34 Example of persistence (weather-window) analysis of total significant wave height ($H_{m0\text{-}Total}$) [m] for WS_{10} [m/s] below 10 m/s at IJV1. The analysis considers a duration of at least 24 hours (non-overlapping) and P=50% from 1979-01-15 to 2022-12-31 with thresholds varying every 0.25 m from 0.5 m up to 5 m for $H_{m0\text{-}Total}$ considering WS_{10} below 10 m/s.

Table 3.29 Example table of persistence (weather-window) analysis table of total significant wave height ($H_{m0\text{-}Total}$) [m] conditioned on WS_{10} [m/s] at IJV1.

Considering a duration of at least 24-hours (non-overlapping) and P=50% the values correspond to the lines shown in Figure 3.34 while the values in parenthesis are one (1) plus/minus standard deviation representing the interannual variability of the period spanning from 1979-01-15 to 2022-12-31.

IJV1 (3.476690°E; 52.987620°N; d=25.8mMSL)
Persistence (1979-01-15–2022-12-31; Δt=3h; $\bar{t}$=1h) SW_{DWF23} Δt = 1.0h, N = 376945 (43.00 years)
Conditioned that WS_{10} is Below 10m/s
Weather $Windows_{P=50\%} \geq$ 24h (Non-Overlapping) [%]

$H_{m0,Total}$ Threshold (m) <	Jan	Feb	Mar	Apr	May	Jun	Jul	Aug	Sep	Oct	Nov	Dec
0.25	0.0 (0.0)	0.0 (0.0)	0.0 (0.5)	0.0 (1.3)	0.0 (2.4)	0.0 (2.9)	0.0 (1.8)	0.0 (2.4)	0.0 (0.9)	0.0 (0.5)	0.0 (0.5)	0.0 (0.0)
0.50	0.0 (3.3)	0.0 (2.7)	0.0 (5.7)	3.2 (5.8)	3.1 (5.2)	6.4 (7.4)	6.2 (9.2)	6.2 (5.6)	3.2 (4.5)	0.0 (1.7)	0.0 (2.2)	0.0 (2.0)
0.75	0.0 (6.5)	3.4 (5.8)	3.2 (9.9)	9.9 (10.0)	12.5 (10.1)	16.1 (11.4)	19.0 (13.9)	15.6 (9.6)	9.6 (7.6)	3.1 (4.9)	0.0 (4.2)	0.7 (3.9)
1.00	3.1 (10.2)	10.4 (7.8)	12.4 (13.9)	21.5 (13.5)	25.1 (13.7)	26.1 (14.1)	33.1 (18.2)	22.4 (12.9)	16.8 (10.8)	6.3 (7.4)	3.2 (7.2)	3.1 (7.3)
1.25	9.4 (12.5)	14.0 (11.4)	21.5 (16.4)	32.9 (17.4)	34.7 (17.1)	42.5 (18.6)	44.5 (21.3)	35.1 (17.0)	26.3 (14.7)	11.3 (9.9)	6.5 (10.6)	9.4 (10.0)
1.50	14.4 (14.9)	20.8 (15.3)	28.1 (19.0)	39.6 (20.8)	44.8 (19.7)	50.6 (21.8)	54.3 (22.6)	41.4 (19.0)	36.4 (17.8)	17.9 (13.1)	13.1 (13.2)	12.6 (11.9)
1.75	21.2 (16.4)	24.6 (18.9)	38.2 (20.3)	49.4 (23.7)	52.4 (22.7)	59.6 (24.1)	61.7 (24.4)	45.8 (21.6)	45.3 (19.7)	26.1 (15.5)	19.6 (15.5)	22.8 (14.5)
2.00	26.9 (17.0)	27.5 (21.5)	41.8 (21.7)	61.4 (25.8)	58.3 (24.7)	63.5 (25.7)	69.8 (25.5)	49.2 (23.5)	50.6 (20.9)	31.6 (17.6)	24.0 (17.2)	28.4 (18.6)
2.25	33.3 (18.2)	38.5 (23.5)	50.1 (22.7)	63.3 (27.6)	63.7 (26.3)	66.3 (26.4)	70.0 (25.9)	55.0 (25.1)	60.8 (22.2)	39.0 (18.7)	31.4 (18.1)	31.2 (19.9)
2.75	43.4 (20.2)	46.3 (25.2)	56.6 (24.4)	64.0 (28.8)	69.2 (27.3)	68.6 (27.6)	74.1 (26.3)	59.7 (26.6)	67.8 (23.6)	48.4 (21.1)	42.5 (21.8)	38.0 (24.0)
3.00	49.3 (20.8)	49.0 (26.7)	61.7 (25.5)	64.4 (29.2)	70.6 (28.0)	70.3 (28.1)	74.1 (26.6)	64.4 (27.1)	70.6 (24.1)	52.7 (21.9)	49.0 (22.0)	44.5 (25.1)
3.50	54.8 (21.6)	53.6 (27.7)	67.1 (26.7)	64.4 (29.7)	70.7 (27.9)	70.1 (28.2)	76.5 (26.7)	64.7 (28.0)	72.9 (25.1)	57.1 (23.8)	57.4 (24.0)	53.4 (26.4)
4.00	61.7 (22.8)	57.0 (28.7)	71.0 (27.9)	65.3 (30.2)	70.8 (28.1)	70.1 (28.4)	76.5 (26.9)	64.7 (27.9)	74.0 (25.4)	61.0 (24.9)	62.6 (26.0)	64.2 (28.1)
4.50	66.9 (23.9)	59.7 (29.0)	76.7 (28.7)	66.3 (30.5)	70.8 (28.2)	70.1 (28.4)	76.5 (26.9)	64.7 (28.0)	74.6 (25.4)	61.0 (24.7)	66.4 (27.5)	70.0 (30.0)
5.00	67.2 (24.4)	65.9 (29.5)	76.9 (29.0)	67.8 (30.6)	70.8 (28.2)	70.1 (28.3)	76.5 (27.0)	64.7 (28.2)	75.0 (25.5)	61.7 (24.8)	69.4 (27.6)	71.0 (30.4)

3.5.2 Wind-wave misalignment

The wind-wave misalignment was defined as the wind direction (WD) minus the mean wave direction (MWD_{Total}) for each model time step. For example, if the wind is coming from south (WD = 180°N) and the MWD_{Total} is from west (MWD_{Total} = 270°N), then the misalignment angle is -90°.

The misalignment analysis was performed for wind conditions at 160 mMSL (WD_{160}) considering total sea state components of the waves:

- MWD_{Total} vs WD_{160}

For IJV1, the wind-wave misalignment between WD_{160} and MWD_{Total} is shown in Figure 3.35 and Figure 3.36, relative to WS_{160} and $H_{m0\text{-}Total}$ respectively.

The misalignment between wind and wave directions (at IJV1) for the total sea-state conditions is high for $H_{m0\text{-}Total}$ < 1 m and WS_{160} < 10 m/s, as can be seen in Figure 3.35 and Figure 3.36 This occurs because during lower sea states, there is a significant swell component which is generated by wind fields far away from the site and which may not be aligned with winds at the site. For higher waves ($H_{m0\text{-}Total}$ > 3.5 m) and stronger wind speeds (WS_{160} > 12 m/s), the misalignment is reduced and ranges from -30° to +30°.

Figure 3.37 and Figure 3.38 displays the probabilities of wind-wave misalignment angles, at IJV1, for total omni-directional waves and for 12 x 30° directional sectors, conditioned on WD_{160} and MWD_{Total}, respectively. The corresponding table for conditioned on MWD_{Total} and on WD_{160} is shown in Table 3.30 and Table 3.31, respectively. The data shows that the maximum probability is usually located in 0° of misalignment, followed by a misalignment of -30° to +30°.

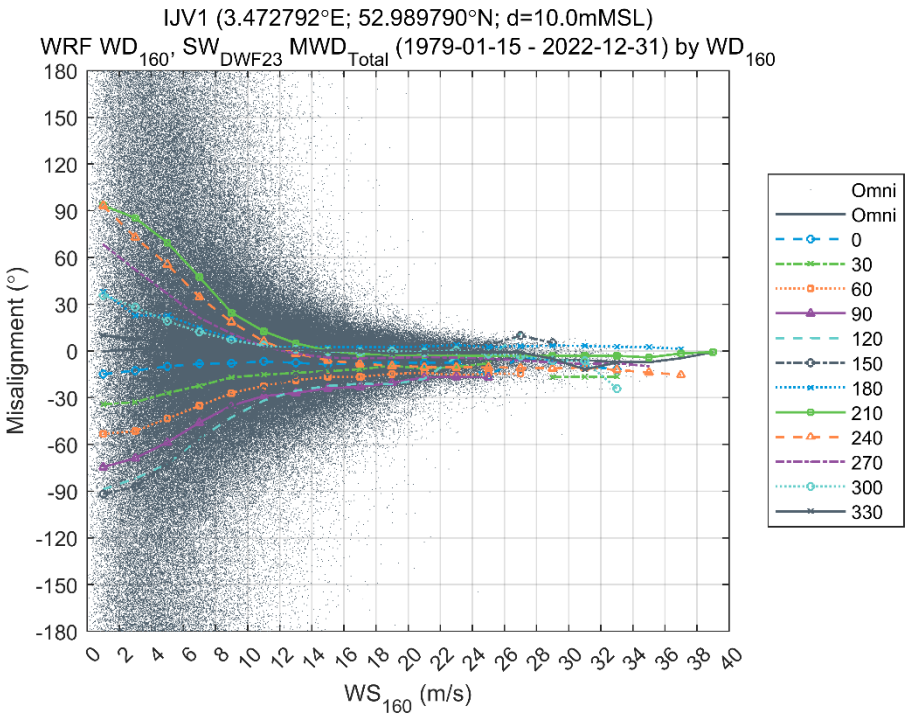

Figure 3.35 Directional wind-wave misalignment (WD_{160} – MWD_{Total}) against wind speed at 160 mMSL (WS_{160}) [m/s] at IJV1.
The grey line shows the Omni-directional values, while the coloured lines show the mean wind wave misalignment for each WD_{160} sector of 30° bin.

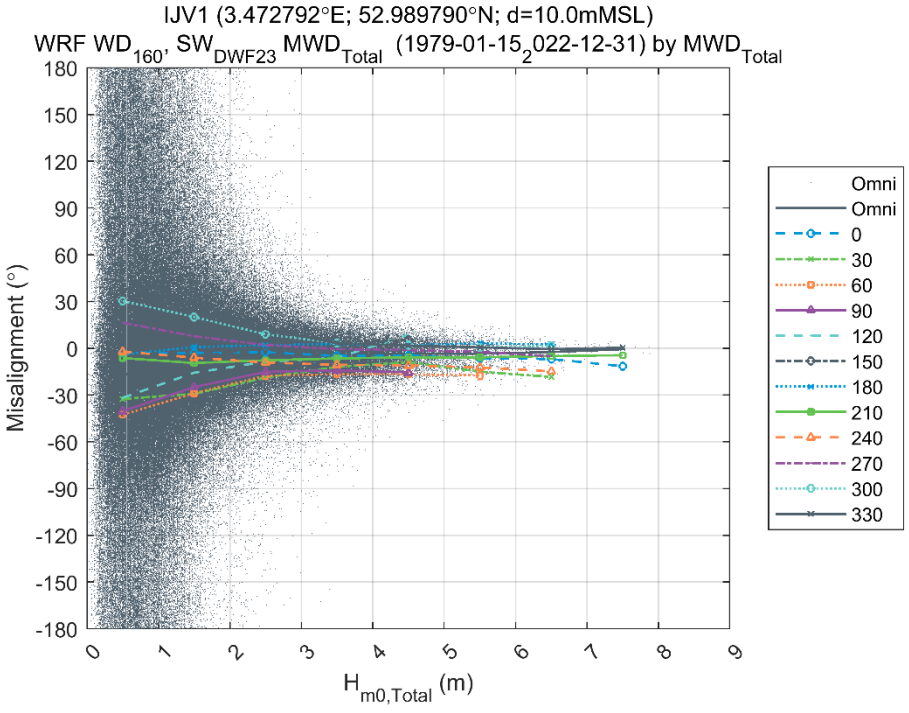

Figure 3.36 Directional wind-wave misalignment (WD_{160} – MWD_{Total}) against significant wave height ($H_{m0-Total}$) [m] at IJV1.
The grey line shows the Omni-directional values, while the coloured lines show the mean wind wave misalignment for MWD_{Total} sector of 30° bin.

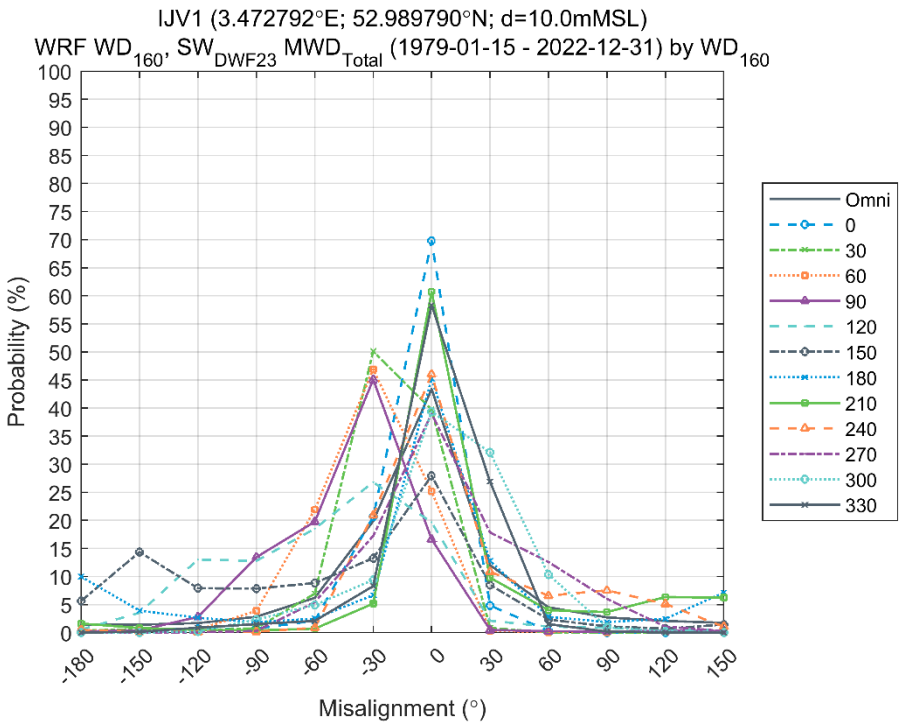

Figure 3.37 Probability of wind-wave misalignment (WD_{160} – MWD_{Total}) conditioned on WD_{160} for total sea state conditions at IJV1.
The grey line shows the Omni-directional values, while the coloured lines show the mean wind wave misalignment for each WD_{160} sector of 30° bin.

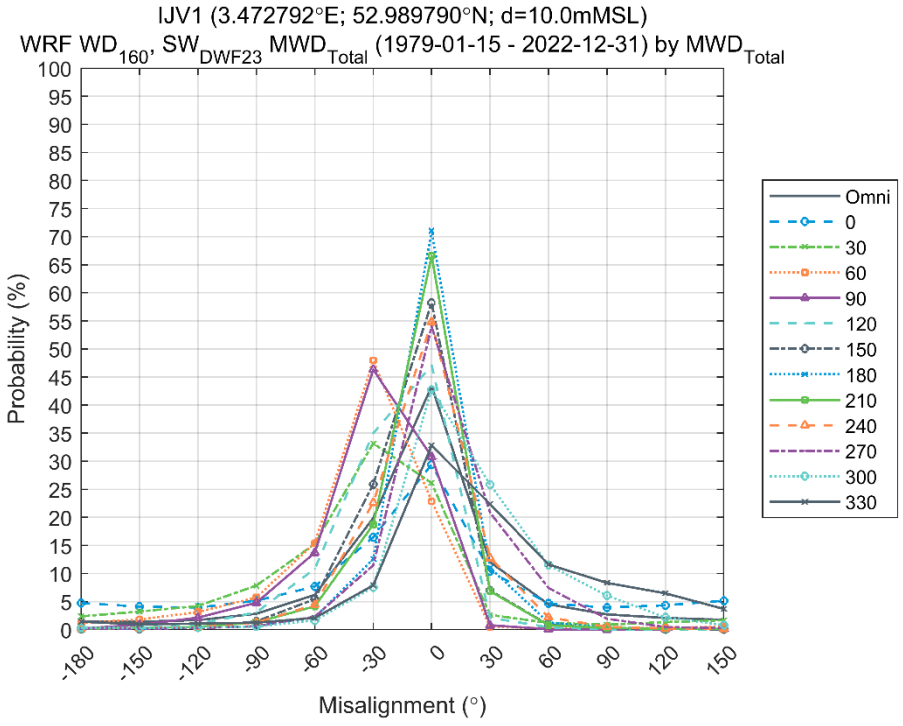

Figure 3.38 Probability of wind-wave misalignment (WD_{160} – MWD_{Total}) conditioned on MWD_{Total} for total sea state conditions at IJV1.
The grey line shows the Omni-directional values, while the coloured lines show the mean wind wave misalignment for each MWD_{Total} sector of 30° bin.

Table 3.30 Probability (%) of wind-wave misalignment by wind direction at 160 mMSL (WD_{160}) conditioned on WD_{160} for total sea state component at IJV1.

The probability analysis considers 1979-01-15 – 2022-12-31.

IJV1 (3.472792°E; 52.989790°N; d=10.0mMSL)
WRF WD_{160}, SW_{DWF23} MWD_{Total} (1979-01-15 - 2022-12-31) by WD_{160}

Misalignment (°)

WD_{160} (°N-from)	[-195--165[	[-165--135[	[-135--105[	[-105--75[	[-75--45[	[-45--15[	[-15-15[	[15-45[	[45-75[	[75-105[	[105-135[	[135-165[
[-15-15[	0.11	0.65	0.68	0.75	2.13	20.67	69.78	4.85	0.32	0.03	0.01	0.02
[15-45[	0.45	0.50	0.40	0.81	6.97	50.11	39.72	0.85	0.05	0.02	0.02	0.12
[45-75[	0.38	0.26	0.52	3.89	21.93	46.91	25.17	0.33	0.10	0.09	0.14	0.28
[75-105[	0.21	0.41	2.82	13.45	19.77	45.10	16.64	0.49	0.25	0.22	0.35	0.31
[105-135[	0.55	3.55	13.03	12.79	18.51	26.81	19.65	2.13	1.09	0.88	0.59	0.43
[135-165[	5.63	14.36	7.92	7.85	8.85	13.28	27.96	8.51	2.34	1.13	0.72	1.44
[165-195[	9.98	3.92	2.66	1.87	2.51	6.68	45.24	12.82	2.82	1.89	2.47	7.14
[195-225[	1.62	0.84	0.48	0.40	0.71	5.17	60.71	9.79	4.00	3.67	6.36	6.23
[225-255[	0.49	0.19	0.14	0.18	0.86	20.95	46.03	10.85	6.59	7.54	5.12	1.05
[255-285[	0.06	0.03	0.07	0.30	5.43	17.25	39.02	17.86	12.58	6.03	1.07	0.30
[285-315[	0.01	0.03	0.21	2.32	4.92	9.42	39.37	32.11	10.37	0.97	0.23	0.04
[315-345[	0.04	0.15	0.89	1.53	2.11	8.31	58.33	26.88	1.53	0.20	0.03	0.01

Table 3.31 Probability (%) of wind-wave misalignment by wind direction at 160 mMSL (WD_{160}) conditioned on MWD_{Total} for total sea state component at IJV1.

The probability analysis considers 1979-01-15 – 2022-12-31.

IJV1 (3.472792°E; 52.989790°N; d=10.0mMSL)
WRF WD_{160}, SW_{DWF23} MWD_{Total} (1979-01-15 - 2022-12-31) by MWD_{Total}

Misalignment (°)

MWD_{Total} (°N-from)	[-195--165[	[-165--135[	[-135--105[	[-105--75[	[-75--45[	[-45--15[	[-15-15[	[15-45[	[45-75[	[75-105[	[105-135[	[135-165[
[-15-15[	4.73	4.12	3.93	5.17	7.68	16.47	29.41	10.38	4.68	3.94	4.34	5.15
[15-45[	2.37	3.23	4.22	7.85	15.27	33.18	26.12	2.63	1.21	0.89	1.35	1.68
[45-75[	1.20	1.83	3.13	5.75	15.42	47.93	22.89	0.50	0.25	0.24	0.32	0.53
[75-105[	0.20	0.86	2.15	4.79	13.72	46.33	30.81	0.80	0.08	0.04	0.07	0.15
[105-135[	0.07	0.28	1.01	3.09	10.84	34.98	47.07	2.13	0.43	0.04	0.01	0.04
[135-165[	0.11	0.13	0.39	1.48	5.44	25.91	58.21	6.99	0.87	0.29	0.09	0.08
[165-195[	0.13	0.20	0.30	0.62	2.18	12.62	71.04	11.00	1.28	0.34	0.18	0.10
[195-225[	0.18	0.29	0.49	1.31	4.15	18.73	66.59	6.84	0.81	0.31	0.17	0.13
[225-255[	0.22	0.29	0.42	1.29	4.43	22.62	54.83	12.78	2.21	0.50	0.23	0.18
[255-285[	0.15	0.18	0.28	0.62	2.31	11.47	54.01	20.85	7.43	1.94	0.47	0.28
[285-315[	0.33	0.34	0.40	0.55	1.65	7.53	42.75	25.85	11.50	6.07	2.21	0.81
[315-345[	1.42	0.94	1.09	1.25	2.10	7.90	32.79	22.37	11.62	8.34	6.48	3.69

3.6 Other metocean parameters

In this section, other metocean parameters analyses are presented. The other metocean parameters and the corresponding data sources are:

- Visibility: The Royal Netherlands Meteorological Institute (KNMI)
- Lightning: LIS/OTD gridded climatology datasets
- Rainfall: WRF dataset
- Snow and ice accretion: WRF dataset
- Sea ice: ERA5 dataset
- Marine growth: scientific literature and species/trait database
- Sea temperature: HD_{UKNS3D} dataset
- Sea salinity: HD_{UKNS3D} dataset
- Sea density: HD_{UKNS3D} dataset
- Air density: WRF dataset
- Relative humidity: WRF dataset
- Air temperature: WRF dataset
- Air pressure: WRF dataset

See details of each data source in Section 4 and 5 of the Metocean modelling report ([3]).

3.6.1 Visibility

The horizontal visibility was not provided for the analyses point IJV1 but was available from the KNMI (see Section 4.3 in [3]) at the stations EPL (2001-2022), F16 (2001-2020), F3 (2011-2022), J6 (2011- 2022), K14 (2001-2022) L9 (2011-2022), LEG (2001-2022) and P11 (2011-2022). The mean visibility and the variations around the mean (standard deviation) on an annual base are shown in Table 3.32 and in Figure 3.39 below. In general, the visibillity is highest in September and lowest during winter/spring.

As no direct measurements of the visibility are available at IJV1, recommendations for this parameter are based on the values of the neighbouring stations. The nearest station to IJV1 is K14 (~33km), therefore values at K14 are recommended to obtain visibility values at IJV1.

Table 3.32 Annual and monthly mean horizontal visibility [km] at the considered stations.
Annual and monthly mean horizontal visibility for 8 stations across the study area.

Station	Annual mean	Jan	Feb	March	April	May	June	July	Aug	Sep	Oct	Nov	Dec
EPL	18.2	15.9	15.8	14.8	16.5	17	17.8	19.5	20.9	22.1	20.3	19.7	17.4
F16	18.9	17.7	16.6	15.3	16.4	18.7	18.9	19.7	20.8	21.6	21.9	20.0	19.6
F3	20.0	19.0	17.9	16.5	17.3	19.0	19.2	20.3	21.9	22.6	22.5	22.7	21.5
J6	19.7	19.3	17.8	15.8	17.8	18.7	18.5	19.7	21.1	22.2	23.0	21.7	20.8
K14	20.5	19.6	18.0	16.6	18.4	19.5	19.1	20.9	22.9	24.0	23.7	22.1	21.2
L9	19.0	16.3	15.8	15.4	17.9	19.1	19.3	21.0	22.6	22.9	20.9	18.6	17.6
LEG	18.8	16.1	15.4	15.4	18.2	18.7	19.5	21.3	22.7	22.8	20.3	18.3	16.5
P11	17.6	16.0	15.0	14.3	17.0	17.7	17.1	18.9	20.4	21.2	19.2	18.5	16.3
Total mean	19.1	17.5	16.5	15.5	17.4	18.6	18.7	20.2	21.7	22.4	21.5	20.2	18.9

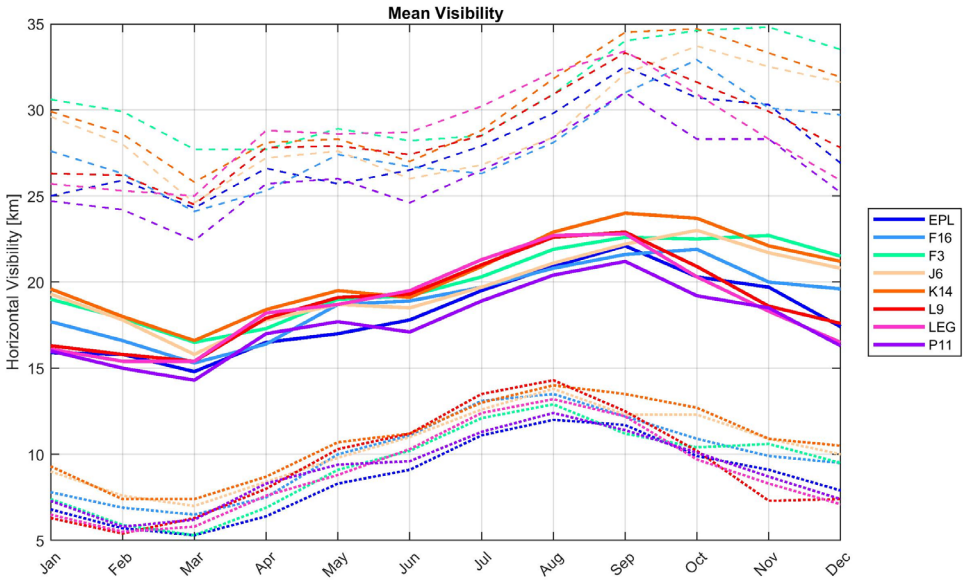

Figure 3.39 Monthly mean of horizontal visibility.
Horizontal visibility [km] where a seasonality can be observed in all stations with higher visibility from August to October and minimum visibility during February to March. Means at the considered stations are shown in solid lines and mean ± standard deviation in dotted lines.

3.6.2 Lightning

Lightning data was taken from the NASA's Global Hydrology Resource Centre (GHRC) and more precisely the LIS/OTD gridded Climatology datasets[7] [16]. Based on the data described in [3] (Section 4.2), the average flash rate density at the IJV1 area is 1.6 fl/km^2/year (0.0044 fl/km^2/day). This number is based on the satellite reading from the High-Resolution Full Climatology (HRFC) dataset more specifically HRFC_COM_FR and contains no smoothing. Figure 3.40 and Figure 3.41 show the monthly and yearly variation of flash rate density at IJV1 area based on the High-Resolution Monthly Climatology (HRMC) and Low-Resolution Monthly Time Series (LRMTS) datasets for the period 1995-01-01 to 2000-01-01 respectively. It should be noted that both HRMC and LRMTS contain extensive smoothing [17]. Therefore, the values are different from the HRFC dataset (discussed in the paragraph above).

The results from HRMC and LRMTS presented here are shown to demonstrate the monthly and yearly variations. As it can be seen, the flash rate in July is on average higher than other months. Flash rate during winter is smaller than summer season.

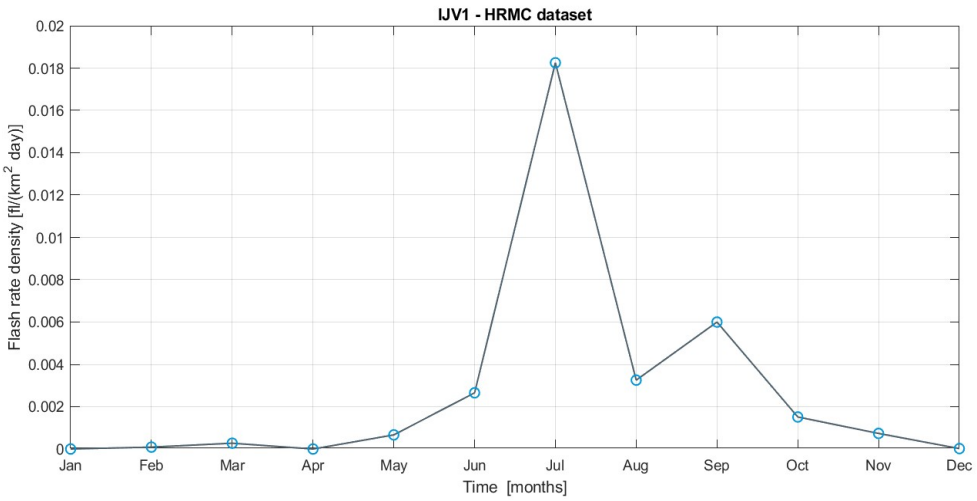

Figure 3.40 Monthly variation of flash rate at IJV1 area based on HRMC data.
The monthly flash rate density (fl/(km^2 day)) are based on the HRMC data for the period 1995-01-01 to 2000-01-01.

[7] LIS/OTD Gridded Lightning Climatology Data Sets (nasa.gov)

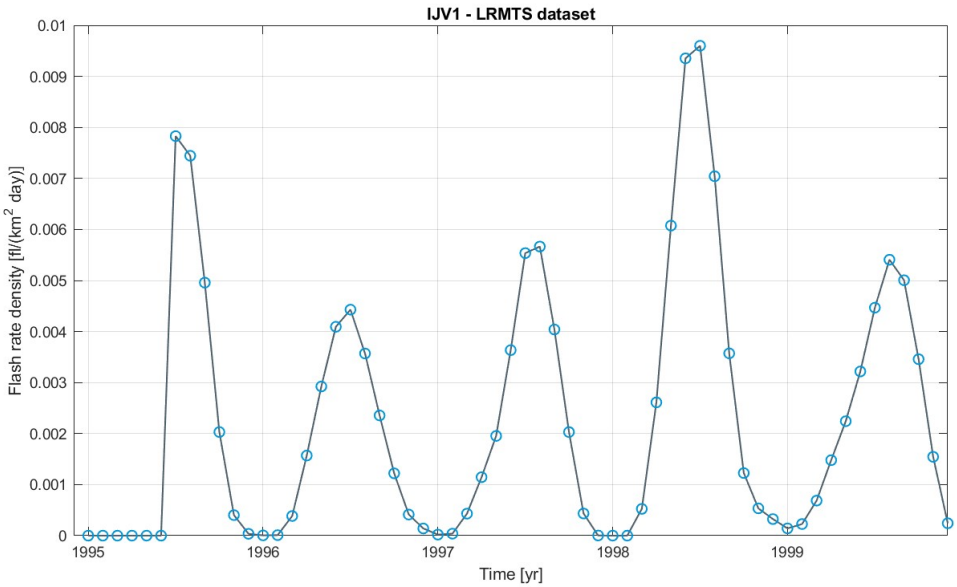

Figure 3.41 Yearly variation of flash rate at IJV1 area based on LRMTS data.
The yearly flash rate density (fl/(km^2 day)) are based on the LRMTS data for the period 1995-01-01 to 2000-01-01.

3.6.3 Rainfall

The rainfall intensity was retrieved from the WRF dataset (see Section 4.1 in [3]) for the period 1979-01-15 to 2022-12-31 at surface level at IJV1. Before the analysis, the rainfall data was resampled from 10 min to 1 hour to align with the units of the rainfall data (mm/h).

The time series data and monthly mean distribution of the rainfall 1h duration intensity is shown in Figure 3.42 and Figure 3.43, respectively. The mean rainfall intensity for all 44 years is 0.08 mm/h and the maximum rainfall event modelled is 31.79 mm/h on 1993-09-08.

The annual and monthly analysis statistics are summarized in Table 3.33

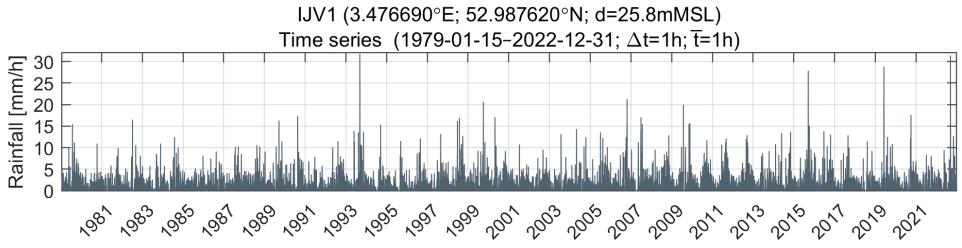

Figure 3.42 Time series of rainfall intensity at IJV1.
Time series of rainfall intensity values shown for the full period of analysis (1979-01-15 to 2022-12-31) for IJV1.

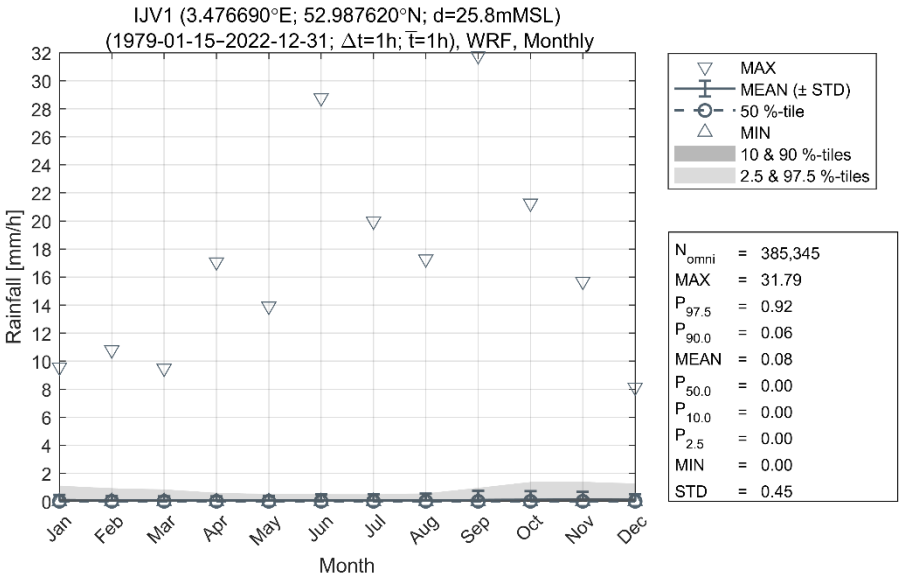

Figure 3.43 Monthly statistics of 1h rainfall intensity at IJV1.
Monthly statistics of rainfall intensity for the full period of analysis (1979-01-15 to 2022-12-31) for IJV1.

Table 3.33 Annual and monthly statistics of 1h rainfall intensity at IJV1.
Annual and monthly statistics table of rainfall intensity for the full period of analysis (1979-01-15 to 2022-12-31) for IJV1.

Rainfall [mm/h]	Annual	Jan	Feb	Mar	Apr	May	Jun	Jul	Aug	Sep	Oct	Nov	Dec
N	385345	32400	29832	32736	31680	32736	31680	32736	32736	31680	32736	31680	32713
MEAN	0.1	0.1	0.1	0.1	0.1	0	0.1	0.1	0.1	0.1	0.1	0.1	0.1
STD	0.5	0.4	0.3	0.3	0.3	0.3	0.4	0.5	0.5	0.7	0.6	0.5	0.4
MIN	0	0	0	0	0	0	0	0	0	0	0	0	0
P5	0	0	0	0	0	0	0	0	0	0	0	0	0
P50	0	0	0	0	0	0	0	0	0	0	0	0	0
P95	0.4	0.6	0.5	0.4	0.2	0.1	0.1	0.1	0.1	0.3	0.6	0.7	0.7
MAX	31.8	9.6	10.8	9.5	17.1	13.9	28.8	20	17.3	31.8	21.3	15.7	8.1

The average annual and monthly rainy days were calculated for the IJV1 location. The daily rainfall was calculated for 3 different thresholds > 0.1, > 0.5 and > 1.0 mm per day and can be seen in Table 3.34. The thresholds were chosen based on [18].

Table 3.34 Annual and monthly statistics of mean rainy days at IJV1.
Annual and monthly statistics of mean rainy days for the full period of analysis (1979-01-15 to 2022-12-31) for IJV1.

Rainy days	Annual	Jan	Feb	Mar	Apr	May	Jun	Jul	Aug	Sep	Oct	Nov	Dec
MEAN [>0.1mm]	200.5	20.7	19.4	16.7	13.6	12.4	13.1	13.3	13.8	16.2	19.9	21.3	22.1
MEAN [>0.5mm]	150.0	15.6	12.8	12.6	9.6	8.9	9.2	9.0	9.9	12.2	15.5	16.9	17.4
MEAN [>1.0mm]	122.5	13.0	10.3	10.5	7.7	7.2	7.4	7.3	8.0	9.9	12.7	14.0	14.6

3.6.4 Snow, ice accretion and sea ice conditions

3.6.4.1 Snow and ice accretion

According to ISO 19901-1 standard [19], ice accretion (or icing) refers to the accumulation of ice or snow on a structure. Ice accretion can induce a loss of production and reduce the lifetime of the wind turbine components [20]. It can also impact maintenance operations. Icing can be categorized into two types: the atmospheric icing and the marine icing. Atmospheric icing includes freezing rain, supercooled fog, and snow, while marine icing mainly occurs by freezing sea spray from breaking waves and/or strong winds blowing over the sea surface. In this report, the calculation of ice accretion is based on the air temperature, the sea surface temperature, and the wind speed.

Atmospheric icing occurs when rain, fog or snow freezes upon the contact with a surface. Required conditions for atmospheric icing are low air temperatures between -20°C and 0°C combined with low wind speeds (less than 10m/s) ([19] and [21]). Based on Figure 3.44 and Table 3.35, it can be calculated that these conditions are met 0.23% of the time in the 44 years (1979-01-15 to 2022-12-31) of analysis at IJV1.

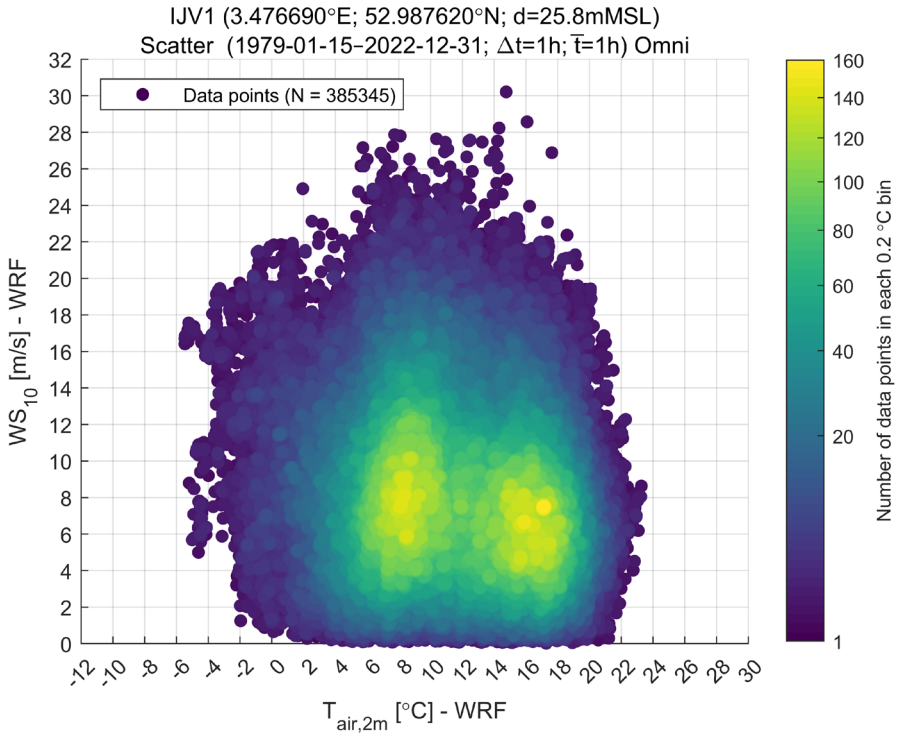

Figure 3.44 Density scatter of the air temperature at 2m against the 10mMSL wind speed at IJV1.
The density scatter was performed for the full period of analysis (1979-01-15 to 2022-12-31) for IJV1.

Table 3.35 Joint assessment of the air temperature at 2m and the 10mMSL wind speeds at IJV1.
The joint assessment table was performed for the full period of analysis (1979-01-15 to 2022-12-31) for IJV1.

IJV1 (3.476690°E; 52.987620°N; d=25.8mMSL)
Frequency of Occurrence [%] (1979-01-15–2022-12-31; Δt=1h; t̄=1h) Omni
$T_{air,2m}$ [°C] - WRF

WS_{10} [m/s] - WRF

	[-12--10[	[-10--8[	[-8--6[	[-6--4[	[-4--2[	[-2-0[	[0-2[	[2-4[	[4-6[	[6-8[	[8-10[	[10-12[	[12-14[	[14-16[	[16-18[	[18-20[	[20-22[	[22-24[	[24-26[	[26-28[	[28-30[	Total	Accum
[30-32[	-	-	-	-	-	-	-	-	-	-	-	-	-	-	-	-	-	-	-	-	-	-	100.0...
[28-30[	-	-	-	-	-	-	-	-	-	-	-	-	-	-	-	-	-	-	-	-	0.001	100.0...
[26-28[	-	-	-	-	-	-	-	-	0.001	0.002	0.001	0.002	0.001	0.001	-	-	-	-	-	-	0.007	99.999
[24-26[	-	-	-	-	-	-	-	-	0.001	0.007	0.009	0.007	0.002	0.001	-	-	-	-	-	-	0.026	99.992
[22-24[	-	-	-	-	-	-	-	0.001	0.002	0.022	0.035	0.028	0.008	0.005	0.001	-	-	-	-	-	0.103	99.966
[20-22[	-	-	-	-	-	0.005	0.005	0.004	0.015	0.063	0.080	0.065	0.036	0.024	0.011	0.002	-	-	-	-	0.310	99.863
[18-20[	-	-	-	-	0.005	0.011	0.020	0.008	0.060	0.168	0.245	0.175	0.124	0.079	0.044	0.008	0.001	-	-	-	0.949	99.554
[16-18[	-	-	-	0.004	0.009	0.015	0.035	0.043	0.118	0.386	0.555	0.450	0.297	0.218	0.137	0.028	0.002	-	-	-	2.297	98.605
[14-16[	-	-	-	0.001	0.009	0.030	0.060	0.105	0.245	0.745	1.076	0.728	0.477	0.487	0.331	0.084	0.004	-	-	-	4.382	96.309
[12-14[	-	-	-	-	0.017	0.058	0.113	0.248	0.521	1.187	1.719	1.174	0.840	0.847	0.686	0.217	0.010	0.001	-	-	7.639	91.926
[10-12[	-	-	-	0.002	0.012	0.041	0.139	0.374	0.875	1.916	2.557	1.721	1.500	1.534	1.361	0.538	0.042	0.001	-	-	12.612	84.287
[8-10[	-	-	-	0.002	0.009	0.058	0.185	0.534	1.150	2.658	3.106	2.262	2.034	2.491	2.344	1.071	0.116	0.003	-	-	18.023	71.675
[6-8[	-	-	-	0.004	0.006	0.063	0.167	0.545	1.371	2.911	3.106	2.363	2.298	3.034	3.218	1.576	0.214	0.009	-	-	20.883	53.652
[4-6[	-	-	-	0.002	0.002	0.051	0.097	0.461	1.246	2.360	2.524	2.034	2.077	2.844	3.066	1.527	0.222	0.003	-	-	18.517	32.769
[2-4[	-	-	-	-	0.001	0.024	0.071	0.309	0.832	1.350	1.323	1.178	1.445	1.712	1.899	0.929	0.099	-	-	-	11.172	14.252
[0-2[	-	-	-	-	-	0.004	0.018	0.083	0.260	0.369	0.297	0.356	0.414	0.487	0.554	0.224	0.015	-	-	-	3.080	3.080
Total	-	-	-	0.016	0.070	0.360	0.910	2.715	6.695	14.141	16.633	12.544	11.554	13.765	13.652	6.204	0.725	0.016	-	-	100.0...	-
Accum	-	-	-	0.016	0.086	0.446	1.356	4.071	10.766	24.907	41.540	54.084	65.638	79.402	93.054	99.258	99.984	100.0...	100.0...	100.0...	100.0...	-	-

Marine icing occurs when sea spray from breaking waves or strong wind blowing over the sea surface freezes upon the contact with a surface. Required conditions for marine icing are wind speed greater than 10m/s, air

temperatures less than the freezing point of seawater, i.e. -1.86°C and sea surface temperature smaller than 8°C. Based on these thresholds and Figure 3.45 and Table 3.36 it was calculated that marine icing occurs 0.24% of the time between 1979-01-15 to 2022-12-31 at IJV1.

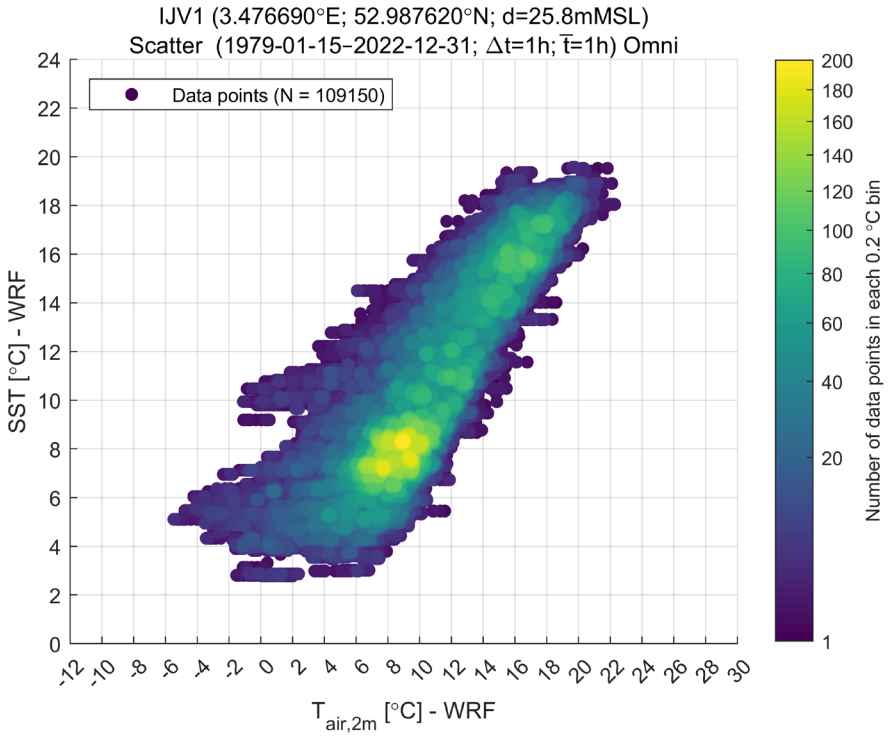

Figure 3.45 Density scatter of the air temperature at 2m against the sea surface temperature SST for 10mMSL-wind speeds larger than 10m/s at IJV1.
The density scatter was performed for the full period of analysis (1979-01-15 to 2022-12-31) for IJV1.

Table 3.36 Joint assessment of the air temperature at 2m and the sea surface temperature SST for 10mMSL-wind speeds larger than 10m/s at IJV1.
The joint assessment was performed for the full period of analysis (1979-01-15 to 2022-12-31) for IJV1.

IJV1 (3.476690°E; 52.987620°N; d=25.8mMSL)
Frequency of Occurrence [%] (1979-01-15–2022-12-31; Δt=1h; t̄=1h) Omni
$T_{air,2m}$ [°C] - WRF

SST [°C] - WRF

	[-12--10[	[-10--8[	[-8--6[	[-6--4[	[-4--2[	[-2-0[	[0-2[	[2-4[	[4-6[	[6-8[	[8-10[	[10-12[	[12-14[	[14-16[	[16-18[	[18-20[	[20-22[	[22-24[	[24-26[	[26-28[	[28-30[	Total	Accum
[22-24[	-	-	-	-	-	-	-	-	-	-	-	-	-	-	-	-	-	-	-	-	-	-	100.0...
[20-22[	-	-	-	-	-	-	-	-	-	-	-	-	-	-	-	-	-	-	-	-	-	-	100.0...
[18-20[	-	-	-	-	-	-	-	-	-	-	-	-	0.004	0.137	0.419	0.660	0.158	0.004	-	-	-	1.382	100.0...
[16-18[	-	-	-	-	-	-	-	-	-	-	-	0.044	0.467	2.727	4.938	2.276	0.048	-	-	-	-	10.499	98.618
[14-16[	-	-	-	-	-	-	-	-	-	0.013	0.096	0.818	2.934	5.786	3.612	0.163	0.001	-	-	-	-	13.423	88.119
[12-14[	-	-	-	-	-	-	-	0.003	0.045	0.215	1.020	2.766	3.971	2.431	0.108	0.001	-	-	-	-	-	10.559	74.696
[10-12[	-	-	-	-	-	0.005	0.086	0.144	0.231	0.663	3.098	4.650	3.642	0.198	0.003	-	-	-	-	-	-	12.720	64.137
[8-10[	-	-	-	-	-	0.014	0.043	0.264	1.032	4.049	8.629	5.787	0.587	0.004	-	-	-	-	-	-	-	20.408	51.417
[6-8[	-	-	-	0.002	0.030	0.104	0.375	0.934	2.712	8.387	8.410	1.269	-	-	-	-	-	-	-	-	-	22.222	31.010
[4-6[	-	-	-	0.026	0.157	0.384	0.678	1.335	2.313	2.458	0.907	0.025	-	-	-	-	-	-	-	-	-	8.282	8.788
[2-4[	-	-	-	-	-	0.058	0.132	0.085	0.151	0.080	-	-	-	-	-	-	-	-	-	-	-	0.506	0.506
[0-2[	-	-	-	-	-	-	-	-	-	-	-	-	-	-	-	-	-	-	-	-	-	-	-
Total	-	-	-	0.027	0.187	0.564	1.314	2.764	6.484	15.864	22.161	15.358	11.604	11.282	9.080	3.099	0.207	0.004	-	-	-	100.0...	-
Accum	-	-	-	0.027	0.214	0.779	2.093	4.857	11.340	27.205	49.366	64.724	76.328	87.610	96.690	99.789	99.996	100.0...	100.0...	100.0...	100.0...	-	-

3.6.4.2 Sea Ice

Sea ice is frozen water which usually forms in the Arctic and Antarctic oceans, and more rarely in mid-latitudes. In this report, sea ice dataset is provided by ERA5 (see Section 5.2 in [3]). As expected, the dataset at IJV1 reveals that no sea ice event occurred on the last 44 years, between 1979-01-15 to 2022-12-31.

3.6.5 Marine growth

Marine growth, often referred to as marine fouling or biofouling, is the accumulation and proliferation of marine organisms, including algae and various animals, on submerged surfaces like ship hulls, buoys, piers, offshore platforms, and other underwater structures. This natural process occurs when marine organisms settle and grow on these surfaces, and it can have several adverse effects on various industries and marine operations.

Numerous factors influence the amount and type of marine growth, including salinity, temperature, depth, current speed, and wave exposure, in addition to biological factors such as food availability, larval supply, presence of predators, and the general biology and physiology of the fouling species.

Within minutes upon introduction of new hard substrates in aquatic environments, fouling organisms will start to colonise the newly introduced surfaces [22]. A succession of species composition is expected, due to the organisms competing for space and thus, the climax species community composition will not be met within the first years [23]. In the beginning, bacteria, eukaryotic organisms, and fungi attach to the surface, eventually forming a biofilm, which function as the basis for macrofauna to adhere to the surface [22, 24]. Then follow the macro-biofouling species, which typically are sessile organisms such as bivalves (e.g., mussels and oysters), calcareous polychaetes, barnacles, sea anemones, hydrozoans, bryozoans as well as macroalgae. Also, motile organisms associated with biofouling communities include, among others, crustaceans, and motile polychaetes, as they exploit the debris associated with filter-feeders such as mussels.

Along with succession in species community, the individual organisms grow larger, creating an increasing thickness of marine growth. Additionally, predators such as starfish and crabs become an integral part of the fouling ecosystem altering the mussel cover. Hence, the marine fouling on the submerged substrates form an entire marine ecosystem.
Developers and operators of offshore structures, including wind farms, are concerned about the additional weight and loads that marine growth adds to structures. Most quantitative studies of biofouling focus on biodiversity on structures. Such studies can be useful for estimating additional weight and loads on structures.

Table 3.37 provides an overview of what can be expected in an offshore structure such as IJmuiden Ver Wind Farm Zone (IJVWFZ), as well as DHI recommendations for calculations on the effect of added marine growth.

Table 3.37 Overview of marine growth in different zones.
Literature based estimations as well as DHI recommendations are presented in this table based on [15, 25-29].

Approximate depth (meters from MSL)	Dominating taxa/*Species*	Expected thickness (mm)	Expected wet weight ($kg\ m^{-2}$)	DHI recommendation Thickness (mm)	DHI recommendation Wet weight ($kg\ m^{-2}$)
Splash zone	Amphipods (1;2) Blue mussel *(Mytilus edulis)* (2) Macroalgae (6)	52.76 (range 0-350) (5)	3 - 4 (3)	150 (4)	25-40 (2)
2	Barnacles (1) Blue mussel (*Mytilus edulis*) (2) Macroalgae (6)	52.76 (range 0-350) (5)	10-18 (3)	150 (4)	25-40 (2)
5	Blue mussel (*Mytilus edulis*) (1; 2) Macroalgae (6)	52.76 (range 0-350) (5)	8 - 10 (3)	150 (4)	25-40 (2)
10	Hydroids, Amphipods, Anthozoa (1; 2) Macroalgae (6)	52.76 (range 0-350) (5)	7 - 27 (3)	150 (4)	25-40 (2)
15-17	Hydroids, Amphipods Anthozoa (1; 2)	52.76 (range 0-350) (5)	14 (3)	150 (4)	25-40 (2)
20 – 35 [30]	Cnidaria, Bivalvia, Hexacorallia	35 [30]			
35 – 45 [30, 31]	Cnidaria, Bivalvia, Hexacorallia	30 [30, 31]			

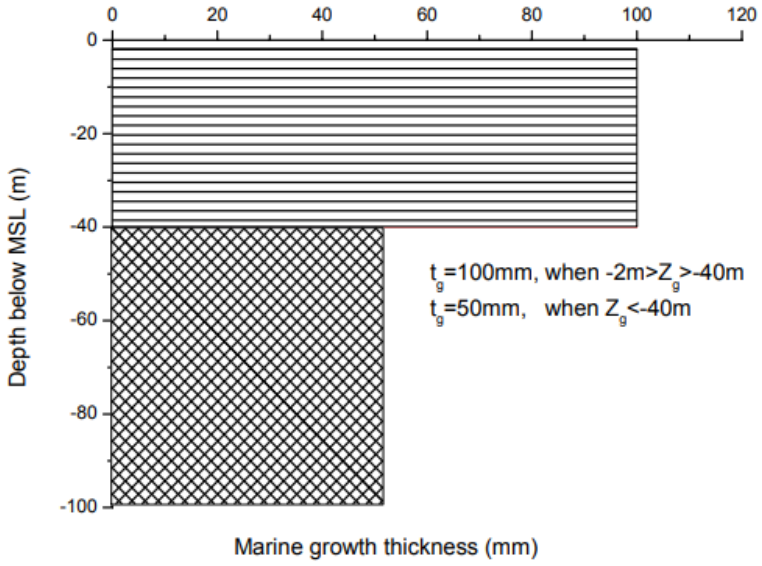

Figure 3.46 Density scatter of the air temperature at 2m against the sea surface temperature SST for 10mMSL-wind speeds larger than 10m/s at IJV1.

The expected values of thickness and wet weight in Table 3.37 does not directly align as they have been pulled from different studies. The combination of species directly determines the relationship of the wet weight and thickness, however, few studies providing this relationship has been made. Nonetheless they provide an impression of what can be expected. Furthermore, studies performed on the wet weight and thickness of the marine biofouling depend on many factors and thus, it is important to keep in mind that outliers may be seen. Thus, the DHI recommendations are relatively more conservative than what has been found in the literature, however, the recommendations are supported by the DNVGL-ST-0437 [15].

While marine growth is a concern for developers of offshore structures, positive effects have also arisen from biofouling on these structures. A study done by Ter Hofstede et al.[32] showed that presence of windfarms has positive effects on the epibenthic communities. Introduction of submerged artificial structures may provide what is known as the artificial reef effect, by ensuring new hard substrates for settlement. These settlements provide new habitat for epibenthic species as well as pelagic organisms such as fish and polychaetes, who are searching for food and protection in these environments. Thus, the artificial reef effect can potentially increase the local biodiversity and biomass [24, 33]. The increased abundance of species near and on the wind farms structures thus provide additional food source for higher trophic levels such as fish, mammals and birds [34, 35]. The study done by [32] also provided a species list from four different Offshore Wind Farms, in the same region as IJmuiden Ver Wind Farm Zone (IJVWFZ).

An overview of the species occurring in the local area of the IJVWFZ [32] is given in Table 3.38 with additional information on their ecological importance/traits as well as growth. Such information can give insights into the type of habitat that is being created. DHI notes that considering timely efforts to enhance biodiversity in the marine environment such information will be highly

valuable in the future. A total of 47 species from 7 different phyla were identified from video footage done in transect of four nearly located Offshore Wind Farms (Princess Amalia (NL), Belwind (B), Gemini (NL) and Luchterduinen (NL)) to IJmuiden Ver (NL). Most species found were associated with the actual wind farm structures, others were found near the structures [32]. Furthermore, species listed in a study done on the OWF, Thornton Bank (B) is added to the species list [28]. This added 2 phyla to the list and 16 species. Thus, Table 3.38 contains a list of species which can be expected to form marine growth on the IJVWFZ.

Table 3.38 Overview of the species occurring in the local area of the IJVWFZ.
Ecological importance/trait information and growth information has been retrieved from the CEFAS database[36], as well as FishBase, SeaLifeBase, WoRMS, Algaebase and MarLIN.

Phylum (*taxa contained*)	Species name	Ecological importance/description of ecological trait	Growth information
Porifera	*Cliona celata*	Suspension feeder, Attached to substratum	Perennial (1-3 years)
	Suberites ficus	Suspension feeder, Attached to substratum(/epibiontic)	Perennial (1-10 years)
Cnidaria (*Anthozoa, Hydroids*	*Actinothoe sphyrodeta*	Suspension feeder, Attached to substratum	*N/A*
	Alcyonium digitatum	Suspension feeder/predator, Attached to substratum	Perennial (>10 years)
	Diadumene cincta	Suspension feeder, Attached to substratum	*N/A*
	Halecium sp.	Suspension feeder/predator, Attached to substratum	Perennial (3-10 years)
	Hydractinia echinate	*Attached to substratum*	*N/A*
	Metridium senile	Suspension feeder/predator, Attached to substratum/epibiontic	Perennial (>10 years)
	Nemertesia sp.	Suspension feeder/predator, Attached to substratum	Perennial (3-10 years)
	Sagartia sp.	*N/A*	*N/A*
	Sagartia undatus	*N/A*	*N/A*
	Cylista elegans	Suspension feeder/predator, Attached to substratum	Perennial (>10 years)
	Cylista troglodytes	Suspension feeder/predator, Attached to substratum	Perennial (>10 years)
	Urticina sp.	Suspension feeder/predator, Attached to substratum	Perennial (3-10 years)
Annelida	*Lanice conchilega*	Suspension feeder, tube-dwelling	Perennial (1-3 years)
	Myrianida (Autolytus) spp	Predator, crawling	Annual/Perennial (less than 1 year to 3 years)
	Spirobranchus triqueter	Suspension feeder, Attached to substratum	Annual/Perennial (less than 1 year to 3 years)
	Cylista troglodytes	Suspension feeder, Attached to substratum	Perennial (>10 years)
Arthropoda (*Amphipods)*	*Cancer pagurus*	Predator, freeliving and shelters in crevice holes	Perennial (>10 years)

Phylum (*taxa contained*)	Species name	Ecological importance/description of ecological trait	Growth information
Arthropoda (*Amphipods*) (continued)	*Caprella* sp.	Predator, Freeliving	Annual
	Homarus gammarus	Ectoparasitic	N/A
	Hyas sp.	Predator/scavenger/(feeds on surface deposit), freeliving (shelters in crevice holes)	Perennial (3-10 years)
	Inachus sp.	Predator/scavenger, freeliving	Perennial (1-3 years)
	Jassa herdmani	Feeds on surface deposit/suspension feeder, Tube-dwelling	Annual/ Perennial (1-3 years)
	Liocarcinus holsatus	Predator/scavenger, freeliving	Perennial (3-10 years)
	Necora puber	Predator/scavenger, freeliving	Perennial (3-10 years)
	Pagurus bernhardus	Predator/scavenger/feeds on surface deposit/suspension feeder, freeliving	Perennial (3-10 years)
	Pisidia longicornis	Suspension feeder, freeliving	Perennial (1-3 years)
	Telmatogeton japonicus	*N/A*	*N/A*
	Balanus perforatus	Suspension feeder, Attached to substratum	Perennial (3-10 years)
	Austrominius modestus	Suspension feeder	N/A
	Hippolyte varians,	Predator/Scavenger, crawling	Perennial (1-3 years)
	Macropodia linaresi	Predator/Scavenger, crawling	*N/A*
	Megabalanus coccopoma	Suspension feeder, Attached to substratum	Perennial (1-3 years)
	Phtisica marina	Predator, crawling	Annual
	Pilumnus hirtellus	Suspension feeder, Attached to substratum	Annual/Perennial (less than 1 year to 3 years)
	Thoralus cranchii	Predator(/Scavenger), freeliving	Perennial (1-3 years)
Mollusca	*Alloteuthis* sp.	Freeliving	*N/A*
	Mytilus edulis	Suspension feeder, Attached to substratum	Perennial (>10 years)
	Sepia officinalis	Predator (Feeds on small molluscs, crabs, shrimps, other cuttlefishes, and juvenile demersal fishes), Freeliving	Perennial (1-3 years)
	Aequipecten opercularis	Suspension feeder, Mobile	Perennial (3-10 years)
	Crepidula fornicata	Suspension feeder, Sessile	Perennial (3-10 years)
	Epitonium clathratulum	Predator, crawling	Perennial (3-10 years)
Bryozoa	*Electra pilosa*	Suspension feeder, Sessile	Annual/Perennial (less than 1 year to 3 years)
Echinodermata	*Asterias rubens*	Predator/scavenger, freeliving	Perennial (3-10 years)
	Astropecten irregularis	Predator/scavenger, freeliving	Perennial (3-10 years)
	Ophiura sp.	Predator/scavenger, freeliving	Perennial (3-10 years)
Chordata	*Callionymus* sp.	Freeliving	*N/A*
	Chelidonichthys lucerna	Predator (Feeds on fish, crustaceans and mollusks), Freeliving	Perennial (>10 years)

Phylum (*taxa contained*)	Species name	Ecological importance/description of ecological trait	Growth information
Chordata (continued)	*Ctenolabrus rupestris*	Predator (Feed on bryozoans, crustaceans and gastropods), Freeliving	Perennial (3-10 years)
	Diplosoma sp.	Attached to substratum	*N/A*
	Entelurus aequoreus	Predator (Feed on small crustaceans and fish fry), Freeliving	Perennial
	Gadus morhua	Predator (Omnivorous; feed at dawn or dusk on invertebrates and fish, including young cod), Freeliving IUCN Red list (Vulnurable)	Perennial (>10 years)
	Gobius sp.	Predator, Freeliving	Perennial
	Mullus surmuletus	Predator (Feed on benthic organisms such as shrimps and amphipods, polychaetes, mollusks, and benthic fishes), Freeliving	Perennial (>10 years)
	Myoxocephalus sp.	Predator, Freeliving	Perennial
	Parablennius gattorugine	Freeliving	*N/A*
	Pholis gunnellus	Predator (Feeds on small crustaceans, polychaetes, mollusks and fish eggs), Freeliving	Perennial (3-10 years)
	Platichthys flesus	Predator (Feed on benthic fauna; small fish and invertebrates), Freeliving	Perennial (>10 years)
	Solea solea	Predator (Feed on worms, mollusks and small crustaceans), Freeliving	Perennial (>10 years)
	Syngnathus sp.	Predator, Freeliving	*N/A*
	Taurulus bubalis	Predator (Feeds on mysids, amphipods (gammarids), decapods, polychaetes, mollusks, ophiuroids and fishes), Freeliving	*N/A*
	Trisopterus sp.	Freeliving	*N/A*
Chlorophyta	*Blidingia minima*	Attached to substratum/epiphyte	Annual
	Ulva intestinalis	Attached to substratum/epiphyte	Annual
	Ulva compressa	Attached to substratum/epiphyte	Annual
Rhodophyta	*Bangia fuscopurpurea*	Attached to substratum/epiphyte	Annual

The species listed in Table 3.38 give an overview of the species that can be anticipated to grow as 'marine growth' on the offshore foundations at IJVWFZ. The information communicated for each species gives insights into the species-specific ecological role and function. Moreover, the lifespan of each species is indicated which reaches a maximum of about 10 years for most of the species.

A newly formed habitat takes about 8 to 10 years to create a climax (fully balanced) species community. Therefore, most of the species that settled initially will persist until this climax community has formed where individual

species abundances will shift over time. The development of the climax community is driven by competition for food and space. One can extrapolate from the information given that a lot of the species are predatorial and therefore are in competition with each other.
The anticipated marine growth information on expected thickness and wet weight depending on the depth zone can be depicted from Table 3.37. The taxa information has been carried over the Table 3.38 so that the various depth zones can be interrelated with the ecological information given. Key information is, that the marine growth thickness at the various depths zones consists of different species assemblages with different ecological functionalities. In depths > 10m significantly lower amounts of vegetative marine growth can be anticipated due to low light intensities characterising water depths >10m.

3.6.6 Sea temperature, salinity, and density

Seawater temperature and salinity at the sea surface layer were adopted from the HD_{UKNS3D} model data (see Section 5.1 in [3]) at the IJV1 location for the period 2013-01-01 to 2022-12-31.

The time series data and monthly mean distribution of the water temperature at the surface is shown in Figure 3.47 and Figure 3.48 respectively. As expected, the water temperatures clearly portray the seasonal cycle of the northern hemisphere, with higher temperatures in summer months (peak in August and September), and lower temperatures in winter months (minimum in February).

The annual and monthly analysis statistics are summarized in Table 3.39.

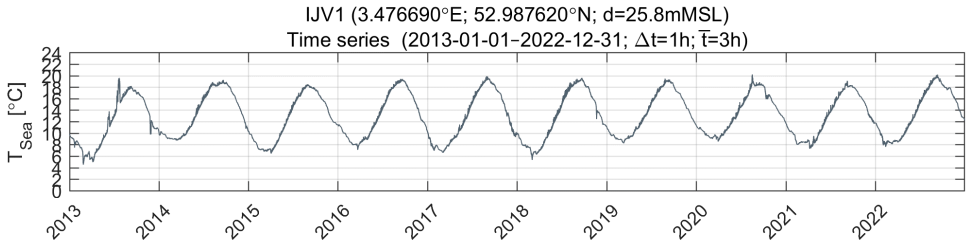

Figure 3.47 Time series of seawater temperature at the surface at IJV1.
Time series of seawater temperature values shown for the full period of analysis (1979-01-15 to 2022-12-31) for IJV1.

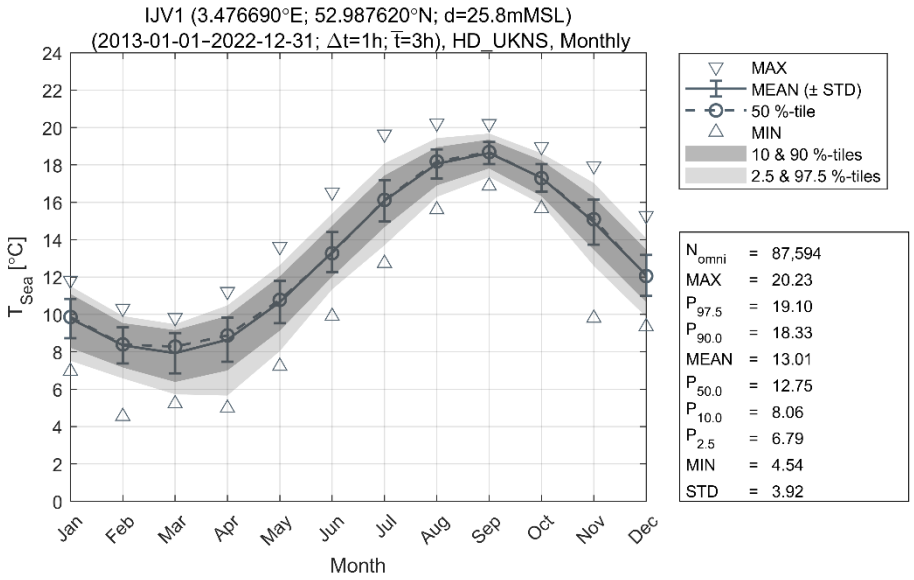

Figure 3.48 Monthly statistics of seawater temperature at the surface at IJV1.
Monthly statistics of seawater temperature is shown for the full period of analysis (1979-01-15 to 2022-12-31) for IJV1.

Table 3.39 Annual and monthly statistics of seawater temperature at the surface at IJV1.
Annual and monthly statistics table of seawater temperature is shown for the full period of analysis (1979-01-15 to 2022-12-31) for IJV1.

Air temperature [C]	Annual	Jan	Feb	Mar	Apr	May	Jun	Jul	Aug	Sep	Oct	Nov	Dec
N	87594	7440	6750	7428	7200	7440	7200	7440	7440	7200	7440	7200	7416
MEAN	13.0	9.8	8.3	7.9	8.6	10.7	13.3	16.1	18.1	18.6	17.3	14.9	12.1
STD	3.9	1.1	1.0	1.1	1.2	1.1	1.1	1.1	0.8	0.6	0.7	1.2	1.1
MIN	4.5	7.0	4.5	5.2	5.0	7.2	9.9	12.7	15.6	16.9	15.7	9.8	9.3
P5	7.2	7.9	7.0	6.0	6.5	8.7	11.6	14.1	16.6	17.6	16.1	13.1	10.2
P50	12.8	9.9	8.4	8.3	8.9	10.8	13.3	16.1	18.2	18.7	17.3	15.1	12.1
P95	18.8	11.3	9.8	9.3	10.3	12.4	15.1	17.7	19.3	19.6	18.4	16.6	13.8
MAX	20.2	11.8	10.3	9.8	11.2	13.6	16.5	19.6	20.2	20.2	19.0	17.9	15.3

The time series data and monthly mean distribution of the sea salinity is shown in Figure 3.49 and Figure 3.50 respectively, with a maximum and minimum salinity of 35.3 and 30.6 PSS-78.

The annual and monthly analysis statistics are summarized in Table 3.40.

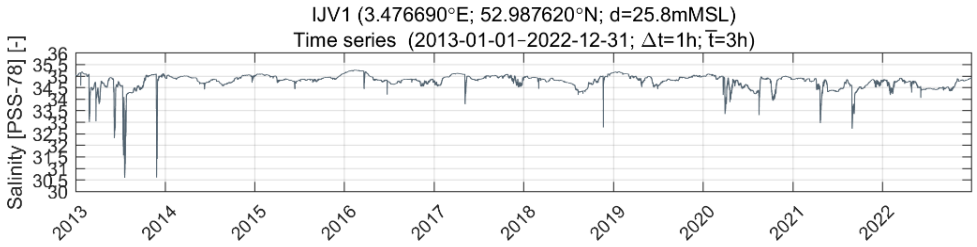

Figure 3.49 Time series of seawater salinity at the surface at IJV1.
Timeseries of seawater salinity is shown for the full period of analysis (1979-01-15 to 2022-12-31) for IJV1.

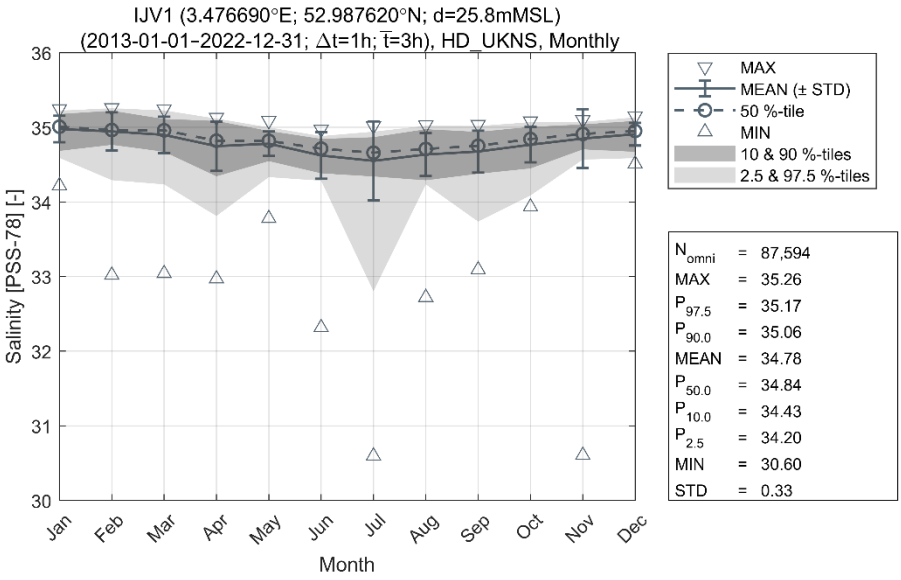

Figure 3.50 Monthly statistics of seawater salinity at the surface at IJV1.
Monthly statistics of seawater salinity is shown for the full period of analysis (1979-01-15 to 2022-12-31) for IJV1.

Table 3.40 Annual and monthly statistics of seawater salinity at the surface at IJV1.
Annual and monthly statistics table of seawater salinity is shown for the full period of analysis (1979-01-15 to 2022-12-31) for IJV1.

Salinity [PSS-78]	Annual	Jan	Feb	Mar	Apr	May	Jun	Jul	Aug	Sep	Oct	Nov	Dec
N	87594	7440	6750	7428	7200	7440	7200	7440	7440	7200	7440	7200	7416
MEAN	34.8	35	34.9	34.9	34.7	34.8	34.6	34.5	34.6	34.7	34.8	34.8	34.9
STD	0.3	0.2	0.3	0.2	0.3	0.2	0.3	0.5	0.3	0.3	0.2	0.4	0.1
MIN	30.6	34.2	33.0	33.0	33.0	33.8	32.3	30.6	32.7	33.1	33.9	30.6	34.5
P05	34.3	34.6	34.4	34.4	34.0	34.4	34.4	34.2	34.3	34.3	34.3	34.6	34.6
P50	34.8	35.0	35.0	35	34.8	34.8	34.7	34.7	34.7	34.8	34.8	34.9	35.0
P95	35.1	35.2	35.2	35.2	35.1	35.0	34.9	34.9	35	35	35.0	35.1	35.1
MAX	35.3	35.2	35.3	35.2	35.1	35.1	35	35	35	35	35.1	35.1	35.1

Sea density was calculated for the IJV1 location using the international one-atmosphere equation of state of seawater derived by [37]. The sea temperature and salinity from the HD_{UKNS3D} model was used to calculate the sea density at the sea surface layer for the period 2013 to 2022.

The time series data and monthly mean distribution of the sea density is shown in Figure 3.51 and Figure 3.52 respectively, with a maximum and minimum salinity of 1021.6 and 1027.5 kg/m^3.

The annual and monthly analysis statistics are summarized in Table 3.41.

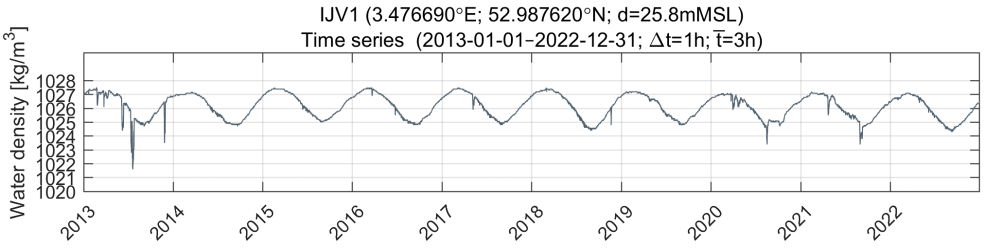

Figure 3.51 Time series of seawater density at the surface at IJV1.
Timeseries of seawater density is shown for the full period of analysis (1979-01-15 to 2022-12-31) for IJV1.

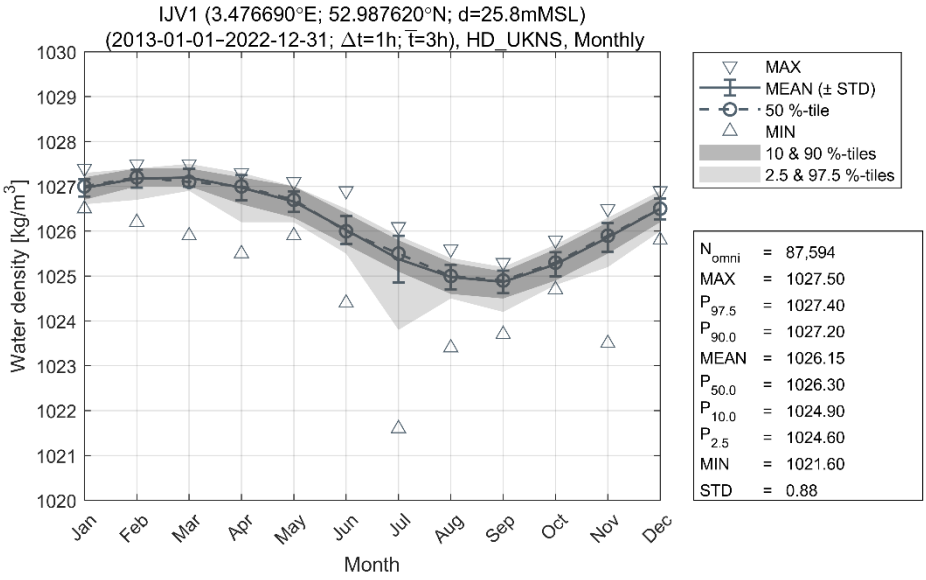

Figure 3.52 Monthly statistics of seawater density at the surface at IJV1.
Monthly statistics of seawater density is shown for the full period of analysis (1979-01-15 to 2022-12-31) for IJV1.

Table 3.41 Annual and monthly statistics of seawater density at the surface at IJV1.
Annual and monthly statistics table of seawater density is shown for the full period of analysis (1979-01-15 to 2022-12-31) for IJV1.

Sea density [kg/m^3]	Annual	Jan	Feb	Mar	Apr	May	Jun	Jul	Aug	Sep	Oct	Nov	Dec
N	87594	7440	6750	7428	7200	7440	7200	7440	7440	7200	7440	7200	7416
MEAN	1026.1	1027	1027.2	1027.2	1027	1026.7	1026	1025.4	1025	1024.9	1025.3	1025.9	1026.5
STD	0.9	0.2	0.2	0.2	0.3	0.2	0.3	0.5	0.3	0.3	0.3	0.3	0.2
MIN	1021.6	1026.5	1026.2	1025.9	1025.5	1025.9	1024.4	1021.6	1023.4	1023.7	1024.7	1023.5	1025.8
P5	1024.8	1026.6	1026.8	1027	1026.4	1026.2	1025.6	1025	1024.6	1024.4	1024.8	1025.4	1026.1
P50	1026.3	1027	1027.2	1027.1	1027	1026.7	1026	1025.5	1025	1024.9	1025.3	1025.9	1026.5
P95	1027.3	1027.3	1027.4	1027.4	1027.3	1027	1026.4	1025.9	1025.4	1025.2	1025.7	1026.3	1026.8
MAX	1027.5	1027.4	1027.5	1027.5	1027.3	1027.1	1026.9	1026.1	1025.6	1025.3	1025.8	1026.5	1026.9

3.6.7 Air density

The air density was retrieved from the WRF dataset (see Section 4.1 in [3]) for the period 1979-01-15 to 2022-12-31 at 160mMSL height (hub height).

The time series data and monthly mean distribution of the air density is shown in Figure 3.53 and Figure 3.54 respectively. The air density is inversely proportional to the air temperature and the specific humidity. It increases in winter with a maximum in February and decreases in summer with a minimum in August. The minimum and maximum air density is 1.1 and 1.3 kg/m^3.

The annual and monthly analysis statistics are summarized in Table 3.42.

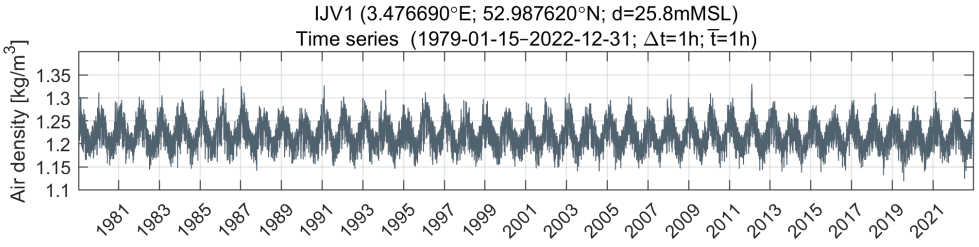

Figure 3.53 Time series of air density at IJV1 at 160mMSL.
Timeseries of air density is shown for the full period of analysis (1979-01-15 to 2022-12-31) for IJV1.

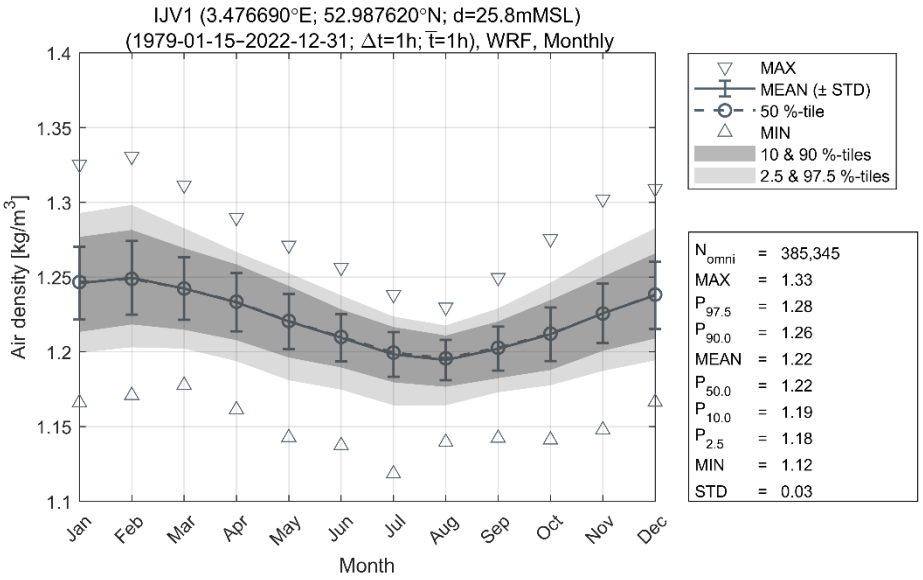

Figure 3.54 Monthly statistics of air density at IJV1 at 160mMSL.
Monthly statistics of air density is shown for the full period of analysis (1979-01-15 to 2022-12-31) for IJV1.

Table 3.42 Annual and monthly statistics of air density at IJV1 at 160mMSL.
Annual and monthly statistics table of air density is shown for the full period of analysis (1979-01-15 to 2022-12-31) for IJV1.

Air Density [kg/m^3]	Annual	Jan	Feb	Mar	Apr	May	Jun	Jul	Aug	Sep	Oct	Nov	Dec
N	385345	32400	29832	32736	31680	32736	31680	32736	32736	31680	32736	31680	32713
MEAN	1.222	1.246	1.249	1.242	1.233	1.220	1.209	1.198	1.195	1.202	1.212	1.226	1.238
STD	0.027	0.024	0.025	0.021	0.019	0.018	0.016	0.015	0.014	0.015	0.018	0.020	0.022
MIN	1.118	1.166	1.171	1.178	1.161	1.143	1.137	1.118	1.139	1.142	1.141	1.148	1.166
P5	1.203	1.228	1.232	1.228	1.220	1.208	1.199	1.189	1.186	1.192	1.199	1.212	1.222
P50	1.220	1.247	1.249	1.242	1.233	1.221	1.210	1.199	1.196	1.203	1.212	1.226	1.238
P95	1.241	1.263	1.267	1.257	1.248	1.234	1.221	1.209	1.204	1.212	1.224	1.239	1.253
MAX	1.331	1.325	1.331	1.311	1.290	1.271	1.256	1.238	1.230	1.250	1.276	1.302	1.309

3.6.8 Relative humidity

The relative humidity was retrieved from the WRF dataset (see Section 4.1 in [3]) for the period 1979-01-15 to 2022-12-31 at 160mMSL height (hub height).

The time series data and monthly mean distribution of the relative humidity is shown in Figure 3.55 and Figure 3.56 respectively. The relative humidity shows a seasonal variation where the highest humidity occurs in January with a mean of 83.7% and the lowest humidity observed in August with a mean of 75.9%.

The annual and monthly analysis statistics are summarized in Table 3.43.

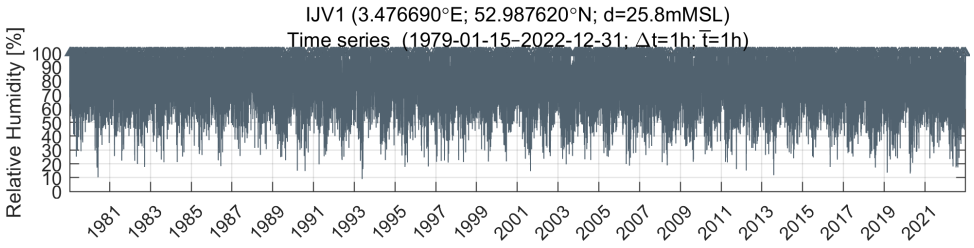

Figure 3.55 Time series of relative humidity at IJV1 at 160mMSL.
Time series of relative humidity is shown for the full period of analysis (1979-01-15 to 2022-12-31) for IJV1.

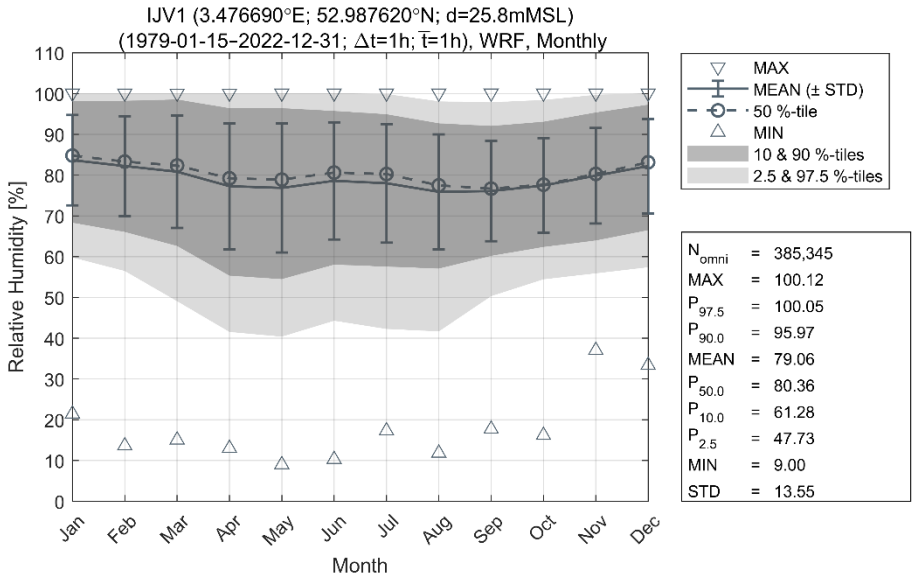

Figure 3.56 Monthly statistics of relative humidity at IJV1 at 160mMSL.
Monthly statistics of relative humidity is shown for the full period of analysis (1979-01-15 to 2022-12-31) for IJV1.

Table 3.43 Annual and monthly statistics of relative humidity at IJV1 at 160mMSL.
Annual and monthly statistics table of relative humidity is shown for the full period of analysis (1979-01-15 to 2022-12-31) for IJV1.

Relative Humidity [%]	Annual	Jan	Feb	Mar	Apr	May	Jun	Jul	Aug	Sep	Oct	Nov	Dec
N	385345	32400	29832	32736	31680	32736	31680	32736	32736	31680	32736	31680	32713
MEAN	79.1	83.7	82.2	80.8	77.3	76.9	78.6	78.0	75.9	76.1	77.5	79.8	82.2
STD	13.6	11.1	12.2	13.8	15.4	15.8	14.4	14.5	14.1	12.3	11.6	11.7	11.6
MIN	9.0	21.4	13.6	15.0	13.0	9.0	10.3	17.3	11.8	17.7	16.2	37.0	33.4
P5	54.4	63.8	61.2	55.9	47.7	46.4	50.1	49.0	48.5	55.3	58.3	59.6	61.5
P50	80.4	84.8	83.3	82.4	79.2	78.9	80.6	80.3	77.5	76.7	77.6	80.3	83.1
P95	99.0	100.0	100.0	100.0	99.4	99.7	99.0	98.1	95.9	95.5	96.3	98.2	99.6
MAX	100.1	100.1	100.1	100.1	100.1	100.1	100.1	100.1	100.1	100.1	100.1	100.1	100.1

3.6.9 Air temperature

The air temperature was retrieved from the WRF dataset (see Section 4.1 in [3]) for the period 1979-01-15 to 2022-12-31 at 160mMSL height (hub height).

The monthly mean distribution of the air temperature at hub height is shown in Figure 3.57 and Figure 3.58. As expected, the temperatures clearly portray the seasonal cycle of the northern hemisphere, with higher temperatures in summer months (peak in July), and lower temperatures in winter months (minimum in January). The annual and monthly analysis statistics are summarized in Table 3.44.

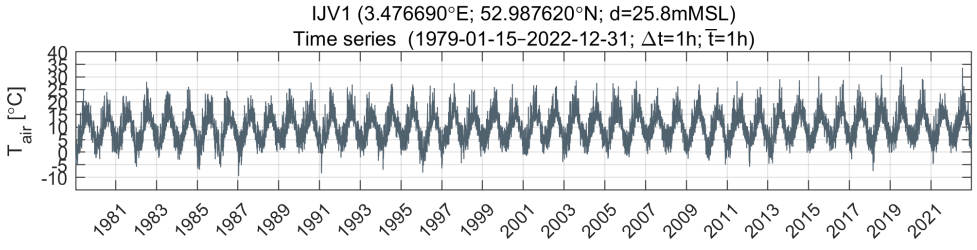

Figure 3.57 Time series of air temperature at IJV1 at 160mMSL.
Time series of air temperature is shown for the full period of analysis (1979-01-15 to 2022-12-31) for IJV1.

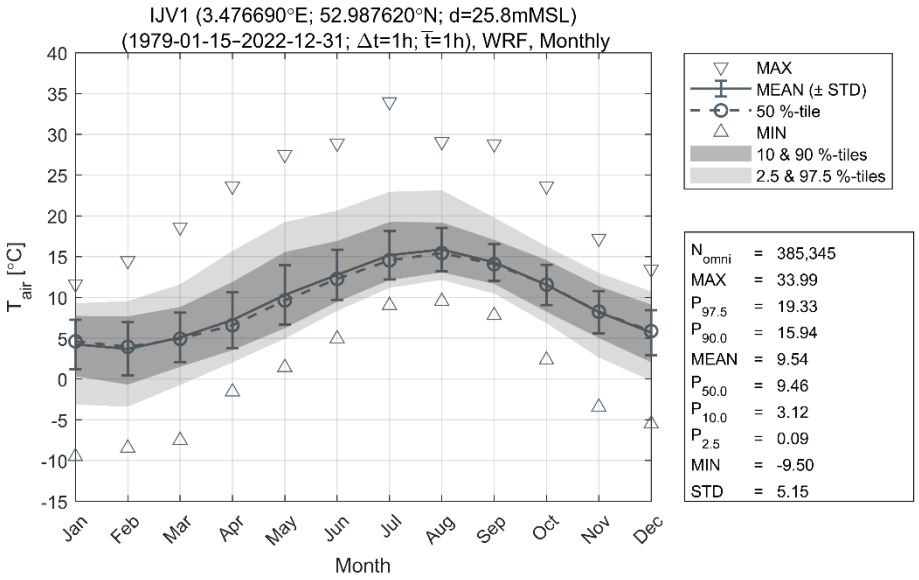

Figure 3.58 Monthly statistics of air temperature at IJV1 at 160mMSL.
Monthly statistics of air temperature is shown for the full period of analysis (1979-01-15 to 2022-12-31) for IJV1.

Table 3.44 Annual and monthly statistics of air temperature at IJV1 at 160mMSL.
Annual and monthly statistics table of air temperature is shown for the full period of analysis (1979-01-15 to 2022-12-31) for IJV1.

Air temperature [C]	Annual	Jan	Feb	Mar	Apr	May	Jun	Jul	Aug	Sep	Oct	Nov	Dec
N	385345	32400	29832	32736	31680	32736	31680	32736	32736	31680	32736	31680	32713
MEAN	9.5	4.2	3.7	5.1	7.2	10.3	12.8	15.2	15.9	14.3	11.5	8.2	5.7
STD	5.1	3	3.3	3.0	3.4	3.6	3.1	3.0	2.6	2.3	2.5	2.6	2.8
MIN	-5.8	-5.8	-5.1	-4.5	-1.0	1.4	4.9	9.0	9.5	7.8	2.3	-2.1	-3.3
P5	1.5	-0.8	-1.3	0.3	2.7	5.6	8.8	11.6	12.6	11.0	7.5	3.8	0.8
P50	9.5	4.6	3.9	4.9	6.6	9.6	12.3	14.5	15.4	14.1	11.6	8.3	5.9
P95	17.5	8.6	8.6	10.1	13.8	17.6	18.9	21.3	21.3	18.3	15.5	12.2	10.0
MAX	34	11.6	14.5	18.6	23.6	27.5	28.9	34	29.1	28.8	23.7	17.2	13.4

3.6.10 Air pressure

The air pressure was retrieved from the WRF dataset (see Section 4.1 in [3]) for the period 1979-01-15 to 2022-12-31 at 160mMSL height (hub height).

The time series data and monthly mean distribution of the air pressure is shown in Figure 3.59 and Figure 3.60 respectively.

The air pressure mean is rather stable around 1014 to 1015 hPa throughout the year with a slight lower air pressure during winter and higher during summer. During winter the air pressure varies more with a minimum of 951.83

and a maximum of 1047.45 hPA compared to summer which has the minimum and maximum air pressure within this range.

The annual and monthly analysis statistics are summarized in Table 3.45.

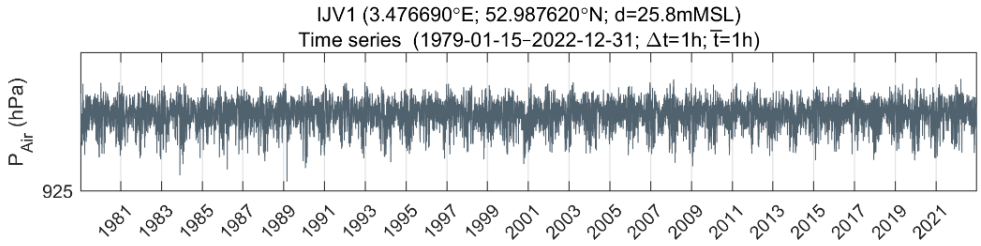

Figure 3.59 Time series of air pressure at IJV1 at 160mMSL.
Time series of air pressure is shown for the full period of analysis (1979-01-15 to 2022-12-31) for IJV1.

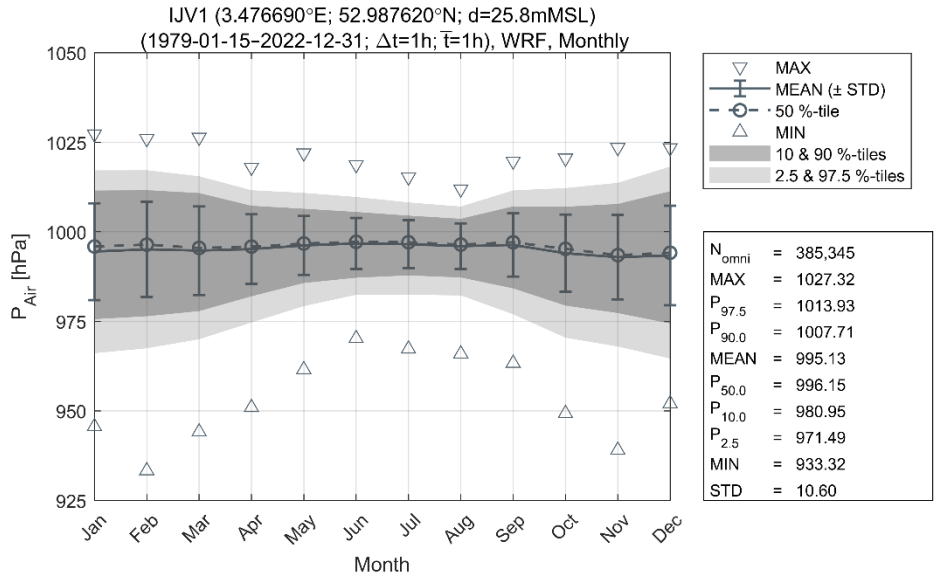

Figure 3.60 Monthly statistics of air pressure at IJV1 at 160mMSL.
Monthly statistics of air pressure is shown for the full period of analysis (1979-01-15 to 2022-12-31) for IJV1.

Table 3.45 Annual and monthly statistics of air pressure at IJV1 at 160mMSL.

Annual and monthly statistics table of air pressure is shown for the full period of analysis (1979-01-15 to 2022-12-31) for IJV1.

Air pressure [hPa]	Annual	Jan	Feb	Mar	Apr	May	Jun	Jul	Aug	Sep	Oct	Nov	Dec
N	385345	32400	29832	32736	31680	32736	31680	32736	32736	31680	32736	31680	32713
MEAN	995.1	994.4	995.1	994.7	995.1	996.2	996.8	996.6	996	996.3	994	992.9	993.4
STD	10.6	13.5	13.3	12.4	9.7	8.2	7.1	6.7	6.3	8.8	10.7	11.8	13.9
MIN	933.3	945.6	933.3	944.1	951.0	961.5	970.2	967.3	965.9	963.3	949.3	939.0	952.0
P5	988.9	985.2	986.7	985.7	988.6	990.6	992.0	992.1	992.0	991.0	986.9	985.2	983.8
P50	996.1	995.9	996.4	995.5	995.9	996.7	997.2	997.1	996.4	997.1	995.2	993.5	994.2
P95	1002.3	1004.3	1005.0	1004.2	1002.5	1001.9	1001.6	1001.4	1000.6	1002.6	1001.7	1001.7	1003.8
MAX	1027.3	1027.3	1026.0	1026.4	1018	1022	1018.7	1015.3	1011.9	1019.7	1020.5	1023.5	1023.4

4 Extreme Conditions Analyses

The extreme metocean condition analyses were based on the WRF high resolution atmospheric model, DHI's 2D HD_{DWF23} hydrodynamic model, and DHI's SW_{DWF23} spectral wave model datasets. The model datasets are available for 44 years (1979-01-15 to 2022-12-31) considering winds, water levels, depth-averaged currents, and waves. The current conditions throughout the water column have been assessed through a theoretical profile. Extreme value analyses were performed based on data extracted from the models at one (1) specified location, namely IJV1, and the results are presented in this report and delivered as accompanying digital appendices.

Extreme value analysis has been performed to summarise the extreme metocean conditions at the IJV1 analysis point. The analysis presented is based on DHI's state-of-the-art Joint Extreme Values Analysis (J-EVA) toolbox. J-EVA is a non-stationary extreme value analysis optimized for both marginal and conditional extreme analysis. The reader is directed to Appendix D, Appendix E, and Appendix F for a full description of the J-EVA methodology. The focus of this section is on the results and therefore does not detail the methodology.

The extreme metocean conditions analyses are summarised in the following sections:

- Wind: Section 4.1
- Water Level: Section 4.2
- Current: Section 4.3
- Wave: Section 4.4
- Other parameters: Section 4.5

Note that for the first year of data (1979), a period of about 14 days has been removed from the beginning of the wind, water levels, depth-averaged currents, and waves datasets to remove any effect of the spin-up of the hydrodynamic and wave models. The same period has been removed from the wind such that all datasets align in start and end date. The analysis was performed at a single location (IJV1), and the directional results are presented for 12 bins (30 degree centered at 0°N, 30°N, …). More details on the extreme metocean condition analyses presented in this report is summarised in Table 4.1.

Table 4.1 Extreme metocean conditions analyses.
The extreme conditions are delivered at **one (1) analysis locations for IJV.** The report presents the results at one location (IJV1), and the full set of results are provided as figures and .xlsx tables in a digital appendix.

Category	Variables	Bins	Return periods [years]	Comment
Wind	WS_{160} H_{m0} | WS_{160} CS_{tot} | WS_{160}	Omni Directional Seasonal	1, 2, 5, 10, 50, 100, 1000, 10000	Averaging periods: 1-h, 10-min, 1-min and 3-sec Heights: 160 mMSL
Water Level	HWL_{Tot}	Omni Seasonal	1, 2, 5, 10, 50, 100, 1000, 10000	N.A.
	LWL_{Tot}	Omni Seasonal		
	HWL_{Res}	Omni Seasonal		
	LWL_{Res}	Omni Seasonal		
Current	CS_{res}, CS_{tot} H_{m0} | CS_{tot}	Omni Directional Seasonal	1, 2, 5, 10, 50, 100, 1000, 10000	Depths: depth-averaged
Waves	H_{m0} T_p | H_{m0} T_{02} | H_{m0} CS_{tot} | H_{m0} WS_{160} | H_{m0} WS_{tot} | H_{m0}	Omni Directional Seasonal	1, 2, 5, 10, 50, 100, 1000, 10000	Total For all WL and LWL
	H_{max} T_{Hmax} | H_{max} $C_{max,\ SWL}$ $C_{max,MSL}$	Omni Directional Seasonal Directional Seasonal	1, 2, 5, 10, 50, 100, 1000, 10000	Total For all WL and LWL
	Wave breaking and limitations		N.A.	

4.1 Wind

Extreme value analysis for wind speed at 160 mMSL are presented in this section, based on the 44-years (1979-01-15 to 2022-12-31) of timeseries data.

Analysis of the extreme wind speed have been performed based on WRF model timeseries data at 160 mMSL. The wind parameters at 160 mMSL have been taken from the interpolated model results. Note that an extreme wind profile has not been assumed. A representative extreme wind speed profile has been provided in conjunction to the extreme value analysis results in Section 4.1.3.

The model results have been taken as representative of 10-minute average. Conversion to other averaging periods have been presented in Section 4.1.4.

Understanding the performance of the WRF model during the peak wind speed events needs to be considered when interpreting the J-EVA results. Considerable time and effort were used in this project to produce a unified-WRF model which was optimised for both normal and extreme conditions. A pre-selected highest 49 storms (between 1979 and 2022) were used in the calibration phase of the WRF model to put emphasis on the model performance during the peak events. The key results are discussed below.

4.1.1 Discussion on model performance for peak wind speed events

Before presenting the extreme value analysis results, it is important to understand the WRF model performance during extreme events. To quantify the performance of the modelled WRF wind speed during the largest storm events, a series of model validations and uncertainty considerations were investigated.

In the North Sea, there are 3 main types of wind measurements available, met mast (cup anemometer or sonic anemometer), fixed LiDAR and floating LiDAR systems (FLS). Met masts are recognised by the offshore wind industry as the measurement type with the lowest uncertainties and thereby highest accuracies, whereas LiDAR have the advantage of measuring at heights closer to the standard wind turbine hub heights. However, the latter is known to have larger uncertainties, especially in extreme wind speed conditions. Further discussions on the measurement types and uncertainty of these used in the North Sea are presented in a report by DNV [38].

Validation of the WRF model has been performed against met mast data at MMIJ at a height lower than the analysis, but the highest available cup anemometer level. Additionally, the height of the model timeseries used in this report (160 mMSL) has been validated using fixed LiDAR's and FLS. Both are presented in the following sections.

A discussion of the uncertainty associated with the measurement data used for validation is given.

Finally, a section with conclusions and recommendations for interpreting the extreme value analysis of wind speed at 160 mMSL is given.

For note, the largest modelled storm peak at 160 mMSL in the WRF model was 39.5 m/s from southwest, corresponding to the "Great Storm" in October 1987, as mentioned in the normal wind conditions analysis section (Section 3.1.1).

This storm peak magnitude is on-par with the largest observed (observed at MMIJ and FINO1 in October 2013).

4.1.1.1 Validation of met mast MMIJ at 100 mMSL

Observed wind speed at Meteomast IJmuiden (MMIJ) are not available for heights above 100 mMSL, which is typically the height of wind turbine hub heights used commonly in the North Sea offshore wind developments. However, as previously mentioned, MMIJ is commonly used in the offshore wind industry as a trusted data source for high quality wind measurement data. Therefore, it has been used here to validate the peak wind speed events at ~ 100 mMSL to aid in understanding the performance of the WRF model. The WRF model and measurements were assumed to be representative of the same averaging period, i.e., 10-minute average.

Presented in Figure 4.1 (upper panel) is a scatter plot of measured wind speed by the cup anemometer at 92 mLAT against the modelled WRF wind speed timeseries at 100 mMSL. It is noted that no vertical shearing has been applied neither to the model nor the measurement. For this comparison, the difference in the wind speed between the two heights was considered small enough to be neglected. The scatter plot shows that for mean wind speed (~ 5-15 m/s) the WRF model compares very well to the observations. For larger wind speed above 20 m/s there is a slight trend which indicated the WRF model overestimates the wind speed compared to the observations. This could be in part down to the difference in the height in which the model and measurements represent. Even when taking this in mind, the scatter plot gives a high level of confidence in the WRF model ability to capture the largest wind speed events.

However, the big exception to this is the WRF model performance for the largest observed peak wind of 37.9 m/s during the St Jude Storm in October 2013. The peak of this storm event in WRF at 100 mMSL is 30.7 m/s. The storm has a peak ratio[8] (PR) of 0.81, indicating an underestimation of the peak wind speed of nearly 20 %. It is well noted that this was likely one of the most extreme storms in the southern North Sea in the past 40 years. Therefore, the underestimation of this event in the WRF model cannot be ignored. Equally, the conclusion on the performance of the modelled peak wind speed in WRF cannot be governed by one storm observed at one location.

Further to this, the largest 5 peak storm events have been validated using a peak-peak plot shown in Figure 4.1 (lower panel) at MMIJ at 92 mLAT. As discussed above, the largest storm event (St Jude 2013) is underestimated considerably by the WRF model, whereas the next 4 peak events are overestimated by the WRF model when compared to observations. For the top 5 storm peaks, the average PR is 0.99.

[8] PR > 1 indicates an overestimation by the model for the storm peak. PR < 1 indicates an underestimation by the model.

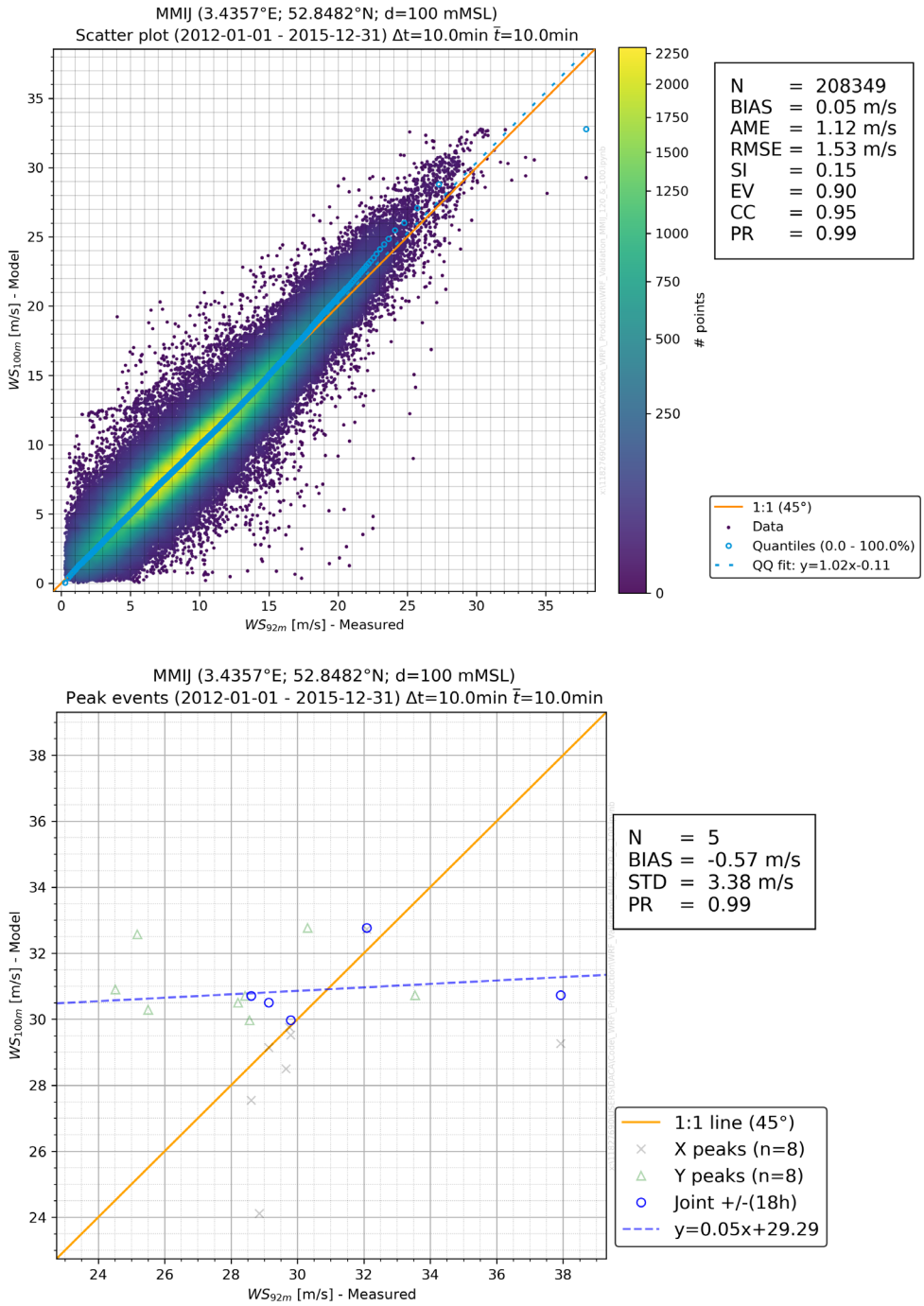

Figure 4.1 Comparison of measured and modelled (WRF) winds at MMIJ station.
Top: Scatter plot comparison. Bottom: peak-peak comparison. Observations are at 92 mLAT and model (WRF) are extracted at 100 mMSL. Observations are from cup anemometer.

In the case of the largest observed storm at MMIJ, a similar underestimation of the peak wind speed at the FINO1 met mast can be found for the same storm, though it is noted that the measurement at FINO1 was taken during a period which could be influenced by wakes from neighbouring operating wind farms.

4.1.1.2 Validation of fixed and floating LiDAR at 160 mMSL

For validation of the WRF modelled wind speeds at the height of the analysis, one must rely on LiDAR measured data, as met mast anemometer data is not

available for such heights. However, one must consider the uncertainty of measurement data recorded by LiDAR in extreme wind conditions. See a longer explanation in Section 4.1.1.3. A discussion on the validation of the WRF model at 160 mMSL is provided in this chapter. All validation plots of the observations at 160 mMSL against the WRF model are presented in Appendix G.1. A summary of the results is described here.

The validation of the peak ratio (PR) of the largest observed storm peak wind speed compared to the WRF model at 160 mMSL was 0.980 indicating that the WRF model peak were on average ~2 % lower than the observations. The validation was performed at 160 mMSL. The WRF model and measurements were assumed to be representative of the same averaging period, i.e., 10-minute average. The observed storm peaks recorded by FLS stations IJVA, IJVB, HKW, HKN, HKZ and TNW were considered, as well as the data from fixed LiDAR at MMIJ, K13a and EPL. Between 2 and 6 peaks were used in the analysis, depending on the number of years of record. The range of PRs for 119 storm peaks were 0.834 to 1.157.

Most notably, the largest storm peak recorded at the IJV project site (~28 m/s) by the two LiDAR buoys (IJVA and IJVB) had an average PR of 0.92, indicating that the model results were underestimating the peak 10-minute wind speed by 8 % at 160 mMSL. This should be considered when interpreting the extreme value analysis results presented for the IJV OWF site.

Similarly, it was concluded when investigating the storm peak ratio's at MMIJ LiDAR at 160 mMSL that the largest storm peak is underestimated by the WRF model at the same height. The largest observed storm at this location (36.0 m/s on 2013-10-28, named St Jude Storm[9] by the press) has a PR of 0.89 indicating the WRF model underestimates the peak wind speed by ~ 11 % for this extreme historical event. However, the accuracy of the MMIJ LiDAR data for this storm was considered very poor. The basis for this conclusion is that the MMIJ met mast recording the same storm at 92 mLAT with a cup anemometer recorded a peak wind of 38 m/s, i.e., a larger peak wind speed at a lower height. Given the question of accuracy of LiDAR measurements in extreme wind conditions, and the better-known accuracy of the cup anemometer on the met mast, the St Jude Storm was discarded from the LiDAR measurement data and not used further in the analysis. Instead, the measured St Jude Storm from the cup anemometer measurement was considered.

4.1.1.3 Discussion on measurement uncertainty

As alluded to previously, a key consideration when assessing the WRF model performance against observed storm peak is the uncertainty of the measurement data. For this analysis, cup anemometer, fixed LiDAR and floating LiDAR systems have been used.

It is widely agreed across the offshore wind industry that cup anemometers are the measurement devices for recording wind speed with the lowest uncertainty. Therefore, they are the preferred measurement device for validation of wind offshore. The report uncertainty of cup anemometers in mean wind conditions is 2 % [38]. Less is reported on the accuracy during extreme wind conditions. However, they are expensive to install, take time to install and are limited in height, and are therefore often not available. Typically met masts record to a

[9] Also known as Cyclone Christian.

height of approximately 100 m, which is nowadays well below wind turbine hub height elevations.

Though LiDAR's have the advantage of having the ability to measure wind speed at heights up to 300 mMSL and being quicker to install on site for the offshore wind industry, the accuracy of the measured data is lower than that of cup anemometers on met masts. Several reports have shown that for mean wind speeds, LiDAR can provide mean wind speed measurements with an accuracy of 2-4% [38]. However, for extreme wind speed little documentation is available. Some investigations by external parties have shown very poor performance of LiDAR (fixed and floating) in the North Sea for a large storm event (St Judy Storm Oct 2013).

4.1.1.4 Conclusions and recommendations

The extreme wind speed analysis presented in this report is for 160 mMSL. To understand the performance of the WRF model which has been used as input to the J-EVA model, peak storm events have been validated in this section.

To summarise the key considerations from the previous sections:

- Largest observed storm (St Jude Storm) is underestimated by ~ 20 % by the WRF model at 100 mMSL at the MMIJ met mast.
- Largest observed storm at the site by the two FLS LiDAR at 160 mMSL is underestimated by ~ 8 % by the WRF model at 160 mMSL.
- Average PR across 9 LiDAR's (3 fixed and 6 floating) for 118 storms with peak wind speed above 24 m/s is 1.00, indicating on average the peak observed wind speeds are represented by the WRF model at 160 mMSL.
- Uncertainty on mean wind speeds recorded by fixed and floating LiDAR reported as between 2-4%. Uncertainty on extreme wind speeds recorded by the same devices is unknown.
- Largest WRF wind speed modelled at 160 mMSL in the 44-year timeseries is 39.5 m/s ("Great Storm" in October 1987). Note this event has not validated due to lack of validation data for this period.

Before concluding on the performance of the WRF model at 160 mMSL used as input to the J-EVA analysis, it is worth noting that the "Great Storm" in October 1987 with a storm peak of similar magnitude, and occurring in October, is present in the WRF timeseries, and is therefore reflected in the J-EVA omni-directional estimate. In other words, the extremes estimated from J-EVA are less affected by the underestimation of the St Jude Storm, which is predicted by J-EVA to have an omni-directional return period of approximately 50 years.

Overall, the peak ratio comparison indicates a very good performance of the WRF model, however the peak wind speed by WRF for the very largest storms shows an underestimation. To quantify the performance of the peak wind speed events modelled by WRF at 160 mMSL, the PR for wind speed above percentiles of the observed wind speed (across 9 measurement sites in the southern North Sea) were calculated. The average PR for each storm peak, where the observed peak wind speed surpasses a calculated percentile of all observed peak wind speeds (as detailed in the second column of Table 4.2), is provided in the third column of Table 4.2 for various percentiles of observed wind speed at 160 mMSL.

Table 4.2 Overview of peak ratio of top 119 storm peaks based on quantile of observed wind speed at 160 mMSL.
Additional note – PR for St Jude Storm measured at MMIJ LiDAR at 160 mMSL was replaced with the PR of the MMIJ cup anemometer at 92 mLAT.

Percentile	Observed wind speed [m/s]	PR average	Number of independent storms included
100%	37.9*	0.81	1
95%	34.2	0.96	4
90%	32.9	0.97	7
75%	30.8	0.96	17
50%	28.5	0.99	35
25%	27.1	0.99	52
10%	25.9	0.99	63
5%	25.4	1.00	66

*Peak wind speed measured at MMIJ at 92 mLAT by a cup anemometer. It is likely this wind speed would be higher at 160 mMSL.

On review of Table 4.2 and the information in the above sections, it is proposed that combination of an adjustment factor based on the performance of the WRF model at 160 mMSL and the uncertainty in LiDAR measurements. The average peak ratio based on the top 5% of observed storms (i.e., top 4 observed storms at 160 mMSL) was found to be 0.96, indicating a 4% underestimation in the peak wind speed by the WRF model compared to the observations. Additionally, a 3% adjustment was included to account for uncertainty of LiDAR measurement (see Section 4.1.1.3). This results in a proposed 7% increase in the extreme wind speed analysis at IJV1 at 160 mMSL. This is summarised in Table 4.3.

Table 4.3 Adjustment factor overview.

Adjustment reason	Adjustment amount [%]
Average peak ratio (95% percentile of wind speed)	4
Uncertainty in LiDAR measurements	3
TOTAL	**7**

Based on this uncertainty, as well as the indications that at the site the model may underestimate the peak wind speed, a 7% increase to the extreme values estimated with J-EVA has been added. Both non-adjusted and adjusted (by 7%) wind speed extreme value results are presented in this report. To add further justification to an adjustment of 7%, the largest storm peaks validated at the IJV site have a peak ratio of 0.99 after the adjustment, giving confidence to the increase extreme value results at 160 mMSL at the IJVWFZ.

Proposing a fixed adjustment based on several unknowns is difficult, however it is believed that the factor presented here of 7% has considered necessary factors to the best ability at the time of completing this report. Should the user find a different adjustment, they may apply this to the unadjusted values presented in the following sections.

Conclusion: To account for uncertainty in the modelled peak wind speed at 160 mMSL, a **7% increase to the extreme wind speed values estimated with J-EVA has been added**. However, non-adjusted and adjusted extreme value results are presented in tables in this report.

Users may use a different adjustment factor to account for larger uncertainty if needed.

4.1.2 Extreme wind speed

Extreme wind speed events are simulated by the J-EVA model. The J-EVA model was ran using peak wind speeds direct from the WRF model. Following the simulation to estimate the extreme value events, an adjustment factor was applied.

To optimise the model simulations, and due to computational resource restrictions, only a subseries of the largest modelled wind speed storm peaks from the full timeseries were retained for the J-EVA simulation. From the independent and identical distributed (IID) storm peak events, the retained storm peak events were selected based on a regression quantile of greater than 0.7. Approximately 1800 storm peaks are retained. Shown in Figure 4.2 are the storm peak events which were retained (right panel) and removed (left panel) for the J-EVA model. A representative sample of storm peaks across directions and season was desired. Additionally, subsequent conditioned parameters, such as H_{m0}, are shown as a check that relevant conditioned storms were retained in the analysis.

Utilizing the J-EVA model, a spline model was then employed to incorporate day of the year and wind direction as covariates in fitting distribution parameters. This process uses retained storm peak events from the hindcast model data. The distribution parameters for the bulk of retained storm peaks were characterised by a truncated gamma distribution, while the tails were described using a Generalised Pareto distribution.

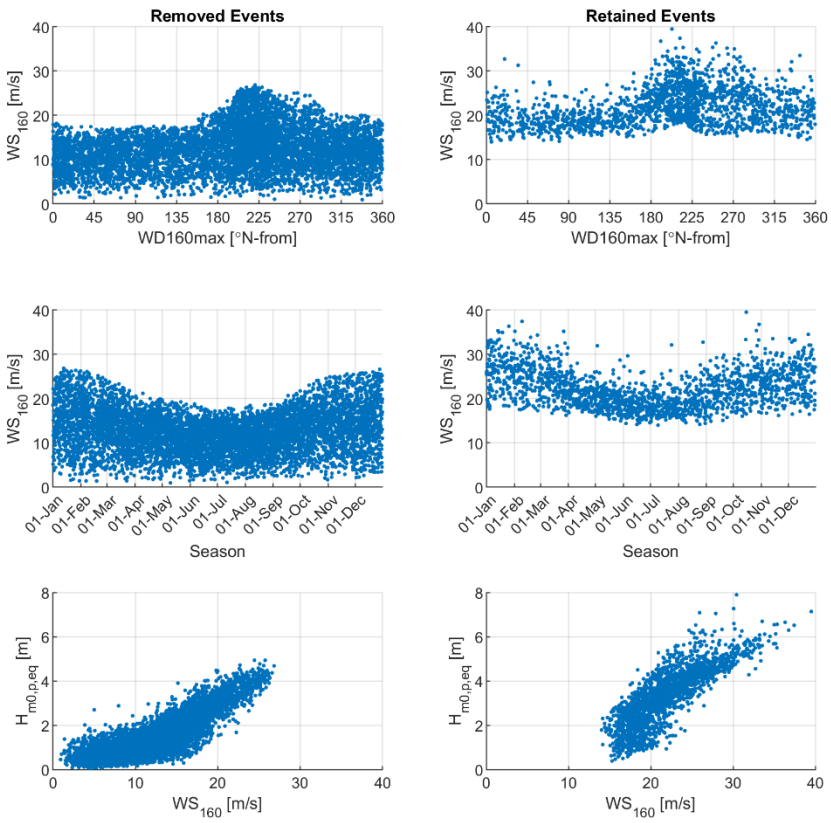

Figure 4.2 **Selected WS at 160 mMSL, WS_{160}, storm peak events at IJV1.** Hindcast storm peak events based on the modelled WRF wind at 160 mMSL. Events above the 0.70 quantiles are retained for the J-EVA analysis.

Presented in Figure 4.3 are the results from the J-EVA model for omni-directional and 8 directional sectors (45° bins). It is important to highlight that the designated number of directional sectors serves solely for visualization purposes. The reported directional analysis are for 12 directional sectors, each representing a 30° bin. Figure 4.3 depicts the annual number of exceedances of both the J-EVA simulation and the hindcast model results. The J-EVA simulated results (blue line) show an excellent representation of the hindcast model storm peak events (black dots joined by a solid line). This gives good confidence in the J-EVA model for wind speed at 160 mMSL. Similarly, Figure 4.4 shows how the J-EVA model captures the seasonality of the hindcast storm peaks. For all subseries (directional and monthly) the hindcast storm peaks are within the J-EVA model credible intervals, indicating that the J-EVA model has incorporated (resampled) the storm peaks in its prediction.

For omni-directional conditions, this largest storm event is shown to be well represented by J-EVA model, as it is for the same event in the directional subseries from southwest. However, the largest modelled storm peak events in October are not well described by the J-EVA model, and the resulting estimated extreme value results are under-estimated for this sector. Despite further tuning of the J-EVA model, little improvement could be found for this sector. Since the J-EVA model performance is poor for the October section, and the magnitude of the largest modelled peak events from WRF are like that

of the omni-directional top events, the J-EVA fit for the October subseries was replaced by the omni-directional fit for this analysis presented in this report.

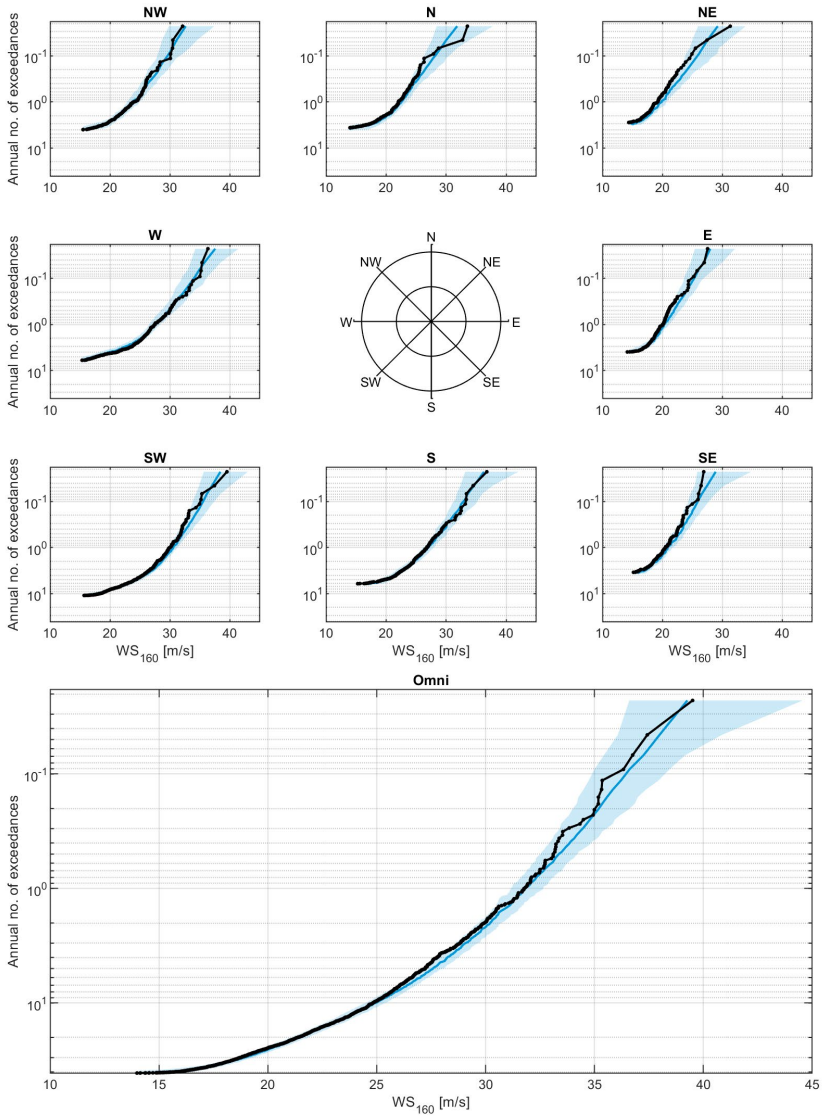

Figure 4.3 Omni-directional and directional annual number of exceedances of WS_{160} at IJV1.
Hindcast data (WRF model) is shown in black. The blue line is the best estimate using the integrated posterior predictive distribution parameters from the J-EVA model. The shaded area is the 2.5-97.5% credible interval.

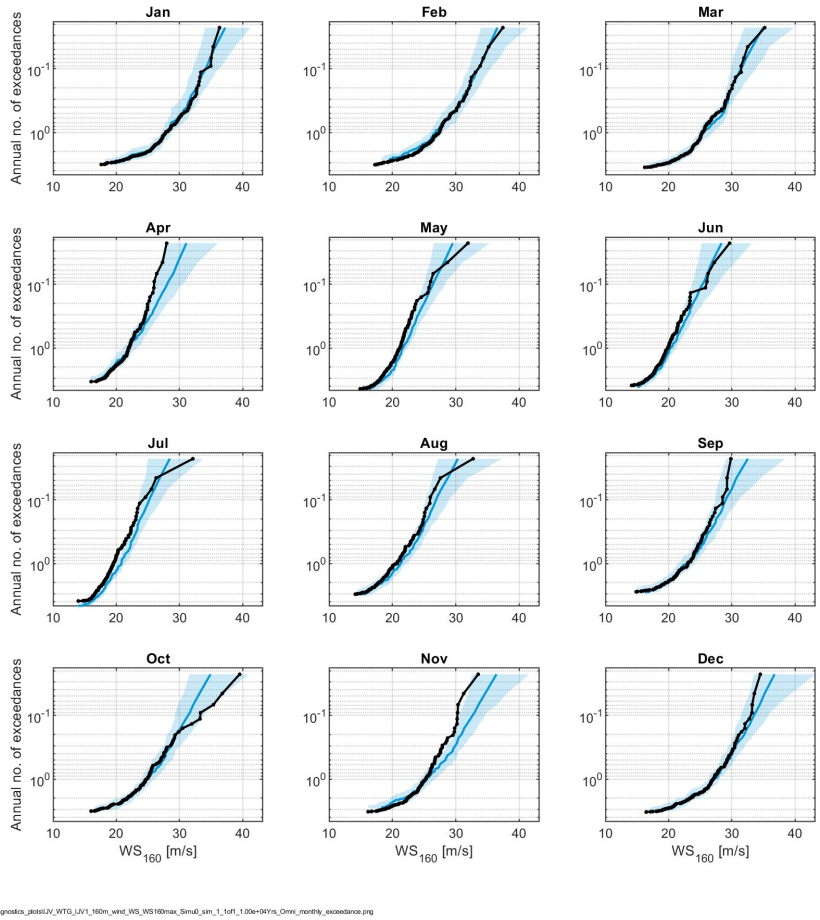

Figure 4.4 Monthly annual number of exceedances of WS_{160} at IJV1. Hindcast data (WRF model) is shown in black. The blue line is the best estimate using the integrated posterior predictive distribution parameters from the J-EVA model. The shaded area is the 2.5-97.5% credible interval. Note: the October fit is to be disregarded as it will be replaced by the omni-directional fit.

Extreme value results for wind speed at 160 mMSL are shown in Figure 4.5 for return period 1- to 100-years and Figure 4.6 for return periods greater than 100-years, as indicated by the green boxes. It is noted that the results presented in the figures has not been adjusted to account for the uncertainty, as discussed above (Section 4.1).

The result of the central J-EVA model fit to the omni-directional wind speed is slightly on the conservative side compared to the plotted hindcast peak wind speed. For this project, this reasonable given the uncertainty in the modelled peak wind speed. The omni-directional, directional (12 sector) and monthly results from the J-EVA analysis for WS_{160} are presented in Table 4.4 and Table 4.6 for the unadjusted and Table 4.5 and Table 4.7 for the adjusted extreme value results by a factor of 7%. The design wind speed, generally defined as the 50-year return period 10-minute hub height wind speed can be used from Table 4.4 or Table 4.5 at IJV1. The dominant directional extreme sector was from 210° and the extreme month is October (after updating the values with the omni directional conditions) followed by January and December.

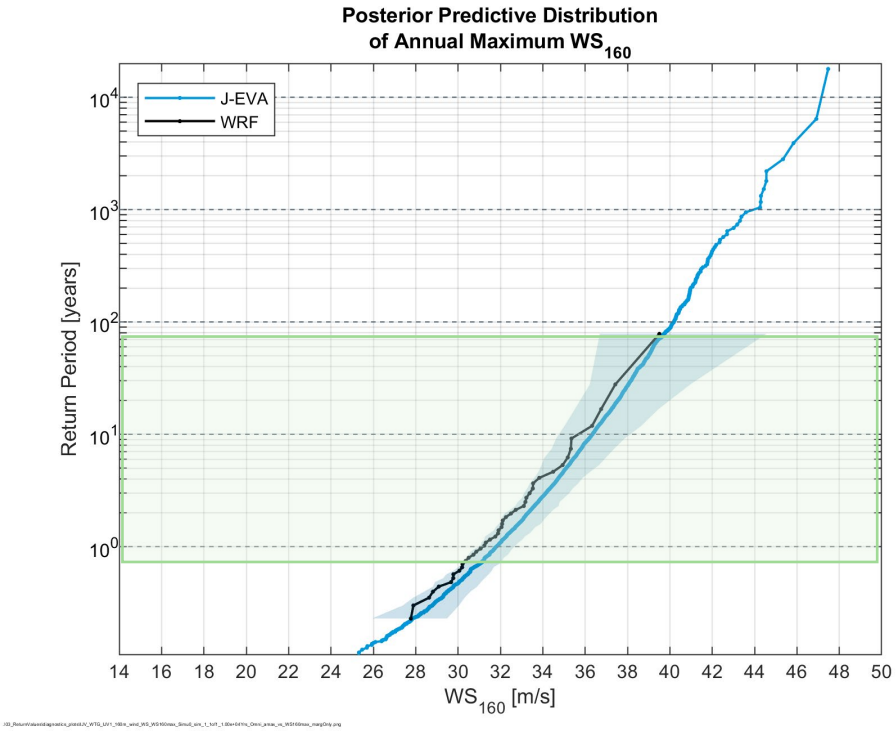

Figure 4.5 Omni-directional extreme wind speed at 160 mMSL (WS_{160}) at IJV1 – 10000-year simulation.
Hindcast data (WRF model) is presented in black. The blue solid line is the posterior predictive distribution parameters from the J-EVA model. The shaded area is the 2.5-97.5% credible interval of the estimate. The green shaded rectangle represents the return values estimated from this 10000-year simulation. The J-EVA fit have not been adjusted to account for uncertainty in the hindcast model peak in the plots.

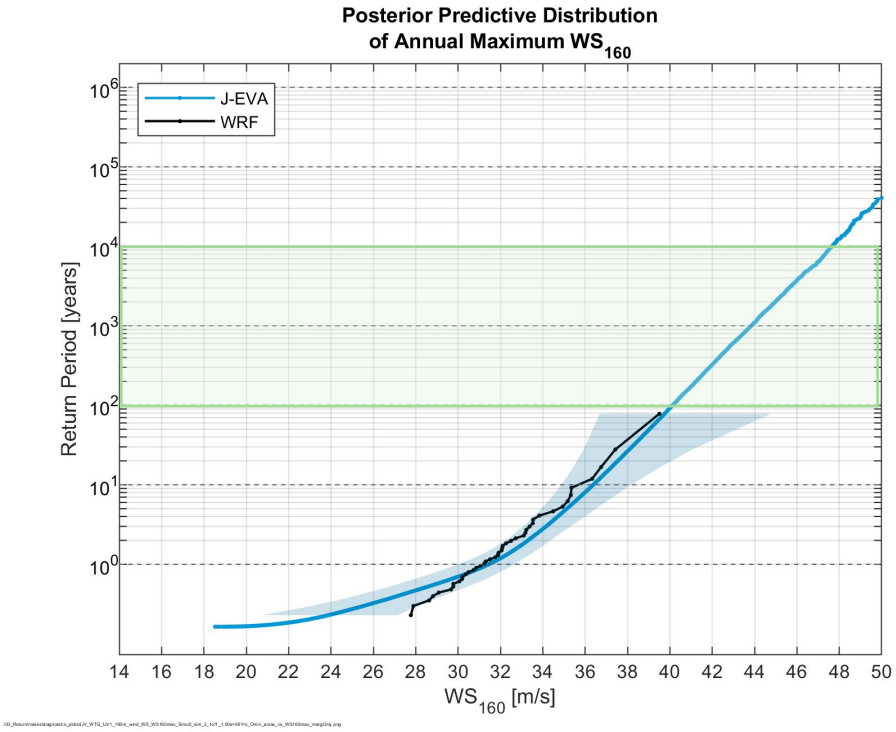

Figure 4.6 Omni-directional extreme wind speed at 160 mMSL (WS_{160}) at IJV1 – 1,000,000-year simulation.
Hindcast data (WRF model) is presented in black. The blue solid line is the posterior predictive distribution parameters from the J-EVA model. The shaded area is the 2.5-97.5% credible interval of the estimate. The green shaded rectangle represents the return values estimated from this 1,000,000-year simulation. The J-EVA fit have not been adjusted to account for uncertainty in the hindcast model peak in the plots.

To account for uncertainty in the modelled peak wind speed at 160 mMSL, a **7% increase to the extreme wind speed values estimated with J-EVA has been added**. Both non-adjusted and adjusted extreme value results are presented in tables in this report.

Table 4.4 Omni-directional and directional (30°) extreme 10 min wind speed at 160 mMSL, WS_{160}, (non-adjusted) at IJV1.

30° Directional Extreme Wind Speed (non-adjusted), WS_{160} [m/s], 160m, 10 min								
Direction (WD [°N-from])	Return Period [years]							
	1	2	5	10	50	100	1000	10000
Omni	31.8	33.3	35.1	36.3	39.0	40.2	43.8	47.7
0	21.4	23.5	25.3	27.0	30.4	31.8	35.4	39.5
30	19.3	21.6	23.4	25.2	28.8	30.4	33.7	37.6
60	18.8	20.7	23.1	24.6	27.6	28.9	32.5	36.0
90	19.6	21.0	22.8	24.2	27.0	28.0	31.5	35.4
120	19.3	20.9	23.2	24.4	27.1	28.0	31.2	34.8
150	20.6	22.3	24.5	25.9	29.0	29.9	33.1	36.9
180	25.3	27.2	29.6	31.1	34.4	35.5	39.3	43.2
210	30.0	31.7	33.7	35.1	37.9	39.0	42.4	45.8
240	28.1	29.5	31.9	33.3	36.3	37.5	41.1	44.8
270	26.3	28.9	31.5	33.2	36.3	37.7	41.7	45.7
300	23.3	26.1	28.2	29.5	32.7	33.7	37.6	41.7
330	21.1	24.3	26.5	28.0	31.0	32.2	36.3	40.5

Table 4.5 Omni-directional and directional (30°) extreme 10 min wind speed at 160 mMSL, WS_{160}, (adjusted by 7%) at IJV1.

30° Directional Extreme Wind Speed (adjusted by 7%), WS_{160} [m/s], 160m, 10 min								
Direction (WD [°N-from])	Return Period [years]							
	1	2	5	10	50	100	1000	10000
Omni	34.0	35.6	37.6	38.8	41.7	43.0	46.9	51.0
0	22.9	25.1	27.1	28.9	32.5	34.0	37.9	42.3
30	20.7	23.1	25.0	27.0	30.8	32.5	36.1	40.2
60	20.1	22.1	24.7	26.3	29.5	30.9	34.8	38.5
90	21.0	22.5	24.4	25.9	28.9	30.0	33.7	37.9
120	20.7	22.4	24.8	26.1	29.0	30.0	33.4	37.2
150	22.0	23.9	26.2	27.7	31.0	32.0	35.4	39.5
180	27.1	29.1	31.7	33.3	36.8	38.0	42.1	46.2
210	32.1	33.9	36.1	37.6	40.6	41.7	45.4	49.0
240	30.1	31.6	34.1	35.6	38.8	40.1	44.0	47.9
270	28.1	30.9	33.7	35.5	38.8	40.3	44.6	48.9
300	24.9	27.9	30.2	31.6	35.0	36.1	40.2	44.6
330	22.6	26.0	28.4	30.0	33.2	34.5	38.8	43.3

To account for uncertainty in the modelled peak wind speed at 160 mMSL, a **7% increase to the extreme wind speed values estimated with J-EVA has been added**. Both non-adjusted and adjusted extreme value results are presented in tables in this report.

Table 4.6 Monthly extreme 10 min wind speed at 160 mMSL, WS_{160}, (non-adjusted) at IJV1.

Monthly Extreme Wind Speed (non-adjusted), WS_{160} [m/s], 160m, 10 min								
	Return Period [years]							
Month	1	2	5	10	50	100	1000	10000
Omni	31.8	33.3	35.1	36.3	39.0	40.2	43.8	47.7
Jan	27.9	30.5	32.6	34.0	36.7	38.1	41.6	45.1
Feb	26.8	29.5	32.0	33.4	36.1	37.3	40.7	44.1
Mar	25.4	28.5	30.0	31.4	34.5	35.6	39.0	42.4
Apr	22.1	24.1	26.4	27.9	30.8	32.0	35.9	39.9
May	21.7	23.1	24.9	26.2	29.1	30.3	33.8	37.6
Jun	20.3	21.9	23.8	25.2	28.1	29.2	32.4	35.9
Jul	20.8	22.3	23.7	25.0	27.9	29.1	32.9	36.8
Aug	21.2	23.4	25.4	26.8	29.8	31.2	35.2	39.2
Sep	23.0	25.2	27.4	28.9	32.0	33.5	37.7	41.6
Oct	31.8	33.3	35.1	36.3	39.0	40.2	43.8	47.7
Nov	25.3	28.4	30.7	32.3	35.9	37.3	41.1	44.9
Dec	27.1	29.3	31.8	33.3	36.5	37.7	41.3	45.0

Table 4.7 Monthly extreme 10 min wind speed at 160 mMSL, WS_{160}, (adjusted by 7%) at IJV1.

Monthly Extreme Wind Speed (adjusted by 7%), WS_{160} [m/s], 160m, 10 min								
	Return Period [years]							
Month	1	2	5	10	50	100	1000	10000
Omni	34.0	35.6	37.6	38.8	41.7	43.0	46.9	51.0
Jan	29.9	32.6	34.9	36.4	39.3	40.8	44.5	48.3
Feb	28.7	31.6	34.2	35.7	38.6	39.9	43.5	47.2
Mar	27.2	30.5	32.1	33.6	36.9	38.1	41.7	45.4
Apr	23.6	25.8	28.2	29.9	33.0	34.2	38.4	42.7
May	23.2	24.7	26.6	28.0	31.1	32.4	36.2	40.2
Jun	21.7	23.4	25.5	27.0	30.1	31.2	34.7	38.4
Jul	22.3	23.9	25.4	26.8	29.9	31.1	35.2	39.4
Aug	22.7	25.0	27.2	28.7	31.9	33.4	37.7	41.9
Sep	24.6	27.0	29.3	30.9	34.2	35.8	40.3	44.5
Oct	34.0	35.6	37.6	38.8	41.7	43.0	46.9	51.0
Nov	27.1	30.4	32.8	34.6	38.4	39.9	44.0	48.0
Dec	29.0	31.4	34.0	35.6	39.1	40.3	44.2	48.2

4.1.3 Extreme wind speed profile

The analysis presented in this report was based on the wind parameters timeseries at 160 mMSL interpolated from the WRF model pressure levels. Therefore, no vertical wind profile was assumed in generating the estimated extreme value analysis for wind speed.

In this section, a representative extreme wind speed profile is presented. Analysis of both the observed and WRF modelled vertical wind profiles is carried out. Conclusions and recommendations are based on both, the measured data and modelled WRF data.

4.1.3.1 Measured extreme wind profile

For measuring extremes, LiDARs are somewhat uncertain due to spatial averaging effects and cross contamination effects [39]. Therefore, measurements from the met mast IJmuiden (MMIJ) are used to analyse the extreme wind profile for the following reasons.

1. MMIJ is very close to IJV1 location (see Figure 2.1 in [2]).
2. Measurements are available at several heights up to 92 mMSL.
3. The quality of the measurements is sufficient for reliable estimation of extreme wind speeds.
4. The period of measurements is sufficiently large to capture significant extreme events.
5. Standard reliable measuring devices (cup and sonic anemometers) are available to measure extreme winds.

Details of the measurements are explained in [2]. For this analysis, wind speeds at two heights, i.e., 58 and 92 m are used denoted as WS_{58} and WS_{92}. Furthermore, wind measurements extrapolated to 30, 60, 100, 120 m using the wind shear coefficient from the met mast measurements on the entire measured dataset are also used, and denoted as WS_{30}, WS_{60}, WS_{100}, WS_{120}, respectively. Although, these measurements are already extrapolated using normal wind shear coefficient, it will still provide an indication of extreme wind shear in comparison to the actual measurement heights.

Figure 4.7 shows the fitted shear coefficient (α) using the power law (see section 6.5 in [2]) using all wind speeds greater than 25 m/s at 92 m and 120 m. The choice of a minimum threshold wind speed of 25 m/s is based on the following.

1. The extreme omni 10-min WS_{160} for one year return period is 31.8 m/s (see section 4.1.2).
2. The threshold corresponds to the 0.99 quantile, which characterize the extreme wind speeds.
3. Approximately four years of measurements are available at MMIJ, which provide a greater possibility of measuring larger wind speeds.

Wind speeds at the largest height (i.e., WS_{92} and WS_{120}) were chosen as the reference due its proximity to the selected hub height in this study. α is estimated by fitting a power-law to WS_{58} and WS_{92} where $WS_{92} > 25$ m/s, and to three different combinations of wind speed measurements, i.e., WS_{30} and WS_{120}, WS_{60} and WS_{120}, and WS_{100} and WS_{120} for all wind speed measurements where $WS_{120} > 25$ m/s. Variation of α is shown as markers in the plot for the corresponding combination. The solid horizontal lines in Figure 4.7 are the optimum value of α obtained by using the corresponding measurement combinations. The optimization is carried out using the Nelder-

Mead simplex method as explained in [40]. Taking the mean of the optimum α results in a mean $\alpha \sim 0.1$ using data from actual measurement heights, and $\alpha \sim 0.11$ using data from extrapolated heights.

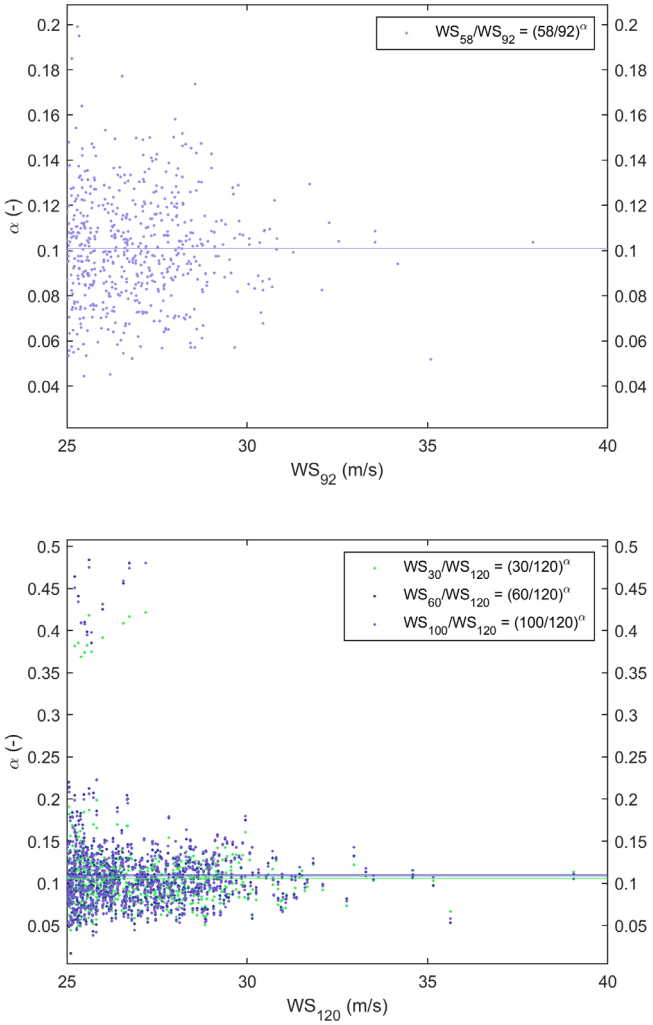

Figure 4.7 Extreme wind profile analysis using measurements from MMIJ. The top figure corresponds to the actual measurement heights. The bottom figure corresponds to heights, where the measurements are extrapolated using wind shear coefficient estimated from all data. The horizontal lines denote the fitted profile to the measurements at the corresponding heights.

4.1.3.2 Extreme Wind Profile using modelled WRF data

The analysis of the extreme wind profile using the modelled WRF data is carried out at 160 m, where storm peaks of WS_{160} identified during the J-EVA (see section 4) are used. Consequently, smaller wind speeds (WS_{160} < 25 m/s) are also selected, which differs from the approach taken while using the measurements, where only the data corresponding to WS_{120} > 25 m/s were selected. Like the measurements, a power law fit is used to estimate the shear coefficient α, and is estimated by fitting a power law to three different combinations of wind speed measurements, i.e., WS_{30} and WS_{160}, WS_{60} and WS_{160}, and WS_{100} and WS_{160}. Figure 4.8 shows the variation of the fitted α for the three different combinations of the wind speeds. Variation of α is shown as markers in the plot for the corresponding combination. The solid horizontal

lines in Figure 4.8 are the optimum value of α obtained by using the corresponding measurement combinations. The optimization is carried out using the Nelder-Mead simplex method as explained in [40]. Taking the mean of the optimum α results in a mean $\alpha = 0.1$ using the modelled WRF data.

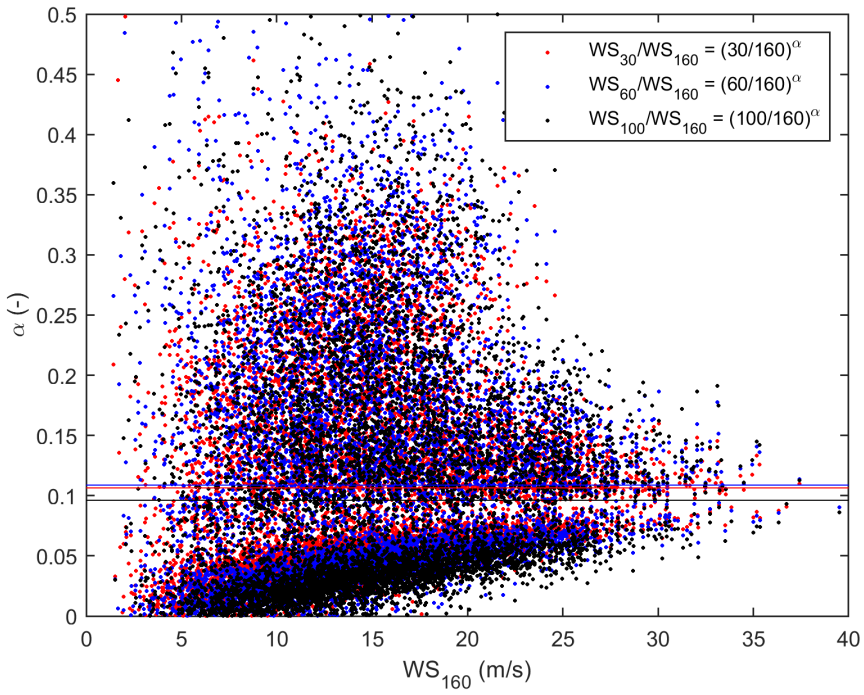

Figure 4.8 Extreme wind profile analysis using modelled WRF data WS_{160}.

4.1.3.3 Recommended extreme wind profile

Following the analysis in sections 4.1.3.1 and 4.1.3.2, it is recommended to use a shear coefficient $\alpha = 0.11$, which agrees well with the IEC 61400-1 standard [10].

4.1.4 Temporal conversion factors for extreme wind speed

For temporal conversion of extreme wind speed to periods other than 10 min the recommendation in Section 2.3.1.2 of [11] is followed [3]. Since the wind is already provided at hub height (160m) the expression related to vertical extrapolation is omitted, and the conversion formula reads:

$$U(T) = U_0\left\{1 - 0.41 I_U \log\left(\frac{T}{T_0}\right)\right\}, \quad \textbf{(4.1)}$$

where U_0 is the 1h (T_0) averaged wind speed and the turbulence intensity at 160m is given by

$$I_U = 0.06\left\{1 + 0.043 U_0\right\}\left(\frac{160}{10}\right)^{-0.22}, \quad \textbf{(4.2)}$$

reflecting the lower turbulent intensity at 160m compared to 10m. From the formulas the extreme wind with a 10 min average periods can be converted to 3 s, 1 min and 1 h values. Conversion multiplication factors (from 10min) are provided for wind speeds of 10, 20, 30, 40 and 50 m/s.

Table 4.8 Extreme wind speed at 160 mMSL multiplication factors for conversion of averaging period from 10 min to 3 s, 1 min and 1 hour.

Wind Speed [m/s]	3 s [-]	1 min [-]	10 min [-]	1 hour [-]
10	1.10	1.04	1.00	0.97
20	1.12	1.05	1.00	0.96
30	1.15	1.07	1.00	0.95
40	1.17	1.08	1.00	0.94
50	1.20	1.09	1.00	0.93

Tables of omni-directional extreme wind speed for 3 s, 1 min, 10 min and 1 hour are provided in Table 4.9 for non-adjusted extreme WS_{160} and Table 4.10 for adjusted WS_{160} by 7% (as discussed in Section 4.1.1).

Table 4.9 Omni directional WS_{160} extreme wind speed for 3 sec, 1 min, 10 min and 1 hour averaging period (non-adjusted)

Omni-directional Extreme Wind Speed (non-adjusted), WS_{160} [m/s], 160m								
	Return Period [years]							
	1	2	5	10	50	100	1000	10000
3 sec	36.7	38.6	40.8	42.3	45.7	47.2	51.8	56.9
1 min	33.9	35.6	37.6	38.9	41.9	43.3	47.3	51.7
10 min	31.8	33.3	35.1	36.3	39.0	40.2	43.8	47.7
1 hour	30.1	31.5	33.2	34.3	36.7	37.8	41.1	44.6

Table 4.10 Omni directional WS_{160} extreme wind speed for 3 sec, 1 min, 10 min and 1 hour averaging period (WS_{160} 10 min adjusted by 7%)

Omni-directional Extreme Wind Speed (adjusted by 7%), WS_{160}, [m/s], 160m								
	Return Period [years]							
	1	2	5	10	50	100	1000	10000
3 sec	39.5	41.5	43.9	45.5	49.2	50.8	55.8	61.3
1 min	36.4	38.2	40.3	41.7	45.0	46.4	50.8	55.5
10 min	34.0	35.6	37.6	38.8	41.7	43.0	46.9	51.0
1 hour	32.2	33.7	35.4	36.6	39.2	40.4	43.8	47.6

4.1.5 Variables conditioned on extreme wind speed

In addition to the marginal extreme WS_{160}, metocean variables conditioned on this extreme wind speed are required. For this, the correlation between WS_{160} and other metocean variables (H_{m0} and CS_{tot}) have been assessed. The results presented as a scatter plot of simulated storm peaks for combined metocean variables from the 1,000,000-year of simulated storms in J-EVA are given in Figure 4.9.

The conditioned variables are obtained by selecting the 50 simulated events that are the closest to the annual maxima for each return periods, and then finding the 5 %, 50 % and 95 % quantiles of the conditioned variable for each event. A consequence of this method is that the conditioned variables do not necessarily increase smoothly with increasing return period, and therefore a fit to the conditioned variables is required to obtain robust estimations.

For this analysis the storm peak equivalent significant wave height $H_{m0,p,eq}$ assumed to be equal to H_{m0} for associated analysis.

A power-law function has been applied to the range of return periods. Here, 'Y' denotes the variables conditioned by WS_{160}, X denotes the associated parameter (CS_{tot} or $H_{m0,p,eq}$) while 'a' and 'b' are fitted parameters.

$$Y = a \cdot X^b \qquad (4.3)$$

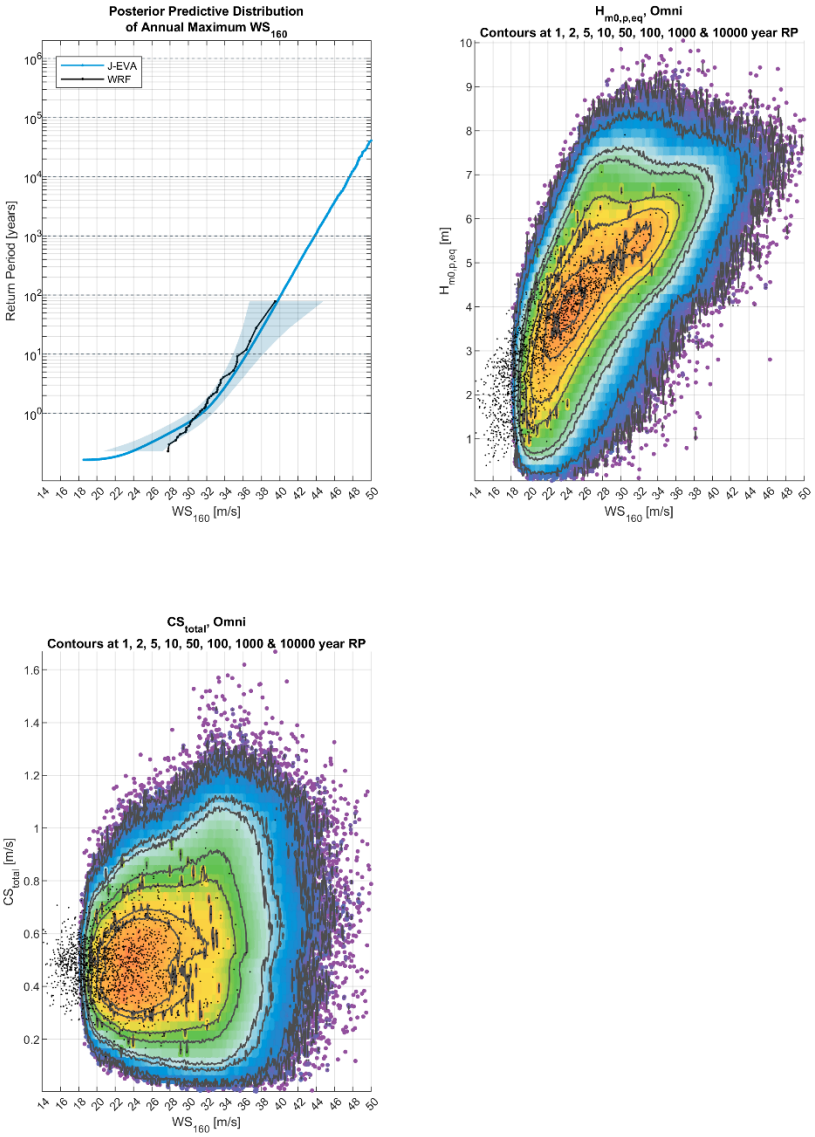

Figure 4.9 Estimates of marginal and conditioned variables from 1,000,000-year simulation at IJV1.

Hindcast data is presented as black markers. The blue solid line (top left) is the posterior predictive distribution. The blue shaded area (top left) is the 2.5-97.5 % credible interval. Contours of conditioned variables shown as coloured dots from the results if a simulation of 1,000,000 years using the posterior predictive distribution at different return periods are shown for $H_{m0,p,eq}$ (top right) and CS_{tot} (lower right) against WS_{160}. Black dots show original hindcast. Warmer colours indicate a higher density of points.

The following figures present the 5%, 50% and 95%-tiles values of the conditioned variables for the omni-directional sector for conditioned $H_{m0,p,eq}$ (Figure 4.10) and CS_{tot} (Figure 4.11).

The conditioned variables were found based on the non-adjusted extreme WS_{160}. The effect of the adjusted extreme WS_{160} on the conditioned variables was assumed to be negligible, and therefore the associated values were not adjusted.

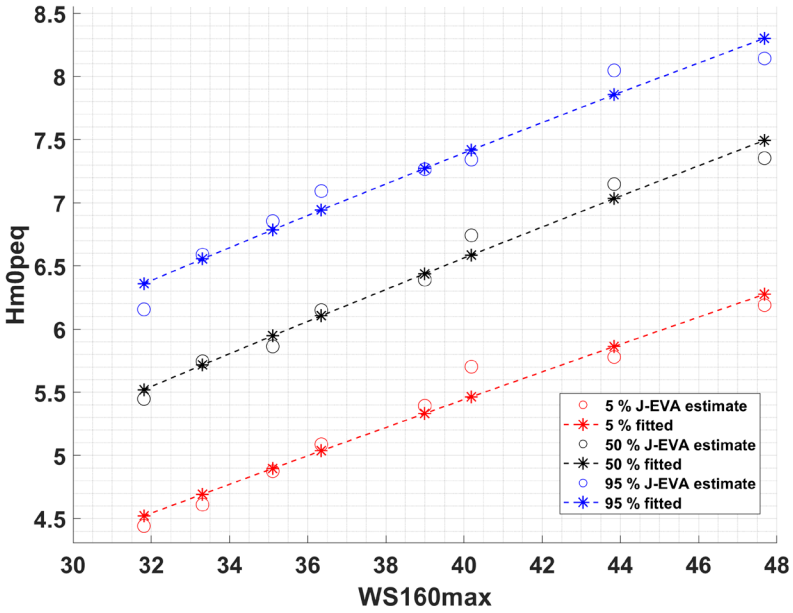

Figure 4.10 $H_{m0,p,eq}$ conditioned on omni-directional WS_{160} at IJV1.
$H_{m0,p,eq}$ associated to extreme WS_{160} for return period 1- to 10000-year from the J-EVA model are shown in as "o" for 5%, 50% and 95%. Polynomial fit to the J-EVA model results are shown as "*" on the dashed line.

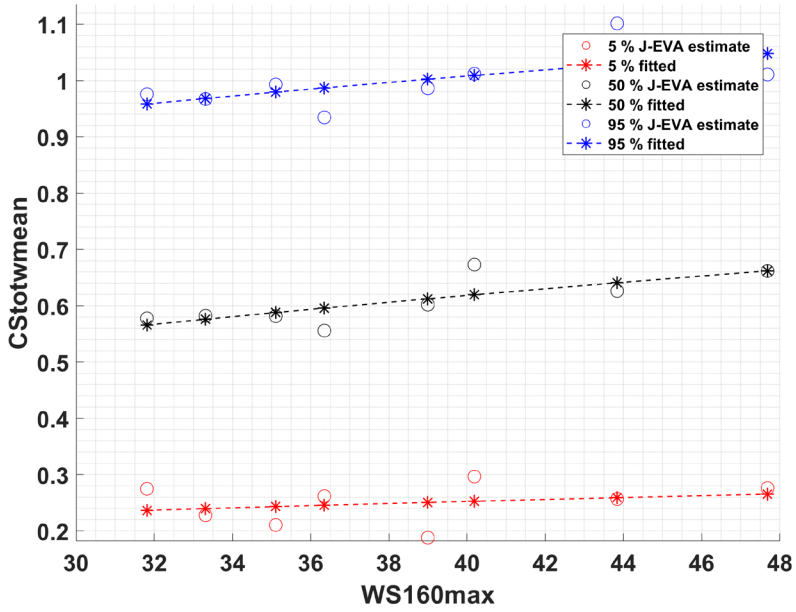

Figure 4.11 CS_{tot} conditioned on omni-directional WS_{160} at IJV1.
CS_{tot} associated to extreme WS_{160} for return period 1- to 10000-year from the J-EVA model are shown in as “o” for 5%, 50% and 95%. Polynomial fit to the J-EVA model results are shown as “*” on the dashed line.

Table 4.11 Variables conditioned on omni-directional extreme WS_{160} at IJV1.
Results of H_{m0} and CS_{tot} conditioned on extreme omni-directional WS_{160} for 5%, 50% and 95%.

Joint Probability, Omni-directional Associated values								
Return Periods [years]	WS_{160} non-adjusted [m/s]	WS_{160} adjusted by 7% [m/s]	H_{m0} [m], 5%	H_{m0} [m], 50%	H_{m0} [m], 95%	CS_{tot} [m/s], 5%	CS_{tot} [m/s], 50%	CS_{tot} [m/s], 95%
1	31.8	34.0	4.5	5.5	6.4	0.2	0.6	1.0
2	33.3	35.6	4.7	5.7	6.6	0.2	0.6	1.0
5	35.1	37.6	4.9	5.9	6.8	0.2	0.6	1.0
10	36.3	38.8	5.0	6.1	6.9	0.2	0.6	1.0
50	39.0	41.7	5.3	6.4	7.3	0.3	0.6	1.0
100	40.2	43.0	5.5	6.6	7.4	0.3	0.6	1.0
1000	43.8	46.9	5.9	7.0	7.9	0.3	0.6	1.0
10000	47.7	51.0	6.3	7.5	8.3	0.3	0.7	1.0

4.2 Water levels

The extreme water level conditions are estimated following the steps outlined in Appendix D. The input water level time series is generated from the HD_{DWF23} model. The storm events selected for the J-EVA analysis are chosen separately for the high, low, total, and residual water levels. Only seasonal variability is considered as explained in Section 2.1 of Appendix D, as there is no directionality associated to water level. Filtering of the storm events is carried out using a criteria of regression quantile larger than 0.80 for the total component and larger than 0.75 for residual water levels on the storm events. The resulting 'retained' and 'removed' events are shown as an example for the HWL_{res} in Figure 4.12. It is observed that water levels events are evenly distributed across all year.

A J-EVA statistical model (see Appendix D and Appendix F) has been set up, in which random events are simulated following a MCMC approach (see Section 4 of Appendix D) to estimate the extremes of the high and low-water levels. The extreme high and low-water levels are presented separately in Section 4.2.1 and Section 4.2.2 respectively.

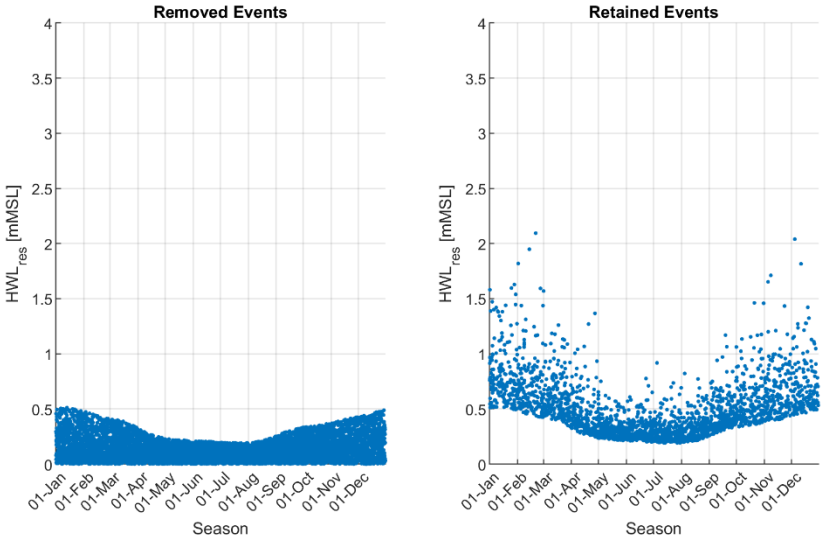

Figure 4.12 Selected events for residual high-water level, HWL_{res} at IJV1. Events above the 0.75 quantiles are retained for the J-EVA analysis.

4.2.1 Extreme high-water levels

The estimation of HWL is based on two different simulations of different lengths (see Appendix D). Figure 4.13 and Figure 4.14 show the posterior predictive distribution of extreme total and residual high-water level, respectively, from a 10000-year simulation, which is used to calculate the posterior predictive distributions for 1-, 2-, 5-, 10-, 50-, and 100-year return periods. These are highlighted by the green shaded area. A larger simulation of 10^6 years is used to estimate extremes with return periods larger than 100 years. An example is depicted in Figure 4.15 for HWL_{res}.

For total high-water levels (Figure 4.13), the model describes the data very well for smaller return periods (< 10 years) as indicated by the dashed black line. For larger return periods, the model provides lower values, but all selected hindcast events are still in the 95% credible interval of the model. Figure 4.14 shows that the model captures well the residual high-water level data for larger return periods (>5 years), and a slight overestimation of the model is observed for smaller return periods.

The monthly exceedance probabilities for total (Figure 4.16) and residual (Figure 4.17) high-water level show that the J-EVA model describes well the hindcast data for most of the months with all input hindcast data in the 95% credible interval. The monthly extreme values are presented in Table 4.12 and Table 4.13 for a maximum period of 10000-year for total and residual high-water levels, respectively.

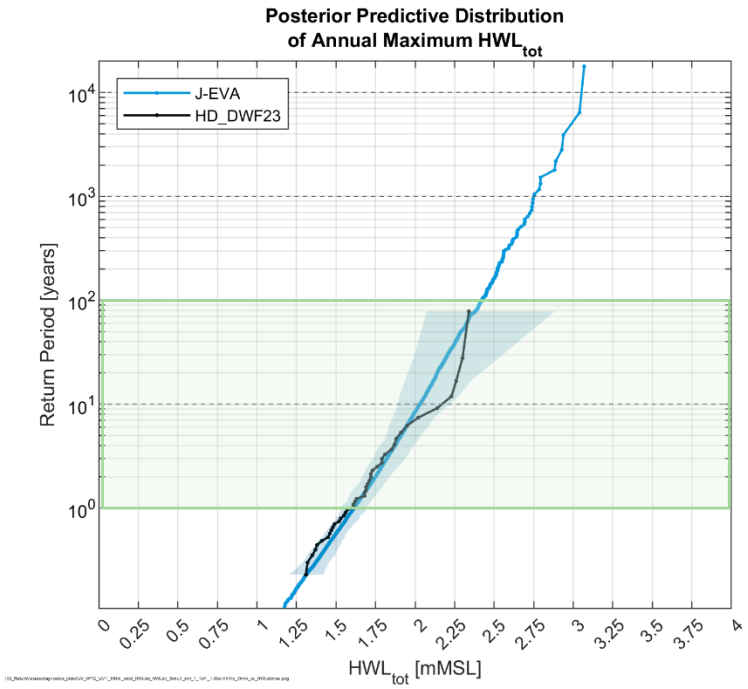

Figure 4.13 Annual extreme total high-water level at IJV1.
Hindcast data is shown in black. The blue line is the posterior predictive distribution. The shaded area is the 2.5-97.5% credible interval of the estimate. The shaded green rectangle represents the return values estimated from this 10000-year simulation.

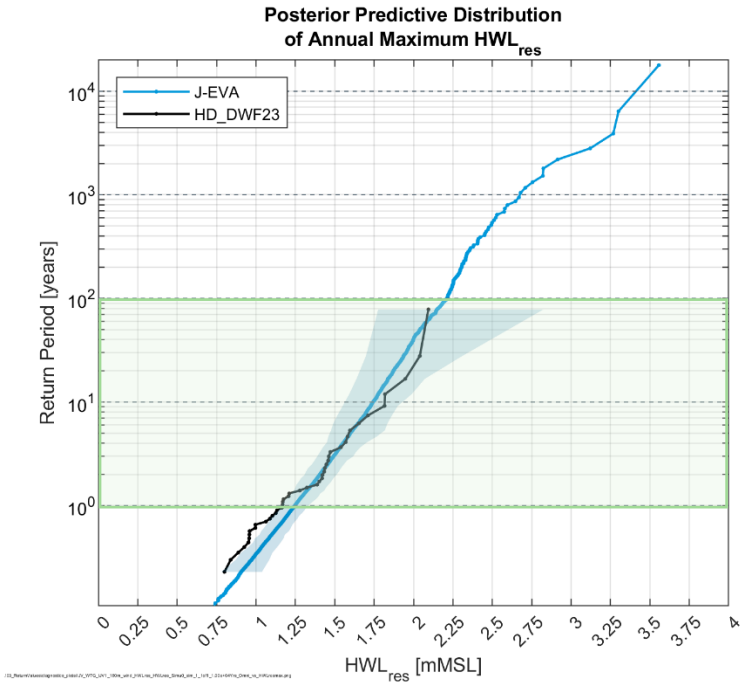

Figure 4.14 Annual extreme residual high-water level at IJV1. Hindcast data is shown in black. The blue line is the posterior predictive distribution. The shaded blue area is the 2.5-97.5% credible interval of the estimate. The shaded green rectangle represents the return values estimated from this 10000-year simulation.

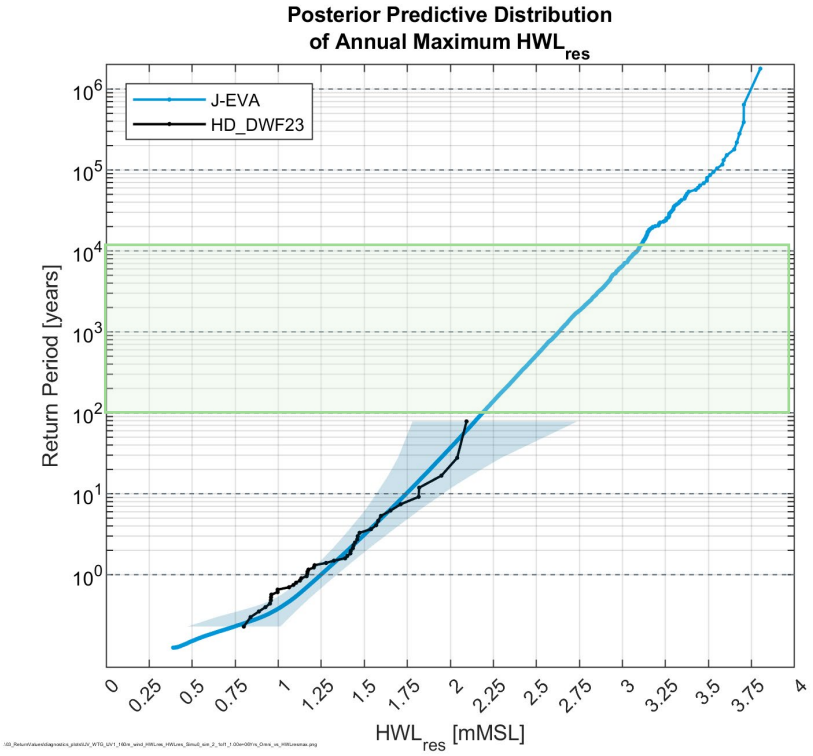

Figure 4.15 Annual extreme residual high-water level at IJV1 with a 10^6-year simulation.

Hindcast data is shown in black. The blue line is the posterior predictive distribution. The shaded blue area is the 2.5-97.5% credible interval of the estimate. The shaded green rectangle represents the return values estimated from this 10^6-year simulation.

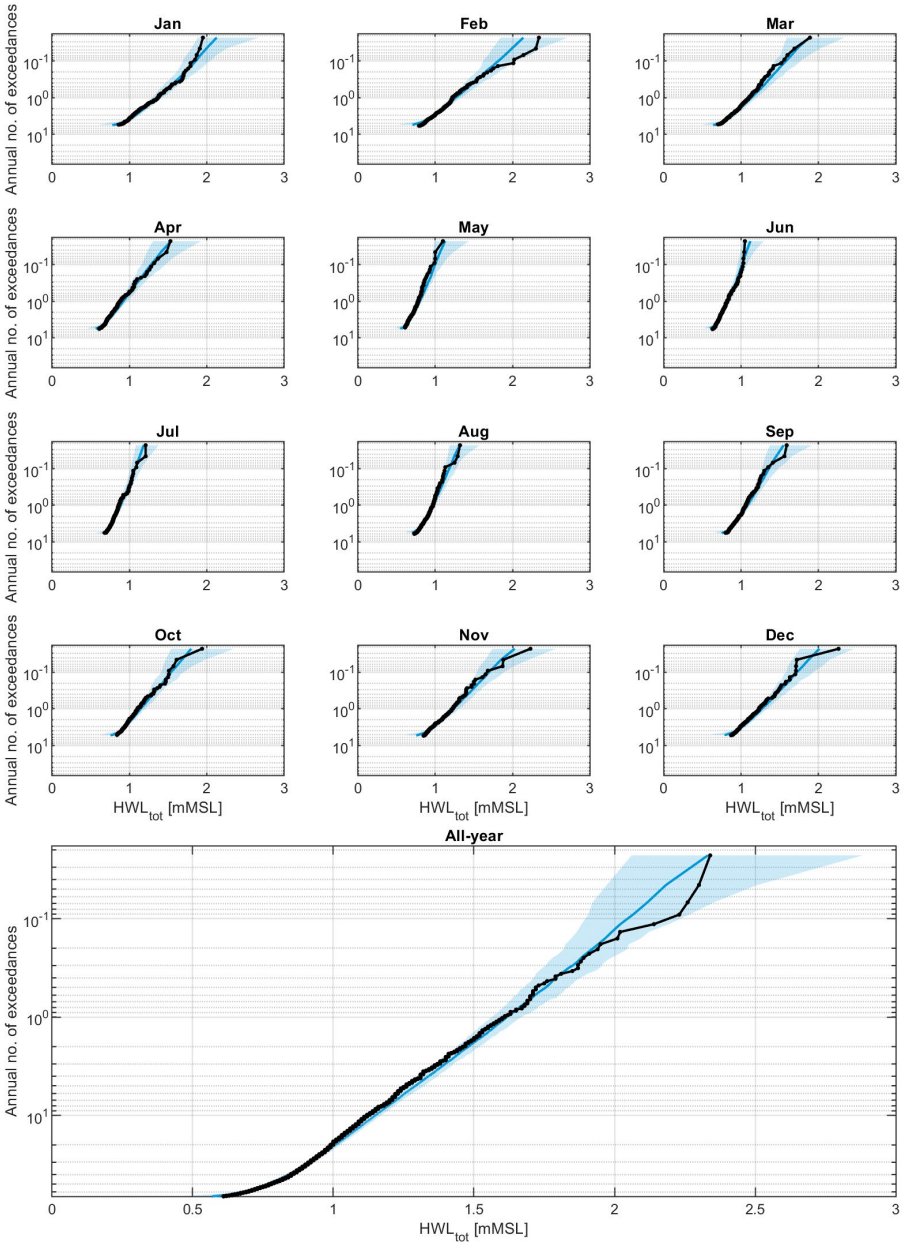

Figure 4.16 Monthly exceedance probability of HWL_{tot} at IJV1.
Hindcast data is shown in black. The blue line is the best estimate using the integrated posterior predictive distribution parameters. The shaded area is the 2.5-97.5% credible interval.

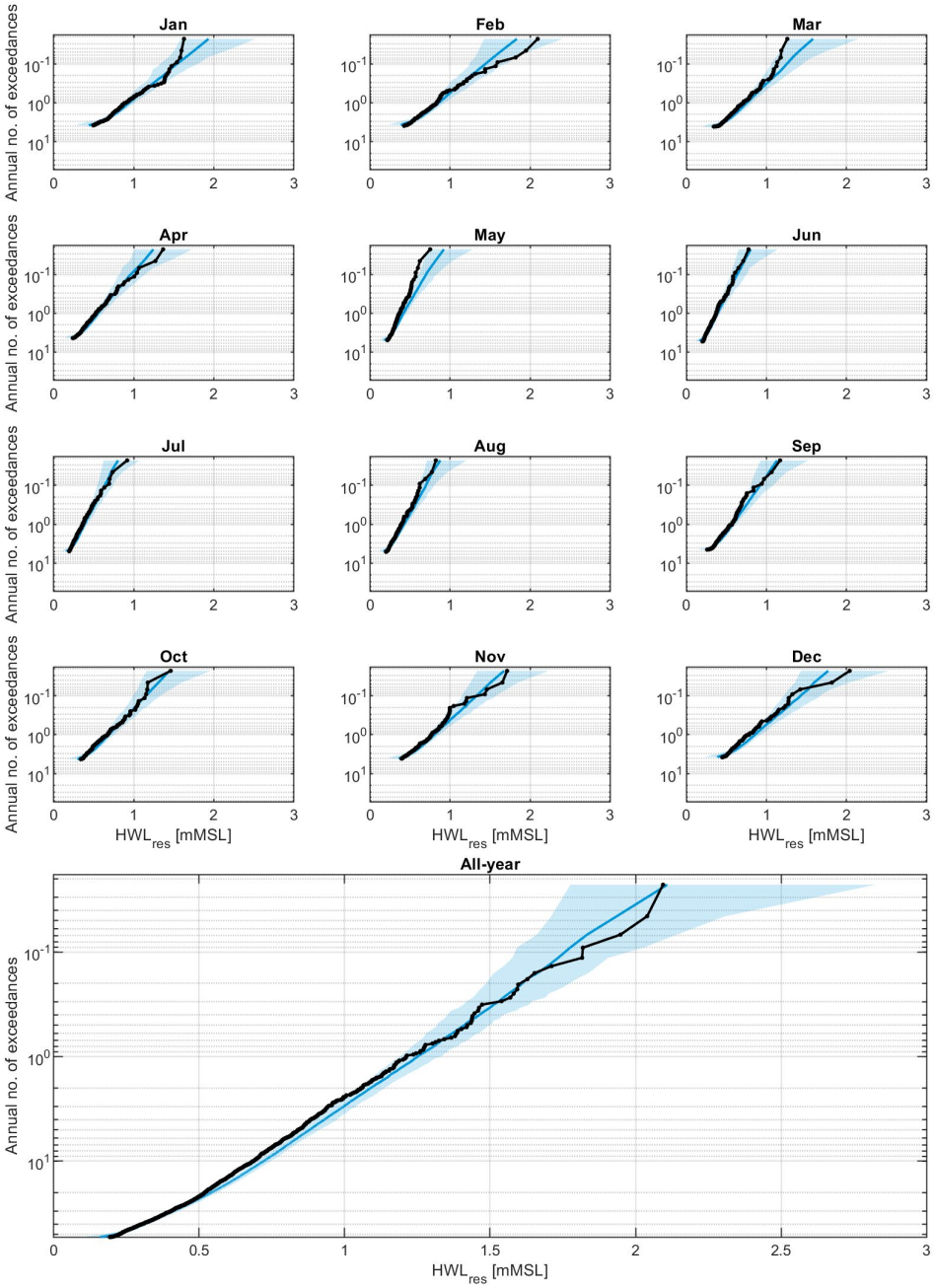

Figure 4.17 Monthly exceedance probability of HWL_{res} at IJV1.
Hindcast data is shown in black. The blue line is the best estimate using the integrated posterior predictive distribution parameters. The shaded area is the 2.5-97.5% credible interval.

Table 4.12 Monthly extreme total high-water level at IJV1.
Levels tare relative to the vertical reference MSL.

Monthly Extreme Total High Water Level, HWLtot [mMSL]								
	Return Period [years]							
Month	1	2	5	10	50	100	1,000	10000
Omni	1.6	1.7	1.9	2.0	2.3	2.4	2.9	3.3
Jan	1.4	1.5	1.7	1.8	2.1	2.2	2.6	3.0
Feb	1.3	1.4	1.6	1.8	2.1	2.2	2.7	3.2
Mar	1.1	1.3	1.4	1.6	1.8	2.0	2.3	2.6
Apr	0.9	1.0	1.2	1.3	1.5	1.6	1.9	2.3
May	0.8	0.9	0.9	1.0	1.1	1.2	1.3	1.6
Jun	0.8	0.9	1.0	1.0	1.1	1.1	1.3	1.4
Jul	0.9	0.9	1.0	1.1	1.2	1.2	1.4	1.5
Aug	1.0	1.0	1.1	1.2	1.3	1.3	1.5	1.6
Sep	1.1	1.2	1.3	1.4	1.5	1.6	1.8	2.1
Oct	1.1	1.3	1.4	1.5	1.8	1.9	2.2	2.6
Nov	1.2	1.4	1.5	1.7	2.0	2.1	2.5	2.9
Dec	1.3	1.4	1.6	1.7	2.0	2.1	2.4	2.8

Table 4.13 Monthly extreme residual high-water level at IJV1.
Levels are relative to the vertical reference MSL.

Monthly Extreme Residual High Water Level, HWLres [m]								
	Return Period [years]							
Month	1	2	5	10	50	100	1,000	10000
Omni	1.2	1.4	1.6	1.7	2.0	2.2	2.6	3.1
Jan	0.9	1.1	1.4	1.5	1.9	2.0	2.5	2.9
Feb	0.9	1.0	1.3	1.4	1.8	1.9	2.4	2.9
Mar	0.8	0.9	1.1	1.2	1.5	1.7	2.1	2.5
Apr	0.6	0.7	0.8	1.0	1.2	1.3	1.6	2.0
May	0.4	0.5	0.6	0.7	0.9	1.0	1.2	1.5
Jun	0.4	0.5	0.6	0.6	0.8	0.8	1.0	1.3
Jul	0.4	0.5	0.6	0.6	0.8	0.8	1.1	1.3
Aug	0.4	0.5	0.6	0.7	0.9	0.9	1.1	1.3
Sep	0.6	0.7	0.8	0.9	1.1	1.2	1.5	1.7
Oct	0.7	0.8	1.0	1.1	1.4	1.5	1.9	2.2
Nov	0.8	1.0	1.2	1.3	1.6	1.7	2.2	2.6
Dec	0.8	1.0	1.2	1.4	1.7	1.9	2.3	2.7

4.2.2 Extreme low-water levels

The estimation of LWL is based on two different simulations of different lengths (see Appendix D). Figure 4.18 and Figure 4.19 show the posterior predictive distribution of extreme total and residual low-water levels, respectively, from 10000-year simulation, which is used to calculate the best estimates for 1-, 2-, 5-, 10-, 50-, and 100-year return periods. These are highlighted by the green shaded area in Figure 4.19 and Figure 4.18. A larger simulation of 10^6 years is used to estimate extremes with return periods larger than 100 years. (see the example provided in Figure 4.15 for HWL_{res}).

Both posterior predictive distributions for total and residual low-water levels describes well the data for return periods larger than 5 years. There is a slight overestimation for smaller return periods.The monthly exceedance probabilities for total (Figure 4.20) and residual (Figure 4.21) low-water levels show that the J-EVA model explains well the hindcast data for all months, and that the credible intervals encompass all the input peak events. The monthly extreme values are presented in Table 4.14 and Table 4.15 for total and residual low-water levels respectively for return periods up to 10000 years.

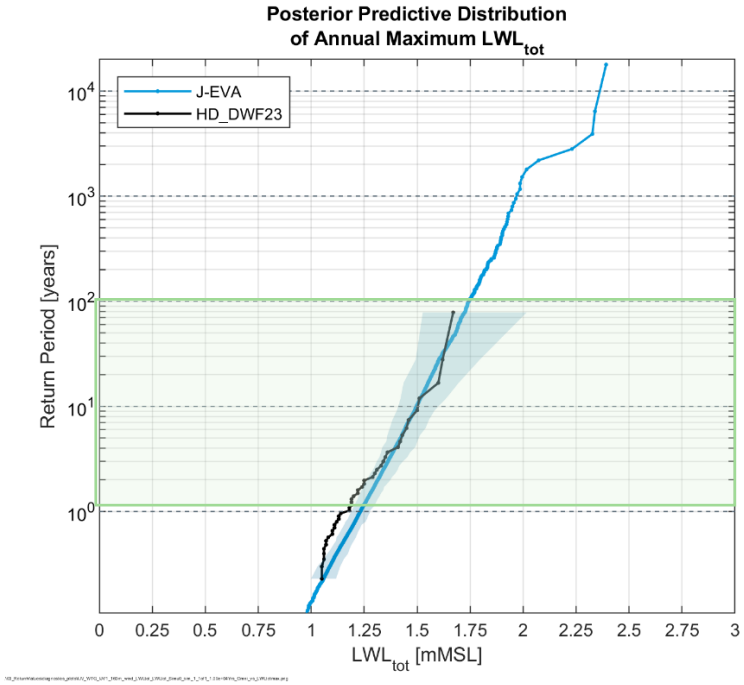

Figure 4.18 Extreme total low-water level at IJV1.
Hindcast data is shown in black. The blue line is the posterior predictive distribution. The shaded area is the 2.5-97.5% credible interval of the estimate. The shaded green rectangle represents the return values estimated from this 10000-year simulation.

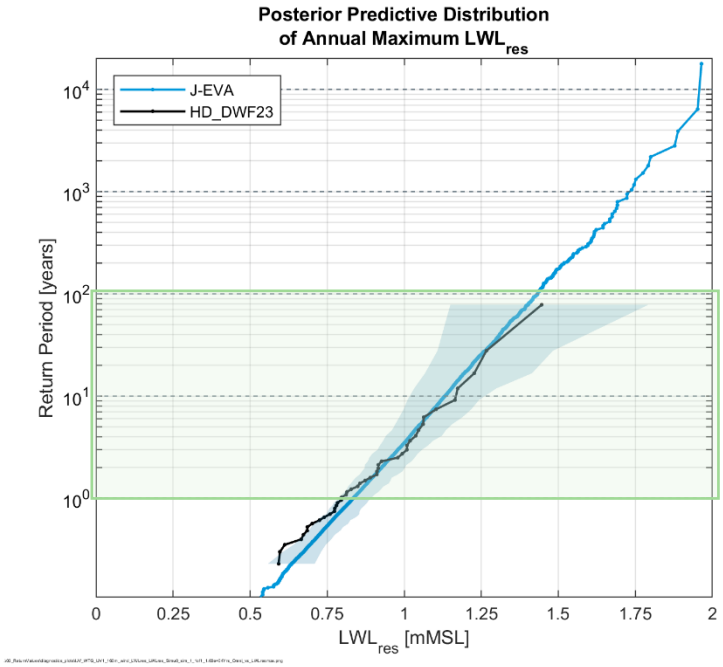

Figure 4.19 Extreme residual low-water level at IJV1.
Hindcast data is shown in black. The blue line is the posterior predictive distribution. The shaded area is the 2.5-97.5% credible interval of the estimate. The shaded green rectangle represents the return values estimated from this 10000-year simulation.

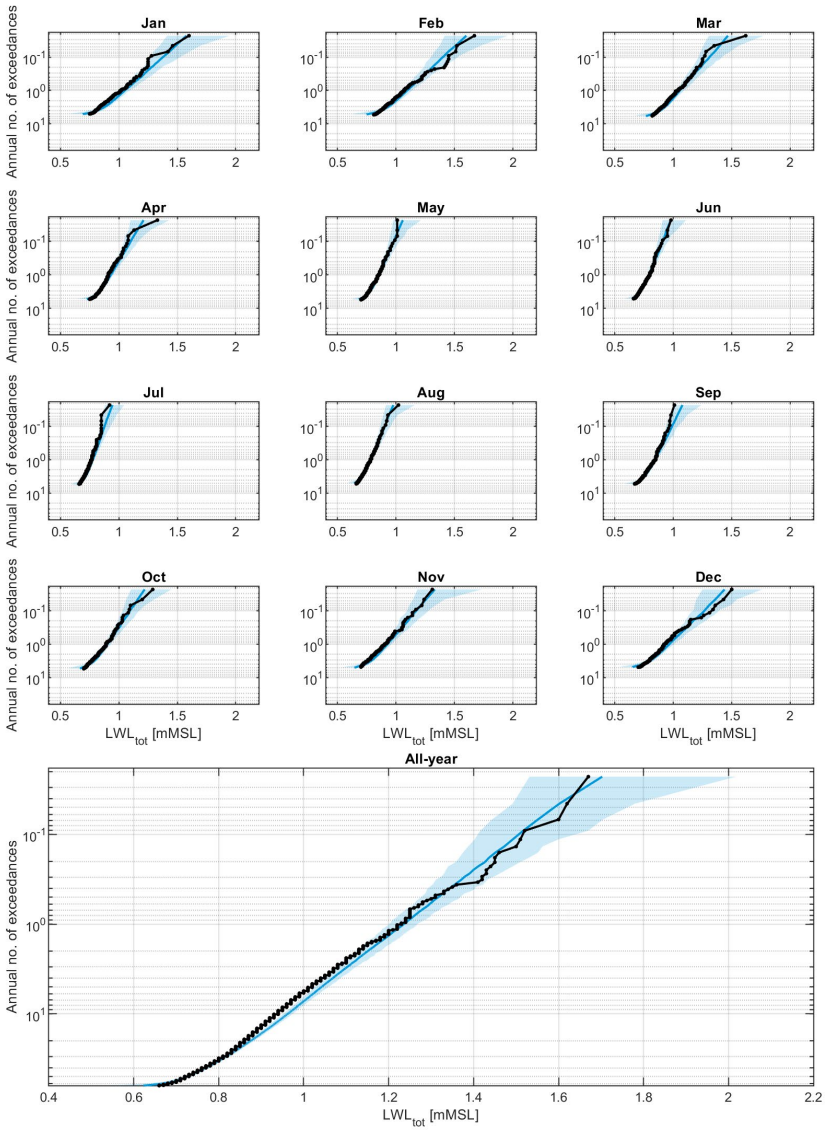

Figure 4.20 Monthly exceedance probability of LWL_{tot} at IJV1
Hindcast data is shown in black. The blue line is the best estimate using the integrated posterior predictive distribution. The shaded area is the 2.5-97.5% credible interval.

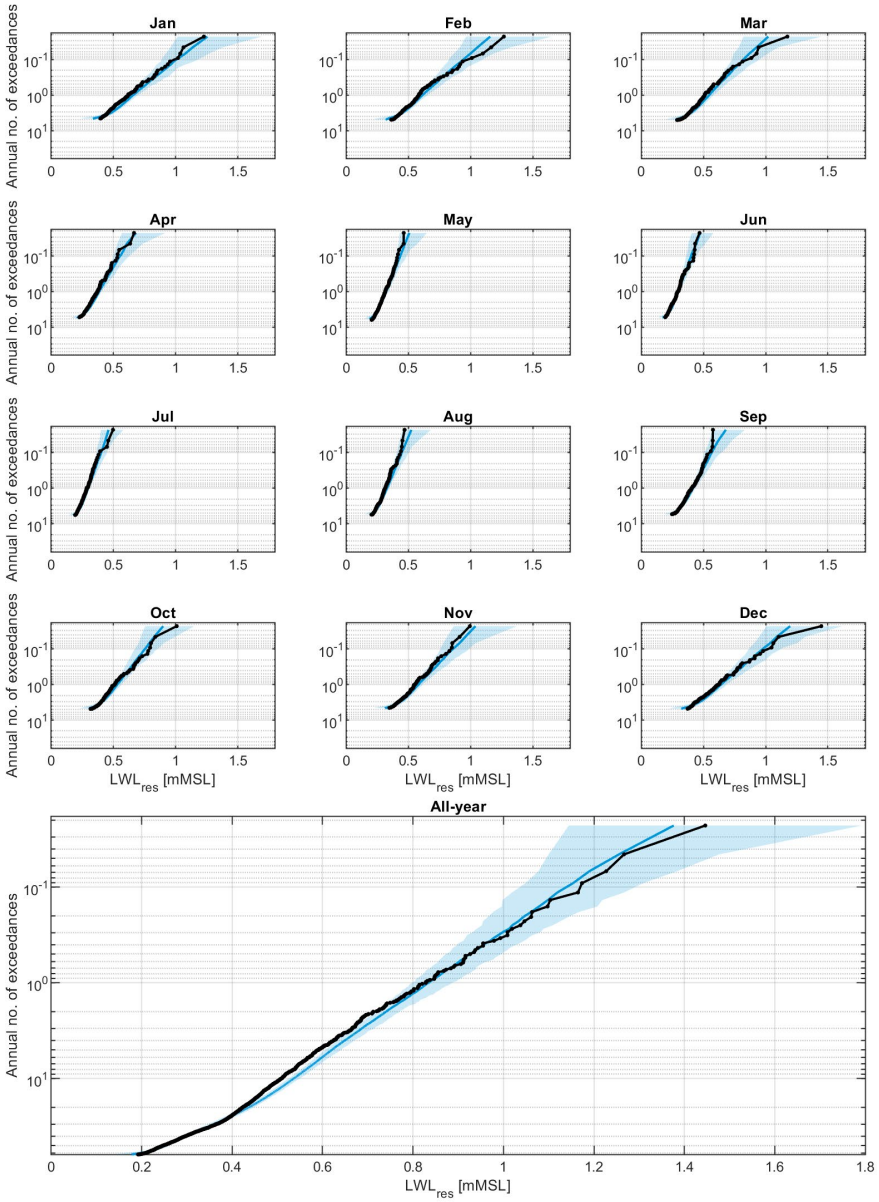

Figure 4.21 Monthly exceedance probability of LWL_{res} at IJV1.
Hindcast data is shown in black. The blue line is the best estimate using the integrated posterior predictive distribution. The shaded area is the 2.5-97.5% credible interval.

Table 4.14 Monthly extreme total low-water level at IJV1.
Levels are relative to the vertical reference MSL.

Monthly Extreme Total Low Water Level, LWLtot [mMSL]								
	Return Period [years]							
Month	1	2	5	10	50	100	1,000	10000
Omni	-1.2	-1.3	-1.4	-1.5	-1.7	-1.7	-2.0	-2.2
Jan	-1.0	-1.1	-1.3	-1.4	-1.6	-1.6	-1.9	-2.1
Feb	-1.1	-1.2	-1.3	-1.4	-1.6	-1.7	-1.9	-2.1
Mar	-1.1	-1.1	-1.2	-1.3	-1.4	-1.5	-1.7	-1.9
Apr	-0.9	-1.0	-1.0	-1.1	-1.2	-1.2	-1.4	-1.5
May	-0.9	-0.9	-0.9	-1.0	-1.0	-1.1	-1.2	-1.3
Jun	-0.8	-0.8	-0.9	-0.9	-1.0	-1.0	-1.1	-1.1
Jul	-0.8	-0.8	-0.8	-0.9	-0.9	-1.0	-1.0	-1.1
Aug	-0.8	-0.8	-0.9	-0.9	-1.0	-1.0	-1.1	-1.2
Sep	-0.8	-0.9	-0.9	-1.0	-1.1	-1.1	-1.2	-1.3
Oct	-0.9	-1.0	-1.0	-1.1	-1.2	-1.3	-1.4	-1.5
Nov	-0.9	-1.0	-1.1	-1.2	-1.3	-1.4	-1.6	-1.8
Dec	-1.0	-1.1	-1.2	-1.3	-1.4	-1.5	-1.7	-2.0

Table 4.15 Monthly extreme residual low-water level at IJV1.
Levels are relative to the vertical reference MSL.

Monthly Extreme Residual Low Water Level, LWLres [m]								
	Return Period [years]							
Month	1	2	5	10	50	100	1,000	10000
Omni	-0.8	-0.9	-1.0	-1.1	-1.3	-1.4	-1.7	-2.0
Jan	-0.7	-0.8	-0.9	-1.0	-1.2	-1.3	-1.6	-1.9
Feb	-0.6	-0.7	-0.8	-0.9	-1.1	-1.2	-1.5	-1.8
Mar	-0.5	-0.6	-0.7	-0.8	-1.0	-1.1	-1.3	-1.5
Apr	-0.4	-0.4	-0.5	-0.5	-0.7	-0.7	-0.9	-1.0
May	-0.3	-0.4	-0.4	-0.4	-0.5	-0.5	-0.6	-0.7
Jun	-0.3	-0.3	-0.4	-0.4	-0.5	-0.5	-0.6	-0.7
Jul	-0.3	-0.3	-0.4	-0.4	-0.5	-0.5	-0.6	-0.6
Aug	-0.3	-0.4	-0.4	-0.4	-0.5	-0.5	-0.6	-0.7
Sep	-0.4	-0.5	-0.5	-0.6	-0.7	-0.7	-0.8	-1.0
Oct	-0.5	-0.6	-0.7	-0.7	-0.9	-0.9	-1.1	-1.3
Nov	-0.6	-0.7	-0.8	-0.8	-1.0	-1.1	-1.3	-1.6
Dec	-0.6	-0.7	-0.9	-1.0	-1.2	-1.3	-1.5	-1.8

4.3 Currents

The extreme current conditions are estimated following the steps outlined in Appendix D. The input depth-averaged current time series is generated from the HD_{DWF23} model. The total current speed is composed of two parts, namely tidal and residual. The residual current contribution can further be decomposed into contributions due to several effects, e.g., wind-driven, density-driven, currents etc. In IJV area, the total currents are generally dominated by the tidal signal (see Section 3.3).

There is a non-linear coupling between the residual and the tidal flow in these relatively shallow water depths, meaning that it is not straightforward to separate the tidal and residual components from the total current: a small negative correlation is observed between the residual and tidal components for the peak events, meaning that there is a small tendency that the largest residual components coincide with low tidal components of current speed in this area. Randomly adding a tidal contribution to the extremes of the residual components would therefore lead to a slight overestimation of the total current speed. Consequently, a separate extreme value model had been set up for the extreme total current speeds.

The extreme values of residual current speeds are presented in Section 4.3.1, while Section 4.3.2 details the results for total current speeds and the associated omni-directional significant wave height and hub height wind speed.

4.3.1 Extreme residual currents

The storm events selected for the J-EVA analysis for residual currents are based on the directional and seasonal variability (see Section 2.1 of Appendix D), with filtering carried out using a criteria of regression quantile > 0.80 that is applied on the depth-averaged residual current speed storm events. The resulting ‘retained’ and ‘removed’ events are shown in Figure 4.22. A lack of storm data is observed for the west to north sectors (between 270°N-to to 360°N-to).

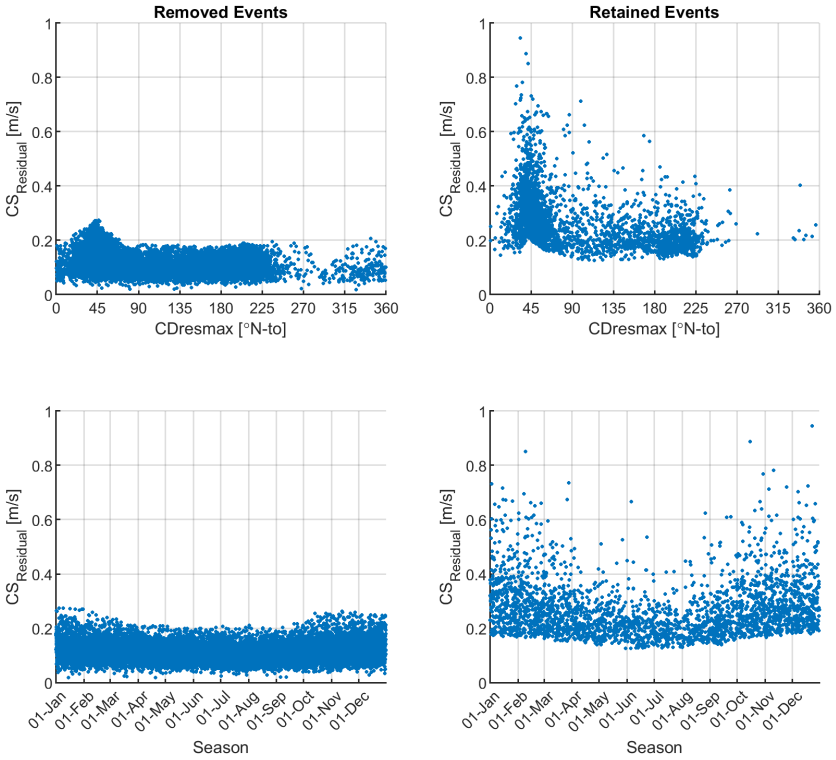

Figure 4.22 Selected events for residual depth-averaged current speed, CS_{res} at IJV1
Events above the 0.80 regression quantile are retained for the J-EVA analysis.

A J-EVA statistical model (see Appendix D and Appendix F) has been set up for extreme residual depth-averaged current speed, in which random events are simulated following a MCMC approach (see Section 4 Appendix D). The current direction (going-to) at the time of peak residual current speed and the time of day (season) are used as covariates.

The estimation of the extreme residual current speeds is based on two different simulations of different lengths (see Appendix D). Figure 4.23 shows the posterior predictive distribution of extreme residual current speeds computed from a 100,000-year simulation, which is used to calculate the return values up to the 100-year return period. These return periods are highlighted by the green shaded area. A larger simulation of 10^7 years is used to estimate extremes with return period larger than 100 years, as shown in Figure 4.24.

The posterior predictive distribution explains well the hindcast data up to a 10-year return period, and a slight underestimation is observed for larger return periods, but the historical peak events remain all in the credible interval.

Figure 4.25 and Figure 4.26 depict the directional (8 directional sectors of 45° bins) and monthly exceedance probability of extreme residual current speed respectively. It should be noted that the number directional sectors are for visualization purposes only. Directional analysis reported are for 12 directional sectors (30° bins). The J-EVA statistical model describes well the hindcast data for all directional sectors. The sector NW remains empty due to the absence of hindcast data in this sector. The J-EVA model leads to higher values in April

and July, but models well the other months, with all hindcast events in the 95% credible intervals.

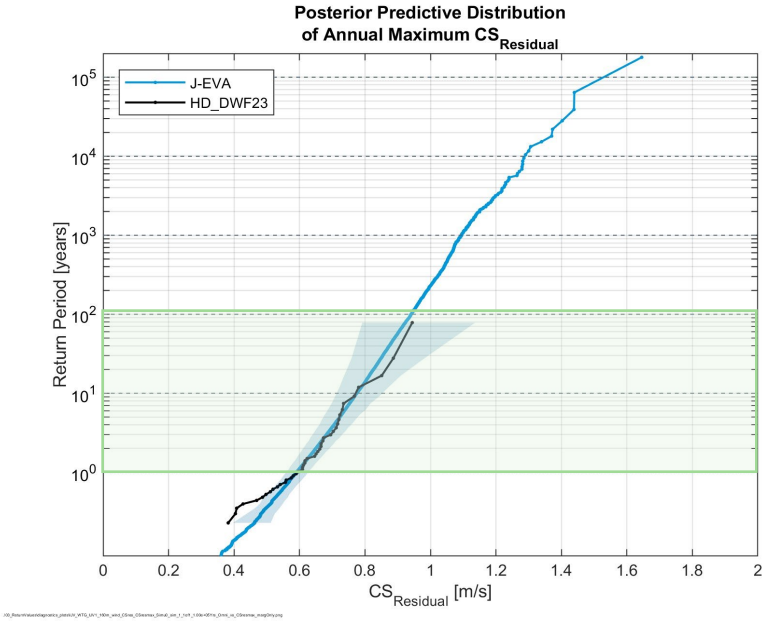

Figure 4.23 Omni-directional extreme residual current speed at IJV1 from a 100,000-year simulation.
Hindcast data is shown in black. The blue line is the posterior predictive distribution. The shaded area is the 2.5-97.5% credible interval of the estimate. The shaded green rectangle represents the return values estimated from this 100,000-year simulation.

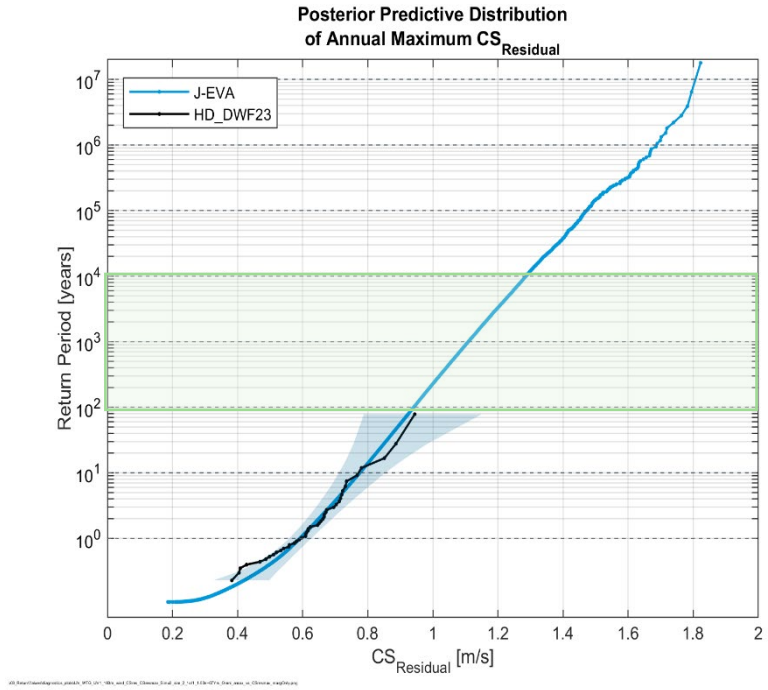

Figure 4.24 Omni-directional extreme residual current speed at IJV1 from a 10^7-year simulation.

Hindcast data is shown in black. The blue line is the posterior predictive distribution. The shaded area is the 2.5-97.5% credible interval of the estimate. The shaded green rectangle represents the return values estimated from this 10^7-year simulation.

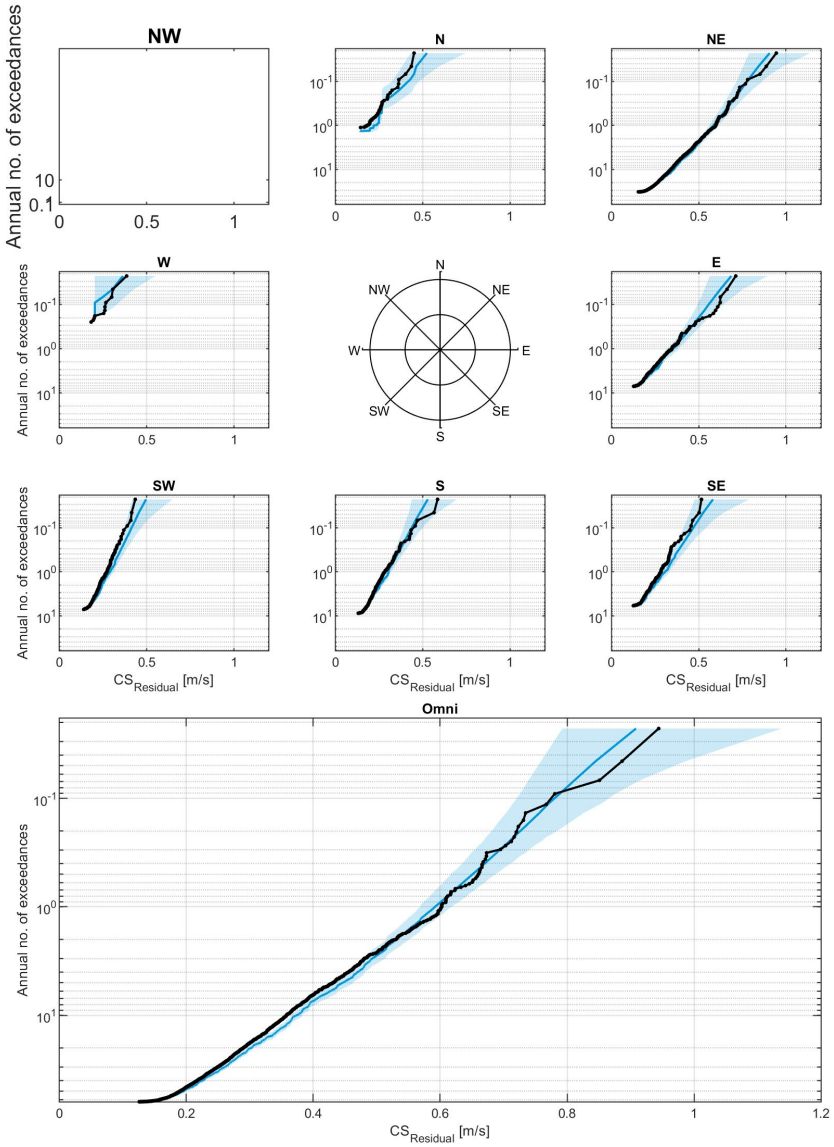

Figure 4.25 Directional exceedance probability of $CS_{Residual}$ at IJV1. Hindcast data is shown in black. The blue line is the best estimate using the integrated posterior predictive distribution. The shaded area is the 2.5-97.5% credible interval.

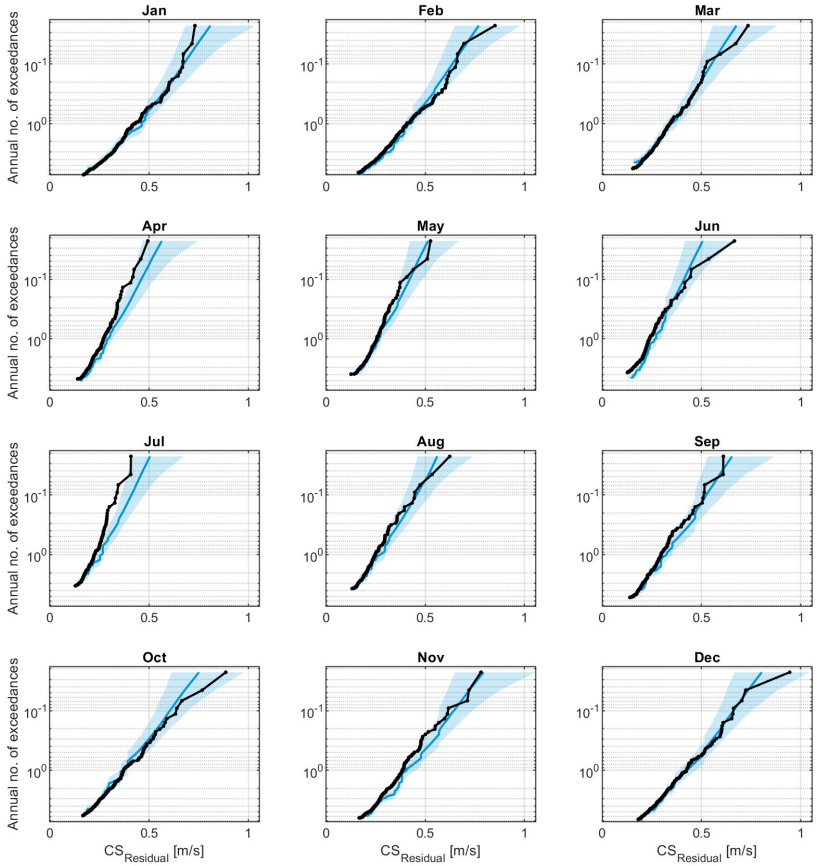

Figure 4.26 Monthly exceedance probability of $CS_{Residual}$ at IJV1. Hindcast data is shown in black. The blue line is the best estimate using the integrated posterior predictive distribution. The shaded area is the 2.5-97.5% credible interval.

To predict extreme values from also those sectors where data are scarce, like the northeast sector, we follow a procedure as explained below:

4. The median of annual maxima of all data (i.e., the 44-year timeseries of residual current speed) has been estimated for each 30° directional sector.
5. The extreme values from J-EVA in the dominant direction (in this case 30°N-to) and its opposite direction (210°N-to) are extracted.
6. The ratio between the median of annual maxima and the extreme values in the dominant direction and its opposite are computed. The ratios are then derived for all directional sectors using linear interpolation.
7. The directional median of annual maxima is scaled accordingly to the derived ratios for each 30° directional sector bin.

The method is illustrated in Figure 4.27. The median of annual maxima is shown in black, while the directional medians scaled using the 30°N-to and 210°N-to sectors are shown with coloured lines for 1-, 2-, 100- and 1,000-year return periods. The grey dots represent the density contours from J-EVA simulation around the dominant peak direction for reference. For the dominant direction, the scaled extreme values match with the J-EVA output. The second peak around 180°N-to is slightly overestimated by the J-EVA model.

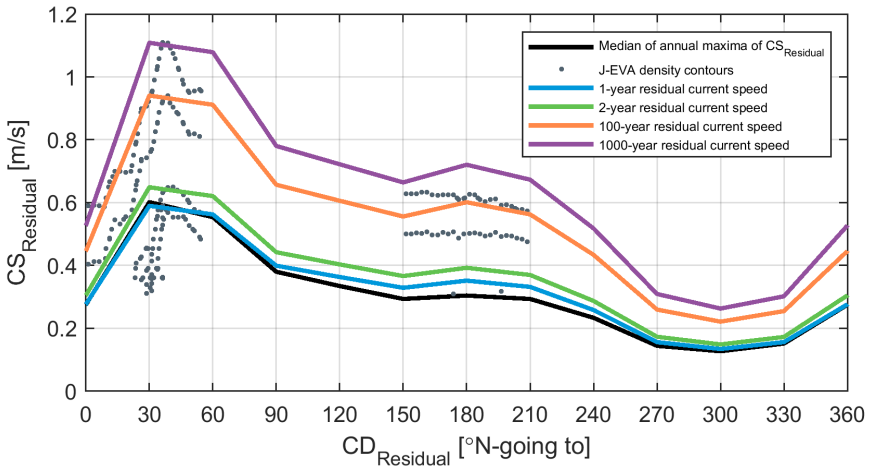

Figure 4.27 Illustration of the method to derive directional $CS_{Residual}$ extremes at IJV1 for non-dominant sectors
The grey dots represent the J-EVA contours for $CS_{Residual}$ [m/s] around the dominant peak for all plotted return periods. The black line shows the median of annual maxima for all directions. The scaled extreme values are shown with the coloured lines.

Table 4.16 and Table 4.17 provide the values at IJV1 of the directional and monthly extreme depth-averaged residual current speeds respectively. The directional extremes (Table 4.16) show larger depth-averaged residual current speed values going towards northeast, which aligns well with the observation made for normal conditions and the current roses showed in Section 3.3.3. Extreme $CS_{Residual}$ are smaller during the summer (Table 4.17), as expected for this area.

Table 4.16 Directional Extreme Depth-averaged Residual Current Speed at IJV1

30° Directional Extreme Depth-Average Residual Current Speed, CSres [m/s]								
Direction (CD [°N-to])	Return Period [years]							
	1	2	5	10	50	100	1000	10000
Omni	0.6	0.6	0.7	0.8	0.9	0.9	1.1	1.3
0	0.3	0.3	0.3	0.4	0.4	0.4	0.5	0.6
30	0.6	0.6	0.7	0.8	0.9	0.9	1.1	1.3
60	0.5	0.6	0.7	0.7	0.9	0.9	1.1	1.3
90	0.4	0.4	0.5	0.5	0.6	0.7	0.8	0.9
120	0.4	0.4	0.4	0.5	0.6	0.6	0.7	0.9
150	0.3	0.4	0.4	0.4	0.5	0.6	0.7	0.8
180	0.3	0.4	0.4	0.5	0.6	0.6	0.7	0.9
210	0.3	0.4	0.4	0.4	0.5	0.6	0.7	0.8
240	0.2	0.3	0.3	0.3	0.4	0.4	0.5	0.6
270	0.2	0.2	0.2	0.2	0.2	0.3	0.3	0.4
300	0.1	0.1	0.2	0.2	0.2	0.2	0.3	0.3
330	0.2	0.2	0.2	0.2	0.2	0.3	0.3	0.4

Table 4.17 Monthly Extreme Depth-averaged Residual Current Speed at IJV1

Monthly Extreme Depth-Average Residual Current Speed, CSres [m/s]								
	Return Period [years]							
Month	1	2	5	10	50	100	1000	10000
Omni	0.6	0.6	0.7	0.8	0.9	0.9	1.1	1.3
Jan	0.4	0.5	0.6	0.7	0.8	0.8	1.0	1.2
Feb	0.4	0.5	0.6	0.6	0.8	0.8	1.0	1.2
Mar	0.3	0.4	0.5	0.5	0.6	0.7	0.8	1.0
Apr	0.3	0.3	0.4	0.4	0.5	0.5	0.7	0.8
May	0.3	0.3	0.3	0.4	0.5	0.5	0.6	0.7
Jun	0.2	0.3	0.3	0.4	0.4	0.5	0.6	0.7
Jul	0.3	0.3	0.3	0.4	0.4	0.5	0.6	0.7
Aug	0.3	0.3	0.4	0.4	0.5	0.5	0.7	0.8
Sep	0.3	0.4	0.4	0.5	0.6	0.7	0.8	1.0
Oct	0.4	0.4	0.5	0.6	0.7	0.8	0.9	1.1
Nov	0.4	0.5	0.5	0.6	0.7	0.8	1.0	1.2
Dec	0.4	0.5	0.6	0.6	0.8	0.8	1.0	1.2

4.3.2 Extreme total currents

The storm events selected for the J-EVA analysis are based on the directional and seasonal variability (see Section 2.1 of Appendix D), with filtering carried out using a criteria of regression quantile >0.80, applied on the depth-averaged total current speed storm events. The resulting 'retained' and 'removed' events are shown in Figure 4.28. The storms of total current speed are mainly observed in two sectors, i.e., going towards north-northeast and to south-southwest, as expected since the currents are dominated by the tidal signal in IJV site (see the tidal depth-averaged current rose in Figure 3.20).

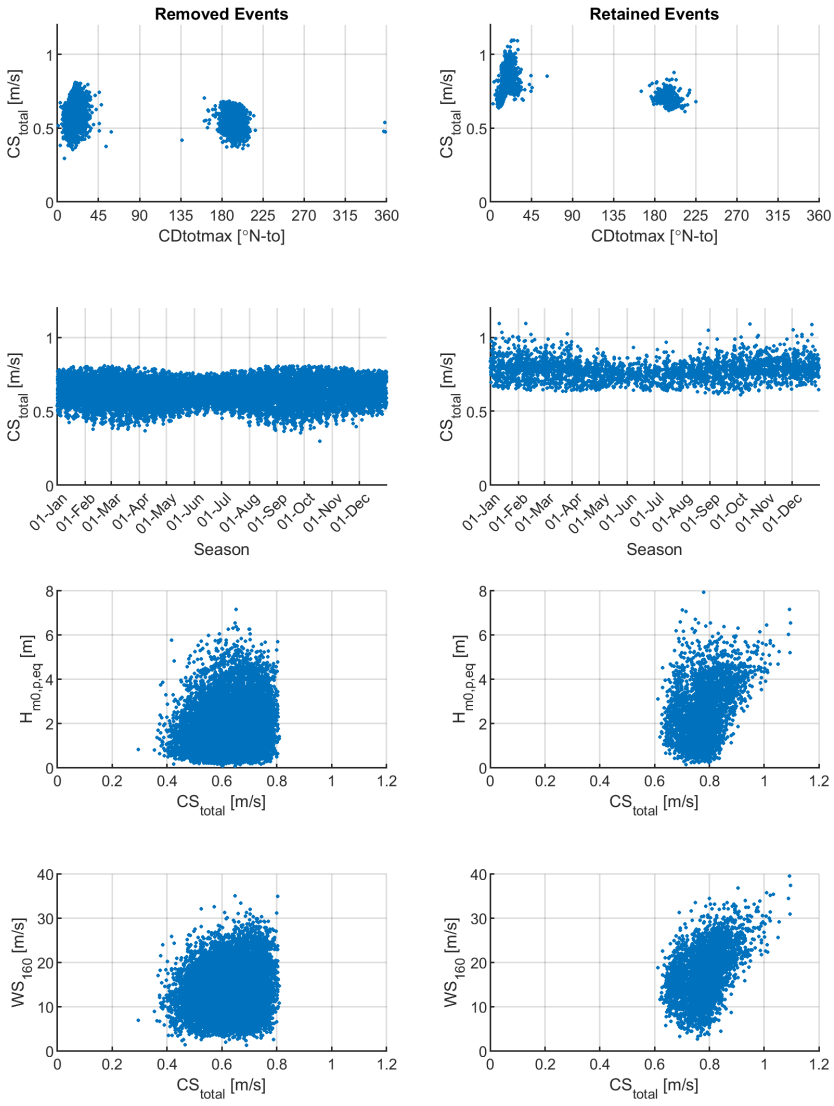

Figure 4.28 Selected events for total depth-averaged current speed, CS_{Total} at IJV1.
Events above the 0.80 regression quantile are retained for the J-EVA analysis.

A J-EVA statistical model (see Appendix D and Appendix F) has been set up for extreme total depth-averaged current speed, using seasons and depth-averaged total current direction as covariates, i.e., in a similar fashion to that of the residual currents.

The estimation of the extreme total current speeds is based on two different simulations of different lengths (see Appendix D). Figure 4.29 shows the posterior predictive distribution of extreme total current speeds computed from a 100,000-year simulation, which is used to calculate the return values up to a 100-year return period. These return periods are highlighted by the green shaded area. A larger simulation of 10^7 years is used to estimate extremes with return periods larger than 100 years, as shown in Figure 4.30.

The posterior predictive distribution explains well the hindcast data, and all peak events are in the credible interval (blue shaded area).

Figure 4.31 and Figure 4.32 show the directional (8 directional sectors of 45° bins) and monthly exceedance probability of extreme total depth-averaged current speed respectively. It should be noted that the number directional sectors are for visualization purposes only. Directional analysis reported are for 12 directional sectors (30° bins). In the dominant directional sectors (north, northeast, and south) the posterior predictive distribution (blue line) describes well the hindcast data (black line). Four historical events from the northeast sectors, also observed in the omni-directional plot, have similar total current speed value leading to a stepwise increase in the hindcast curve. This is explained by the large proportion of tide for these events, which represents 57 % of the total component on average for the 4 largest events. The J-EVA statistical model describes well most of the monthly sectors, with all peak events within the credible intervals.

Using the same method described for residual current speed in Section 4.3.1, the missing directional extreme values have been estimated from the median of annual maxima.

Table 4.18 and Table 4.19 summarise the extreme values at IJV1 for the directional and monthly depth-averaged total current extreme analysis respectively. The high return periods have similar extreme values as the residual currents, but the lower return periods have higher values. This is due to the significant non-random tidal signal contributing to the total currents as explained above.

Table 4.20 provides the values of the associated extreme significant wave height and wind speed at 160 m.

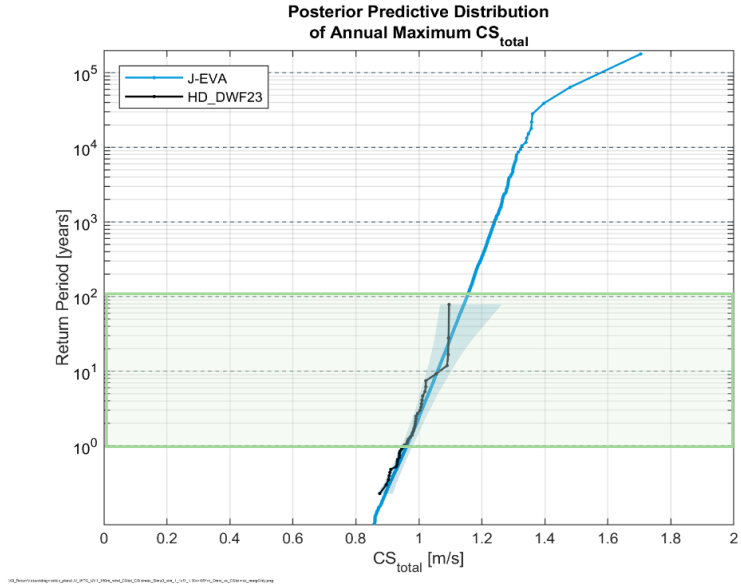

Figure 4.29 Omni-directional extreme total current speed at IJV1 from a 100,000-year simulation.
Hindcast data is shown in black. The blue line is the posterior predictive distribution. The shaded area is the 2.5-97.5% credible interval of the estimate. The shaded green rectangle represents the return values estimated from this 100,000-year simulation.

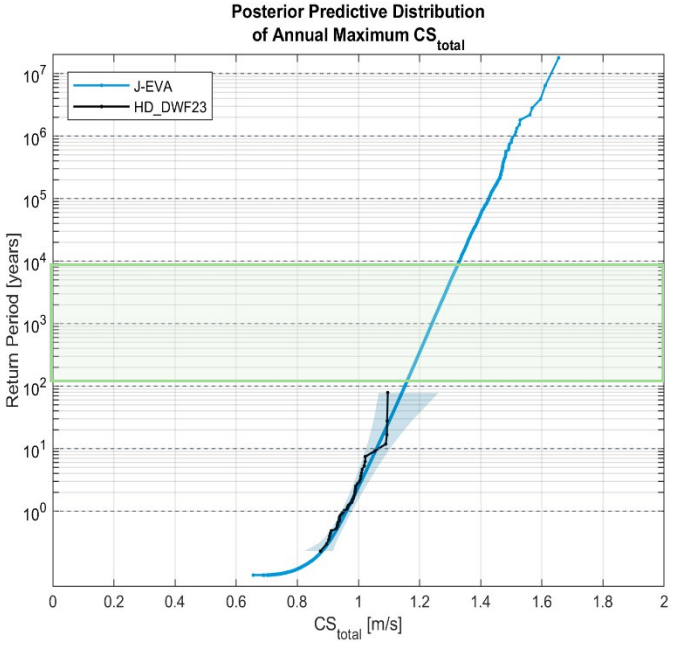

Figure 4.30 Omni-directional extreme total current speed at IJV1 from a 10^7-year simulation.
Hindcast data is shown in black. The blue line is the posterior predictive distribution. The shaded area is the 2.5-97.5% credible interval of the estimate. The shaded green rectangle represents the return values estimated from this 10^7-years simulation.

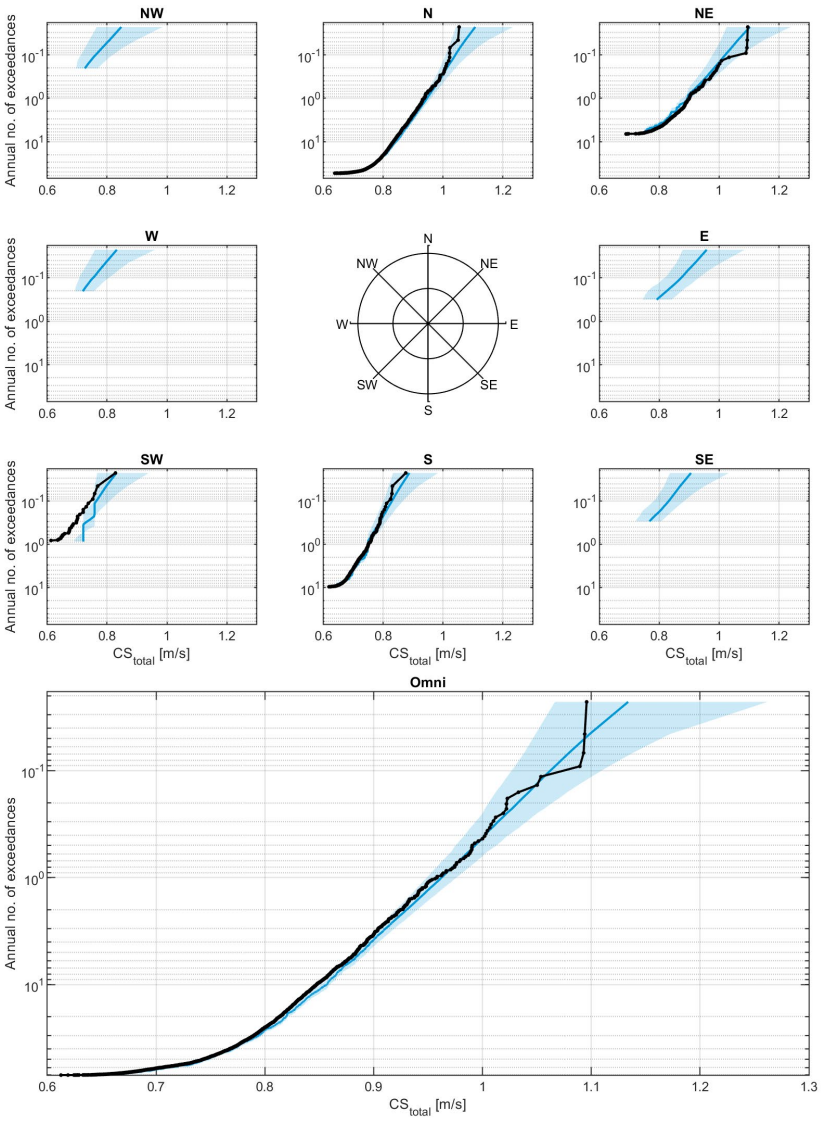

Figure 4.31 Directional exceedance probability of CS_{Total} at IJV1.
Hindcast data is shown in black. The blue line is the best estimate using the integrated posterior predictive distribution parameters. The shaded area is the 2.5-97.5% credible interval.

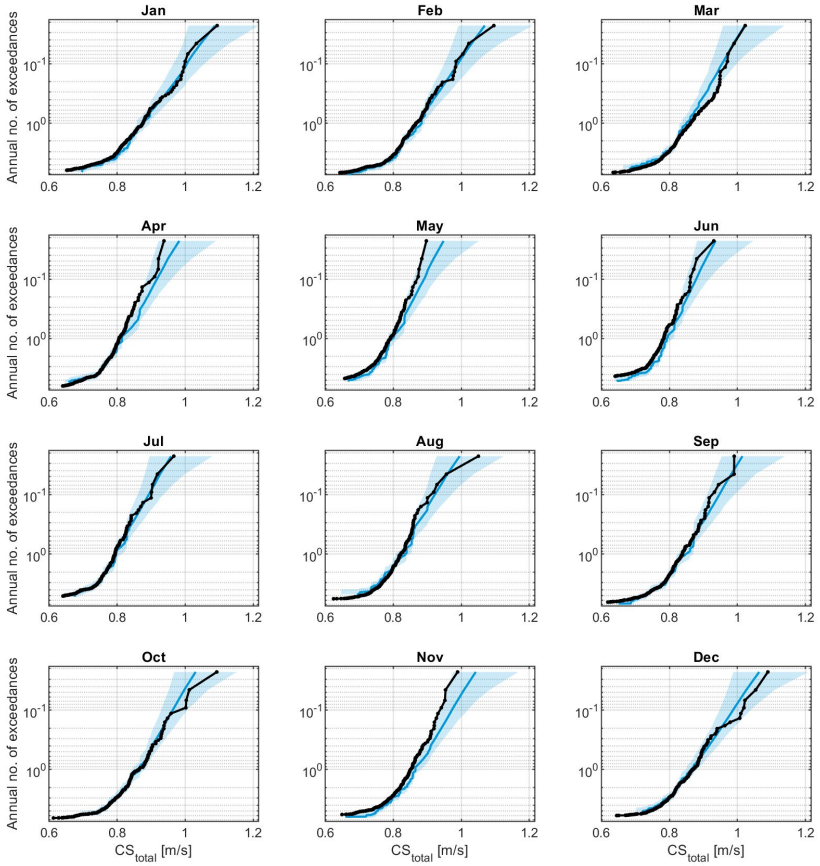

Figure 4.32 Monthly exceedance probability of CS_{Total} at IJV1.
Hindcast data is shown in black. The blue line is the best estimate using the integrated posterior predictive distribution parameters. The shaded area is the 2.5-97.5% credible interval.

Table 4.18 Directional extreme depth-averaged total current speed at IJV1.

30° Directional Extreme Depth-Average Total Current Speed, CStot [m/s]								
Direction (CD [°N-to])	Return Period [years]							
	1	2	5	10	50	100	1000	10000
Omni	1.0	1.0	1.0	1.1	1.1	1.2	1.2	1.3
0	0.8	0.9	0.9	0.9	1.0	1.0	1.1	1.2
30	1.0	1.0	1.0	1.1	1.1	1.2	1.2	1.3
60	0.7	0.7	0.7	0.8	0.8	0.8	0.9	0.9
90	0.6	0.6	0.6	0.6	0.7	0.7	0.7	0.8
120	0.5	0.6	0.6	0.6	0.7	0.7	0.7	0.8
150	0.6	0.7	0.7	0.7	0.8	0.8	0.8	0.9
180	0.8	0.8	0.8	0.9	0.9	0.9	1.0	1.1
210	0.8	0.8	0.8	0.8	0.9	0.9	1.0	1.1
240	0.5	0.6	0.6	0.6	0.6	0.7	0.7	0.8
270	0.4	0.4	0.4	0.4	0.5	0.5	0.5	0.6
300	0.3	0.3	0.4	0.4	0.4	0.4	0.4	0.5
330	0.4	0.4	0.4	0.4	0.5	0.5	0.5	0.6

Table 4.19 Monthly extreme depth-averaged total current speed at IJV1.

Monthly Extreme Depth-Average Total Current Speed, CStot [m/s]								
	Return Period [years]							
Month	1	2	5	10	50	100	1000	10000
Omni	1.0	1.0	1.0	1.1	1.1	1.2	1.2	1.3
Jan	0.9	0.9	1.0	1.0	1.1	1.1	1.2	1.3
Feb	0.9	0.9	1.0	1.0	1.1	1.1	1.2	1.3
Mar	0.9	0.9	0.9	1.0	1.0	1.0	1.1	1.2
Apr	0.8	0.9	0.9	0.9	1.0	1.0	1.1	1.1
May	0.8	0.8	0.9	0.9	0.9	1.0	1.0	1.1
Jun	0.8	0.8	0.9	0.9	0.9	1.0	1.0	1.1
Jul	0.8	0.8	0.9	0.9	1.0	1.0	1.1	1.1
Aug	0.8	0.9	0.9	0.9	1.0	1.0	1.1	1.2
Sep	0.8	0.9	0.9	0.9	1.0	1.0	1.1	1.2
Oct	0.9	0.9	0.9	1.0	1.0	1.0	1.1	1.2
Nov	0.9	0.9	0.9	1.0	1.0	1.1	1.1	1.2
Dec	0.9	0.9	0.9	1.0	1.1	1.1	1.2	1.3

4.3.3 H_{m0} conditioned on extreme total current

The correlation between CS_{tot} and H_{m0} is presented in Figure 4.33 for the 10^7-year of simulated storms in J-EVA.

The conditioned variables are obtained by selecting the 500 simulated events that are the closest to the annual maxima for each return periods, and then finding the 5 %, 50 % and 95 % quantiles of the conditioned variable in each event. A consequence of this method is that the conditioned variables do not necessarily increase smoothly with increasing return period, and therefore a fit to the conditioned variables is required to obtain robust estimations.

For this analysis the storm peak equivalent significant wave height $H_{m0,p,eq}$ assumed to be equal to H_{m0} for associated analysis.

A power-law function has been applied to the range of return periods. Here, 'Y' denotes the variables conditioned by CS_{tot}, while 'a' and 'b' are fitted parameters.

$$Y = a \cdot CS_{tot}^{\ b} \qquad (4.4)$$

The following sections present the 5%, 50% and 95%-tiles values of the conditioned variables for the omni-directional sector.

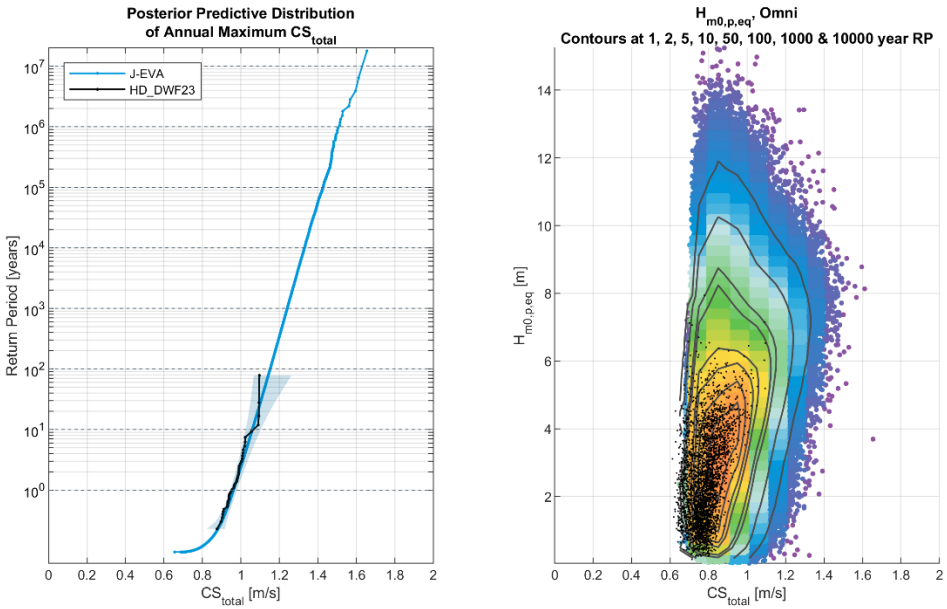

Figure 4.33 Estimates of marginal and conditioned variables from 10^7-year simulation at IJV1.
Left panel: hindcast data is presented as black markers. The blue solid line (top left) is the posterior predictive distribution. The blue shaded area (top left) is the 2.5-97.5 % credible interval.
Right panel: contours of conditioned variables shown as coloured dots from the results of a simulation of 10^7 years using the posterior predictive distribution at different return periods are shown for H_{m0} against CS_{tot}. Black dots show original hindcast. Warmer colours indicate a higher density of points.

Figure 4.34 shows the extreme CS_{tot} for each return period against H_{m0} and fit based on (4.4), while Table 4.20 provides the omni-directional 5%-, 50%- and 95%-tiles of H_{m0} conditioned on CS_{tot} at IJV1.

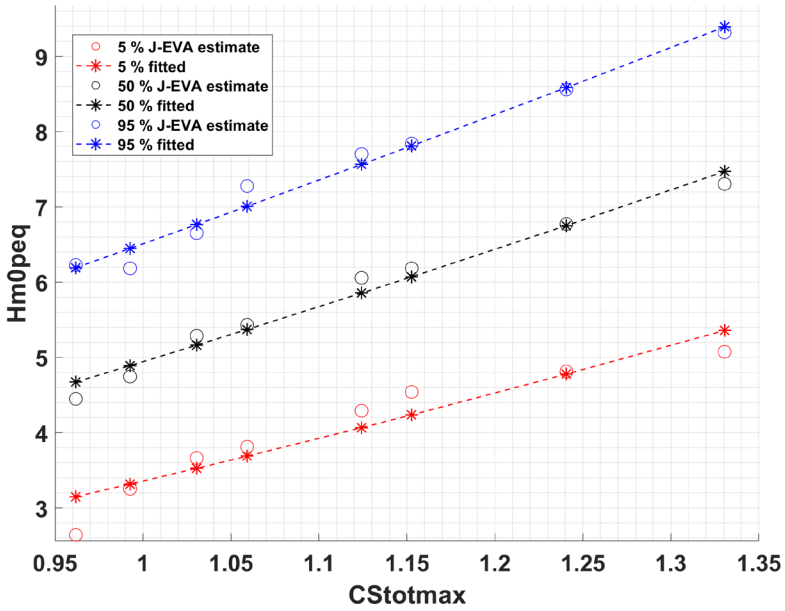

Figure 4.34 Omni-directional H_{m0} conditioned on CS_{tot} at IJV1.

Table 4.20 Omni-directional extremes of H_{m0} conditioned on CS_{tot} at IJV1.

Joint Probability, Omni-directional Associated values				
Return Periods [years]	CS_{tot} [m/s]	H_{m0} [m], 5%	H_{m0} [m], 50%	H_{m0} [m], 95%
1	1.0	3.2	4.7	6.2
2	1.0	3.3	4.9	6.4
5	1.0	3.5	5.2	6.8
10	1.1	3.7	5.4	7.0
50	1.1	4.1	5.9	7.6
100	1.2	4.2	6.1	7.8
1000	1.2	4.8	6.8	8.6
10000	1.3	5.4	7.5	9.4

4.3.4 Extreme current profile

The current profile is computed separately for the tidal and the residual components following [10] and [11]. The profiles described in section 3.3.1 cannot be directly used for the extremes since they are based on the 50% data. For the extremes, 99% of the measured data is considered.

Current profiles under extreme conditions are analysed using the following approach.

1. Guidelines from the IEC [10] and DNV [11] standards are used to establish a current profile.
2. Data from four (4) measuring stations, namely IJVA, IJVB, NWA and NWB, are used in combination with the design standards [10, 11] for tidal component only.
3. A power law coefficient α is recommended to derive current profiles under extreme conditions at IJV1 for tidal component and the residual near-seabed current.
4. A linear relationship between the depth-averaged and surface current is recommended for the residual surface current.

For the tidal component, a power law profile described in [10] is recommended. For the residual component, a linear profile described in [10] and [11] is recommended.

4.3.4.1 Tidal component

Figure 4.35 shows the current profiles (using all data) at the four locations as well as the 99% of the measurements. Theoretical profile is plotted using Eq. (3.2) and a typical value of $\alpha = 1/7$ is used. From Figure 3.8, it is not very apparent whether $\alpha = 1/7$ provides the best fit, except at IJVA. Therefore, further investigation is carried out to find the best α fit at the four measurement stations.

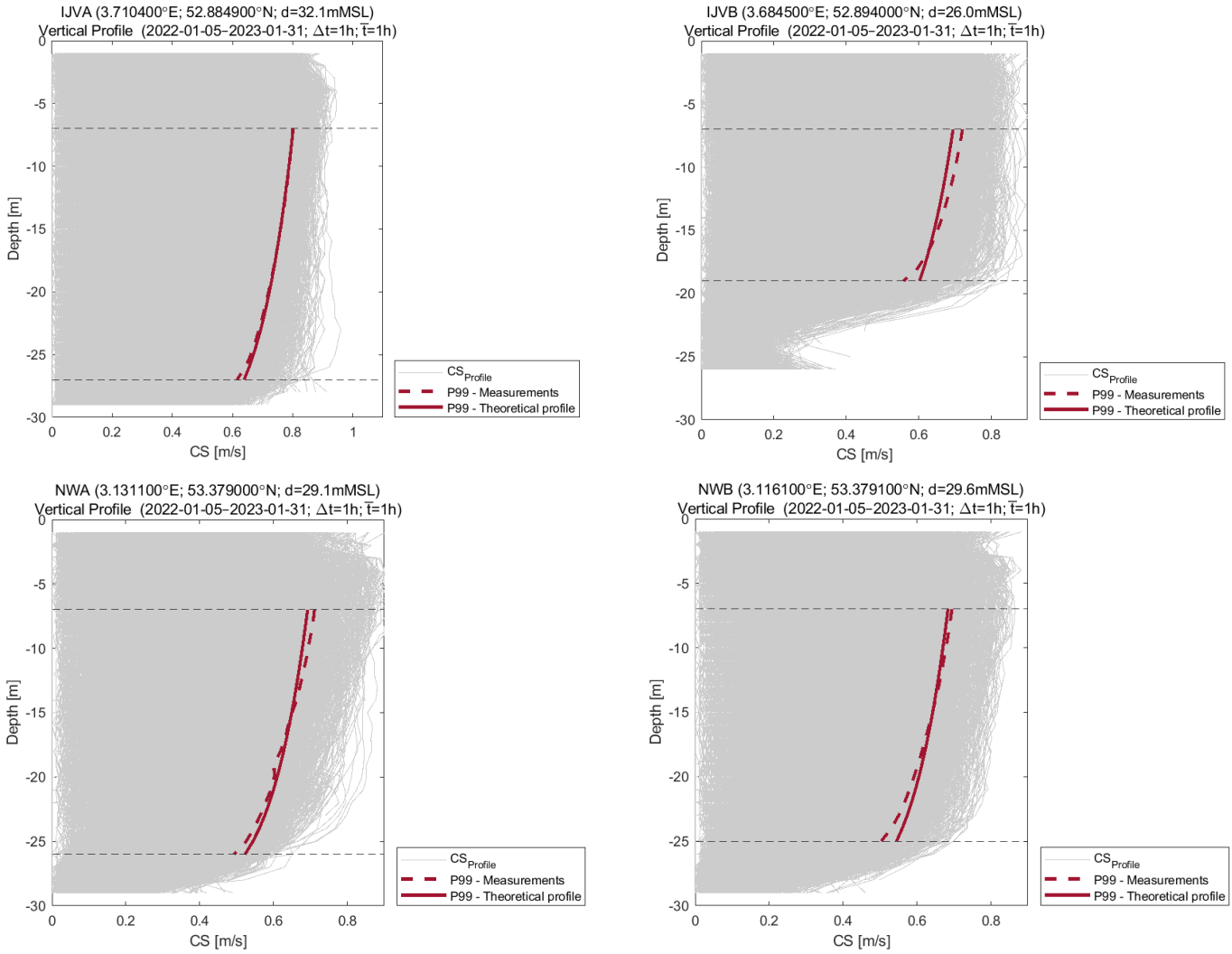

Figure 4.35 Measured and fitted current profiles at IJVA (top left), IJVB (top right), NWA (bottom left), and NWB (bottom right).
Theoretical profile is obtained using $\alpha = 1/7$ at all stations. The 99% profiles are also shown.

Figure 4.36 - Figure 4.39 show the variation in the fitted current profile using Eq. (3.2) for different values of α at the four measurement stations. The measurements correspond to the 99% of the measurements at each depth bin. The measurements and theoretical profile have been normalized by the depth-averaged value at each station. The current speed at 2/5th depth is considered as depth average current speed.

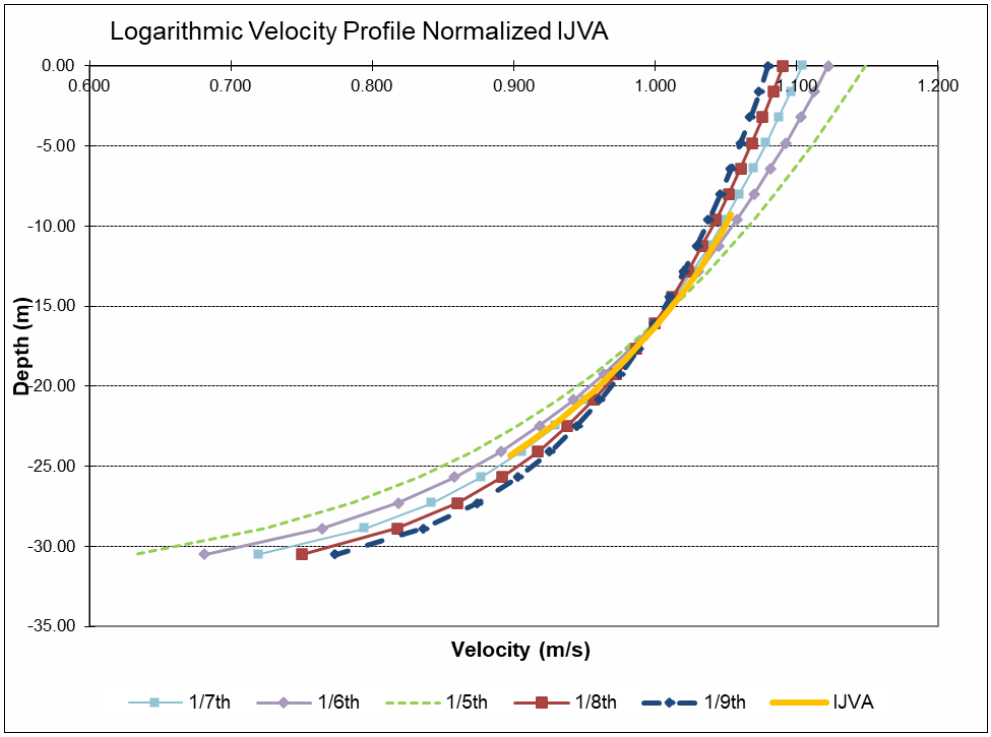

Figure 4.36 Normalized Current Profile at IJVA for extreme conditions. The data shows several profiles with distinct α values for the period of analyses (2022-05-01 to 2023-01-31). Measured profile (99%) is shown as solid yellow line.

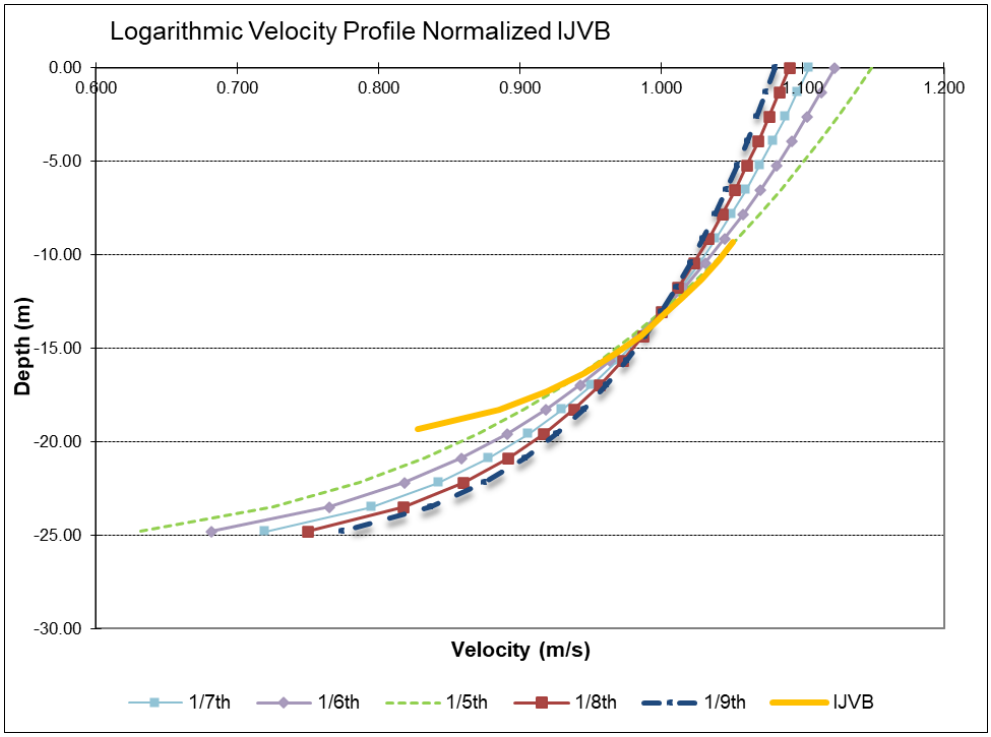

Figure 4.37 Normalized Current Profile at IJVB for extreme conditions. The data shows several profiles with distinct α values for the period of analyses (2022-05-01 to 2023-01-31). Measured profile (99%) is shown as solid yellow line.

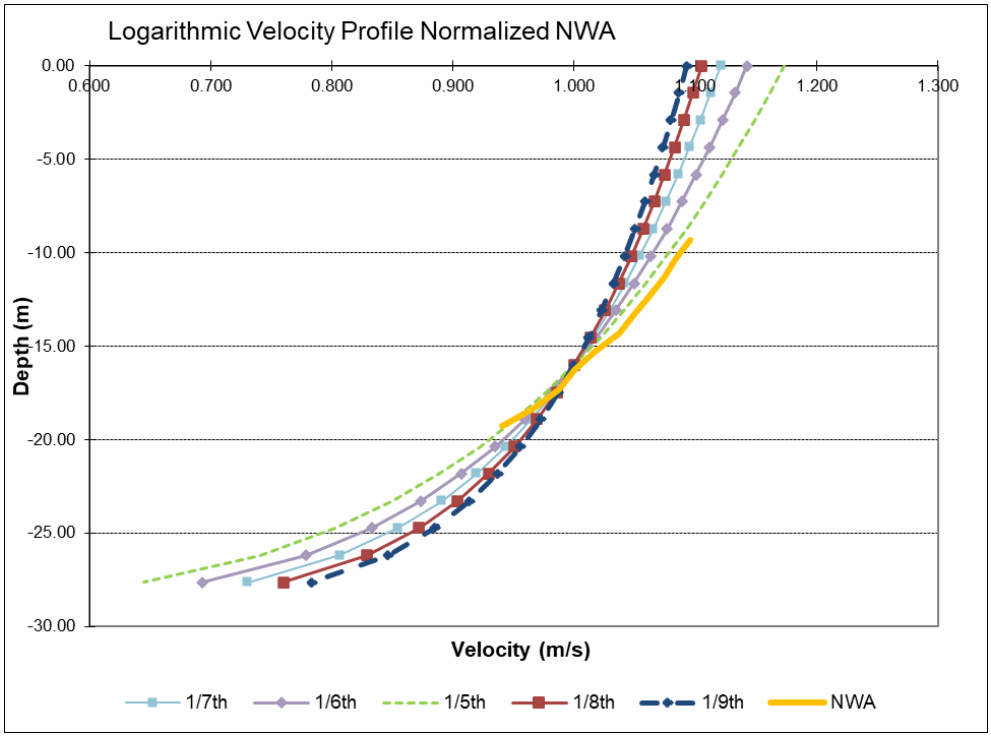

Figure 4.38 Normalized Current Profile at NWA for extreme conditions. The data shows several profiles with distinct α values for the period of analyses (2022-05-01 to 2023-01-31). Measured profile (99%) is shown as solid yellow line.

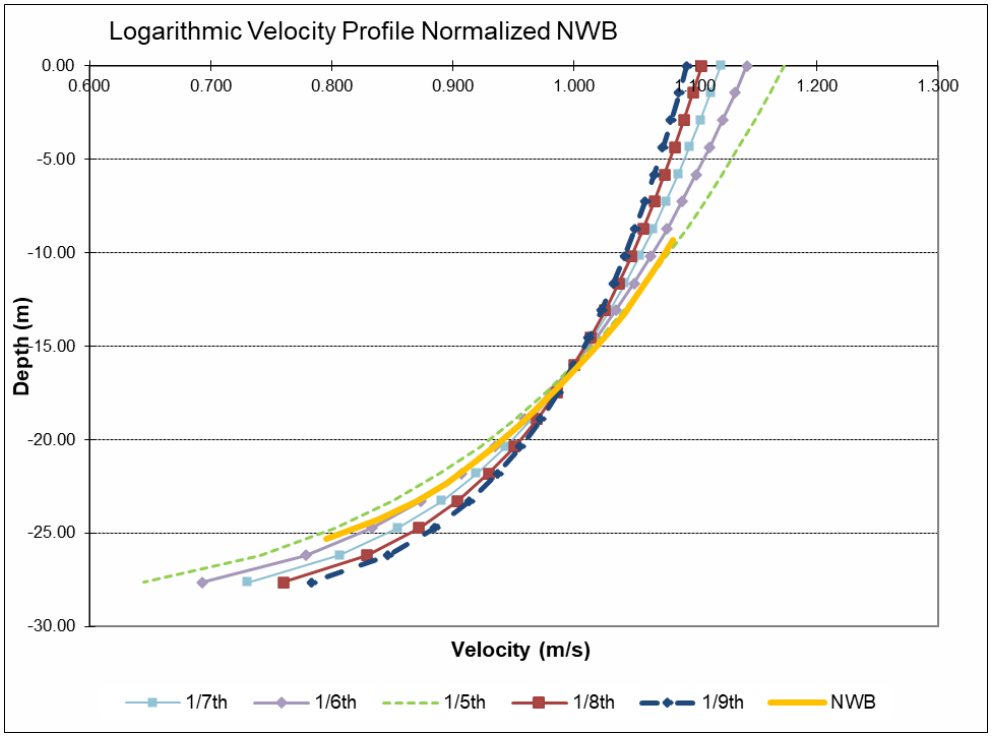

Figure 4.39 Normalized Current Profile at NWB for extreme conditions. The data shows several profiles with distinct α values for the period of analyses (2022-05-01 to 2023-01-31). Measured profile (99%) is shown as solid yellow line.

Considering IJVA (Figure 4.36), the best fit for depth-averaged currents is for $\alpha = 1/7$. For IJVB, as seen in Figure 4.37, a value of $\alpha = 1/5$ seems to be the most appropriate. For both NWA and NWB (Figure 4.38 and Figure 4.39), a value of $\alpha = 1/5$ shows to be the best fit over all water column. Except at IJVA, $\alpha = 1/5$ gives the best fit at the three stations, i.e., IJVB, NWA, and NWB. From Figure 4.36, it is seen that at IJVA, using $\alpha = 1/5$, the current speeds will be slightly conservative near the surface, whereas they will be slightly less conservative near the seabed.

Given all considerations, it is **recommended** to use $\alpha = 1/5$ **for tidal component of current speeds in extreme design conditions**. Assuming the current speed at 2/5th depth to be representative of the depth average current speed, we get,

$$\mathrm{CS}_{\mathrm{Tide-Surf}} = \frac{6}{5} \times \mathrm{CS}_{\mathrm{Tide-Dep}} \tag{4.5}$$

4.3.4.2 Residual component

Apart from the linear current profile, the IEC standard [10] has also suggested using a simple scaling with the wind speed such that the residual surface current speed can be estimated as $\mathrm{CS}_{\mathrm{Residual}}(0) = 0.01 \times \mathrm{WS}_{\mathrm{10-1hour}}$, where WS_{10} is the 1-hour average wind speed at 10 m height. Alternatively, the DNV standards [11] specify $\mathrm{CS}_{\mathrm{Residual}}(0) = (0.015 - 0.03) \times \mathrm{WS}_{\mathrm{10-1hour}}$. At IJV1, $\mathrm{WS}_{\mathrm{10\text{-}1hour}}$ ~ 31 m/s for a 1000-year return period. Using the IEC standard, $\mathrm{CS}_{\mathrm{Residual}}(0)$ = 0.3 m/s, whereas using the DNV standards, $\mathrm{CS}_{\mathrm{Residual}}(0)$ will be between 0.5 – 0.9 m/s for a 1000-year return period. Considering that the residual current is mainly driven by wind, and that it becomes smaller than $\mathrm{CS}_{\mathrm{Residual-Dep}}$, which for a 1000 year return period is 1.1 m/s, an approach using a simple scaling factor is deemed unrealistic and unconservative.

Therefore, for the residual currents, the following linear equation is recommended for the current profile (see [10] and [11]).

$$\mathrm{CS}_{\mathrm{Residual}}(z) = \mathrm{CS}_{\mathrm{Residual}}(0) \times \left(\frac{d_0 + z}{d_0}\right) \tag{4.6}$$

where d_0 is the reference depth at which the wind-driven current is zero. The profile can be visualised in three ways depending on the water depth d as shown in Figure 4.40.

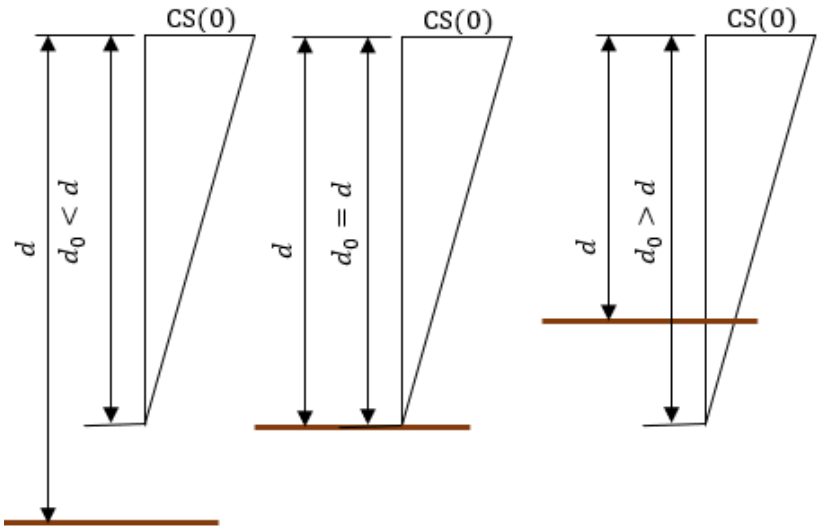

Figure 4.40 Linear profile of the wind induced residual current speed. Three scenarios of the linear profile depending on the relation between the water depth and the reference depth d_0.

The surface residual current speed can be calculated using the definition of the depth-average current speed, which is the area under the profile curve up to the water depth. It is to be noted that when $d_0 > d$, the current speed is not zero at the seabed and even has a magnitude below the seabed, which is not physical. Therefore, when $d_0 > d$ the schematic corresponding to the middle figure of Figure 4.40 is assumed to be applicable. From the schematic on the left in Figure 4.40,

$$\mathrm{CS}_{\mathrm{Residual-Dep}} = \frac{1}{d} \times \frac{1}{2} \times d_0 \times \mathrm{CS}_{\mathrm{Residual}}(0) = \left(\frac{\mathrm{d_0}}{2\mathrm{d}}\right) \mathrm{CS}_{\mathrm{Residual}}(0) \qquad \textbf{(4.7)}$$

Whereas for the schematic in the middle of Figure 4.40,

$$\mathrm{CS}_{\mathrm{Residual-Dep}} = \frac{1}{d_0} \times \frac{1}{2} \times d_0 \times \mathrm{CS}_{\mathrm{Residual}}(0) = \left(\frac{1}{2}\right) \mathrm{CS}_{\mathrm{Residual}}(0) \qquad \textbf{(4.8)}$$

The IEC standard recommends using $d_0 = 20$m, whereas the DNV standard recommends using $d_0 = 50$m. At IJV1, $d = 25.8$ m, therefore, using the IEC standards, the left schematic in Figure 4.40 is applicable, which gives $\mathrm{CS}_{\mathrm{Residual}}(0) = 2.58 \times \mathrm{CS}_{\mathrm{Residual-Dep}}$. From the experience of DHI carrying out metocean analyses in the neighbouring areas, this relation will give too large values of $\mathrm{CS}_{\mathrm{Residual}}(0)$. Therefore, we apply the schematic in the middle of Figure 4.40, which we believe will still give a reasonable but conservative estimate of $\mathrm{CS}_{\mathrm{Residual}}(0)$ using Eq. (4.8).

Given all considerations, it is **recommended** to use $\mathrm{CS}_{\mathrm{Residual-Surf}} = 2 \times \mathrm{CS}_{\mathrm{Residual-Dep}}$ **for the residual component of the surface current speeds in extreme design conditions**. For example, for a 100-year return period using $\mathrm{CS}_{\mathrm{Residual\text{-}Dep}}$ = 0.9 m/s (see Table 4.16), we get $\mathrm{CS}_{\mathrm{Residual\text{-}Surf}}$ = 1.8 m/s.

For the **near-seabed currents**, using Eq. (4.8) resulted in too small values of $\mathrm{CS}_{\mathrm{Residual,near-seabed}}$. It is therefore **recommended** to apply a power law [10] to the near-seabed residual currents using Eq. (3.2) for both components, residual and tidal, where $\alpha = 1/5$.

4.4 Waves

The analysis of extreme waves is presented in this section. The analysis is based on the 44-years (1979-01-15 to 2022-12-31) timeseries data extracted from the SW_{SWF23} model. The model results are interpreted as representative of 3-hour average.

The extreme values of significant wave height are presented in Section 4.4.1, and the results of the associated variables are presented in Section 4.4.2. Maximum individual wave height and crest height are detailed in Section 4.4.3 and Section 4.4.4, respectively. Finally, the wave breaking assessment is described in Section 4.4.5.

4.4.1 Extreme significant wave height, H_{m0}

This section provides monthly and directional extremes of the significant wave height. The extreme wave conditions are estimated following the steps outlined in Appendix D.

The storm events selected for the J-EVA analyses are based on the directional and seasonality variability (see Section 2.1 of Appendix D) with selection criteria of regression quantile larger than 0.7 and inverse wave age larger than 1. These filtering criteria are applied on the combined normalised storm events comprising of H_{m0}, CS_{res} and WS_{160}. The combination of the time series has been chosen in order not to miss any peaks of associated variables (CS_{res} and WS_{160}) shifted in time relative to H_{m0}. The resulting 'retained' and 'removed' events are shown in Figure 4.41. It is observed that peaks of significant wave height are evenly distribution across all year and peak wave direction (PWD).

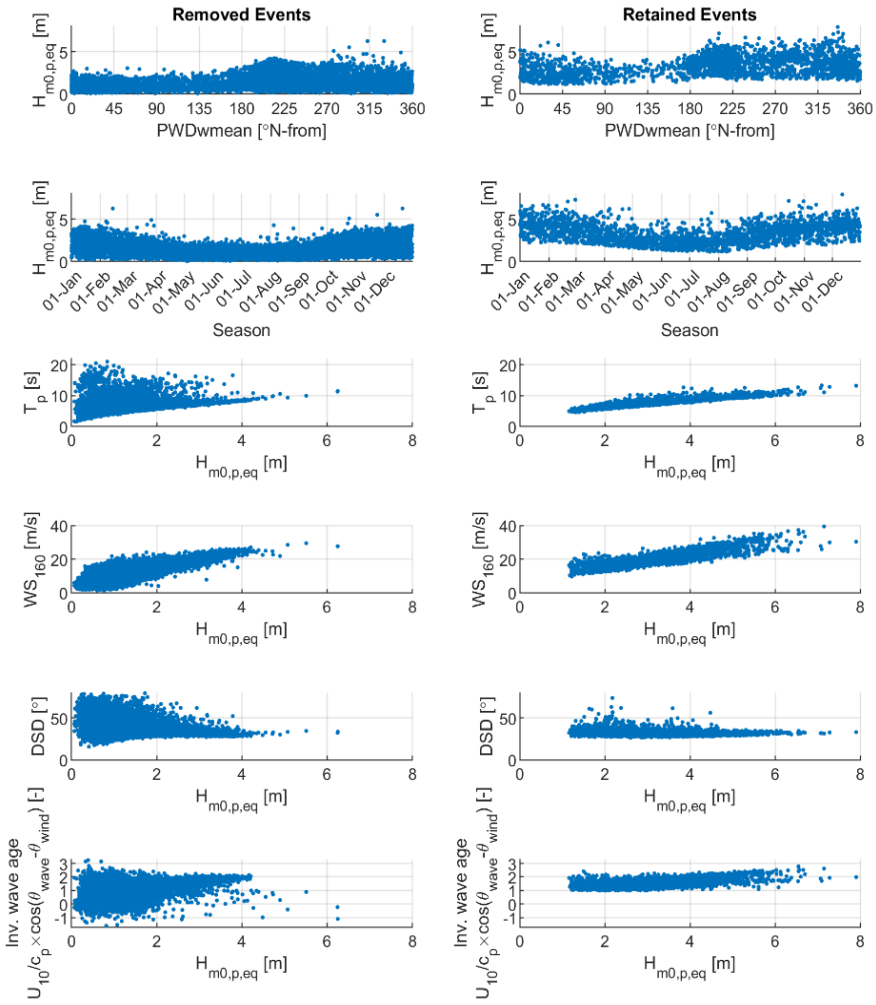

Figure 4.41 Selected events for significant wave height, H_{m0}, at IJV1. Events above the 0.70 regression quantile and with an inverse wave age larger than 1 are retained for the J-EVA analysis. The associated variables T_p (third row), WS_{160} (fourth row) and directional spreading DSD (fifth row), and the inverse wave age (last row) are shown.

A J-EVA statistical model (see Appendix D and Appendix F) has been set up for extreme significant wave heights and conditioned (associated) variables, in which random events are simulated following a MCMC approach (see Section 4 of Appendix D). Afterwards the J-EVA storm model is used to estimate the evolution in time of possible peak events using the time evolution observed in the historical storms (see Appendix D and Appendix E).

The storm model peak wave direction (PWD) and time of day (season) have been used as covariates and the model fitted to characteristic storm variable values ($H_{m0,p,eq}$, ln σ_{eq}, T_p. etc.). Furthermore, the long-term distribution of $H_{m0,p,eq}$ (equivalent peak H_{m0} from the storm model) has been limited to 0.6 times the water depth (see Section 7 of Appendix D). This is considered a rather conservative estimate for the depth limited H_{m0}.

The estimation of the extreme $H_{m0,p,eq}$ is based on two different simulations of different lengths. Figure 4.42 shows the posterior predictive distribution of extremes significant wave height from a 50,000-year simulation, which is used to calculate the best estimate for 1-, 2-, 5-, 10-, 50- and 100-year return

periods. These return periods are highlighted by the green shaded area. Extreme values with return periods larger than 100 years are estimated from a $5x10^6$ year simulation, as shown in Figure 4.43.

The posterior predictive distribution models very well the hindcast data for all return periods.

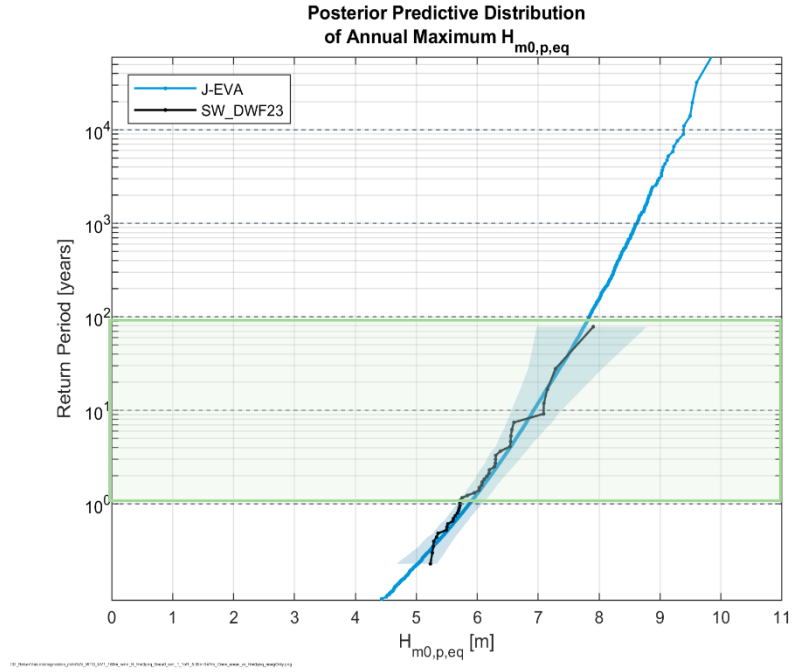

Figure 4.42 Annual extreme significant wave height at IJV1.
Hindcast data is presented in black. The blue solid line is the posterior predictive distribution. The shaded area is the 2.5-97.5% credible interval of the estimate. The green shaded rectangle represents the return values estimated from this 50,000-year simulation.

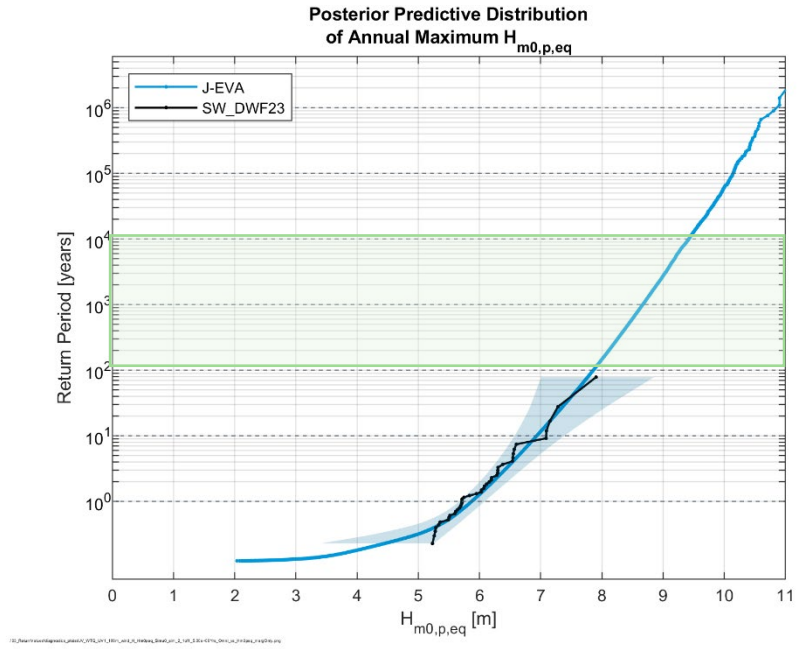

Figure 4.43 Annual extreme significant wave height at IJV1 from a 5x10^6-year simulation.
Hindcast data is presented in black. The blue solid line is the posterior predictive distribution. The shaded area is the 2.5-97.5% credible interval of the estimate. The green shaded rectangle represents the return values estimated from this 5x10^6-year simulation.

Figure 4.44 and Figure 4.45 depict the directional (8 directional sectors of 45° bins) and monthly exceedance probability of extreme equivalent peak $H_{m0,p,eq}$ respectively. It should be noted that the number directional sectors are for visualization purposes only. Directional analysis reported are for 12 directional sectors (30° bins). The J-EVA statistical model captures well the hindcast peak events for omni-directional and all directional sectors. It is observed that the statistical model overestimated the historical events for a few months, like May and March, and underestimates others, like April, but all the most extreme events are within the 95% credible intervals.

The extreme values of significant wave heights are then estimated by applying the J-EVA storm model (see Appendix D and Appendix E), i.e., resolving the individual sea state and time evolution of the storm. From now on we will thus be looking at H_{m0} instead of $H_{m0,p,eq}$.

Table 4.21 and Table 4.22 summarise the extreme significant wave height results at IJV1 for directional and monthly sectors respectively. These results are generated considering all water levels. The most dominant directional sectors those between 300°N and 0°N, i.e., from northwest to northeast, which is similar as those for normal conditions (see wave roses in Section 3.4.2). As expected for this region the most extreme significant wave heights happen during the winter.

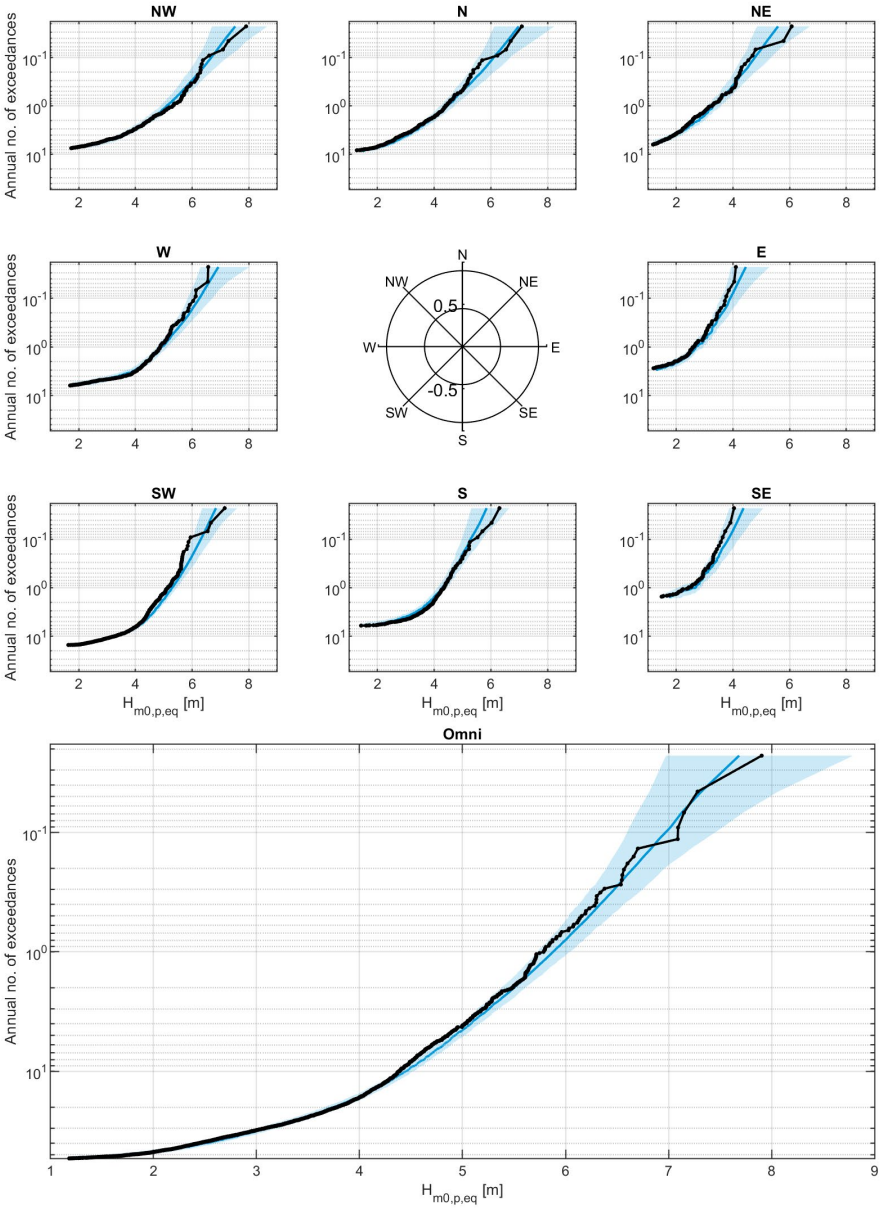

Figure 4.44 Directional exceedance probability of H_{m0} at IJV1.
Hindcast data is shown in black. The blue line is the best estimate using the integrated posterior predictive distribution parameters. The shaded area is the 2.5-97.5% credible interval.

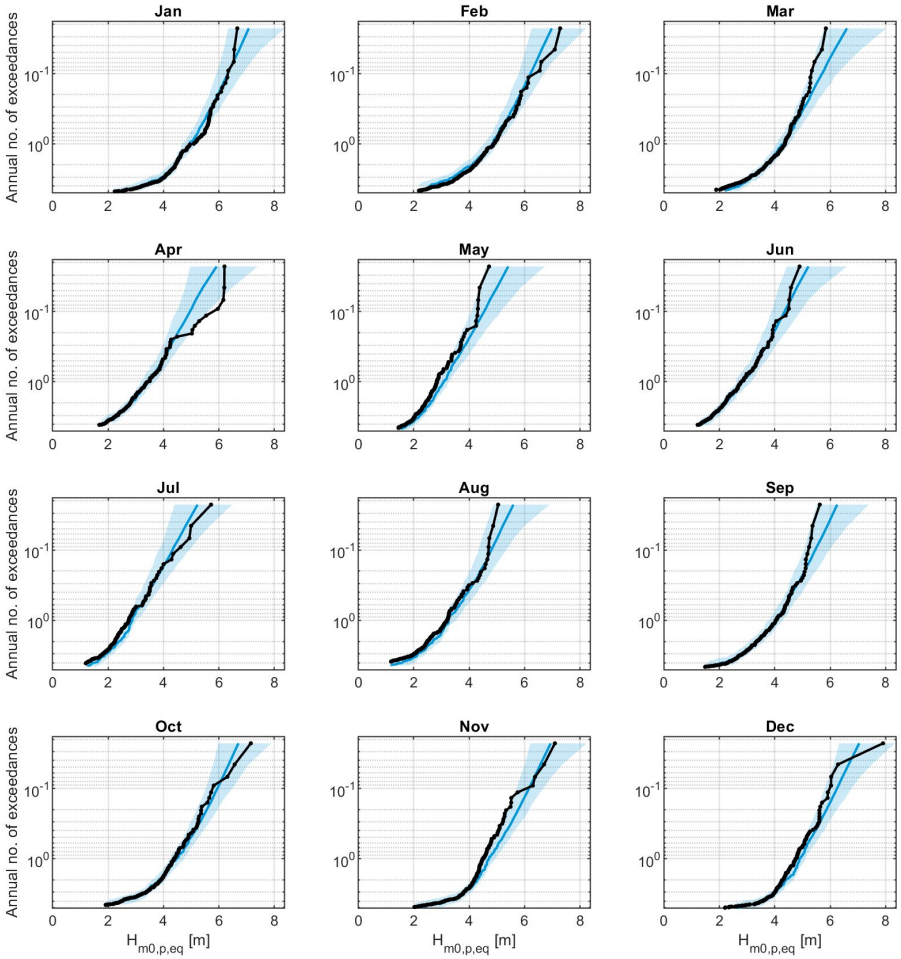

Figure 4.45 Monthly exceedance probability of H_{m0} at IJV1.
Hindcast data is shown in black. The blue line is the best estimate using the integrated posterior predictive distribution parameters. The shaded area is the 2.5-97.5% credible interval.

Table 4.21 Directional extreme significant wave height at IJV1.
Extreme results considering all water levels.

30° Directional Extreme Significant Wave Height, H_{m0} [m]								
Direction (PWD [°N-from])	Return Period [years]							
	1	2	5	10	50	100	1000	10000
Omni	5.9	6.2	6.7	7.0	7.6	7.9	8.7	9.5
0	4.4	4.9	5.6	6.0	6.8	7.1	8.0	8.7
30	3.5	4.0	4.5	4.9	5.7	6.0	6.8	7.5
60	3.1	3.6	4.0	4.4	5.1	5.3	6.1	6.7
90	2.8	3.3	3.6	3.9	4.4	4.6	5.1	5.6
120	2.7	3.0	3.4	3.7	4.2	4.4	4.9	5.3
150	2.9	3.4	3.7	4.0	4.5	4.6	5.1	5.6
180	4.3	4.7	5.0	5.3	5.8	6.0	6.7	7.3
210	5.3	5.6	6.0	6.3	6.7	6.9	7.5	8.0
240	5.0	5.4	5.8	6.1	6.7	6.9	7.6	8.3
270	5.1	5.5	5.9	6.2	6.8	7.1	7.8	8.6
300	5.1	5.5	6.0	6.3	7.0	7.2	7.9	8.7
330	5.1	5.7	6.3	6.7	7.5	7.8	8.6	9.4

Table 4.22 Monthly extreme significant wave height at IJV1.
Extreme results considering all water levels.

Monthly Extreme Significant Wave Height, H_{m0} [m]								
Month	Return Period [years]							
	1	2	5	10	50	100	1000	10000
Omni	5.9	6.2	6.7	7.0	7.6	7.9	8.7	9.5
Jan	5.0	5.4	6.0	6.3	7.0	7.3	8.2	9.0
Feb	4.8	5.3	5.8	6.2	6.9	7.2	8.2	8.9
Mar	4.3	4.8	5.3	5.7	6.5	6.8	7.8	8.7
Apr	3.4	4.0	4.5	4.9	5.8	6.2	7.2	8.0
May	3.1	3.5	4.1	4.5	5.3	5.7	6.6	7.4
Jun	2.8	3.4	3.9	4.3	5.1	5.4	6.3	7.1
Jul	2.9	3.3	3.9	4.3	5.1	5.4	6.3	7.1
Aug	3.3	3.8	4.4	4.8	5.5	5.8	6.7	7.5
Sep	4.0	4.5	5.1	5.4	6.2	6.4	7.3	8.1
Oct	4.5	5.0	5.6	5.9	6.6	6.9	7.7	8.5
Nov	4.7	5.2	5.8	6.1	6.9	7.2	8.0	8.8
Dec	4.9	5.3	5.9	6.2	7.0	7.3	8.2	9.0

4.4.2 Variables conditioned on H_{m0}

The correlation between H_{m0} and other variables is presented in Figure 4.46 for the $5x10^6$-year of simulated storms in J-EVA.

The conditioned variables are obtained by selecting the 125 simulated events that are the closest to the annual maxima for each return period, and then

finding the 5%, 50% and 95% quantile of the conditioned variable in each event. A consequence of this method is that the conditioned variables do not necessarily increase smoothly with increasing return period, and therefore a fit to the conditioned variables is required to obtain robust estimations.

Power-law or linear functions have been applied to the range of return periods. Here, 'Y' denotes the variables conditioned by H_{m0}, while 'a' and 'b' are fitted parameters.

$$Y = a \cdot H_{m0}{}^{b} \tag{4.9}$$

$$Y = a \cdot H_{m0} + b \tag{4.10}$$

The power-law (equation (4.9)) is used for all associated wave periods, current speed and wind speed and the linear function (equation (4.10)) is used for water levels.

It is noted that for conditioned variables the directional or monthly values can sometimes exceed that of omni. This could for example be in case omni-directional waves are dominated by wind-sea, while a certain sector is dominated by swell. In this case the swell-dominated directional sector could have a higher value of T_p compared to the omni-directional sector.

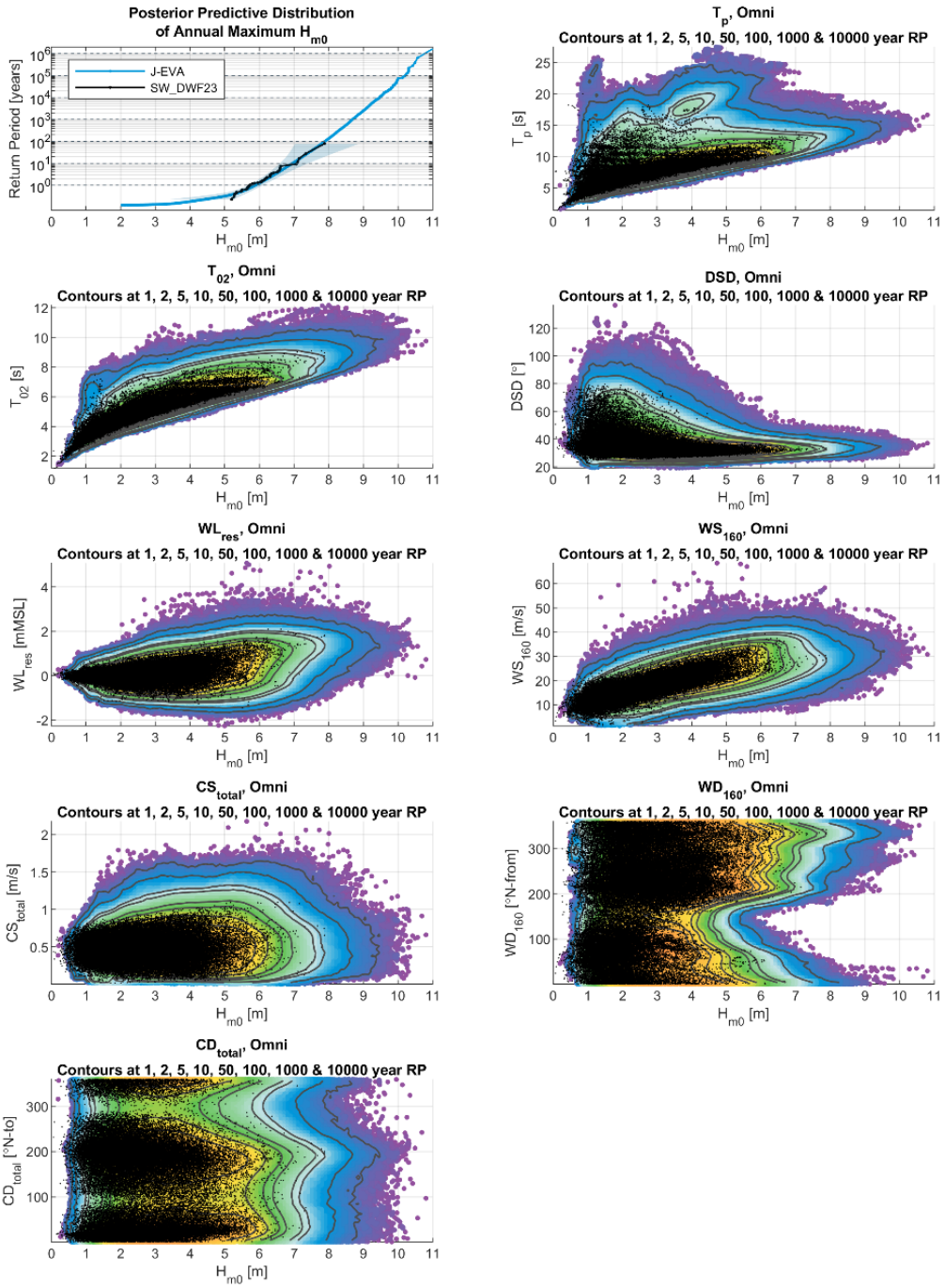

Figure 4.46 Estimates of marginal and conditioned variables from 50,000-year simulation at IJV1.

Hindcast data is presented as black markers. The blue solid line (top left) is the posterior predictive distribution. The blue shaded area (op left) is the 2.5-97.5 % credible interval. Contours of conditioned variables shown as coloured dots from the results if a simulation of $5x10^6$ years using the posterior predictive distribution at different return periods are shown for T_p (top right), T_{02} (second row left), DSD (second row right), WL_{res} (third row left), WS_{160} (third row right), CS_{total} (fourth row left), WD_{160} (fourth row right) and CD_{total} (last row left) against H_{m0}. Black dots show original hindcast. Warmer colours indicate a higher density of points.

4.4.2.1 T_p conditioned on H_{m0}

Figure 4.47 shows the extreme H_{m0} for each return period against T_p and fit based on (4.9), while Table 4.23 and Table 4.24 provide the 50 %-tiles of T_p conditioned on H_{m0} at IJV1 for directional and monthly sectors respectively.

The 5, 50, and 95%-tile values at IJV1 are provided in the digital appendix attached to this report.

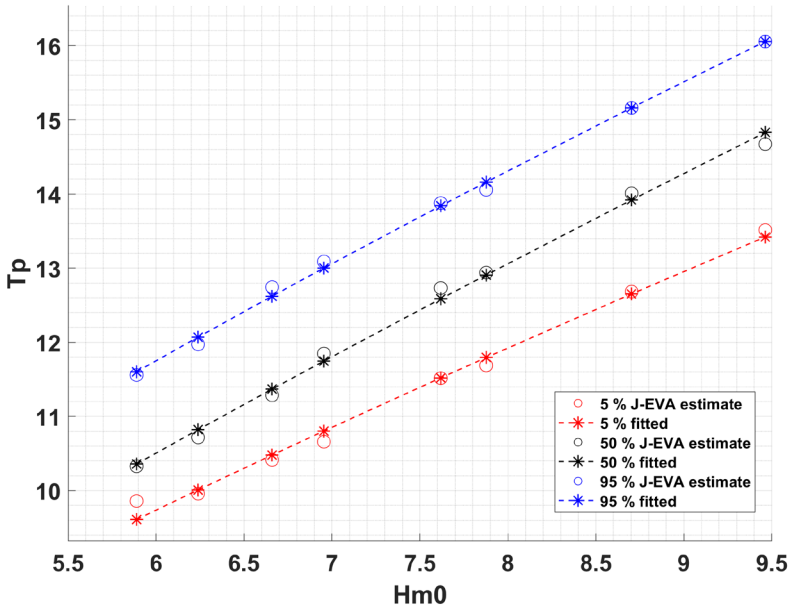

Figure 4.47 Omni-directional T_p conditioned on H_{m0} at IJV1.
T_p associated to extreme H_{m0} for return period 1- to 10000-year from the J-EVA model are shown in as “o” for 5%, 50% and 95%. Polynomial fit to the J-EVA model results are shown as “*” on the dashed line.

Table 4.23 Directional extremes of T_p conditioned on H_{m0} at IJV1.
All water levels are considered.

30° Directional Associated Peak Wave Period, T_p [s] 50%								
Direction (PWD [°N-from])	Return Period [years]							
	1	2	5	10	50	100	1000	10000
Omni	10.4	10.8	11.4	11.7	12.6	12.9	13.9	14.8
0	9.9	10.4	11.1	11.6	12.4	12.7	13.5	14.2
30	8.3	8.9	9.6	10.0	10.9	11.2	12.0	12.7
60	7.4	8.1	8.7	9.1	10.0	10.2	11.1	11.8
90	6.5	7.1	7.5	7.8	8.3	8.5	9.0	9.4
120	6.4	6.8	7.2	7.6	8.0	8.2	8.6	9.0
150	6.9	7.4	7.7	8.0	8.4	8.6	9.0	9.4
180	8.5	8.9	9.2	9.5	10.0	10.2	10.8	11.3
210	9.7	10.0	10.3	10.6	11.0	11.2	11.7	12.1
240	9.3	9.6	10.0	10.3	10.8	10.9	11.5	12.1
270	9.2	9.6	10.0	10.3	10.9	11.1	11.8	12.4
300	9.8	10.2	10.7	11.0	11.6	11.8	12.5	13.1
330	10.4	11.0	11.7	12.1	12.9	13.1	13.9	14.6

Table 4.24 Monthly extremes of T_p conditioned on H_{m0} at IJV1.
All water levels are considered.

Monthly Associated Peak Wave Period, T_p [s] 50%								
Month	Return Period [years]							
	1	2	5	10	50	100	1000	10000
Omni	10.4	10.8	11.4	11.7	12.6	12.9	13.9	14.8
Jan	9.3	9.9	10.5	10.9	11.8	12.1	13.1	14.0
Feb	9.3	9.8	10.5	10.9	11.7	12.1	13.1	13.9
Mar	8.5	9.2	10.0	10.5	11.5	12.0	13.2	14.3
Apr	7.7	8.5	9.3	9.8	10.9	11.4	12.5	13.5
May	7.4	8.0	8.9	9.4	10.5	10.9	12.0	12.9
Jun	7.1	7.9	8.7	9.2	10.2	10.5	11.6	12.4
Jul	7.5	8.0	8.7	9.2	10.0	10.3	11.1	11.8
Aug	7.6	8.3	9.0	9.5	10.3	10.6	11.5	12.2
Sep	8.4	9.0	9.7	10.1	10.9	11.2	12.0	12.8
Oct	8.8	9.4	10.1	10.6	11.4	11.7	12.6	13.4
Nov	9.1	9.8	10.4	10.9	11.7	12.1	13.0	13.8
Dec	9.4	9.9	10.6	11.0	11.9	12.2	13.3	14.2

T_{02} conditioned on H_{m0}

Figure 4.48 shows the extreme H_{m0} for each return period against T_{02} and fit based on (4.9), while Table 4.25 and Table 4.26 provide the 50 %-tiles of T_{02} conditioned on H_{m0} at IJV1 for directional and monthly sectors respectively.

The 5, 50, and 95%-tile values at IJV1 are provided in the digital appendix attached to this report.

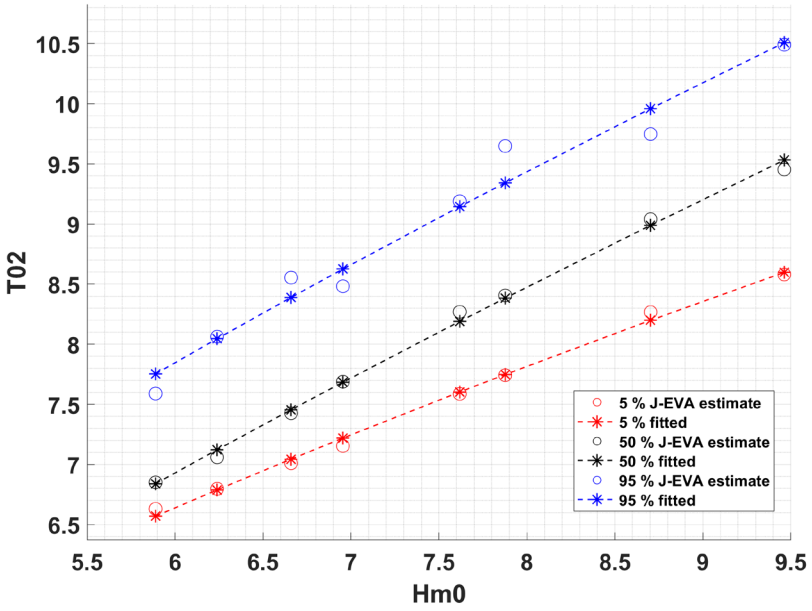

Figure 4.48 Omni-directional T_{02} conditioned on H_{m0} at IJV1.
T_{02} associated to extreme H_{m0} for return period 1- to 10000-year from the J-EVA model are shown in as "o" for 5%, 50% and 95%. Polynomial fit to the J-EVA model results are shown as "*" on the dashed line.

Table 4.25 Directional extremes of T_{02} conditioned on H_{m0} at IJV1.
All water levels are considered.

30° Directional Associated Mean Zero-Crossing Wave Period, T_{02} [s] 50%								
Direction (PWD [°N-from])	Return Period [years]							
	1	2	5	10	50	100	1000	10000
Omni	6.8	7.1	7.5	7.7	8.2	8.4	9.0	9.5
0	6.5	6.9	7.4	7.6	8.1	8.3	8.8	9.2
30	5.6	5.9	6.3	6.5	7.0	7.1	7.6	7.9
60	5.1	5.4	5.8	6.0	6.5	6.6	7.1	7.4
90	4.7	5.0	5.3	5.5	5.8	5.9	6.2	6.5
120	4.6	4.9	5.1	5.3	5.6	5.7	6.0	6.2
150	4.8	5.2	5.4	5.6	5.8	5.9	6.2	6.4
180	5.8	6.0	6.3	6.4	6.7	6.8	7.1	7.4
210	6.5	6.6	6.8	7.0	7.2	7.3	7.5	7.8
240	6.3	6.5	6.7	6.8	7.1	7.2	7.5	7.8
270	6.3	6.5	6.8	7.0	7.3	7.4	7.7	8.1
300	6.6	6.9	7.1	7.3	7.7	7.8	8.2	8.5
330	6.9	7.3	7.7	7.9	8.4	8.6	9.0	9.4

Table 4.26 Monthly extremes of T_{02} conditioned on H_{m0} at IJV1.
All water levels are considered.

Monthly Associated Mean Zero-Crossing Wave Period, T_{02} [s] 50%								
	Return Period [years]							
Month	1	2	5	10	50	100	1000	10000
Omni	6.8	7.1	7.5	7.7	8.2	8.4	9.0	9.5
Jan	6.2	6.6	7.0	7.2	7.7	7.9	8.5	9.1
Feb	6.2	6.6	6.9	7.2	7.7	7.9	8.5	8.9
Mar	5.8	6.2	6.7	6.9	7.6	7.8	8.5	9.2
Apr	5.3	5.8	6.3	6.6	7.3	7.6	8.3	8.9
May	5.1	5.5	6.0	6.3	7.0	7.2	7.9	8.4
Jun	4.9	5.4	5.9	6.1	6.7	6.9	7.5	7.9
Jul	5.1	5.5	5.9	6.1	6.6	6.8	7.2	7.6
Aug	5.3	5.7	6.1	6.3	6.8	7.0	7.4	7.9
Sep	5.7	6.1	6.5	6.7	7.2	7.3	7.8	8.3
Oct	6.0	6.3	6.7	7.0	7.5	7.6	8.1	8.6
Nov	6.1	6.5	6.9	7.2	7.7	7.9	8.5	8.9
Dec	6.3	6.6	7.0	7.3	7.9	8.1	8.8	9.3

4.4.2.2 WL_{tot} conditioned on H_{m0}

Figure 4.49 shows the extreme H_{m0} for each return period against WL_{tot} and fit based on (4.10), while Table 4.27 provides the 5 %-, 50 %- and 95 %-tiles of WL_{tot} conditioned on H_{m0} at IJV1 for omni-directional.

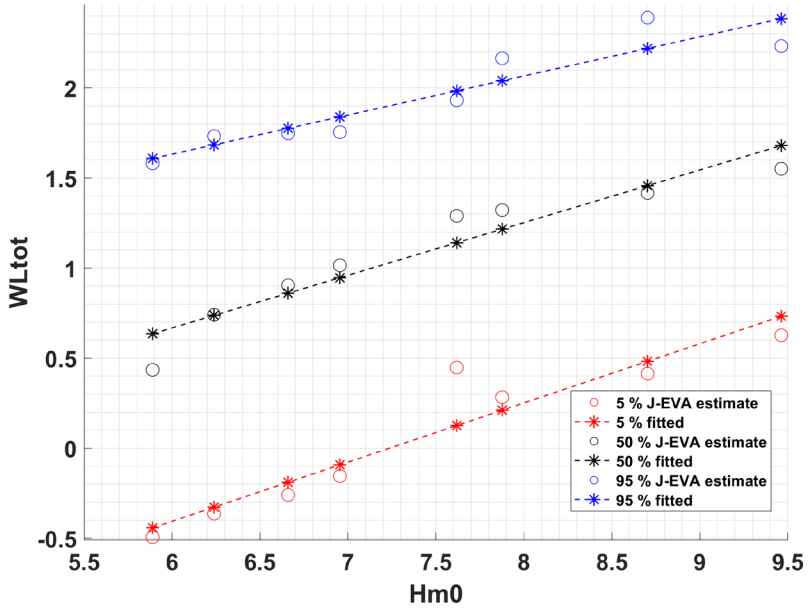

Figure 4.49 Omni-directional total water level conditioned on H_{m0} at IJV1
WL_{tot} associated to extreme H_{m0} for return period 1- to 10000-year from the J-EVA model are shown in as “o” for 5%, 50% and 95%. Polynomial fit to the J-EVA model results are shown as “*” on the dashed line.

Table 4.27 Omni-directional extremes of WL_{tot} conditioned on H_{m0} at IJV1. All water levels are considered.

Joint Probability, Omni-directional Associated values							
Return Periods [years]	H_{m0} [m]	H_{max} [m]	C_{max}, SWL [m]	C_{max}, MSL [m]	WL_{tot} [m], 5%	WL_{tot} [m], 50%	WL_{tot} [m], 95%
1	5.9	11.0	7.1	7.9	-0.4	0.6	1.6
2	6.2	11.7	7.6	8.5	-0.3	0.7	1.7
5	6.7	12.6	8.2	9.2	-0.2	0.9	1.8
10	7.0	13.2	8.6	9.8	-0.1	0.9	1.8
50	7.6	14.6	9.6	11.0	0.1	1.1	2.0
100	7.9	15.2	10.1	11.5	0.2	1.2	2.0
1000	8.7	17.0	11.5	13.0	0.5	1.5	2.2
10000	9.5	18.6	12.8	14.4	0.7	1.7	2.4

4.4.2.3 CS_{tot} conditioned on H_{m0}

Figure 4.50 shows the extreme H_{m0} for each return period against CS_{tot} and fit based on (4.9) while Table 4.28 provides the 5 %-, 50 %- and 95 %-tiles of CS_{tot} conditioned on H_{m0} at IJV1 for omni-directional. As no trend, or a decreasing trend is observed, a mean value has been applied instead of a power-low fit. No correlation is observed between CS_{tot} and H_{m0} because of the relatively strong tidal signal in the total current.

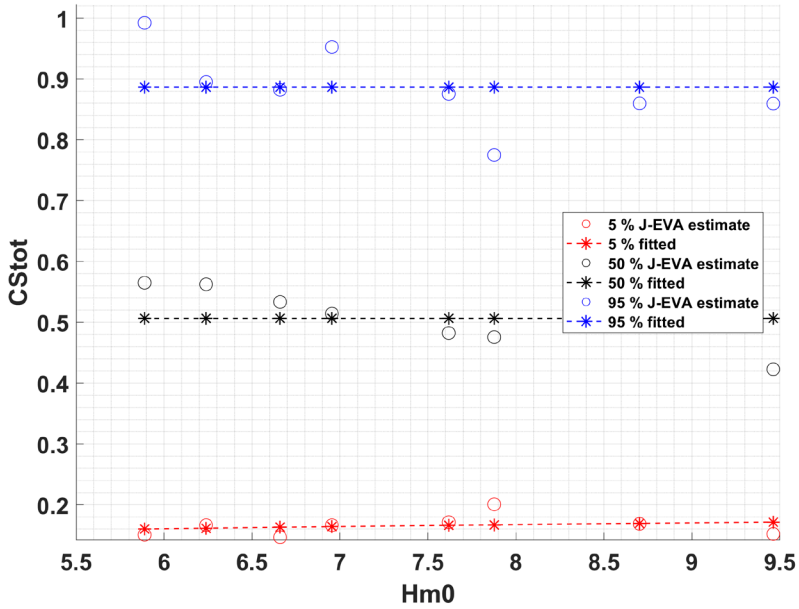

Figure 4.50 Omni-directional total current speed conditioned on H_{m0} at IJV1. CS_{tot} associated to extreme H_{m0} for return period 1- to 10000-year from the J-EVA model are shown in as “o” for 5%, 50% and 95%. Polynomial fit to the J-EVA model results are shown as “*” on the dashed line.

Table 4.28 Omni-directional extremes of CS_{tot} conditioned on H_{m0} at IJV1. All water levels are considered.

Joint Probability, Omni-directional Associated values							
Return Periods [years]	H_{m0} [m]	H_{max} [m]	C_{max}, SWL [m]	C_{max}, MSL [m]	CS_{tot} [m/s], 5%	CS_{tot} [m/s], 50%	CS_{tot} [m/s], 95%
1	5.9	11.0	7.1	7.9	0.2	0.5	0.9
2	6.2	11.7	7.6	8.5	0.2	0.5	0.9
5	6.7	12.6	8.2	9.2	0.2	0.5	0.9
10	7.0	13.2	8.6	9.8	0.2	0.5	0.9
50	7.6	14.6	9.6	11.0	0.2	0.5	0.9
100	7.9	15.2	10.1	11.5	0.2	0.5	0.9
1000	8.7	17.0	11.5	13.0	0.2	0.5	0.9
10000	9.5	18.6	12.8	14.4	0.2	0.5	0.9

4.4.2.4 WS_{160} conditioned on H_{m0}

As detailed in Section 4.1, a 7% increase to the extreme wind speed values is applied. This increase has also been applied to the associated wind speeds to extreme significant wave heights. Figure 4.51 shows the extreme H_{m0} for each return period against non-adjusted WS_{160} and fit based on (4.9). The same fit from (4.9) has been applied to the adjusted WS_{160}

Table 4.29 provides the 5 %-, 50 %- and 95 %-tiles of WS_{160}, both non-adjusted and adjusted, conditioned on H_{m0} at IJV1 for omni-directional.

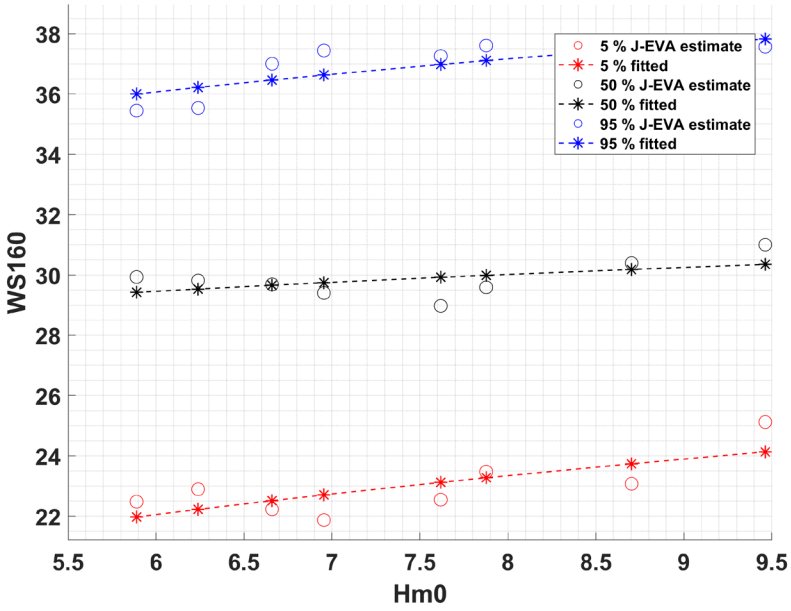

Figure 4.51 Omni-directional non-adjusted wind speed at 160m conditioned on H_{m0} at IJV1.

WS_{160} (non-adjusted) associated to extreme H_{m0} for return period 1- to 10000-year from the J-EVA model are shown in as “o” for 5%, 50% and 95%. Polynomial fit to the J-EVA model results are shown as “*” on the dashed line.

Table 4.29 Omni-directional extremes of WS_{160} conditioned on H_{m0} at IJV1.
All water levels are considered. Both non-adjusted and adjusted by 7% wind speeds at 160 m are provided.

Joint Probability, Omni-directional Associated values										
Return Periods [years]	H_{m0} [m]	H_{max} [m]	$C_{max,SWL}$ [m]	$C_{max,MSL}$ [m]	WS_{160} non-adjusted [m/s], 5%	WS_{160} non-adjusted [m/s], 50%	WS_{160} non-adjusted [m/s], 95%	WS_{160} adjusted by 7% [m/s], 5%	WS_{160} adjusted by 7% [m/s], 50%	WS_{160} adjusted by 7% [m/s], 95%
1	5.9	11.0	7.1	7.9	22.0	29.4	36.0	23.5	31.5	38.5
2	6.2	11.7	7.6	8.5	22.2	29.5	36.2	23.8	31.6	38.7
5	6.7	12.6	8.2	9.2	22.5	29.7	36.5	24.1	31.8	39.1
10	7.0	13.2	8.6	9.8	22.7	29.7	36.6	24.3	31.8	39.2
50	7.6	14.6	9.6	11.0	23.1	29.9	37.0	24.7	32.0	39.6
100	7.9	15.2	10.1	11.5	23.3	30.0	37.1	24.9	32.1	39.7
1000	8.7	17.0	11.5	13.0	23.7	30.2	37.5	25.4	32.3	40.1
10000	9.5	18.6	12.8	14.4	24.1	30.3	37.8	25.8	32.4	40.4

4.4.3 Extreme maximum wave height, H_{max}

For conservative reasons, the extreme maximum wave height, H_{max}, was derived using Forristall short-term distribution [41]. The difference between the values of H_{max} derived from Glukhovskiy [42] and from Forristall are shown in Table 4.30, hence using Gluskhovskiy short-term distribution would lead to slightly smaller maximum individual wave height values for the higher return periods.

Table 4.30 Difference between $H_{max,Glukhovskiy}$ and $H_{max,Forristall}$ at IJV1
Difference = $H_{max,Forristall} - H_{max,Glukhovskiy}$. Results are given for omni-directional and considering all water levels.

Return periods [years]	1	50	10000
Difference [m]	-0.1	0.3	0.9

The directional extreme results for H_{max} at IJV1 are provided in Table 4.31.

The most extreme conditions are observed for peak wave direction coming from northwest (330°N-from), which aligns with the observations made for extreme significant wave height (see Section 4.4.1).

Table 4.32 summarises the monthly extreme H_{max} for all water levels. Similarly, to the H_{m0}, the most extreme conditions are observed during the winter.

Table 4.31 Directional extreme maximum individual wave height at IJV1
Extreme results considering all water levels.

30° Directional Extreme Maximum Wave Height, H_{max} [m]								
Direction (PWD [°N-from])	Return Period [years]							
	1	2	5	10	50	100	1000	10000
Omni	11.0	11.7	12.6	13.2	14.6	15.2	17.0	18.6
0	7.9	8.9	10.1	10.9	12.4	13.1	14.9	16.6
30	6.3	7.3	8.4	9.1	10.7	11.3	12.9	14.3
60	5.8	6.7	7.7	8.3	9.8	10.3	11.9	13.2
90	5.2	6.1	6.9	7.4	8.4	8.8	10.1	11.3
120	4.8	5.6	6.3	6.9	8.0	8.4	9.6	10.6
150	5.3	6.1	6.9	7.4	8.4	8.8	9.9	11.0
180	7.8	8.4	9.2	9.7	10.8	11.2	12.6	14.0
210	9.8	10.4	11.2	11.7	12.9	13.3	14.7	16.1
240	9.1	9.8	10.7	11.3	12.6	13.1	14.6	16.1
270	9.3	10.1	11.0	11.6	13.0	13.5	15.3	17.0
300	9.3	10.1	11.1	11.7	13.1	13.6	15.4	17.0
330	9.3	10.3	11.6	12.4	14.1	14.7	16.7	18.4

Table 4.32 Monthly extreme maximum individual wave height at IJV1.
Extreme results considering all water levels.

Monthly Extreme Maximum Wave Height, H_{max} [m]								
	Return Period [years]							
Month	1	2	5	10	50	100	1000	10000
Omni	11.0	11.7	12.6	13.2	14.6	15.2	17.0	18.6
Jan	9.2	10.1	11.2	11.9	13.4	14.0	16.0	17.7
Feb	8.9	9.9	10.9	11.6	13.1	13.8	15.7	17.4
Mar	7.9	8.8	9.9	10.6	12.1	12.8	14.9	16.7
Apr	6.3	7.3	8.4	9.1	10.7	11.3	13.4	15.1
May	5.7	6.5	7.6	8.4	9.9	10.6	12.4	14.0
Jun	5.3	6.3	7.3	8.1	9.6	10.1	12.0	13.7
Jul	5.4	6.2	7.2	8.0	9.6	10.1	11.9	13.4
Aug	6.0	7.0	8.1	8.9	10.3	10.8	12.7	14.5
Sep	7.5	8.4	9.4	10.1	11.6	12.1	13.9	15.6
Oct	8.3	9.3	10.4	11.1	12.6	13.2	14.9	16.6
Nov	8.8	9.7	10.7	11.5	13.0	13.6	15.5	17.1
Dec	9.2	10.0	11.0	11.7	13.2	13.8	15.8	17.6

4.4.3.1 Associated wave period, T_{Hmax}

Figure 4.52 shows the extreme H_{max} for each return period against T_{Hmax} and fit based on (4.7, while Table 4.33 and provide the 50%-tiles of T_{Hmax} conditioned on H_{max} at IJV1 for directional and monthly sectors respectively.

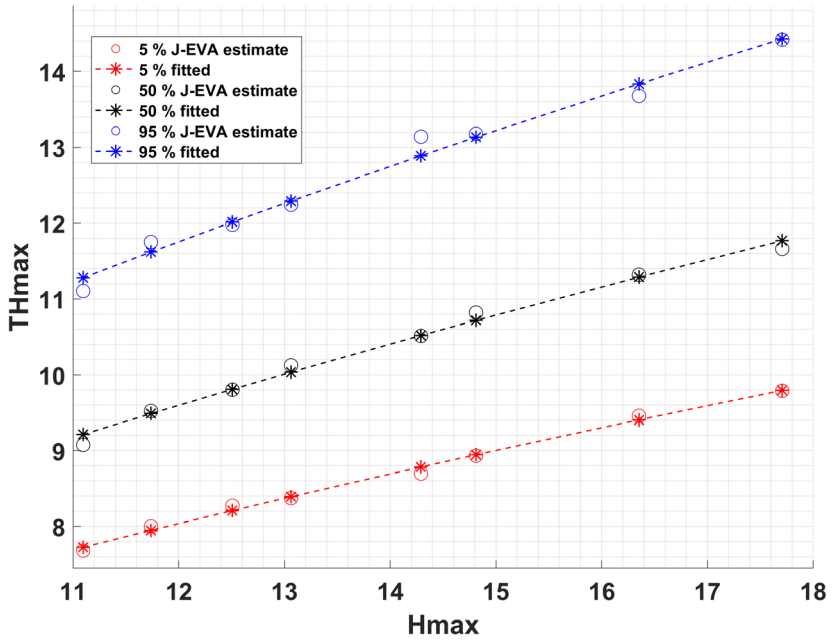

Figure 4.52 Omni-directional T_{Hmax} conditioned on H_{max} at IJV1.
T_{Hmax} associated to extreme H_{max} for return period 1- to 10000-year from the J-EVA model are shown in as “o” for 5%, 50% and 95%. Polynomial fit to the J-EVA model results are shown as “*” on the dashed line.

Table 4.33 Directional extremes of T_{Hmax} conditioned on H_{max} at IJV1.
All water levels are considered.

30° Directional Associated Period, T_{Hmax} [s] 50%								
Direction (PWD [°N-from])	Return Period [years]							
	1	2	5	10	50	100	1000	10000
Omni	9.2	9.5	9.8	10.0	10.5	10.7	11.3	11.9
0	8.7	9.2	9.7	10.0	10.5	10.7	11.4	11.9
30	7.5	7.9	8.4	8.7	9.3	9.6	10.1	10.6
60	6.7	7.1	7.6	7.9	8.5	8.8	9.4	9.8
90	6.1	6.5	6.8	7.0	7.4	7.5	7.9	8.2
120	6.0	6.3	6.6	6.8	7.2	7.3	7.7	8.0
150	6.3	6.7	7.0	7.1	7.5	7.6	7.9	8.2
180	7.6	7.9	8.1	8.3	8.6	8.8	9.2	9.5
210	8.7	8.8	9.0	9.2	9.5	9.6	9.9	10.2
240	8.3	8.5	8.8	9.0	9.3	9.5	9.9	10.2
270	8.3	8.6	8.9	9.1	9.5	9.7	10.1	10.6
300	8.7	9.0	9.3	9.5	9.9	10.1	10.6	11.0
330	9.2	9.6	10.1	10.4	10.9	11.1	11.7	12.1

Table 4.34 Monthly extremes of T_{Hmax} conditioned on H_{max} at IJV1.
All water levels are considered.

Monthly Associated Period, T_{Hmax} [s] 50%								
Month	Return Period [years]							
	1	2	5	10	50	100	1000	10000
Omni	9.2	9.5	9.8	10.0	10.5	10.7	11.3	11.9
Jan	8.4	8.8	9.2	9.5	10.1	10.3	11.0	11.6
Feb	8.2	8.7	9.1	9.4	10.0	10.3	11.0	11.6
Mar	7.7	8.2	8.8	9.1	9.8	10.1	11.1	11.8
Apr	7.0	7.6	8.2	8.6	9.4	9.7	10.6	11.4
May	6.8	7.2	7.9	8.3	9.0	9.3	10.1	10.8
Jun	6.5	7.1	7.7	8.1	8.9	9.1	10.0	10.7
Jul	6.7	7.1	7.6	8.0	8.7	8.9	9.6	10.1
Aug	6.9	7.4	8.0	8.3	9.0	9.2	9.9	10.6
Sep	7.7	8.1	8.5	8.8	9.4	9.6	10.2	10.8
Oct	7.9	8.4	8.9	9.2	9.8	10.0	10.7	11.3
Nov	8.3	8.7	9.1	9.4	10.0	10.3	10.9	11.5
Dec	8.3	8.7	9.2	9.5	10.1	10.3	11.1	11.8

4.4.4 Extreme maximum wave crest, C_{max}

The extreme maximum wave crest, C_{max}, were derived based on the Forristall short-term wave height distribution [41].

The maximum wave crest is given relative to still water level (SWL) and relative to mean sea level (MSL). The latter, $C_{max,MSL}$, is derived by convoluting the short-term distribution with the simultaneous residual water level.
The directional and monthly extreme results for the maximum crest height relative to SWL, $C_{max,SWL}$, are summarised in Table 4.35 and Table 4.36 respectively. The directional and monthly extreme results for the maximum crest height relative to MSL, $C_{max,MSL}$ are summarised in Table 4.37 and Table 4.38. The values relative to MSL are always larger than the crest heights relative to SWL, as expected, except for the non-dominant sectors, i.e., between 60 and 150 °N-from due to the short fetch to land resulting in less positive storm surge associated with storms from these directions. Similarly, to extreme significant wave height and maximum individual wave height, the dominant sectors for $C_{max,MSL}$ and $C_{max,SWL}$ is the 330 °N sector, and during the winter.

Table 4.35 Directional extreme maximum crest height relative to SWL at IJV1.
Extreme results considering all water levels.

30° Directional Extreme Maximum Crest Height, SWL, C_{max}, SWL [m]								
Direction (PWD [°N-from])	Return Period [years]							
	1	2	5	10	50	100	1000	10000
Omni	7.1	7.6	8.2	8.6	9.6	10.1	11.5	12.8
0	4.9	5.6	6.4	6.9	8.0	8.5	9.9	11.3
30	3.9	4.5	5.2	5.8	6.8	7.2	8.4	9.5
60	3.6	4.2	4.8	5.3	6.2	6.6	7.7	8.7
90	3.3	3.8	4.4	4.7	5.4	5.7	6.6	7.4
120	3.0	3.5	4.0	4.4	5.1	5.4	6.2	7.0
150	3.3	3.8	4.4	4.7	5.4	5.7	6.5	7.2
180	4.9	5.4	5.9	6.2	7.0	7.3	8.3	9.3
210	6.3	6.7	7.3	7.6	8.5	8.8	9.9	10.9
240	5.8	6.3	6.9	7.3	8.2	8.6	9.8	10.9
270	5.9	6.4	7.1	7.5	8.5	8.9	10.2	11.6
300	5.8	6.4	7.1	7.5	8.5	8.9	10.2	11.5
330	5.8	6.5	7.4	8.0	9.2	9.7	11.2	12.6

Table 4.36 Monthly extreme maximum crest height relative to SWL at IJV1.
Extreme results considering all water levels.

Monthly Extreme Maximum Crest Height, SWL, C_{max}, SWL [m]								
	Return Period [years]							
Month	1	2	5	10	50	100	1000	10000
Omni	7.1	7.6	8.2	8.6	9.6	10.1	11.5	12.8
Jan	5.9	6.5	7.2	7.7	8.8	9.2	10.7	12.1
Feb	5.6	6.3	7.0	7.5	8.6	9.1	10.5	11.9
Mar	5.0	5.6	6.3	6.8	7.8	8.3	9.9	11.3
Apr	3.9	4.6	5.3	5.8	6.8	7.3	8.7	10.0
May	3.6	4.1	4.8	5.3	6.3	6.7	8.0	9.2
Jun	3.3	3.9	4.6	5.1	6.1	6.5	7.8	9.0
Jul	3.3	3.8	4.5	5.0	6.1	6.5	7.7	8.8
Aug	3.8	4.4	5.1	5.6	6.6	6.9	8.3	9.6
Sep	4.7	5.3	6.0	6.5	7.5	7.9	9.1	10.4
Oct	5.2	5.9	6.6	7.1	8.2	8.6	9.9	11.2
Nov	5.6	6.2	6.9	7.4	8.5	9.0	10.3	11.6
Dec	5.8	6.4	7.1	7.6	8.6	9.1	10.6	12.0

Table 4.37 Directional extreme maximum crest height relative to MSL at IJV1.
Extreme results considering all water levels.

30° Directional Extreme Maximum Crest Height, MSL, C_{max}, MSL [m]								
	Return Period [years]							
Direction (PWD [°N-from])	1	2	5	10	50	100	1000	10000
Omni	7.9	8.5	9.2	9.8	11.0	11.5	13.0	14.4
0	5.5	6.2	7.1	7.7	9.0	9.5	11.1	12.5
30	4.1	4.7	5.4	5.9	7.0	7.5	8.6	9.8
60	3.6	4.1	4.7	5.2	6.1	6.5	7.6	8.6
90	3.2	3.7	4.1	4.5	5.2	5.4	6.3	7.0
120	2.8	3.3	3.8	4.2	4.9	5.2	5.9	6.6
150	3.2	3.7	4.3	4.6	5.3	5.6	6.4	7.2
180	4.9	5.4	5.9	6.3	7.1	7.4	8.5	9.6
210	6.5	6.9	7.5	7.8	8.7	9.0	10.1	11.2
240	6.3	6.8	7.4	7.9	8.9	9.3	10.5	11.7
270	6.7	7.4	8.1	8.6	9.6	10.0	11.4	12.9
300	6.8	7.5	8.3	8.8	10.0	10.4	11.8	13.2
330	6.7	7.5	8.6	9.2	10.6	11.2	12.8	14.3

Table 4.38 Monthly extreme maximum crest height relative to MSL at IJV1. Extreme results considering all water levels.

Monthly Extreme Maximum Crest Height, MSL, C_{max}, MSL [m]								
	Return Period [years]							
Month	1	2	5	10	50	100	1000	10000
Omni	7.9	8.5	9.2	9.8	11.0	11.5	13.0	14.4
Jan	6.4	7.1	8.0	8.6	9.9	10.5	12.2	13.7
Feb	6.1	7.0	7.8	8.4	9.8	10.3	11.9	13.3
Mar	5.4	6.1	6.9	7.5	8.9	9.4	11.3	12.9
Apr	4.2	4.9	5.7	6.3	7.6	8.2	9.9	11.3
May	3.8	4.4	5.1	5.7	6.9	7.4	8.8	10.1
Jun	3.6	4.2	4.9	5.5	6.6	7.0	8.4	9.6
Jul	3.7	4.2	4.9	5.5	6.7	7.1	8.4	9.5
Aug	4.1	4.7	5.6	6.1	7.2	7.6	9.0	10.3
Sep	5.1	5.8	6.6	7.1	8.2	8.6	10.0	11.4
Oct	5.7	6.5	7.4	8.0	9.2	9.7	11.2	12.6
Nov	6.1	6.8	7.7	8.3	9.6	10.2	11.7	13.2
Dec	6.3	7.0	7.8	8.5	9.7	10.3	11.9	13.6

4.4.5 Wave breaking, P_{break}

No explicit individual wave breaking probability distribution exists, but the limiting breaking height formulation by [43] is a generally accepted approximation for the wave height limit at intermediate water depths, where the wave breaking is a function of both wave steepness and wave height to water depth ratio. This approach is adopted in J-EVA. The individual wave height limit, H_b, is given by:

$$\frac{H_b}{L_0} = A\left\{1 - \exp\left(-1.5\frac{\pi d}{L_0}\left(1 + 11\tan^{4/3}\theta\right)\right)\right\} \quad \textbf{(4.11)}$$

where L_0 is the deep-water wavelength, d the water depth and θ the seabed slope. The randomness of irregular sea is accounted for by the proportionality index A, which is varying from 0.12 to 0.18, according to [43].

The breaker height formulation by [43] has been combined with the extreme value estimates of individual wave height (H_{max} and T_{Hmax}) to predict the probability that the maximum waves are breaking. Based on [43], we assume the breaking probability to vary linearly from 0 at A = 0.12 to 1 at A = 0.18. The probability P_{break} that an individual wave of height H_{max} and period T_{Hmax} is breaking is estimated from:

$$P_{break} = \begin{cases} 0 & A \le 0.12 \\ \dfrac{A}{0.06} - 2 & 0.12 < A \le 0.18 \\ 1 & A > 0.18 \end{cases} \quad \textbf{(4.12)}$$

A qualitative statement on the frequency of occurrence is made at IJV1. Table 4.39 and Table 4.40 provides the directional and monthly wave breaking probability P_{break}.

Table 4.39 Directional Wave Breaking Probability, P_{break} at analysis location IJV1.

30° Directional Wave Breaking Probability, Pbreak [-]								
Direction (PWD [°N-from])	Return Period [years]							
	1	2	5	10	50	100	1000	10000
Omni	0.4	0.4	0.5	0.5	0.7	0.7	0.9	1.0
0	0.1	0.1	0.1	0.2	0.3	0.4	0.6	0.9
30	0.0	0.0	0.1	0.1	0.2	0.3	0.5	0.7
60	0.0	0.0	0.1	0.1	0.2	0.3	0.4	0.7
90	0.0	0.1	0.1	0.1	0.2	0.3	0.4	0.7
120	0.0	0.0	0.1	0.1	0.2	0.2	0.4	0.6
150	0.0	0.0	0.1	0.1	0.2	0.2	0.4	0.6
180	0.1	0.2	0.2	0.2	0.4	0.4	0.6	0.9
210	0.3	0.3	0.4	0.5	0.6	0.6	0.8	1.1
240	0.2	0.3	0.3	0.4	0.5	0.6	0.8	1.0
270	0.2	0.3	0.4	0.4	0.5	0.6	0.8	1.1
300	0.2	0.2	0.3	0.3	0.5	0.5	0.7	1.0
330	0.1	0.2	0.3	0.3	0.5	0.5	0.8	1.1

Table 4.40 Monthly Wave Breaking Probability, P_{break} at analysis location IJV1.

Monthly Wave Breaking Probability, Pbreak [-]								
	Return Period [years]							
Month	1	2	5	10	50	100	1000	10000
Omni	0.4	0.4	0.5	0.5	0.7	0.7	0.9	1.0
Jan	0.2	0.3	0.3	0.4	0.5	0.6	0.8	1.0
Feb	0.2	0.2	0.3	0.4	0.5	0.6	0.8	1.0
Mar	0.1	0.1	0.2	0.2	0.4	0.4	0.6	0.9
Apr	0.0	0.1	0.1	0.1	0.2	0.2	0.5	0.7
May	0.0	0.0	0.0	0.1	0.1	0.2	0.4	0.6
Jun	0.0	0.0	0.0	0.1	0.1	0.2	0.3	0.6
Jul	0.0	0.0	0.0	0.1	0.1	0.2	0.4	0.6
Aug	0.0	0.1	0.1	0.1	0.2	0.3	0.4	0.7
Sep	0.1	0.1	0.2	0.2	0.3	0.4	0.6	0.9
Oct	0.1	0.2	0.3	0.3	0.4	0.5	0.7	0.9
Nov	0.2	0.2	0.3	0.3	0.5	0.5	0.7	1.0
Dec	0.2	0.3	0.3	0.4	0.5	0.6	0.8	1.0

4.5 Other parameters: rainfall

Extreme condition analysis was performed for the rainfall intensity at IJV1 for the period 1979-01-15 to 2022-12-31, based on the data from the WRF dataset. The sensitivity test for the extreme value analyses were run for the 44 years of data for rainfall at IJV1 using different distribution fits for 100-year extreme. The considered distributions for rainfall conditions include 2-parameter Truncated Weibull, 2-parameter Weibull, exponential and generalized pareto distributions with both Least Squares (LS) and Maximum Likelihood (ML) estimations for average annual peak (AAP) of 0.5 to 5.

Testing against different candidate distributions of which 2-parameter Truncated Weibull distribution using the LS estimation with AAP of 2 seemed to perform the best fit.

1-, 5-, 10-, 50-, and 100-year extreme for the rainfall extremes 1h duration was performed and presented in Figure 4.53. The extreme values for rainfall are presented in Table 4.41.

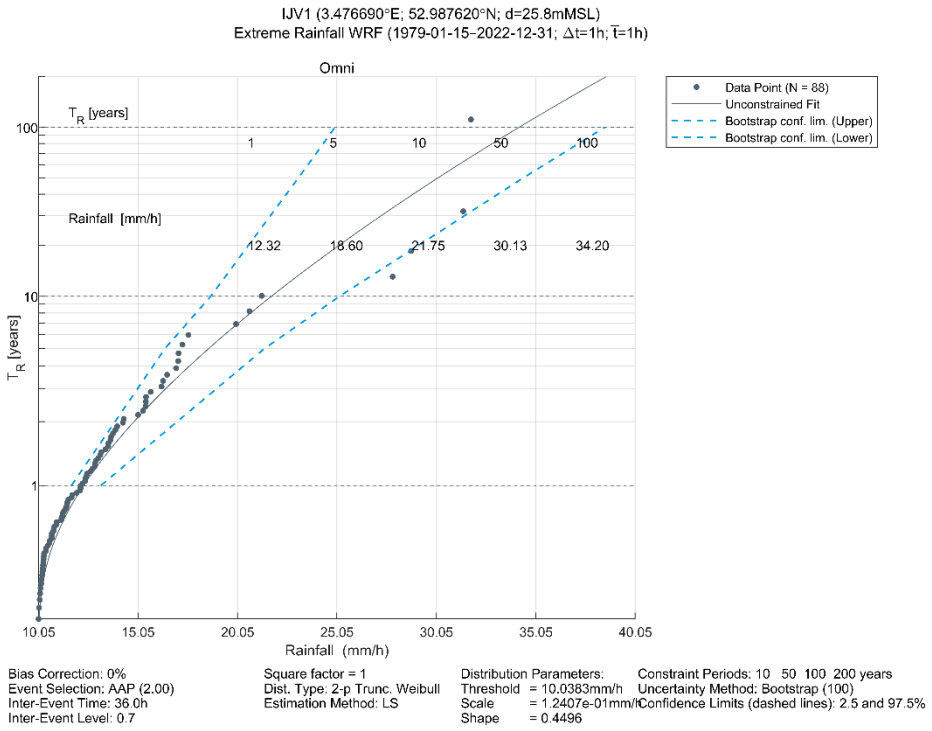

Figure 4.53 Estimate of extreme rainfall at analysis point IJV1 for 1-, 5-, 10-, 50-, and 100-year extreme.
2-p Truncated Weibull distribution fitted to rainfall data along with the extreme values at different return period [years]. 2.5% and 97.5% confidence bounds are shown with dashed blue line.

Table 4.41 Estimate of extreme rainfall at IJV1.

Rainfall [mm/h]	Return period [years]				
	1	5	10	50	100
Omni Lower bnd	11.7	16.4	18.7	23.1	25.0
Omni Central Est.	12.3	18.6	21.8	30.1	34.2
Omni Upper bnd	13.2	21.4	25.2	34.4	38.5

5 Differences in the Metocean Conditions with Previous Studies in the Area

A feasibility study of the IJVWFZ has been conducted earlier by DHI [44], where extreme value analysis with J-EVA was carried out at an analysis location IJV (3.700593°, 52.936914°) to the east of the IJV1 location analysed in this study (see Figure 5.1). The water depth at IJV is 24.8 mMSL, whereas that at IJV1 is 25.8 mMSL (see Table 2.1). The aim of this section is to summarize the main differences in the normal and extreme conditions between the analysis point IJV from the earlier study [44] and IJV1 in the current study.

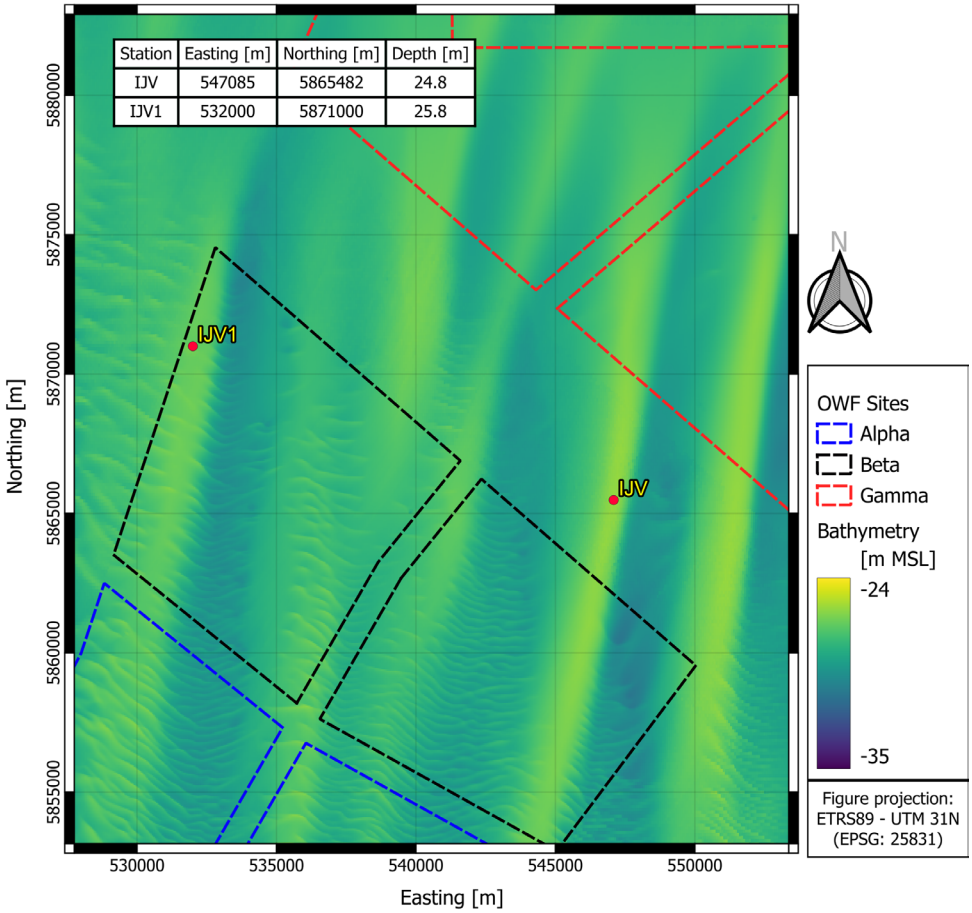

Figure 5.1 Location of the analysis points IJV and IJV1.
The wind farm zones contain the local survey bathymetry. The bathymetry outside the wind farm zones is filled with EMODnet. Comparison of EMODnet and local survey bathymetry is provided in [3].

Two major differences between the earlier study [44] and the current study are noted.

1. The present study uses a novel approach, where the same wind model is used for the WRA and forcing the HD and SW (ocean) models resulting in a unified WRA-metocean modelling and analysis approach.
2. A high resolution WRF model has been developed and used in this study, whereas the global reanalysis model, CFSR (CFSv2 from 2011,

from here on named CFSR from period 1979-2023), with coarser resolution was used in [44].

Differences and improvements in the modelling compared to earlier studies is provided in section 6 of [3].

5.1 Normal conditions summary

This section provides a summary of the differences in the normal conditions at IJV and IJV1 for wind, water levels, currents, and waves.

5.1.1 Wind

Figure 5.2 shows the wind rose at IJV (100 mMSL) and IJV1 (160 mMSL). The wind roses are very similar to each other, both in terms of directions and frequency of occurrence, despite using two different wind models, i.e., CFSR at IJV and WRF at IJV1. Differences in wind directions due to height differences is considered negligible.

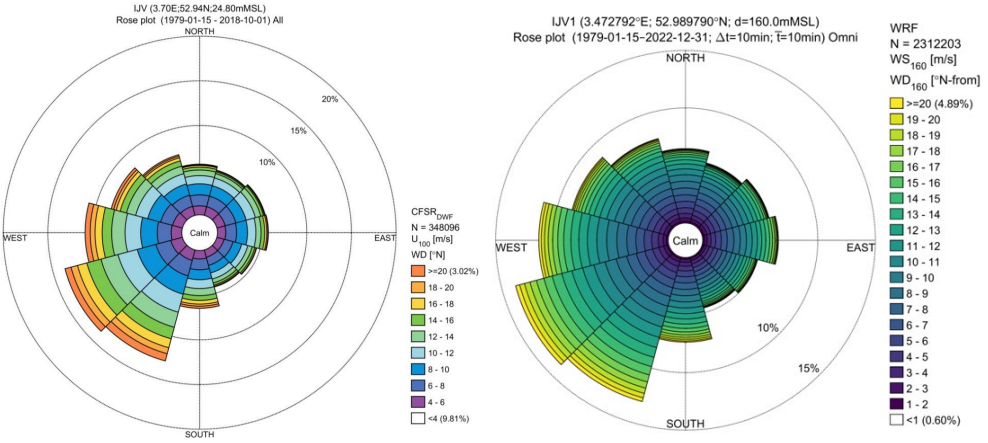

Figure 5.2 Wind rose plots using of WS_{100} – WD_{100} at IJV (left) and WS_{160} – WD_{160} IJV1 (right).

Table 5.1 provides the annual statistics for WS_{160} at IJV and IJV1. The mean wind speeds are very similar to each other. However, a notable difference is the modelled maximum wind speed, which is 2.3 m/s larger at IJV1 than at IJV. It is noted that WS_{160} at IJV was obtained by applying a power law (see section 6.5 in [2]) to the 10 mMSL modelled CFSR time series using $\alpha = 0.075$ (see section 3.3.1.4 in [44]). At IJV1, WS_{160} is directly an output of the model, where the winds are obtained at different pressure levels, and subsequently interpolated to different heights, amongst others, at 160 m.

Table 5.1 Main statistics of WS_{160} at IJV and IJV1.

Analysis Point	Parameter	Mean [m/s]	Min [m/s]	Max [m/s]	Std [m/s]
IJV	WS_{160}	10.2	0	37.2	4.9
IJV1		10.3	0.03	39.5	5.21

5.1.2 Water levels

Table 5.2 shows the differences in the astronomical tidal water levels at IJV and IJV1. The tidal levels are similar at both locations, particularly the HAT and LAT values. Smaller differences can be attributed to differences in the MIKE 21 Flow Model FM, where version 2017 (service pack 3) was used at IJV (see section 4.1 in [44]), whereas version 2022 is used at IJV1 (see section 3.2.1 in [3]). Furthermore, the tidal analysis at IJV included data assimilation between 1999 and 2017, whereas at IJV1, data assimilation is carried out for a larger period between 1993 and 2022.

Table 5.2 Tidal levels at IJV and IJV1 [mMSL].

Tidal levels	Analysis Point	
	IJV [mMSL]	IJV1 [mMSL]
HAT	0.8	0.89
MHWS	0.6	0.52
MHWN	0.4	0.22
MSL	0.0	0.00
MLWN	-0.5	-0.31
MLWS	-0.8	-0.66
LAT	-1.0	-0.90

5.1.3 Currents

Figure 5.3 shows the rose plots for total depth-averaged current speeds at IJV and IJV1. Considerable differences can be observed between IJV and IJV1, both in terms of directions and frequency of occurrence. At IJV, the currents are more dominated by the north-east and south-west sectors. Similar observations are made at IJV1, however, the frequency of occurrence in the dominant sectors is lower at IJV1 than at IJV. At IJV1, the north and the south sectors are also more significant than the same sectors at IJV. Differences in the current roses could be attributed to the differences in the background HD model as explained in section 5.1.2.

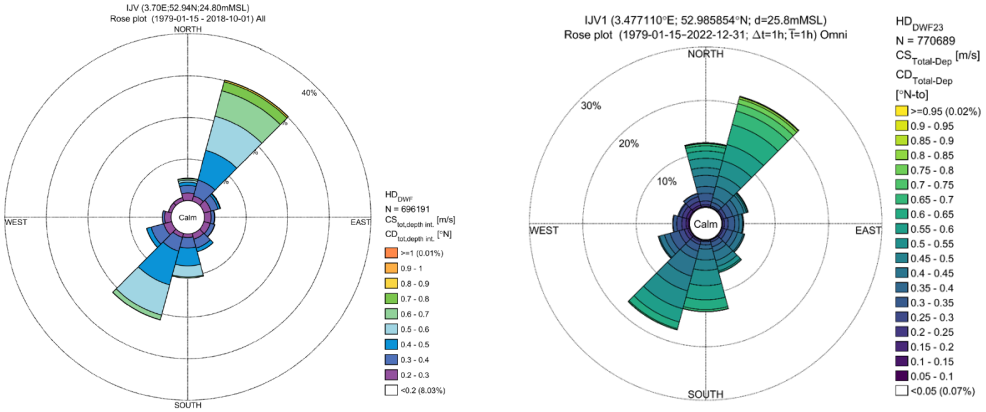

Figure 5.3 Current rose plots of $CS_{Total\text{-}Dep}$ – $CD_{Total\text{-}Dep}$ [m/s] at IJV (left) and IJV1 (right).

Table 5.3 shows the annual statistics of depth-averaged total current speeds at IJV and IJV1, which are quite similar at both sites. It is interesting to note that the annual statistics are only slightly impacted (up to ~15 cm/s) by the differences in the background HD model, as observed for the current roses in Figure 5.3.

Table 5.3 Main statistics of $CS_{Total-Dep}$, $CS_{Tide-Dep}$ and $CS_{Residual-Dep}$ [m/s] at IJV and IJV1.

Analysis Point	Parameter	Mean [m/s]	Min [m/s]	Max [m/s]	STD [m/s]
IJV	$CS_{Total-Dep}$	0.4	0.0	1.1	0.2
	$CS_{Tide-Dep}$	0.4	0.0	0.8	0.2
	$CS_{Residual-Dep}$	0.1	0.0	0.8	0.1
IJV1	$CS_{Total-Dep}$	0.44	0.00	1.10	0.14
	$CS_{Tide-Dep}$	0.43	0.08	0.87	0.14
	$CS_{Residual-Dep}$	0.08	0.00	0.94	0.06

5.1.4 Waves

Figure 5.4 shows the rose plots for total H_{m0} at IJV and IJV1. Like for the total current speeds, considerable differences can be observed between IJV and IJV1, both in terms of directions and frequency of occurrence. At IJV, the waves are more dominated by the north-west and south-west sectors, whereas the dominant sectors at IJV1 are north and south-west. The frequency of occurrence is also quite different at the two sites. Most of the waves occur in the dominant sectors at IJV1, whereas the waves are more spread out at IJV. Since the wind speed and direction are quite similar at the two sites, the differences in the wave roses are most likely due to the differences in the background MIKE 21 SW Spectral Wave FM Model, where version 2017 was used at IJV (see section 5.1 in [44]), whereas version 2022 is used at IJV1 (see section 3.3.1 in [3]). Also, differences in the local bathymetry could contribute to the difference.

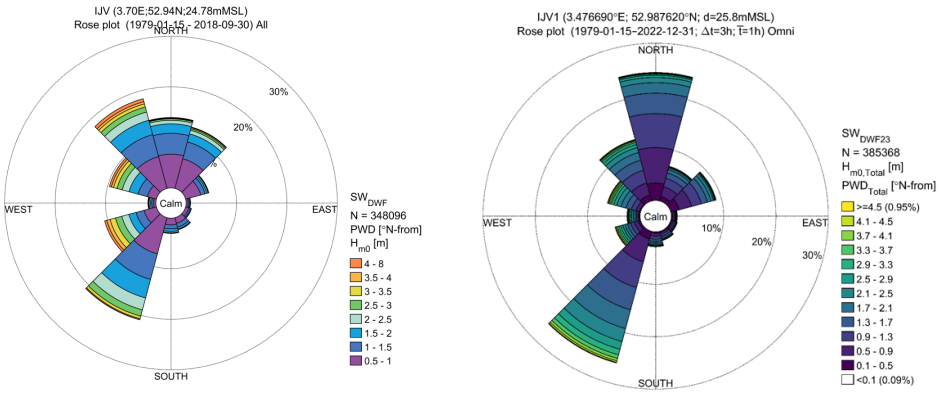

Figure 5.4 Wave rose of $H_{m0-Total}$ [m] at IJV (left) and IJV1 (right). PWD is used for plotting the rose.

Table 5.4 shows the annual statistics of total H_{m0} and the associated periods at IJV and IJV1, which are quite similar at both sites. It is interesting to note that the annual statistics are not impacted by the differences in the background SW model, as observed for the wave roses in Figure 5.4.

Table 5.4 Main statistics of $H_{m0\text{-}Total}$ [m], $T_{p\text{-}Total}$ [s], and $T_{01\text{-}Total}$ [s] at IJV and IJV1.

Analysis Point	Parameter	Mean [m/s]	Min [m/s]	Max [m/s]	STD [m/s]
IJV	$H_{m0\text{-}Total}$ [m]	1.44	0.05	8.31	0.91
	$T_{p\text{-}Total}$ [s]	6.86	1.12	28.57	2.72
	$T_{02\text{-}Total}$ [s]	4.10	1.07	9.79	1.09
IJV1	$H_{m0\text{-}Total}$ [m]	1.47	0.02	7.88	0.94
	$T_{p\text{-}Total}$ [s]	7.18	1.02	25.60	2.70
	$T_{02\text{-}Total}$ [s]	4.09	0.73	11.86	1.08

5.2 Extreme conditions summary

This section provides a summary of the differences in the extreme conditions at IJV and IJV1 for wind, water levels, currents, and waves. It is noted that the DHI's J-EVA method (see Appendix D) was applied in both studies to estimate the extreme conditions at IJV and IJV1. For uniformity, the comparisons are made up to a return period of 1000 years, since the 10000 years extreme values at IJV were only available for wave parameters.

5.2.1 Wind

Table 5.5 shows the omni-directional extreme wind speeds at IJV and IJV1 at 160 m height. There is a significant reduction (~10 – 11%) in the extreme wind speeds at IJV1 compared to those estimated at IJV. It is noted that the wind time series at IJV were modelled using CFSR data, which has a representative averaging period of 2 hours (see section 3.3.1.2 of [44]), whereas the WRF wind model used at IJV1 has a representative averaging period of 10 minutes (see section 3.1.1 of [3]). Therefore, larger extreme wind speeds at IJV seem counter-intuitive compared to those at IJV1. However, the following should be considered while comparing the extreme winds at the two sites.

1. CFSR winds are known to overestimate the wind peaks. Examples of peak ratios of around 12 % could be seen routinely when comparing with the measurements (see section 3.3.1.5 in [44]).
2. The extreme winds at IJV at 160 m height are obtained by applying two scaling factors to the estimated extreme winds at 10 m, which is the actual modelled output of the CFSR time series. Frøya scaling [11] is used to convert from 2-hours to 10-min wind speeds, whereas a shear coefficient of $\alpha = 0.1$ (see section 8.3.2 in [44]) is applied to convert from 10 m to 160 m wind speeds.

At IJV1, as described in section 4.1, overall, statistically the WRF model captures the storm peaks. The numbers provided in Table 5.5 are non-adjusted and including the 7% increase explained section 4.1.

Table 5.5 Omni-directional extreme 10 min wind speed at 160 mMSL, WS_{160}, at IJV and IJV1.
IJV1 omni-directional extreme 10 min values are given for non-adjusted and adjusted (by 7%) values.

Omni Extreme Wind Speed, WS_{160} [m/s], 160m, 10 min							
Analysis Point	Return Period [years]						
	1	2	5	10	50	100	1000
IJV	35.2	36.9	39.1	40.6	43.7	45.0	49.3
IJV1 (non-adjusted)	31.8	33.3	35.1	36.3	39.0	40.2	43.8
IJV1 (adjusted by 7%)	34.0	35.6	37.6	38.8	41.7	43.0	46.9

5.2.2 Water levels

Table 5.6 shows the omni extreme total high- and low-water levels at IJV and IJV1. While HWL_{tot} are quite similar at both sites, the LWL_{tot} at IJV1 is slightly smaller than that at IJV. It is noted that at IJV, the water level extremes were estimated relative to LAT, whereas at IJV1, they were estimated relative to MSL. The results at IJV were therefore corrected to MSL using the difference between MSL and LAT for IJV as given in Table 5.2. A better comparison would be possible if the water level extremes at IJV were estimated relative to MSL.

Table 5.6 Omni extreme total high-water and lowe-water level at IJV and IJV1.

Analysis Point	Return Period [years]						
	1	2	5	10	50	100	1000
	Omni Extreme Total High Water Level, HWLtot [mMSL]						
IJV	1.7	1.9	2.0	2.1	2.4	2.5	2.9
IJV1	1.6	1.7	1.9	2.0	2.3	2.4	2.9
	Omni Extreme Total Low Water Level, LWLtot [mMSL]						
IJV	-1.4	-1.5	-1.7	-1.7	-1.9	-2.0	-2.3
IJV1	-1.2	-1.3	-1.4	-1.5	-1.7	-1.7	-2.0

5.2.3 Currents

Table 5.7 shows the omni-directional extreme depth-averaged total current speeds CS_{tot} at IJV and IJV1 along with the associated H_{m0}. The CS_{tot} extremes are almost the same at IJV and IJV1. However, the associated H_{m0} is significantly larger at IJV1 than at IJV. One reason could be that IJV1 is selected corresponding to the largest 50-yr H_{m0}, whereas IJV was selected using median annual maximum location, which did not correspond to the maximum value in the site (see Figure (6.1) in [44]).

Table 5.7 Omni-directional extreme depth-averaged total current speed and associated H_{m0} at IJV and IJV1.

Analysis Point	Return Period [years]						
	1	2	5	10	50	100	1000
	Omni Extreme Depth-Average Total Current Speed, CStot [m/s]						
IJV	1.0	1.0	1.0	1.1	1.1	1.1	1.2
IJV1	1.0	1.0	1.0	1.1	1.1	1.2	1.2
	Omni Associated H_{m0} to CS_{tot} [m]						
IJV	3.9	4.4	4.3	4.6	5.2	5.1	5.8
IJV1	4.7	4.9	5.2	5.4	5.9	6.1	6.8

Waves

Table 5.8 shows the omni-directional marginal and associated extreme wave parameters at IJV and IJV1. There is hardly any variation in any parameter between IJV and IJV1.

Table 5.8 Omni-directional marginal and associated extreme wave parameters at IJV and IJV1.

Analysis Point	Return Period [years]						
	1	2	5	10	50	100	1000
	Omni Extreme Significant Wave Height, H_{m0} [m]						
IJV	5.7	6.1	6.6	6.9	7.7	8.0	8.9
IJV1	5.9	6.2	6.7	7.0	7.6	7.9	8.7
	Omni Associated Peak Wave Period, T_p [s] 50%						
IJV	10.6	11.0	11.6	12.0	12.8	13.2	14.1
IJV1	10.4	10.8	11.4	11.7	12.6	12.9	13.9
	Omni Associated Mean Zero-Crossing Wave Period, T_{02} [s] 50%						
IJV	7.7	8.0	8.4	8.7	9.2	9.4	10.1
IJV1	6.8	7.1	7.5	7.7	8.2	8.4	9.0
	Omni Associated CS_{tot} to H_{m0} [m/s]						
IJV	0.5	0.5	0.4	0.5	0.5	0.6	0.5
IJV1	0.5	0.5	0.5	0.5	0.5	0.5	0.5
	Omni Extreme Maximum Wave Height, H_{max} [m]						
IJV	10.6	11.4	12.3	13.0	14.5	15.0	17.0
IJV1	11.0	11.7	12.6	13.2	14.6	15.2	17.0
	Omni Associated Period, T_{Hmax} [s] 50%						
IJV	9.1	9.5	10.0	10.2	10.8	10.8	11.5
IJV1	9.2	9.5	9.8	10.0	10.5	10.7	11.3
	Omni Extreme Maximum Crest Height, SWL, C_{max}, SWL [m]						
IJV	6.7	7.3	8.0	8.5	9.6	10.0	11.6
IJV1	7.1	7.6	8.2	8.6	9.6	10.1	11.5

6 Accessing the Metocean Data and Analyses on the MOOD Data Portal

This section provides a brief overview of the IJmuiden Ver online database, which is hosted on DHI's MetOcean-On-Demand (MOOD) online data portal https://www.metocean-on-demand.com/.

6.1 Web based database and datasets

The datasets available in the MOOD platform is called DWF23 (from Dutch Wind Farms 2023).

It is important to note that the DWF23 dataset covers a large area within the Dutch North Sea sector. Certification will be carried out in the year 2024. The HKN, HKZ, HKW and TNW datasets [29, 45-47] (separate from DWF23) were already certified.

Figure 6.1 shows a screen shot of the DWF23 datasets on MOOD. Once a point is selected within the database polygon, which comprises all investigation areas, the DWF23 datasets are automatically selected and shown in the dataset context menu on the right (Waves, Ocean, and Atmosphere). Points can be modified by drag-and-drop or by the provision of coordinates (in geographical or UTM coordinates). The point can be renamed, and multi-point selection is possible.

From the dataset context menu, the user has access to Metadata, Validation, Analytics and Reports for each dataset. Via the 'Add to Chart' button, the time series can be added for later download. The period 1979-01-01 07:00 to 2022-12-31 23:00 is available and selected by default. The selected period can be modified and will be applied to the analytics and to the download of data.

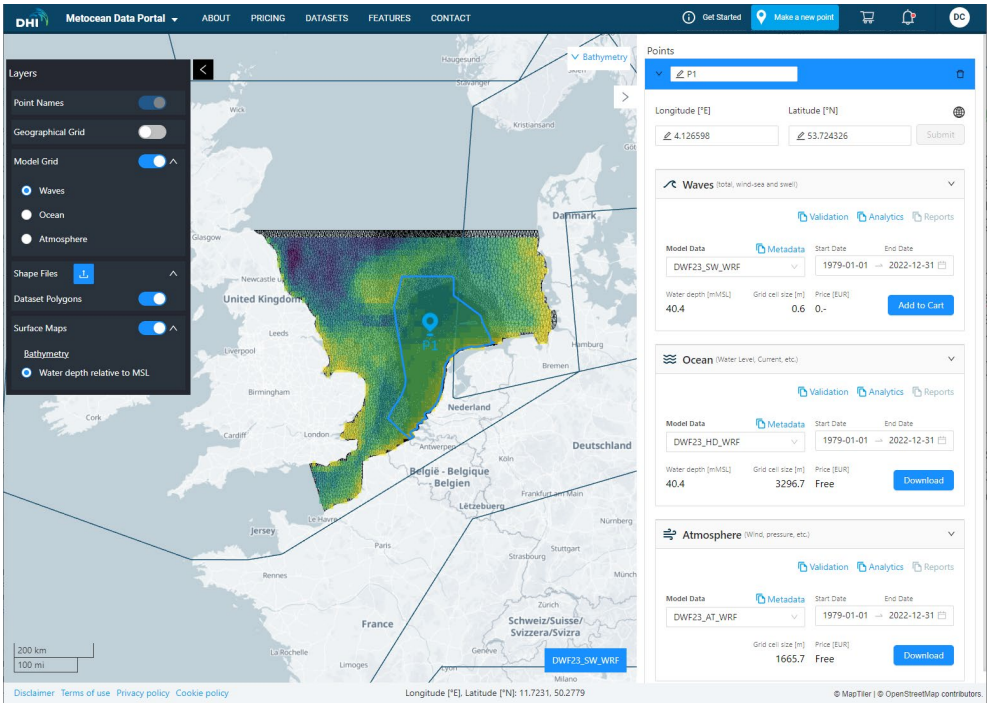

Figure 6.1 View of DWF23 datasets on the online data portal MOOD. Screen view of https://www.metocean-on-demand.com/ after selection of a point within the DWF23 dataset. The dataset context menu appears to the right and the layers context menu to the left.

6.2 Time series

The available time series are summarized in Table 6.1, which specifies the dataset names on MOOD, the underlying models, as well as post-processing steps. The time series are available at each grid point of the respective model mesh within the DWF23 area. This corresponds to 91,013 elements for the HD_{DWF23} (hydrodynamic) model, 89,410 elements for the SW_{DWF23} (wave) model, and 19,200 elements for the WRF (atmospheric) model.

Table 6.1 Available DWF23 datasets and time series.
MOOD dataset names, their underlying models and post-processing steps applied to the model outputs, reference for further details and included parameters.

MOOD dataset	Model	Details	Modelled and pre-processed parameters
DWF23_SW_WRF	SW_{DWF23}	Section 3.3 in [3]	H_{m0}, T_p, T_{01}, T_{02}, PWD, MWD, DSD $H_{m0,Sea}$, $T_{p,Sea}$, $T_{01,Sea}$, $T_{02,Sea}$, $PWD_{,Sea}$, $MWD_{,Sea}$, $DSD_{,Sea}$ $H_{m0,Swell}$, $T_{p,\ Swell}$, $T_{01,\ Swell}$, $T_{02,\ Swell}$, $PWD_{,\ Swell}$, $MWD_{,\ Swell}$, $DSD_{,\ Swell}$ (wave-age sea/swell separation)
DWF23_HD_WRF	HD_{DWF23}	Section 3.2 in [3]	WL_{tot}, $CS_{tot,2DH}$, $CD_{tot,2DH}$
DWF23_AT_10min	WRF	Section 3.1 in [3] and [2]	10-minute data: WS_z, WD_z, $Tair_z$, RH_z with Z=[10, 30, 60, 100, 120, 140, 160, 200, 250, 300] mMSL. MSLP, SST, DWSR, Precipitation, PBL height.
DWF23_AT_1h	WRF	Section 3.1 in [3] and [2]	1-hour data: $AirPres_z$, $AirDen_z$, @ Z=[10, 30, 60, 100, 120, 140, 160, 200, 250, 300] mMSL.

6.3 On-the-fly analytics

Various types of analyses (rose, scatter diagrams, occurrence tables, persistence, etc.) are available on-the-fly through the MOOD online database. Users can define their own set of thresholds for any given parameter and analysis. There is also a possibility for limiting the data coverage period to any given sub-period for specific analyses.

DHI notes that the tidal components of WL and CS mentioned in Table 6.1 need to be downloaded through the Analytics by running tidal analysis.

6.4 Surface maps

Surface maps of selected statistics of normal metocean conditions, tidal water levels and extreme metocean conditions will be provided in the database in the second quarter of the year 2024.

6.5 Reports

Two types of pre-processed reports (normal and extreme conditions) are available as Excel (.xlsx) tables at the analysis point (IJV1). Normal and extreme conditions data for the entire feasibility domain area will be available in the second quarter of the year 2024.

7 References

[1] RVO. "IJmuiden Ver - General Information." https://offshorewind.rvo.nl/cms/view/5c06ac88-c12f-4903-89f3-27d66937b7e9/general-information-ijmuiden-ver (accessed 2023).

[2] OWC, "IJmuiden Ver Wind Farm Zones: Wind Resource Assessment," The Netherlands, 2023. [Online]. Available: https://offshorewind.rvo.nl/file/download/d61bb7ce-25eb-43dc-942f-60149f7d33b7/ijv_20231127_dhi_report-wind-resource-assessment-f.pdf

[3] DHI, "IJmuiden Ver Wind Farm Zone: Part A, Metocean Modelling," 2023.

[4] E. Commission, "English Style Guide: A handbook for authors and translators in the European Commission," 2023.

[5] S. B. Pope, *Turbulent Flows*. Cambridge University Press, 2000, p. 806.

[6] D. L. Codiga, "Unified Tidal Analysis and Prediction Using the UTide Matlab Functions. Techinal Report 2011-01," Graduate School of Oceanography, University of Rhode Island, Narragansett, 2011.

[7] R. Pawlowicz, B. Beardsley, and S. Lentz, "Classical tidal harmonic analysis including error estimates in MATLAB using T-TIDE," *Computers &,* no. 28, pp. 929-937, 2002.

[8] M. G. G. Foreman, J. Y. Cherniawsky, and V. A. Ballantyne, "Versatile Harmonic Tidal Analysis: Improvements and Applications," *Journal of Atmospheric and Oceanic Technology,* no. 26, pp. 806-817, 2009.

[9] K. E. Leffler and D. A. Jay, "Enhancing tidal harmonic analysis: Robust (hybrid L-1/L-2) solutions," *Continental Shelf Research,* no. 29, pp. 78-88, 2009.

[10] *Wind energy generation systems – Part 3-1: Design Requirements for fixed offshore wind turbines. Ed. 1.0*, IEC-61400-3-1, 2019.

[11] *Environmental Conditions and Environmental Loads*, DNV-RP-C205, DNV, 2021. [Online]. Available: https://brandcentral.dnv.com/fr/gallery/10651/others/1ca64bb105ca4c80a5d287814db8f2e3_hi.pdf

[12] K. Torsethaugen and S. Haver, "Simplified double peak spectral model for ocean waves.," in *14th ISOPE*, 2004, Toulon, France.

[13] M. K. Ochi and E. N. Hubble, "Six-parameter wave spectra," in *15th Coastal Engineering Conference*, 1976, pp. 301-328.

[14] K. Hasselmann and D. Olbers, "Measurements of wind-wave growth and swell decay during the Joint North Sea Wave Project (JONSWAP)," *Ergänzung zur Deut. Hydrogr. Z., Reihe A (8),* vol. 12, pp. 1-95, 1973. [Online]. Available: https://epic.awi.de/id/eprint/10163/.

[15] *Loads and site conditions for wind turbines*, DNV-ST-0437, DNV, 2021.

[16] D. J. Cecil. *LIS/OTD Gridded Lightning Climatology Data Collection, Version 2.3.2015*, NASA EOSDIS Global Hydrology Resource Center Distributed Active Archive Center, Huntsville, Alabama, U.S.A., doi: http://dx.doi.org/10.5067/LIS/LIS-OTD/DATA311.

[17] D. J. B. Cecil, D. E.; Blackeslee, R. J., "Gridded lightning climatology from TRMM-LIS and OTD: Dataset description," *Atmospheric Research,* vol. 135-136, pp. 404-414, 2014.

[18] H. a. K. Reiser, Haim, "Rainfall uncertainty in the Mediterranean: Definitions of the daily rainfall threshold (DRT) and the rainy season length (RSL)," *Theoretical and Applied Climatology,* vol. 97, pp. 151-162, 2009, doi: 10.1007/s00704-008-0055-z.

[19] E. standard, "EN ISO 19901-1 Petroleum and Gas Industries - Specific requirements for offshore structures - Part 1: Metocean design and operating considerations," 2005.

[20] F. Lamraoui, G. Fortin, R. Benoit, J. Perron, and C. Masson, "Atmospheric icing impact on wind turbine production," *Cold Regions Science and Technology,* vol. 100, pp. 36-49, 2014/04/01/ 2014, doi: https://doi.org/10.1016/j.coldregions.2013.12.008.

[21] I. E. 19906, "Petroleum and natural gas industries - Artic offshore structures (ISO 19906:2010)," 2010.

[22] J. A. Callow and M. E. Callow, "Trends in the development of environmentally friendly fouling-resistant marine coatings," *Nature Communications,* vol. 2, no. 1, p. 244, 2011/03/22 2011, doi: 10.1038/ncomms1251.

[23] K. Dahl, J. G. Støttrup, C. Stenberg, U. C. Berggreen, and J. H. Jensen, "Best practice for restoration of stone reefs in Denmark (Codes of Conduct)," Tech Rep 91. DCE− Danish Centre for Environment and Energy, Aarhus …, 2016.

[24] P. D. Causon and A. B. Gill, "Linking ecosystem services with epibenthic biodiversity change following installation of offshore wind farms," *Environmental Science and Policy,* Review vol. 89, pp. 340-347, 2018, doi: 10.1016/j.envsci.2018.08.013.

[25] I. De Mesel, F. Kerckhof, A. Norro, B. Rumes, and S. Degraer, "Succession and seasonal dynamics of the epifauna community on offshore wind farm foundations and their role as stepping stones for non-indigenous species," *Hydrobiologia,* Article vol. 756, no. 1, pp. 37-50, 2015, doi: 10.1007/s10750-014-2157-1.

[26] R. Krone, L. Gutow, T. J. Joschko, and A. Schröder, "Epifauna dynamics at an offshore foundation–implications of future wind power farming in the North Sea," *Marine environmental research,* vol. 85, pp. 1-12, 2013.

[27] L. Almeida and J. Coolen, "Modelling thickness variations of macrofouling communities on offshore platforms in the Dutch North Sea," *Journal of Sea Research,* vol. 156, p. 101836, 2020.

[28] F. Kerckhof, A. Norro, T. Jacques, and S. Degraer, "Early colonisation of a concrete offshore windmill foundation by marine biofouling on the Thornton Bank (southern North Sea)," *Offshore wind farms in the Belgian part of the North Sea: State of the art after two years of environmental monitoring,* pp. 39-51, 2009.

[29] DHI, "Metocean desk study and database for Dutch Wind Farm Zones, Hollandse Kust (Noord)," RVO, NL, Project Nr. 11822658, Final 2.4, 2019. [Online]. Available: https://offshorewind.rvo.nl/files/view/a93c15aa-622d-4fc7-b44e-e90db8a46588/hkn_20191018_dhi_metocean-study-f.pdf

[30] T. van der Stap, J. W. P. Coolen, and H. J. Lindeboom, "Marine Fouling Assemblages on Offshore Gas Platforms in the Southern North Sea: Effects of Depth and Distance from Shore on Biodiversity," *PLOS ONE,* vol. 11, no. 1, p. e0146324, 2016, doi: 10.1371/journal.pone.0146324.

[31] A. Schröder, C. Orejas, and T. Joschko, "Benthos in the Vicinity of Piles: FINO 1 (North Sea)," in *Offshore Wind Energy: Research on Environmental Impacts*, J. Köller, J. Köppel, and W. Peters Eds. Berlin, Heidelberg: Springer Berlin Heidelberg, 2006, pp. 185-200.

[32] R. Ter Hofstede, F. Driessen, P. Elzinga, M. Van Koningsveld, and M. Schutter, "Offshore wind farms contribute to epibenthic biodiversity in the North Sea," *Journal of Sea Research,* vol. 185, p. 102229, 2022.

[33] J. Loxton *et al.*, "Setting an agenda for biofouling research for the marine renewable energy industry," *International Journal of Marine Energy,* Article vol. 19, pp. 292-303, 2017, doi: 10.1016/j.ijome.2017.08.006.

[34] J. Reubens, S. Degraer, and M. Vincx, "The ecology of benthopelagic fishes at offshore wind farms: a synthesis of 4 years of research," *Hydrobiologia,* vol. 727, pp. 121-136, 2014.

[35] D. J. Russell *et al.*, "Marine mammals trace anthropogenic structures at sea," *Current Biology,* vol. 24, no. 14, pp. R638-R639, 2014.

[36] D. S. Clare, S. G. Bolam, P. S. McIlwaine, C. Garcia, J. M. Murray, and J. D. Eggleton, "Biological traits of marine benthic invertebrates in Northwest Europe," *Scientific Data,* vol. 9, no. 1, p. 339, 2022.

[37] F. J. Millero and A. Poisson, "International one-atmosphere equation of state of seawater," *Deep Sea Research Part A. Oceanographic Research Papers,* vol. 28, no. 6, pp. 625-629, 1981/06/01/ 1981, doi: https://doi.org/10.1016/0198-0149(81)90122-9.

[38] DNVGL, "Assessment Wind Measurement Program North Sea," Netherlands' Enterprise Agency, 14-2781, Rev. 1, 2014. [Online]. Available: https://offshorewind.rvo.nl/file/download/fa117a7e-825c-4766-949c-5405c6ea779f/1425640012assessment%20wind%20measurement%20program%20north%20sea.pdf

[39] A. Sathe, M. Courtney, J. Mann, and R. Wagner, "How good are remote sensors at measuring extreme winds?," in *European Wind Energy Association (EWEA)*, Brussels, 2011.

[40] J. C. Lagarias, J. A. Reeds, M. H. Wright, and P. E. Wright, "Convergence Properties of the Nelder--Mead Simplex Method in Low Dimensions," *SIAM Journal on Optimization,* vol. 9, no. 1, pp. 112-147, 1998, doi: 10.1137/s1052623496303470.

[41] G. Z. Forristall, "Wave Crest Distributions: Observations and Second-Order Theory," *Journal of Physical Oceanography,* vol. 30, no. 8, pp. 1931-1943, 2000, doi: dx.doi.org/10.1175/1520-0485(2000)030<1931:wcdoas>2.0.co;2.

[42] B. K. Glukhovskiy, "Investigation of sea wind waves," in *Proceedings of the Sea Climatology Conference, Paris, France*, 1966, pp. 51-71.

[43] Y. Goda, "Reanalysis of Regular and Random Breaking Wave Statistics," *Coastal Engineering Journal,* pp. 71-106, 2010.

[44] DHI, "Metocean Desk Study and Database for Dutch Wind Farm Zones: Feasibility level study for IJmuiden Ver, Ten Noorden van de Waddeneilanden & Hollandse Kust (west)," RVO, NL, 2019. [Online]. Available: https://offshorewind.rvo.nl/file/download/d5225475-6790-49ff-a21f-e4d9a95436b8/hkw_tnw_ijv_20190328_metocean-desk-study-f.pdf

[45] DHI, "MetOcean Study - Wind farm zone Hollandse Kust (zuid) and Hollandse Kust (noord) v2.3," RVO.nl, Utrecht, 2017.

[46] DHI, "Metocean desk study and database for Dutch Wind Farm Zones, Hollandse Kust (West)," Project Nr. 11822658, Final 0.5, 2020. [Online]. Available: https://offshorewind.rvo.nl/files/view/378260ad-a965-4dec-8182-70b61bc5e118/hkw_20220725_dhi_metocean-desk-study-report-f.pdf

[47] DHI, "Ten noorden van de Waddeneilanden (TNW) Wind Farm Zone: Metocean Desk Study," The Netherlands, 2022. [Online]. Available: https://offshorewind.rvo.nl/file/download/4878bc26-52b4-43e3-b5d0-a77837de1a21/tnw_20220706_dhi_mds-report_final.pdf

Appendix A Quality Indices

See next pages.

DHI Model Quality Indices (QI's)

Contents

Revisions

Date	Description	Initials
2021-08-13	Version 1.0.	PDG
2022-11-24	Version 1.1; table formatting updated.	SJA

Nomenclature

Abbreviation	Explanation
QI	Quality Index
POT	Peak-Over-Threshold

1 Model Quality Indices

To obtain an objective and quantitative measure of how well the model data compared to the observed data, several statistical parameters, so-called quality indices (QI's), are calculated.

Prior to the comparisons, the model data is synchronised to the time stamps of the observations so that both time series had equal length and overlapping time stamps. For each valid observation, measured at time t, the corresponding model value is found using linear interpolation between the model time steps before and after t. Only observed values that had model values within ± the representative sampling or averaging period of the observations are included (e.g., for 10-min observed wind speeds measured every 10 min compared to modelled values every hour, only the observed value every hour is included in the comparison).

The comparisons of the synchronised observed and modelled data are illustrated in (some of) the following figures:

- Time series plot including general statistics
- Scatter plot including quantiles, QQ-fit and QI's (density-coloured dots)
- Histogram of occurrence vs. magnitude or direction
- Histogram of bias vs. magnitude
- Histogram of bias vs. direction
- Dual rose plot (overlapping roses)
- Peak event plot including joint (coinciding) individual peaks

The quality indices are described below, and their definitions are listed in Table 1.1. Most of the quality indices are based on the entire dataset, and hence the quality indices should be considered averaged measures and may not be representative of the accuracy during rare conditions.

The MEAN represents the mean of modelled data, while the bias is the mean difference between the modelled and observed data. AME is the mean of the absolute difference, and RMSE is the root-mean-square of the difference. The MEAN, BIAS, AME and RMSE are given as absolute values and relative to the average of the observed data in percent in the scatter plot.

The scatter index (SI) is a non-dimensional measure of the difference calculated as the unbiased root-mean-square difference relative to the mean absolute value of the observations. In open water, an SI below 0.2 is usually considered a small difference (excellent agreement) for significant wave heights. In confined areas or during calm conditions, where mean significant wave heights are generally lower, a slightly higher SI may be acceptable (the definition of SI implies that it is negatively biased (lower) for time series with high mean values compared to time series with lower mean values (and same scatter/spreading), although it is normalised).

EV is the explained variation and measures the proportion [0 - 1] to which the model accounts for the variation (dispersion) of the observations.

The correlation coefficient (CC) is a non-dimensional measure reflecting the degree to which the variation of the first variable is reflected linearly in the variation of the second variable. A value close to 0 indicates very limited or no (linear) correlation between the two data sets, while a value close to 1 indicates a very high or perfect correlation. Typically, a CC above 0.9 is considered a high correlation (good agreement) for wave heights. It is noted that CC is 1 (or -1) for any two fully linearly correlated variables, even if they are not 1:1. However, the slope and intercept of the linear relation may be different from 1 and 0, respectively, despite CC of 1 (or -1).

The QQ line slope and intercept are found from a linear fit to the data quantiles in a least-square sense. The lower and uppermost quantiles are not included on the fit. A regression line slope different from 1 may indicate a trend in the difference.

The peak ratio (PR) is the average of the Npeak highest model values divided by the average of the Npeak highest observations. The peaks are found individually for each dataset through the Peak-Over-Threshold (POT) method applying an average annual number of exceedances of 4 and an inter-event time of 36 hours. A general underestimation of the modelled peak events results in a PR below 1, while an overestimation results in a PR above 1.

An example of a peak plot is shown in Figure 1.1. 'X' represents the observed peaks (x-axis), while 'Y' represents the modelled peaks (y-axis), based on the POT methodology, both represented by circles ('o') in the plot. The joint (coinciding) peaks, defined as any X and Y peaks within ±36 hours[1] of each other (i.e., less than or equal to the number of individual peaks), are represented by crosses ('x'). Hence, the joint peaks ('x') overlap with the individual peaks ('o') only if they occur at the same time exactly. Otherwise, the joint peaks ('x') represent an additional point in the plot, which may be associated with the observed and modelled individual peaks ('o') by searching in the respective X and Y-axis directions, see example with red lines in Figure 1.1. It is seen that the 'X' peaks are often underneath the 1:1 line, while the 'Y' peaks are often above the 1:1 line.

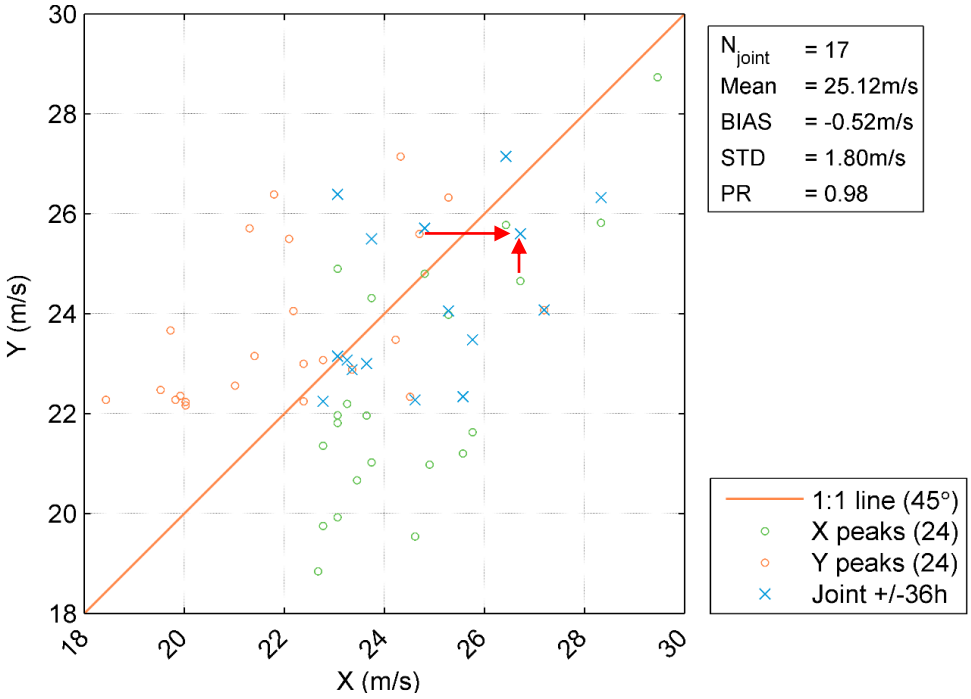

Figure 1.1 Example of peak event plot (wind speed)

[1] 36 hours is chosen arbitrarily as representative of an average storm duration. Often the measured and modelled peaks are within 1-2 hours of each other.

Table 1.1 Definitions of model quality indices (X = Observation, Y = Model)

Abbreviation	Description	Definition
N	Number of data (synchronised)	–
MEAN	Mean of Y data Mean of X data	$\frac{1}{N}\sum_{i=1}^{N} Y_i \equiv \overline{Y}$, $\frac{1}{N}\sum_{i=1}^{N} X_i \equiv \overline{X}$
STD	Standard deviation of Y data Standard deviation of X data	$\sqrt{\frac{1}{N-1}\sum_{i=1}^{N}(Y-\overline{Y})^2}$, $\sqrt{\frac{1}{N-1}\sum_{i=1}^{N}(X-\overline{X})^2}$
BIAS	Mean difference	$\frac{1}{N}\sum_{i=1}^{N}(Y-X)_i = \overline{Y}-\overline{X}$
AME	Absolute mean difference	$\frac{1}{N}\sum_{i=1}^{N}(\lvert Y-X\rvert)_i$
RMSE	Root-mean-square difference	$\sqrt{\frac{1}{N}\sum_{i=1}^{N}(Y-X)_i^{\,2}}$
SI	Scatter index (unbiased)	$\frac{\sqrt{\frac{1}{N}\sum_{i=1}^{N}(Y-X-\mathrm{BIAS})_i^{\,2}}}{\frac{1}{N}\sum_{i=1}^{N}\lvert X_i\rvert}$
EV	Explained variance	$\frac{\sum_{i=1}^{N}(X_i-\overline{X})^2-\sum_{i=1}^{N}[(X_i-\overline{X})-(Y_i-\overline{Y})]^2}{\sum_{i=1}^{N}(X_i-\overline{X})^2}$
CC	Correlation coefficient	$\frac{\sum_{i=1}^{N}(X_i-\overline{X})(Y_i-\overline{Y})}{\sqrt{\sum_{i=1}^{N}(X_i-\overline{X})^2\sum_{i=1}^{N}(Y_i-\overline{Y})^2}}$
QQ	Quantile-Quantile (line slope and intercept)	Linear least square fit to quantiles
PR	Peak ratio (of N_{peak} highest events)	$PR=\frac{\sum_{i=1}^{N_{peak}}Y_i}{\sum_{i=1}^{N_{peak}}X_i}$

Appendix B Persistence

See next pages.

DHI Persistence (Weather Windows)

Contents

Revisions

Date	Description	Initials
2021-08-13	Version 1.0.	PDG

Nomenclature

Abbreviation	Explanation
H_{m0}	Zeroth moment significant wave height [m]
P	Percentile

1 DHI Persistence (Weather Windows)

The persistence (also known as weather window and/or downtime) is defined as a continued occurrence of a given minimum duration which a given parameter's value remains higher or lower than a given threshold. A weather window is defined as a continued occurrence during which the given conditions (duration and threshold) are fulfilled, while downtime is defined as the remainder periods (i.e., all periods that are not weather windows). The sum of weather windows and downtime for any given condition thus equals 100% of the time.

The durations may be defined as either 'Overlapping' or 'Non-overlapping'. Overlapping duration refers to persistence that includes the fraction of duration at the end of each weather window, while non-overlapping duration includes whole number of windows only. Overlapping duration thus results in higher occurrence of weather windows (and lower occurrence of downtime). The thresholds may be defined as being either above or below a given value depending on what is critical for the parameter in question. The default is the 'Overlapping' method.

An illustration of persistence over 1 month (31 days) is presented in Figure 1.1. As an example, the persistence for an overlapping duration ≥ 1 day (24 hours) and a threshold H_{m0} < 4.0m yields weather windows of 93.2% of the time (28.9 days) and corresponding downtime of 6.8% (2.1 days) during that month.

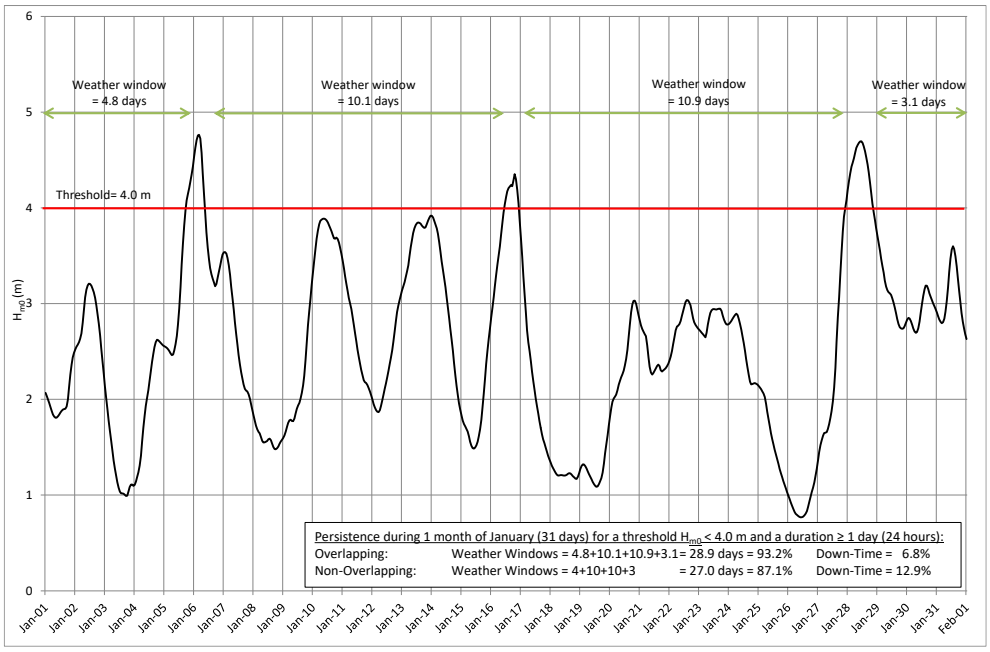

Figure 1.1 Example of persistence over one month

The uncertainty related to yearly variations may be estimated by calculating the persistence statistics for each available year and subsequently derive the mean, standard deviation, and/or any given certainty percentile. A percentile (P) above 50% in this case refers to a more conservative estimate (i.e., less weather windows and more downtime) and vice versa.

The persistence statistics are presented in graphical and tabular format as a percentage of time during each considered interval (e.g., month). Windows stretching through more than one interval contributes with a corresponding fraction of the window to each of the intervals.

Appendix C Extreme Value Analysis (EVA)

See next pages.

DHI Extreme Value Analysis (EVA)

Contents

Revisions

Date	Description	Initials
2021-08-13	Version 1.0.	PDG

Nomenclature

Abbreviation	Explanation
C	Individual crest level [m]
C_{max}	Maximum (highest) individual crest level [m]
C_{mp}	Most probable maximum individual crest level in a storm event [m]
H_{m0}	Zeroth moment significant wave height [m]
H	Individual (trough-crest) wave height [m]
H_{max}	Maximum (highest) individual (trough-crest) wave height [m]
H_{mp}	Most probable maximum individual wave height in a storm event [m]
T_R	Return period [years]

1 DHI Extreme Value Analysis (EVA)

This document describes the DHI extreme value analysis (EVA).

1.1 Summary of approach

Extreme values with conditioned long return periods are estimated by fitting a probability distribution to historical data. Several distributions, data selection and fitting techniques are available for estimation of extremes, and the estimated extremes are often rather sensitive to the choice of method. However, it is not possible to choose a preferred method only on its superior theoretical support or widespread acceptance within the industry. Hence, it is common practice to test several approaches and make the final decision based on goodness of fit.

The typical extreme value analyses involved the following steps:

1. Extraction of independent identically-distributed events by requiring that events are separated by at least 36 hours (or similar), and that the value between events had dropped to below 70% (or similar) of the minor of two consecutive events. The extraction is conducted individually for omni and directional/seasonal subsets respectively.
2. Fitting of extreme value distribution to the extracted events, individually for omni and directional/seasonal subsets. Distribution parameters are estimated either by maximum likelihood or least-square methods. The following analysis approaches are used (see Section 1.2 for details):
   - Fitting the Gumbel distribution to annual maxima.
   - Fitting a distribution to all events above a certain threshold (the Peak-Over-Threshold method). The distribution type can be exponential, truncated Weibull or 2-parameter Weibull to excess.
3. Constraining of subseries to ensure consistency with the omni/all-year distribution; see Section 1.4 for details.
4. Bootstrapping to estimate the uncertainty due to sampling error; see Section 1.6 for details.
5. Values of other parameters conditioned on extremes of one variable are estimated using the methodology proposed in [1] (Heffernan & Tawn).

Figure 1.1 shows an example of EVA based on 38 years of hindcast data and a Gumbel distribution fitted to the annual maxima using max. likelihood.

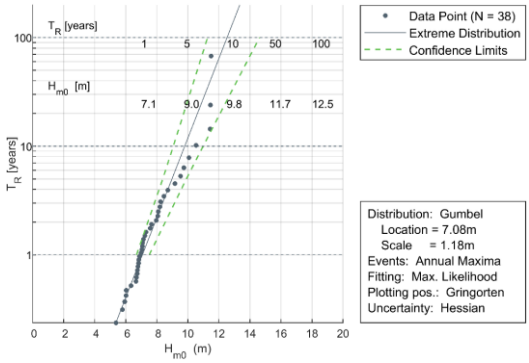

Figure 1.1 Example of traditional extreme value analysis of H_{m0}.
A Gumbel distribution fitted to the annual maxima using maximum likelihood.

1.2 Long-term distributions

The following probability distributions are often used in connection with extreme value estimation:

- 2-parameter Weibull distribution
- Truncated Weibull distribution

- Exponential distribution
- Gumbel distribution

The 2-parameter Weibull distribution is given by:

$$P(X < x) = 1 - \exp\left(-\left(\frac{x}{\beta}\right)^{\alpha}\right) \quad (1.1)$$

with distribution parameters α (shape) and β (scale). The 2-parameter Weibull distribution used in connection with Peak-Over-Threshold (POT) analysis is fitted to the excess of data above the threshold, i.e., the threshold value is subtracted from data prior to fitting.

The 2-parameter *truncated* Weibull distribution is given by:

$$P(X < x) = 1 - \frac{1}{P_0}\exp\left(-\left(\frac{x}{\beta}\right)^{\alpha}\right) \quad (1.2)$$

with distribution parameters α (shape) and β (scale) and the exceedance probability, P_0, at the threshold level, γ, given by:

$$P_0 = \exp\left(-\left(\frac{\gamma}{\beta}\right)^{\alpha}\right) \quad (1.3)$$

The 2-parameter truncated Weibull distribution is used in connection with Peak-Over-Threshold analysis, and as opposed to the non-truncated 2-p Weibull, it is fitted directly to data, i.e., the threshold value is **not** subtracted from data prior to fitting.

The exponential distribution is given by:

$$P(X < x) = 1 - \exp\left(-\left(\frac{x-\mu}{\beta}\right)\right), \quad x \geq \mu \quad (1.4)$$

with distribution parameters β (scale) and μ (location). Finally, the Gumbel distribution is given by:

$$P(X < x) = \exp\left(-\exp\left(\frac{\mu - x}{\beta}\right)\right) \quad (1.5)$$

with distribution parameters β (scale) and μ (location).

1.3 Individual wave and crest height

Short-term distributions

The short-term distributions of individual wave heights and crests conditional on H_{m0} are assumed to follow the distributions proposed by Forristall, (Forristall G. Z., 1978) and (Forristall G. Z., 2000). The Forristall wave height distribution is based on Gulf of Mexico measurements, but experience from the North Sea has shown that these distributions may have a more general applicability. The Forristall wave and crest height distributions are given by:

$$P(X > x \mid H_{m0}) = \exp\left(-\left(\frac{x}{\alpha H_{m0}}\right)^{\beta}\right) \quad (1.6)$$

where the distribution parameters, α and β, are as follows:

Forristall wave height: α = 0.681 β = 2.126

Forristall crest height (3D): $\alpha = 0.3536 + 0.2568 \cdot S_1 + 0.0800 \cdot Ur$

$\beta = 2 - 1.7912 \cdot S_1 - 0.5302 \cdot Ur + 0.284 \cdot Ur^2$

$$S_1 = \frac{2\pi}{g}\frac{H_{m0}}{T_{01}^2} \quad \text{and} \quad U_r = \frac{H \cdot L^2}{d^3}$$

For this type of distribution, the distribution of the extremes of a given number of events, N, (waves or crests) converges towards the Gumbel distribution conditional on the most probable value of the extreme event, H_{mp} (or C_{mp} for crests):

$$P(h_{\max} \mid H_{mp}) = \exp\left(-\exp\left(-\ln N\left(\left(\frac{h_{\max}}{H_{mp}}\right)^{\beta} - 1\right)\right)\right) \qquad (1.7)$$

1.3.1 Individual waves (modes)

The extreme individual wave and crest heights are derived using the storm mode approach, (Tromans, P.S. and Vanderschuren, L., 1995). The storm modes, or most probable values of the maximum wave or crest in the storm (H_{mp} or C_{mp}), are obtained by integrating the short-term distribution of wave heights conditional on H_{m0} over the entire number of sea states making up the storm. In practice, this is done by following these steps:

1. Storms are identified by peak extraction from the time series of significant wave height. Individual storms are taken as portions of the time series with H_{m0} above 0.7 times the storm peak, H_{m0}.
2. The wave (or crest) height distribution is calculated for each sea state above the threshold in each individual storm. The short-term distribution of H (or C) conditional on H_{m0}, $P(h|H_{m0})$, is assumed to follow the empirical distributions by Forristall (see Section 1.3). The wave height probability distribution is then given by the following product over the n sea states making up the storm:

$$P(H_{\max} < h) = \prod_{j=1}^{n_{seastates}} P(h \mid H_{m0,j})^{N_{waves,j}} \qquad (1.8)$$

with the number of waves in each sea state, N_{waves}, being estimated by deriving the mean zero-crossing period of the sea state. The most probable maximum wave height (or mode), H_{mp}, of the storm is given by:

$$P(H_{\max} < h) = \frac{1}{e} \qquad (1.9)$$

This produces a database of historical storms each characterised by its most probable maximum individual wave height which is used for further extreme value analysis.

1.3.2 Convolution of short-term variability with long-term storm density

The long-term distribution of individual waves and crests is found by convolution of the long-term distribution of the modes (subscript $_{mp}$ for most probable value) with the distribution of the maximum conditional on the mode given by:

$$P(H_{\max}) = \int_0^\infty P(h_{\max} \mid H_{mp}) \cdot p(H_{mp}) dH_{mp}$$
$$= \int_0^\infty \exp\left(-\exp\left(-\ln N \left(\left(\frac{h}{H_{mp}} \right)^{\beta} - 1 \right) \right) \right) \cdot p(H_{mp}) dH_{mp} \quad (1.10)$$

The value of N, which goes into this equation, is determined by defining equivalent storm properties for each individual storm. The equivalent storms have constant H_{m0} and a duration such that their probability density function of H_{max} or C_{max} matches that of the actual storm. The density functions of the maximum wave in the equivalent storms are given by:

$$p(H_{\max} \mid H_{m0,eq}, N_{eq}) = \frac{d}{dH} \left[1 - \exp\left(-\left(\frac{H_{\max}}{\alpha \cdot H_{m0,eq}} \right)^{\beta} \right) \right]^{N_{eq}} \quad (1.11)$$

The β parameter in eq. (1.10) comes from the short-term distribution of individual crests, eq. ((1.6), and is a function of wave height and wave period. Based on previous studies, it has been assessed that the maximum crest heights are not sensitive to β_C for a constant value of 1.88 and hence, it is decided to apply β_C = 1.88. The number of waves in a storm, N, was conservatively calculated from a linear fit to the modes minus one standard deviation.

1.4 Subset extremes

Estimates of subset (e.g., directional, and monthly) extremes are required for several parameters. To establish these extremes, it is common practice to fit extreme value distributions to data sampled from the population (i.e., the model database) that fulfils the specific requirement e.g., to direction, i.e., the extremes from each direction are extracted and distributions fitted to each set of directional data in turn. By sampling an often relatively small number of values from the data set, each of these directional distributions is subject to uncertainty due to sampling error. This will often lead to the directional distributions being inconsistent with the omnidirectional distribution fitted to the maxima of the entire (omnidirectional) data set. Consistency between directional and omnidirectional distributions is ensured by requiring that the product of the n directional annual non-exceedance probabilities equals the omnidirectional, i.e.:

$$\prod_{i=1}^{n} F_i(x, \hat{\theta}_i)^{N_i} = F_{omni}(x, \hat{\theta}_{omni})^{N_{omni}} \quad (1.12)$$

where N_i is the number of sea states or events for the i'th direction and $\hat{\theta}_i$, the estimated distribution parameter. This is ensured by estimating the distribution parameters for the individual distributions and then minimising the deviation:

$$\delta = \sum_{x_j} \left[-\ln\left(-N_{omni} \ln F_{omni}(x, \hat{\theta}_{omni}) \right) + \ln\left(-\sum_{i=1}^{n} N_i \ln F_i(x_j, \hat{\theta}_i) \right) \right]^2 \quad (1.13)$$

Here x_j are extreme values of the parameter for which the optimisation is carried out, i.e., the product of the directional non-exceedance probabilities is forced to match the omnidirectional for these values of the parameter in question.

The directional extremes presented in this report are given without scaling, that is, a T_{yr} event from direction i will be exceeded once every T years on the average. The same applies for monthly extremes. A T_{yr} monthly event corresponds to the event that is exceeded once (in that month) every T years, which is the same as saying that it is exceeded once every *T*/12 years (on average) of the climate for that month.

1.4.1 Optimised directional extremes

The directional extremes are derived from fits to each subseries data set meaning that a T_R year event from each direction will be exceeded once every T_R years on average. Having e.g., 12 directions, this means that **one** of the directions will be exceeded once every T_R/12 years on average. A 100-year event would thus be exceeded once every 100/12 = 8⅓ years (on average) from **one** of the directions.

For design application, it is often required that the summed (overall) return period (probability) is T_R years. A simple way of fulfilling this would be to take the return value corresponding to the return period T_R times the number of directions, i.e., in this case the 12x100 = 1200-year event for each direction. However, this is often not optimal since it may lead to very high estimates for the strong sectors, while the weak sectors may still be insignificant.

Alternatively, an optimised set of directional extreme values may be produced for design purpose in addition to the individual values of directional extremes described above. The optimised values are derived by increasing (scaling) the individual T_R values of the directions to obtain a summed (overall) probability of T_R years while ensuring that the extreme values of the strong sector(s) become as close to the overall extreme value as possible. In practice, this is done by increasing the T_R of the weak directions more than that of the strong sectors but ensuring that the sum of the inverse directional T_R's equals the inverse of the targeted return period, i.e.:

$$\sum_{i=1}^{n} \frac{1}{T_{R,i}} = \frac{1}{T_{R,\text{omni}}} \qquad (1.14)$$

where n is the number of directional sectors and $T_{R,omni}$ is the targeted overall return period.

1.5 Uncertainty assessment

The extreme values are estimated quantities and therefore all associated with uncertainty. The uncertainty arises from several sources:

Measurement/model uncertainty

The contents of the database for the extreme value analysis are associated with uncertainty. This type of uncertainty is preferably mitigated at the source – e.g., by correction of biased model data and removal of obvious outliers in data series. The model uncertainty can be quantified if simultaneous good quality measurements are available for a reasonably long overlapping period.

True extreme value distribution is unknown

The distribution of extremes is theoretically unknown for levels above the levels contained in the extreme value database. There is no justification for the assumption that a parametric extreme value distribution fitted to observed/modelled data can be extrapolated beyond the observed levels. However, it is common practice to do so, and this obviously is a source of uncertainty in the derived extreme value estimates. This uncertainty, increasing with decreasing occurrence probability of the event in question, is not quantifiable but the metocean expert may minimise it by using experience and knowledge when deciding on an appropriate extreme value analysis approach. Proper inclusion of other information than direct measurements and model results may also help to minimise this type of uncertainty.

Uncertainty due to sampling error

The number of observed/modelled extreme events is limited. This gives rise to sampling error which can be quantified by statistical methods such as Monte Carlo simulations or bootstrap resampling. The results of such an analysis are termed the confidence limits. The confidence limits (see Section 1.6) should **not** be mistaken for the total uncertainty in the extreme value estimate.

Settings of the analysis (judgement)

Any EVA involves the need to define the various settings of the analysis (threshold, distribution, and fitting method), which introduces subjectivity to the analysis. The sensitivity of these settings can be assessed by comparing the resulting extreme values, and the goodness of fit can, to some extent, be objectively assessed by statistical measures. However, standard practice typically includes manual inspection of the fitted distributions. Hence, the final settings, and thus results, relies on the experience and preference of the metocean expert conducting the analysis ('engineering judgement'). The tail of the distributions (the values of long the return periods) can be particularly sensitive to the settings of the analysis.

1.6 Confidence limits

The confidence limits of extreme estimates are established from a bootstrap analysis or a Monte Carlo simulation.

The bootstrap analysis estimates the uncertainty due to sampling error. The bootstrap consists of the following steps:

1. Construct a new set of extreme events by sampling randomly with replacement from the original data set of extremes
2. Carry out an extreme value analysis on the new set to estimate T-year events

An empirical distribution of the T-year event is obtained by looping steps 1 and 2 many times. The percentiles are read from the resulting distribution.

In the Monte Carlo simulation, the uncertainty is estimated by randomly generating many samples that have the same statistical distribution as the observed sample.

The Monte Carlo simulation can be summarised in the following steps:

1. Randomly generating a sample consisting of N data points, using the estimated parameters of the original distribution. If the event selection is based on a fixed number of events, N is set equal to the size of original data set of extremes. If the event selection is based on a fixed threshold, the sample size N is assumed to be Poisson-distributed.
2. From the generated sample, the parameters of the distribution are estimated, and the T-year return estimates are established.

Steps 1 and 2 are looped numerous times, whereby an empirical distribution of the T-year event is obtained. The quartiles are read from the resulting distribution.

1.7 Joint probability analyses (JPA)

Values of other parameters conditioned on extremes of one variable are estimated using the methodology proposed in [1] (Heffernan & Tawn). This method consists in modelling the marginal distribution of each variable separately. The variables are transformed from physical space, X, to standard Gumbel space by the relationship:

$$Y = \mathrm{LN}\left(-\mathrm{LN}\left(F\left(X, \hat{\theta}\right)\right)\right) \qquad (1.15)$$

where $F(X, \hat{\theta})$ denotes the distribution function of the variable, X, with estimated parameters, $\hat{\theta}$. No restriction is given on the marginal model of the variables. A combination of the empirical distribution for the bulk of events and a parametric extreme value distribution function fitted to the extreme tail of data was adopted here. For parameters which may have both a positive and a negative extreme such as the water level conditioned on wave height, both the positive and the negative extreme tail are modelled parametrically.

The dependence structure of the two variables is modelled in standard Gumbel distribution space, conditioning one variable by the other. The model takes the form:

$$(Y_2|Y_1 = y_1) = ay_1 + y_1^b Z \qquad (1.16)$$

with Y_1 being the conditioning variable and Y_2 the conditioned. The residual, Z, is assumed to converge to a normal distribution, G, with increasing y_1. The parameters, $\hat{a}$ and $\hat{b}$, are found from regression and the parameters, $\hat{\mu}$ and $\hat{\sigma}$, of the normal distribution, G, estimated from the residuals, Z:

$$Z = \frac{y_2 - a \cdot y_1}{y_1^b} \qquad (1.17)$$

Figure 1.2 shows an example of the modelled dependence structure for H_{m0} and water level in standard Gumbel space. Figure 1.3 shows the same in physical space. The model is clearly capable of describing the positive association between wave heights and water level for this condition and appears also to capture the relatively large spreading.

The applied joint probability model is event-based. This means that independent events of the conditioning parameter are extracted from the model data. The combined inter-event time and inter-event level criterion described in Section 1.1 is applied to isolate independent events of the conditioning parameter. The conditioned parameter is extracted from the model time series at the point in time of the peak of the conditioning parameter. Time averaging of the conditioned parameter is often carried out prior to data extraction to reduce the influence of phases in the analysis (the fact that the water level may not peak at the same time as the peak wave height for instance).

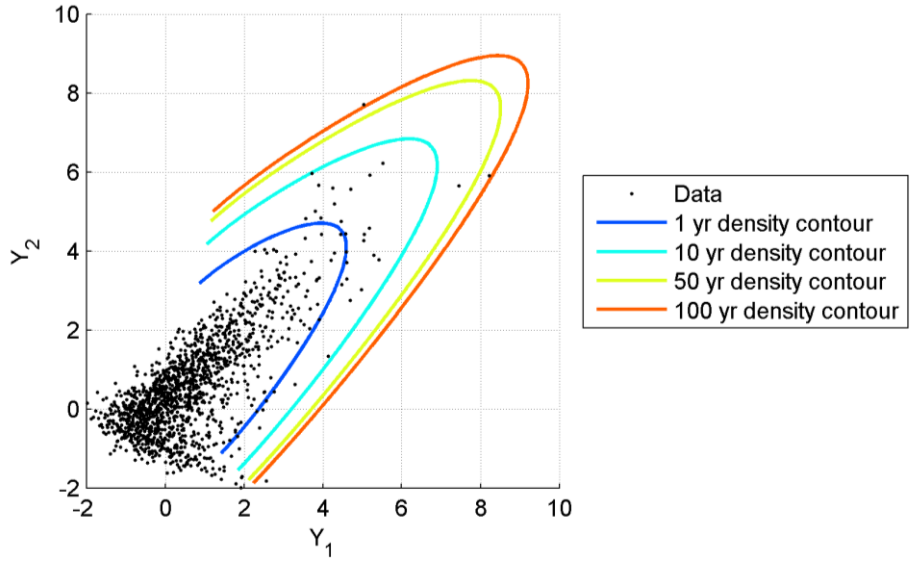

Figure 1.2 Dependence structure of H_{m0} and water level transformed into standard Gumbel space.

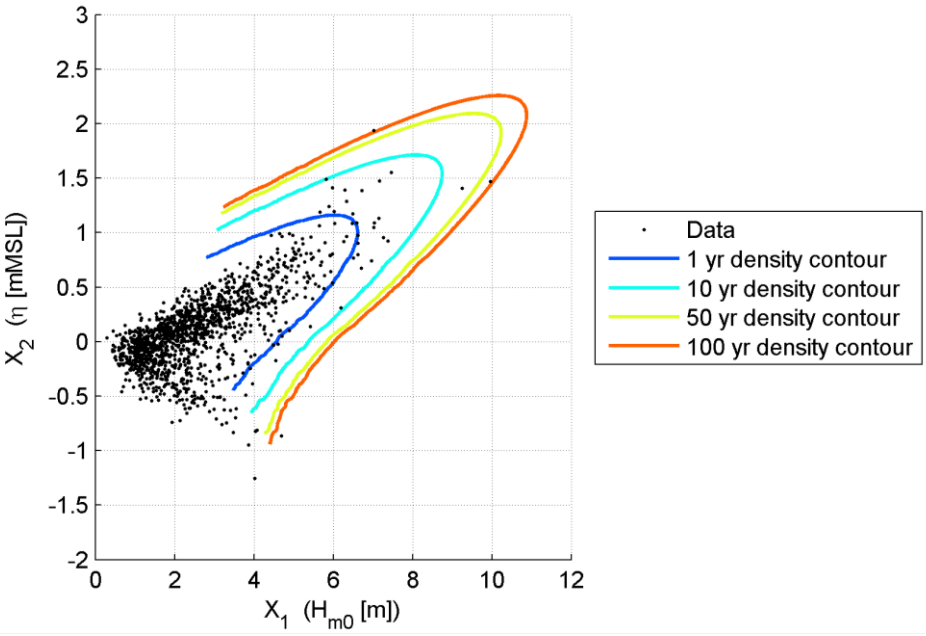

Figure 1.3 Dependence structure of H_{m0} and water level in physical space

1.8 References

[1] J. E. Heffernan and J. A. Tawn, “A conditional approach for multivariate extreme values,” *Journal of the Royal Statistical Society. Series B,* vol. 66, no. 3, pp. 497-546, 2004.

Appendix D J-EVA Summary

See next pages.

DHI J-EVA Summary

Contents

Revisions

Date	Description	Initials
2023-11-13	Version 1.0	AMSA
2023-12-03	Version 1.1	AMSA

Nomenclature

Abbreviation	Explanation
CS	Current speed [m/s]
WS	Wind speed [m/s]
H_{m0}	Spectral significant wave height [m]
$H_{mo,p,eq}$	Equivalent Gauss-bell shaped storm peak H_{m0} [m]
H_{max}	Maximum (highest) individual (trough-crest) wave height [m]
C_{max}	Maximum (highest) individual crest height [m]
T_p	Spectral peak wave period [s]
T_{02}	Zero crossing wave period [s]
q_r	Quantile, or r, i.e., q_{50} is the 0.5 quantile.

T_r	Return Period
N_e	Number of exceedances

1 Joint Extreme Values Analysis (J-EVA)

J-EVA (Joint-Extreme Value Analysis) is DHI's implementation of a consistent directional-seasonal extreme value analysis method incorporating a Markov Chain Monte Carlo (MCMC) Bayesian inference approach to include the statistical uncertainty in the estimate of extreme values. It is based on the work in [1].

J-EVA comprises of two models, 1) a storm model, and 2) a statistical model. Both models are outlined in the following subsections which highlight the most relevant components of each. A concise step-by-step overview of the J-EVA methodology is as follows:

1. Extreme events (storms) are identified from modelled hindcast according to criteria ensuring independent events. The local peaks are identified from the corresponding time series of the variables for which extreme values are estimated. As an example, at least 36 hours between peaks and a required drop in the time series value of 0.7 times the value of the lowest of the surrounding peaks is required.
2. Characteristic storm variables are computed as explained in section 2.1 of [1].
3. The identified storms that are selected by their peak magnitude and duration are further filtered using some criteria, e.g., regression quantile, inverse wave age criteria (only for wave parameters), combination of quantile and inverse wave age etc.
4. From the J-EVA statistical model a spline model is constructed and fitted (both marginal distributions and conditional distributions between the storm parameters) to the storms with covariates for direction (e.g., wave, current, or wind direction) and season (e.g., day in year) when appropriate. It is also possible to use only one covariate, e.g., for water levels. The spline model varies smoothly across the covariates.
5. Posterior distributions of model parameters are found using a Markov Chain Monte Carlo (MCMC) approach. The posterior predictive distributions implicitly include uncertainties through the propagated errors in the prediction.
6. Many events (typically > 500,000 years) are sampled from the posterior distributions. Additionally, for waves, the real storm trajectories (displaying intra-storm variation and hence resolving the individual sea states) are simulated from matching the simulated storms with the historical storm time series using the J-EVA storm model.
7. Extreme values with return period T_r-years are then given by the $(N/T_r)^{th}$ largest value in N years of simulations.

While presenting the results of the J-EVA analysis, a credible interval is always presented as a shaded area. A credible interval is a concept used in Bayesian statistics, which is the central theme of the J-EVA analysis. The concept of credible interval is very different from the concept of the confidence interval used in frequentist statistics approach. A credible interval is simply the central portion of the posterior distribution that contains a chosen percentage of the values. For example, a range of 2.5% - 97.5% interval can be chosen that is equal to 95% credible interval. In other words, given the observed (hindcast model) data characterised by the likelihood function, the effect that is characterized by the posterior distribution has a 95 % probability of falling within this range.

2 J-EVA storm model

The J-EVA storm model makes use of the evolution in time (also termed intra-storm evolution) of historical storm events to make predictions of the evolution in time of possible events with extremely low exceedance probability.

A detailed description of the J-EVA storm model is given in Section 2 of Hansen, et al. [1]. Outlined here is a concise description of the storm model. It is to be noted that the storm model is currently used only for estimating the wave parameters such as H_{m0}, T_p, etc.

Storm events evolve in time with a build-up phase, a storm peak, and a decay as the storm moves away and/or a low-pressure system decay. It is important to accurately model this time evolution and not just the storm peak itself, as the time evolution has a direct impact on the short-term response, e.g., C_{max}. Directionality is also important in this context as wind and wave direction typically shift during a storm passage. The J-EVA storm model is used to capture this evolution of relevant metocean variables (H_{m0}, T_p, etc.) in storm events.

The individual waves and crests are stochastic processes with distributions conditional on the underlying sea state properties. This also means that not only storm peak H_{m0}, but also storm duration become important. These are estimated in the J-EVA storm model.

A storm that lasts for many hours is more likely to produce an abnormal wave crest compared to a storm that decays rapidly. This was already treated by Tromans and Vanderschuren in their most probable maximum response model [2]. The application of the Tromans and Vanderschuren model has been adapted to characterise the storm magnitude, not by the most probable maximum response, but rather by the storm peak significant wave height $H_{m0,p,eq}$ of an ‘‘equivalent storm’’ exhibiting a Gaussian bell-shaped profile in time. Storm duration is then quantified using the standard deviation σ_{eq} of the Gaussian bell, expressed in multiples of the spectral zero-crossing period. The latter is like Tromans and Vanderschuren’ N parameter. Read further in Section 2.1 of Hansen, et al. [1].

2.1 Directional and seasonal variability

J-EVA treats directional and seasonal variations in the statistical distribution of metocean variables (e.g., H_{m0}) using non-stationary extreme value distributions. This means that the distributions can vary with season and direction, according to the information in the historical extreme events.

The non-stationarity is implemented using penalised B-splines that allow for smooth variations of distribution parameters in multiple dimensions. This is done to capture the significant directional and seasonal variations in the wind, wave, and current conditions. Read further on the penalised B-splines in Section 2.2 of Hansen, et al. [1].

For datasets with directionally or seasonally distinct distributions, it is possible to use only one covariate. For example, the marginal distribution of water level is direction-less and only fitted with a seasonal covariate.

3 J-EVA statistical model

The J-EVA statistical model is used to estimate the statistical distribution of the characteristic storm values (see section 2.1 in [1]) of the metocean variables returned by the J-EVA storm model.

A detailed description of the J-EVA statistical model is given in Section 2.2 of Hansen, et al. [1]. What follows is an outline of the basis of the statistical model.

This model has a three-step process:

1. The independent estimate of non-stationary marginal models for each model parameter,
2. The estimation of the non-stationary conditional extreme models; and,
3. The estimation of the rate of occurrence of storm events by a Poisson process.

All parameters in 1) to 3) are inferred by Markov Chain Monte Carlo (MCMC) Bayesian inference.

MCMC is a statistical method to approximate a posterior distribution by randomly sampling in a probabilistic space, hence it utilises the known data. This technique has the advantage that the model parameters of interest are represented by statistical posterior distributions rather than fixed values and hence also provides an estimate of the uncertainty.

The marginal distributions are estimated using the assumption that the marginal probability distribution of each variable can be expressed as the sum of three parts. The first part describes the bulk of the data by a truncated gamma distribution using Bayesian inference with sample log-likelihood. While the second and third parts consisting of the upper and lower tails (if relevant) are then assumed to follow Generalised Pareto (GP) distributions. The tails are defined as exceedances of upper and lower quantile thresholds of the marginal distribution given covariates with specified non-exceedance probabilities.

3.1 Estimation of the model parameters

The estimation of the model parameters is carried out using Bayesian MCMC techniques. Model parameters, in this case, refer to the distribution parameters for the truncated gamma and GP distributions. Rather than using a single value for the model parameters, this method utilises a distribution of the model parameters which are then sampled from. A prior, or best-guess, based on the hindcast data is used to initiate the MCMC method. A cross validation scheme is applied to evaluate the predictive power of the spline model.

J-EVA integrates over uncertainty when providing extreme value estimates. This type of extreme value estimate is called posterior predictive. This is particularly important when J-EVA returns extreme value estimates for return periods far beyond the duration of the historical time series (from measurement or hindcast model) used for estimation, as the uncertainty in the estimates increases for increasing return periods. By integrating over the uncertainty, one accounts for the increased uncertainty and the provided extreme value estimates become more robust.

Posterior predictive distributions of metocean variables (e.g, H_{m0}, CS) are obtained by integrating across the posterior distributions of the model parameters and subsequently simulating many years. In practice this is done by integrating over a random set of iterations in the MCMC chains. Extreme values for various return periods are given by quantiles of the posterior predictive distributions (see Eq. 3.1). Using this approach, the extreme values provided by J-EVA implicitly include statistical uncertainty in contrast to stationary EVA used by DHI where bootstrapping is often performed providing confidence intervals.

The extremes calculated from shorter hindcast time series are not necessarily higher than extremes obtained from longer time series (even though the statistical uncertainty is higher), as the estimated extremes depend on the data itself. However, when everything else is equal, increased uncertainty will result in increased extreme value estimates, when posterior predictive estimation is used.

Results in the form of posterior predictive extreme values (of e.g., H_{m0}, C_{max}) are obtained from quantiles (q_r) in the distribution of the annual maximum. The relationship between quantile and return period is given by:

$$q_r = \exp\left(-\frac{1}{T_r}\right) \quad \text{Eq. 3.1}$$

For the evolution of each storm event needed for determining the long term distributions of the short-term responses (H_{max} and C_{max}) the J-EVA storm model is applied again to scale the simulated events with the physical correct historical events.

3.2 Conditional extreme model

A conditional extremes model, adopted from Heffernan and Tawn, [3], is used to model the joint probabilities. This type of joint probability model models the distributions of variables conditioned on one of the variables being extreme and is therefore useful for modelling the distribution of e.g., wave period or water level conditioned on extreme significant wave height. Figure 3.1 shows an example of a joint distribution of T_p and H_{m0} from 50,000 years simulated data compared to hindcast data. Likewise, parameters relevant for C_{max} (i.e., T_{01} and T_{02} and WL) are conditioned on extreme H_{m0}.

The conditional extreme model is further described in Section 1.4 and Section 5.3 of Hansen, et al. [1].

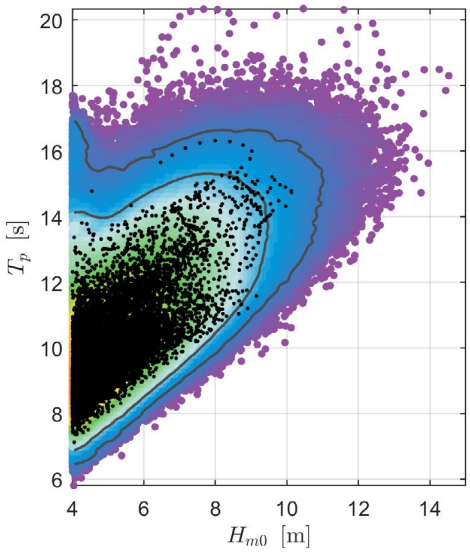

Figure 3.1 Example of joint distribution of T_p and H_{m0} [1].
T_p on H_{m0} for each sea-state in the simulated storms. Scatter plots of 50,000 years of simulated data (coloured round markers) compared to hindcast data (black dots); "warmer" colours indicate a higher rate of occurrence of simulated events. Solid lines represent directional density contours for the 10- and 100-year marginal extreme values.

4 J-EVA simulation

The concept of simulation is used to obtain the extreme value estimates based on the fitted statistical model parameters as explained in Section 3.1 and 3.2. The number of exceedances N_e of an extreme value is used as input, which is then applied on the largest chosen return period T_r. For example, if the largest T_r = 10,000 years, and if N_e is chosen as 50, then the number of simulations carried out for estimating the 10,000-year extreme are $5x10^5$. Extremes estimated for T_r<10,000 years will then have more exceedances contributing to the robustness of the estimate.

4.1 Directional Scaling

The concept and the need of directional scaling is explained in Forristall [4]. The concept itself is independent of the method used for estimating the extreme values. The directional scaling is applied to the estimated directional extremes following the recommendations in DNV [5].

In J-EVA, the implementation is carried out while simulating the extremes. In summary, a two-step scaling procedure is implemented for the marginal extremes.

1. The directional extremes are simulated for return periods corresponding to half the number of directional sectors. For example, if 16 directional sectors are used, this corresponds to simulating the directional extremes for return periods T_r = [1, 5, 10, 50, 80, 100, 1000, 10000] x 16/2 = [8, 40, 80, 400, 640, 800, 8000, 80000] years.
2. The estimated directional extremes are capped with the omnidirectional extreme corresponding to the original return periods. For example, if in step 1, the estimated H_{m0} = 14.9 m corresponding to a direction of 315° mean wave direction for T_r = 80000 years, then it is capped with H_{m0} = 14.6 m that corresponds to an omnidirectional H_{m0} for T_r = 10000 years.

The estimated fit parameters based on the unscaled extremes are used to evaluate the conditioned variables of the scaled extremes.

4.2 Simulation Optimization

The simulations used to obtain the extreme value estimates are optimised depending on the requested return periods, such that the very long simulations required to estimate extreme values with long return periods only include the relevant events above a high threshold, i.e., quantile of the storms. Shorter simulations with no threshold are then made for the short return period extremes. If the directional scaling is applied, and if the largest T_r = 80,000 years, then the optimization is carried out such that up to $T_r \leq 100$ years, the estimates are based on simulations of 80,000 years, while for $100 < T_r < 80{,}000$, the estimates are based on simulations of $N_e \times 80{,}000$ years.

5 Convolution of short-term distributions

The predicted events from the J-EVA storm model are numerically folded with the wave height and crest level distributions (e.g., Forristall [6] or Glukhovskiy [7]) to estimate the long-term distribution of the individual wave heights and crest levels. For further information, the reader is referred to Section 4 of Hansen, et al. [1].

The total water level is modelled conditionally on the extreme significant wave height. A total water level therefore becomes available for every storm and for every sea state in the storm such that it can be used in the short-term distribution.

6 Sampling of tidal signal

Tide is a deterministic process and thus not eligible for extreme value assessments assuming a random population, hence, to comply with statistical requirements, tidal variations are introduced separately to the extreme value estimation.

Water levels concurrent with waves are introduced via a model for the distribution of residual water level conditional on extreme H_{m0}, followed by the addition of a sampled tidal signal. By using this method, it has been assumed that the tide has no influence on H_{m0} nor on the residual water level. This assumption is often valid in intermediate to deep waters but may not be valid in shallow areas with the significant tide.

Tidal water level signals are sampled for every storm event from a hindcast tidal data series from within a period with similar seasonality to account for seasonal bias. The total water level, i.e., the distance from a fixed datum (MSL or LAT) to the still water level (SWL), is the sum of the residual and tidal water levels. It is, therefore, straightforward to include the effect of tide and surge on the extreme crest elevations in a statistically consistent manner.

Similarly, tidal current flow is sampled and combined with the residual current flow conditioned on the extreme waves.

7 Limitations on wave height

Wave breaking is implicitly accounted for via a depth-dependent reduction in the hindcast modelled H_{m0} (due to increased energy dissipation in the white-capping, bottom-friction, and wave breaking source terms).

Furthermore, for the long-term distribution of $H_{m0,p,eq}$ (equivalent peak H_{m0} from the storm model) has been limited to 0.6 times the water depth in the statistical model. This is considered a conservative estimate of the maximum depth-limited significant wave height. Actual evidence of depth limits to significant wave height in field data sets is very rare. However, based on previous experience including literature studies, there is no knowledge of values higher than 0.6 being reported anywhere.

In exposed and shallow areas, this will significantly limit the tail of the H_{m0} distribution, see Figure 7.1 for a graphical example, when comparing to other standard EVA approaches. The extrapolation of the extreme distribution extends past the expected physical limit of 0.6 times the water depth (in this example case, the water depth is approximately 17m).

Wave breaking is however not accounted for in the Forristall short-term distribution of C_{max} and only indirectly for some short-term distributions of H_{max}. (i.e., the Glukhovskiy distribution).

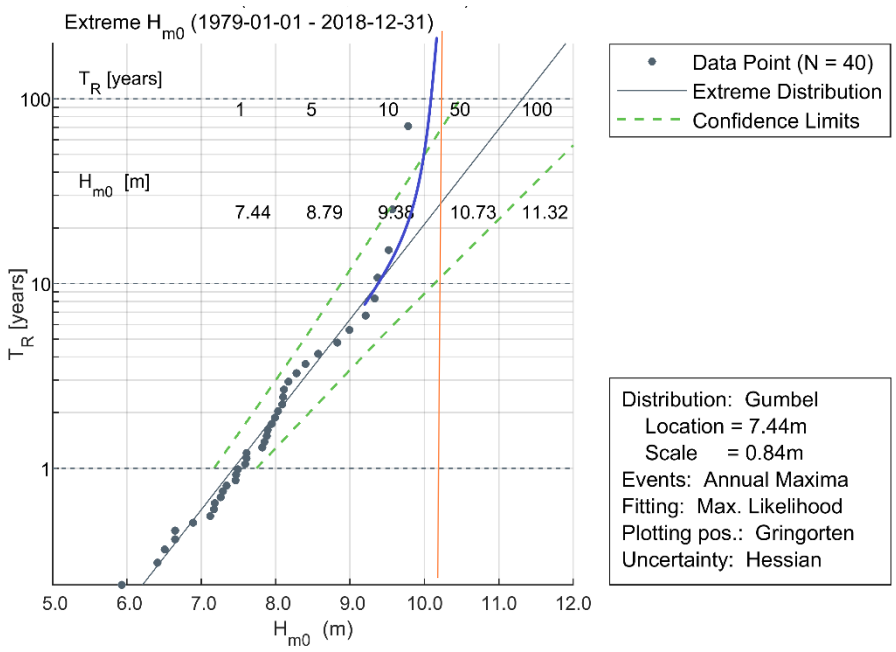

Figure 7.1 Example of extreme value distribution of H_{m0} at a water depth of 17 m with a Gumbel distribution fitted to the annual maxima using maximum likelihood (grey line). No limiting wave breaking is inferred. Upper limit of H_{m0} assumed as 0.6 x 17 = 10.2m shown by the orange line.
In such cases the limit of H_{m0} due to water depth in the J-EVA storm model would effectively reduce the extreme H_{m0} at the tail, also below the actual limit, i.e., towards the blue line.

8 References

[1] H. F. Hansen, D. Randell, A. R. Zeeberg, and P. Jonathan, "Directional–seasonal extreme value analysis of North Sea storm conditions," *Ocean Engineering,* vol. 195, 2020, doi: 10.1016/j.oceaneng.2019.106665.

[2] P. S. Tromans and L. Vanderschuren, "Response Based Design Conditions in the North Sea: Application of a New Method," presented at the Offshore Technology Conference, Houston, Texas, 1995. [Online]. Available: dx.doi.org/10.4043/7683-MS.

[3] J. E. Heffernan and J. A. Tawn, "A conditional approach for multivariate extreme values," *Journal of the Royal Statistical Society. Series B,* vol. 66, no. 3, pp. 497-546, 2004.

[4] G. Z. Forristall, "On the Use of Directional Wave Criteria," *Journal of Waterway, Port, Coastal, and Ocean Engineering,* vol. 130, no. 5, pp. 272-275, 2004, doi: 10.1061/(asce)0733-950x(2004)130:5(272).

[5] *Environmental Conditions and Environmental Loads*, DNV-RP-C205, DNV, 2021.

[6] G. Z. Forristall, "Wave Crest Distributions: Observations and Second-Order Theory," *Journal of Physical Oceanography,* vol. 30, no. 8, pp. 1931-1943, 2000, doi: dx.doi.org/10.1175/1520-0485(2000)030<1931:wcdoas>2.0.co;2.

[7] A. J. Battjes and W. H. Groenendijk, "Wave height distributions on shallow foreshore," *Coastal Enginnering,* vol. 40, no. 3, pp. 161-182, 2000.

Appendix E J-EVA Storm Model

See next pages.

DHI J-EVA Storm Model

Contents

Revisions

Date	Description	Initials
2021-08-13	Version 1.0.	SJA/JABE
2021-10-11	Version 1.1: Hansen et al. 2020 reference added	SJA

Nomenclature

Abbreviation	Explanation
CD	Current direction [°N] (flowing towards, true North, clockwise positive)
CS	Current speed [m/s]
WD	Wind direction [°N] (coming from, true North, clockwise positive)
WS	Wind speed [m/s]
H_{m0}	Zeroth moment significant wave height [m]
$H_{m0,p,eq}$	Equivalent Gauss-bell shaped storm peak H_{m0} [m]
H	Individual (trough-crest) wave height [m]
H_{max}	Maximum (highest) individual (trough-crest) wave height [m]
H_{mp}	Most probable maximum individual wave height in a storm event [m]
T_p	Spectral peak period [s]
T_{02}	Second moment wave period [s]
MWD	Mean Wave Direction [°N] (coming from, true North, clockwise positive)
PWD	Peak Wave Direction [°N] (coming from, true North, clockwise positive)
σ_{eq}	Equivalent Gauss-bell shaped storm standard deviation [no. of wave cycles]

1 DHI J-EVA Storm Model

The theory and methodology behind the DHI J-EVA storm model are described here. The methodology is based on the work presented in Hansen et al. (2020) [1].

The J-EVA (Joint-Extreme Values Analysis) storm model is a model for the description of wave characteristics of storm events. The model is used in conjunction with the J-EVA statistical model to describe the long-term distribution of individual wave and crest heights and possibly also wave-induced structural loading.

The model defines characteristic storm variables from the historical hindcast or measured record of slowly time-varying variables such as (but not limited to) significant wave height, peak period, mean or peak wave direction, storm surge and wind speed. These characteristic values are suitable for statistical modelling using the J-EVA statistical model. The statistical modelling of characteristic storm variables will allow for generation of long series of simulated storm parameters. The J-EVA storm model can then be applied in reverse to generate intra-storm time series of the slowly varying variables.

Numerical folding with any short-term distribution model of wave or crest height or a structural load or load response may be carried out on the intra-storm time series to generate the long-term distribution of the response.

1.1 Characterisation of Historical Storms

The J-EVA storm model is applied on a time series of slowly varying environmental variables. This time series must include the significant wave height and a measure of the mean wave period but can include any other environmental variable of interest. The time series must be on an equidistant time axis with sufficiently small-time step size that the time-evolution of the storm events of interest are adequately resolved.

The steps followed to convert this continuous time series into individual storm events and then to characterise each event are described in this section.

1.2 Wave Height and Storm Duration

Storm events are identified by their significant wave height. Standard metocean techniques for separating the continuous time series of significant wave heights into individual (storm) events consist in defining a minimum time separation between consecutive storm peaks and moreover often an additional requirement that the level must have dropped below a fraction of the minor of consecutive peaks in order for those to be defined as two separate events. This additional requirement ensures that storms with long durations are not unintentionally split into separate events.

The time series of H_{m0} is de-clustered into independent events by requiring that there is a pre-specified minimum interevent time between events. The minimum interevent time is dependent on the meteorological events generating the storms but is typically in the order of 18-36 hours for extra-tropical cyclones. Moreover, events are only separated if the significant wave height has passed below 75% of the minor of two adjacent events.

The distribution of the maximum short-term response in each historical storm is then calculated. The empirical short-term distribution of individual wave height H conditional on H_{m0} by Forristall (1978) is typically applied, though the actual choice of short-term distribution model is not important, as long as the distribution is continuous. The Forristall (1978) short-term distribution of H conditional on H_{m0}, $P(H < h|H_{m0})$, is given by:

$$P(H < h|H_{m0}) = 1 - \exp\left(-\left(\frac{h}{0.681H_{m0}}\right)^{2.126}\right) \qquad (1.1)$$

The distribution of the maximum wave in storm i, $H_{max,i}$ is given by the following product over the n_i sea states making up storm i:

$$P\left(H_{max,i} < h\right) = \prod_{j=1}^{n_i} P\left(H < h | H_{m0,j}\right)^{N_j} \quad (1.2)$$

The number of waves in sea state j, N_j, is estimated by dividing the duration of the sea state (time step size in the input time series) by the mean zero-crossing period[1] over the sea state. The most probable storm maximum wave height, $H_{mp,i}$, is found by solving the following equation for h:

$$P\left(H_{max,i} < h\right) = \frac{1}{\exp\left(1\right)} \approx 0.37 \quad (1.3)$$

It is shown in the original work by Tromans and Vanderschuren (1995), that when $P(H|H_{m0})$ is of a Weibull type distribution, Eq. (1.2) converges to a generalised Gumbel distribution:

$$P\left(H_{max,i} < h\right) \sim \exp\left(-\exp\left(-\ln N_i \left(\left(\frac{h}{H_{mp,i}}\right)^{\alpha} - 1\right)\right)\right) \quad (1.4)$$

where α is the shape factor of the wave height distribution (=2.126 in the Forristall 1978 distribution) and N_i is the equivalent number of waves in the storm.

The duration of the storm and thereby the value of N is related to the narrowness of the distribution of the storm maximum wave. Storms with long durations and thereby many sea states of similar magnitude will have a narrower distribution of the storm maximum wave, compared to those storms in which the maximum wave will come within a relatively short period in time (i.e. within very few sea states).

This property is used in the J-EVA storm model to characterise storms by peak magnitude and a duration. A Gauss-bell shaped curve is chosen to represent the variation in time of H_{m0}. The variation in time of H_{m0} is defined by equivalent storm peak, H_{m0}, hereafter termed $H_{m0,p,eq}$, and equivalent storm duration given by the Gauss-bell standard deviation, σ_{eq}, as:

$$H_{m0}(t^*) = H_{m0,p,eq} \times \exp\left(-\frac{(t^*)^2}{2\sigma_{eq}^2}\right) \quad (1.5)$$

t^* is a pseudo-time measured in *number of wave cycles* and can be converted to true time by use of the slowly varying mean wave period. Thus, $t^* = 0$ at the storm peak ($H_{m0} = H_{m0,p,eq}$) and any $t^* < 0$ defines the number of wave cycles that will pass before the storm peak is reached, whereas any $t^* > 0$ defines the number of wave cycles that have passed since the storm peak.

Best-fit values of the peak ($H_{m0,p,eq}$) and standard deviation (σ_{eq}) of the Gauss-bell shaped storm are found by mean-square error minimisation of the differences between the actual storm maximum wave height probability density and that of the Gauss-bell shaped storm. The minimisation is carried out as follows:

Sea states with $H_{m0} < 0.75 \times H_{m0,p,eq}$ are found to have insignificant impact on the distribution of storm maximum wave height and can be neglected[2]. From Eq. (1.5), we have that the Gauss-bell shaped storm will cross under 75% of $H_{m0,p,eq}$ at a distance from the peak of $0.759\sigma_{eq}$ waves. Hence, we create an evenly spaced vector, $\boldsymbol{t}_m^*$ of m points, $\boldsymbol{t}_m^* \in [-0.759\sigma_{eq}; 0.759\sigma_{eq}]$ and evaluate H_{m0} along this vector for storm i:

$$H_{m0}(\boldsymbol{t}_m^*) = H_{m0,p,eq,i} \times \exp\left(-\frac{(\boldsymbol{t}_m^*)^2}{2\sigma_{eq,i}^2}\right) \quad (1.6)$$

[1] The second moment period T_{02} is used as a proxy for the zero-crossing period when spectral wave model hindcast data is used as input

[2] Though sea states with less than 75% of the peak significant wave height have negligible influence on the most probable maximum wave in the storm, sea states down to 65% of peak significant wave height have been included in the build-up of the storm, as these typically contain some of the steepest sea states, and the maximum wind speed may also fall early in the storm trajectory.

Each point along this vector represents a sea state of $1.52\sigma_{eq,i}/m$ waves. The distribution of the maximum wave in the storm is now given by Eq. (1.2), i.e.:

$$P\left(H_{max,i} < h\right) = \prod_{j=1}^{m} P\left(H < h | H_{m0}\left(t^*_{m,j}\right)\right)^{1.52\sigma_{eq,i}/m} \quad (1.7)$$

The probability density is obtained by numerical differentiation of Eq.(1.7) and the squared difference of this probability density function and that of the actual storm is computed. Minimisation of the squared difference is carried out by changing the values of $H_{m0,p,eq,i}$ and $\sigma_{eq,i}$, whereby best-fit values of these parameters are obtained for storm i.

Two examples of storm characterisation are shown in Figure 1.1. The first storm (top panel) is an example of a persistent storm lasting for many hours, while the second storm (bottom panel) is more intense in its peak but lasting only a few hours. These differences are reflected in the relative values of $H_{m0,p,eq}$ and σ_{eq}.

1.3 Associated Environmental Variables

Characteristic storm values of all associated environmental variables to be included in the subsequent joint-probability analysis are required. Examples associated variables are:

- Peak wave direction, PWD
- Peak period, T_p
- Second moment period, T_{02}
- Directional spreading, σ_θ
- Residual water level, WL_{rsdl}
- Residual current speed, CS_{resi} and direction CD_{rsdl}
- Wind speed, WS and wind direction WD

These variables vary during the storm and weighted average values are calculated to provide a characteristic value of the variable for each storm. The weight factor, w_j, for sea states $j, j = 1{:}n_i$ where n_i is the number of sea states in storm i, are computed from the contribution of the individual sea states to the total storm most probable maximum wave, H_{mp}:

$$w_j = \alpha\left(H_{mp,1:n} - H_{mp,1:n,\sim j}\right) \quad (1.8)$$

where $H_{mp,1:n}$ is the most probable maximum wave height of the storm considering all sea states in the storm and $H_{mp,1:n,\sim j}$ is the most probable maximum wave height when sea state j is omitted and α is a normalisation factor. An overbar (e.g. $\overline{T_p}$) is used to denote a characteristic (weighted average) value of an environmental variable.

The characteristic storm second moment period $\overline{T_{02}}$ is shown in Figure 1.1 for the two examples storms. $\overline{T_{02}}$ takes values close to the values at the storm peak.

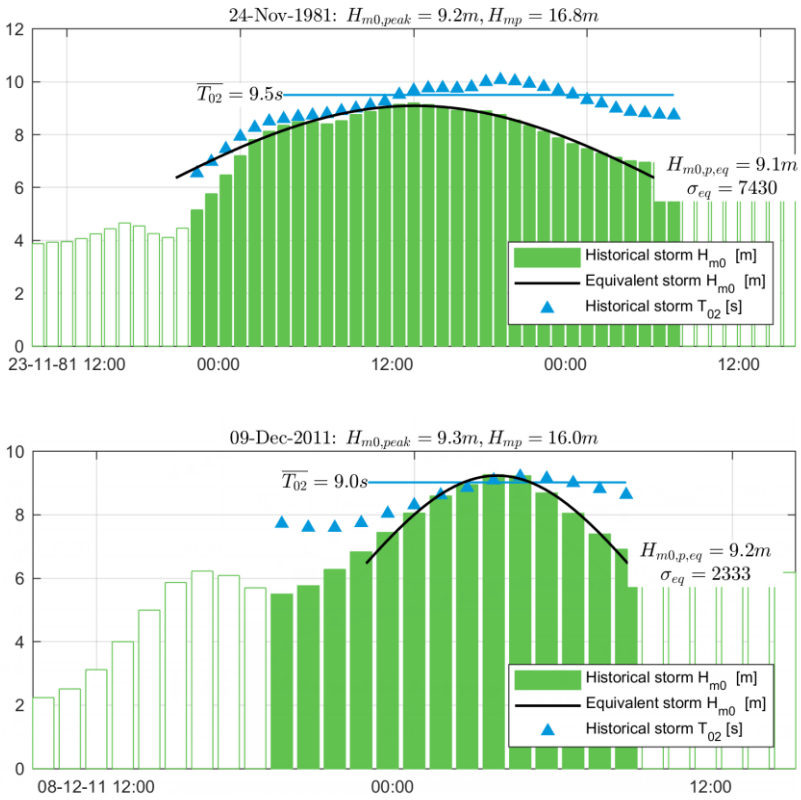

Figure 1.1 Two examples of hindcast historical storms and storm model parameterisation. Vertical green bars[3]: Hourly values of H_{m0}. Blue triangles: Hourly values of T_{02}. Characteristic storm variables $H_{m0,p,eq}, \sigma_{eq}$ and $\overline{T_{02}}$ values printed on figure.

1.4 Simulation of Intra-Storm Variation

The J-EVA storm model is also used to simulate intra-storm variation of the environmental variables model. The intra-storm variation refers to the hourly variation of the variables during a storm event exemplified by for instance the build-up and subsequent decay of wind speed and significant wave height, the rotation of the mean wave direction and the increase in wave age from steep young wind waves during build-up to swell waves during storm decay.

The simulation of intra-storm variation consists in matching up simulated storms with similar historical storms followed by a scaling of the similar historical storm time series.

1.4.1 Similarity and Storm Resampling

A methodology developed to identify the historical storms most similar to the simulated storm is described in this section. The method builds on a flexible concept of storm dissimilarity. The smaller the dissimilarity, the more representative the historical storm is assumed to be of the simulated storm.

The dissimilarity criteria are established in order to select a historical storm to represent the storm modelled through the J-EVA statistical model. The dissimilarity criteria are inspired by Feld et.al (2015).

In the following, Ω is used to denote any characteristic storm variable (e.g. $H_{m0,p,eq}$ or $\overline{T_p}$) and ω to denote the corresponding intra-storm variable (H_{m0} or T_p).

[3] The filled bars mark the sea states which are retained from each storm for subsequent intra-storm simulation, see section 1.4.

Dissimilarity is first calculated for each variable listed below as follows for historical storm, i, and simulated storm, k:

$$d_{\Omega,\mathrm{i,k}} = \left|\Omega_{HIST,i} - \Omega_{SIM,k}\right| / \sigma_{\Omega} \quad (1.9)$$

with σ_{Ω}[4] being the standard deviation of this variable through all included historical storms. This weight factor is found to provide a reasonable balance between the various variables, but it is possible to apply weight factors in addition to this, in order to better match for instance significant wave height between historical and simulated storms.

Dissimilarities are calculated for the relevant variable which may be considered important in terms of describing the storm evolution.

Overall storm dissimilarity for simulated storm k, d_k, is calculated by summing up the square of the individual dissimilarities, for each historical storm, i.e.:

$$d_k^2 = \sum_{i=1}^{n} \sum_{\Omega=1}^{v} d_{\Omega,\mathrm{i,k}}^2 \quad (1.10)$$

where $\Omega = 1{:}\,v$ represent the v different environmental variables included in the dissimilarity criterion. After having ranked the historical storms in terms of (dis)similarity, one of the most similar historical storms is picked randomly amongst the least dissimilar ones. The randomly selected storm is then used to represent the intra-storm variability of the modelled storm, after appropriate scaling (see next section) is conducted.

Typically, the representative storm is selected amongst the 20 most similar storms, but the end results are not very sensitive to this number because of the applied scaling.

1.4.2 Historical Storm Scaling

Having sampled a historical storm amongst the most similar ones, the intra-storm variation of the historical storm is scaled such that the characteristic storm variables of the scaled storm matches those of the simulated storm.

The proposed scaling methodology assumes that a constant scaling factor applies for the entire storm. As water levels vary around zero, a reference level of 10 meters below the sea surface is used in order to avoid division by zero.

Scaling of the selected historical storm variables to generate the time series of simulated storms is conducted as follows:

1. Establish a scaling or correction factor based on the characteristic storm variables of the simulated (subscript SIM) and selected historical storm (subscript $HIST$) using the generic formulation:

$$\alpha_{\Omega} = \Omega_{SIM} / \Omega_{HIST} \quad (1.11)$$

2. Correct the historical storm time series of parameter ω_{HIST} to obtain the intra-storm variability of the simulated storm, $\omega_{SIM.j}$, as follows (for time step j)):

$$\omega_{SIM,j} = \alpha_{\Omega} \cdot \omega_{HIST,j} \quad (1.12)$$

Specifically, for directional variables (wind, wave and current directions, here generalised by the notation θ), a rotation rather than scaling is applied:

$$\alpha_{\theta} = \overline{\theta_{SIM}} - \overline{\theta_{HIST}} \quad (1.13)$$

The intra-storm variability of the directional variable is then obtained as (at time step j):

$$\theta_k = \alpha_{\theta} + \theta_{HIST,j} \quad (1.14)$$

[4] σ_{MWD} and σ_{Season} correspond to half of the standard deviation of the corresponding parameters, to account for their periodicity.

Typically, peak (or mean) wave direction is used as a co-variate (distributions vary with wave direction) and wind and current directions are not simulated in the J-EVA statistical model. In this case, the wave direction rotation factor, $\alpha_{\mathrm{PWD},}$ is also used to rotate the current and wind direction time series such that wind-wave and current-wave misalignment from the historical storm is maintained in the simulated storm.

For residual water levels, that can also take negative values, the scaling is done relative to a minimum level, WL_{ref}, that is never surpassed:

$$WL_j = \left(WL_{HIST,j} + WL_{Ref}\right)\frac{\overline{WL_{SIM}} + WL_{ref}}{\overline{WL_{HIST}} + WL_{Ref}} - WL_{Ref} \qquad (1.15)$$

The reference water level could be taken as the water depth at the site, which in practice would mean that the water level in the simulated storm would be the water level in the historical storm shifted by the difference $\overline{WL_{SIM}} - \overline{WL_{HIST}}$. Typically, we use $WL_{Ref} = 10\,m$, which implies a moderate scaling of the water levels beyond the scaling that is coming from the simulated value from the long-term model, $\overline{WL_{SIM}}$.

In addition to the adjustment of the time series values, the time is also scaled in order to maintain the number of waves in the storm, and therefore keep H_{max} and C_{max} estimates the same. The time scaling is performed as follows:

$$Time_{SIM} = Time_{HIST} \cdot \alpha_{T_{02}} \cdot \alpha_{\sigma_{eq}} \qquad (1.16)$$

with $\alpha_{T_{02}}$ and $\alpha_{\sigma_{eq}}$ being the scaling factors applicable for T_{02} and storm duration σ_{eq}, respectively.

It follows from this scaling method that an exact recovery of the historical storm is obtained in the case of an exact match between the simulated and historical characteristic storm variables.

Storms are defined to begin at the last up-crossing of 60% of peak H_{m0} prior to the peak and end at the first down-crossing of 75% of peak H_{m0} after the storm peak. Sea states with H_{m0} > 75% of peak H_{m0} are contributing to the distribution of the maximum wave within a storm. The extension down to 60% of peak H_{m0} at the storm build-up is introduced to ensure that the peak wind speed is included in the storm. The sea states thus included are marked as filled bars in Figure 1.1. Storm peaks must as a minimum be separated by the specified inter-event time, typically between 18 and 36 hours for extra-tropical cyclones, to be treated as separate events.

1.5 Heights and Periods of Individual Waves

The methods described in the previous sections define a way of developing time series of the slowly varying parameters (H_{m0}, T_p etc.) in each simulated storm, whereby we obtain the long-term distribution of the slowly varying parameters. From these time series we can easily derive the long-term distribution of individual wave and crest heights.

The individual wave and crest heights are stochastic variables conditional on the properties of the underlying sea state, and their distributions are typically termed the short-term distributions. We use Monte Carlo simulation to fold these short-term distribution with the long-term distribution of the underlying slowly varying sea state parameters. This Monte Carlo simulation involves sampling a maximum short-term response for every sea state in every simulated storm.

The Forristall crest height distribution is used here as an example of how to sample the hourly maximum of a short-term response. The inverse cumulative distribution function of the hourly maximum Forristall crest height is given by:

$$F^{-1}(\eta_{max}) = H_{m0}\alpha\left(-\ln\left(1 - P^{\frac{1}{N}}\right)\right)^{\frac{1}{\beta}} \qquad (1.17)$$

where:

P Non-exceedance probability

N	Number of waves in sea state	($\approx 3600s/T_{02}$ for a one-hour sea state)
α	Distribution shape	$\sqrt{2}/4 + 0.2568S_1 + 0.0800Ur$ (Forristall Crest)
β	Distribution shape	$2 - 1.7912S_1 - 0.5302Ur + 0.2824Ur^2$ (Forristall Crest)
		$S_1 = \frac{2\pi}{g}\frac{H_{m0}}{T_{01}^2}$
		$Ur = \frac{H_{m0}}{k_1^2 d^3}$
k_1	Wave number for frequency	$1/T_{01}$
d	Water depth	

The Monte Carlo analysis simply consists in sampling the non-exceedance probability P randomly and independently for every sea state and calculate the corresponding η_{max}. Note that the short-term distribution varies from sea state to sea state as the parameters H_{m0}, T_{01}, T_{02} and the water depth may vary (the latter due to effects of tide and surge). The long-term distribution of annual maximum crest height and corresponding extreme value estimates are derived by considering only annual maximum crest height, as explained in Eq. (1.5).

Crest height relative to a fixed datum are obtained by adding tide and surge values for each sea state prior to extraction of annual maxima.

1.5.1 Associated Wave Periods

The period of individual maximum waves (T_{Hmax}) will vary because of varying sea state characteristics (variability of T_p given H_{m0}) but also because of the randomness of the sea state itself. The most probable period, given a sea state (wave spectrum), is well approximated by the so-called linear new wave, [2], but there is obviously some random variability around this most probable value. This latter variability has been combined (convolved) with the random variability of the sea state characteristics by simulating linear random wave trains from a frequency spectrum for the sea states giving rise to the annual maximum waves and extracting the period of the highest wave from each simulation. Any frequency spectrum can be used for this, but the JONSWAP spectrum is typically adopted.

To obtain stable empirical conditional distributions of the wave periods many simulated sea states are required.

1.6 References

[1] P. S. Tromans and L. Vanderschuren, “Response Based Design Conditions in the North Sea: Application of a New Method,” *OTC-7683,* pp. 387-397, 1995.

[2] P. S. Tromans, A. R. Anaturk and P. Hagemeijer, “A new model for the kinematics of large ocean waves- Application as a design wave.,” *International Society of Offshore and Polar Engineers,* 1991.

[3] G. Feld, D. Randell, Y. Wu, K. Ewans and P. Jonathan, “Estimation of Storm Peak and Intra-Storm Directional-Seasonal Design Conditions in the North Sea,” *OMAE,* 2015.

[4] G. Z. Forristall, “On the Statistical Distribution of Wave Heights in a Storm,” *Journal of Geophysical Research,* pp. 2353-2358, 1978.

[5] H. Hansen, D. Randell, A. Zeeberg and P. Jonathan, “Directional-seasonal extreme value analysis of North Sea storm conditions,” *Ocean Engineering,* vol. 194, p. 34, 2020.

Appendix F J-EVA Statistical Model

See next pages.

DHI J-EVA Statistical Model

Contents

Revisions

Date	Description	Initials
2021-08-13	Version 1.0.	SJA/JABE
2021-10-11	Version 1.1 – Reference to Hansen et al. 2020 added	SJA

Nomenclature

Abbreviation	Explanation
iid	Independent Identically Distributed (random variable)
LT	Lower Tail
MCMC	Markov Chain Monte Carlo
UT	Upper Tail

1 DHI J-EVA Statistical Model

This document describes the theory and methodology of the DHI J-EVA statistical model. The methodology is based on the work presented in Hansen et al. (2020) [1].

The J-EVA (Joint-Extreme Values Analysis) statistical model is a tool for making extreme value analysis of a set of parameters with a-priori unknown joint dependence properties. Application of J-EVA requires as input a set of independent 'events' with concurrent values of the parameters being modelled. A typical example is storm peak significant wave heights, associated wave period, storm surge, wind speed, but the tool is generic and can model any kind of stochastic non-discrete parameters, as long as they fulfil the requirements of independence and identical distribution (iid). The input data may come from measurements or numerical hindcast models or a combination hereof, and the usual requirements to data consistency and quality also apply here.

Covariates may be defined if a-priori knowledge about variations in extremal properties is suspected. Typical examples of covariates are direction and/or season. Non-parametric smooth variations with covariate(s) are implemented using a B-spline technique (see Section 1.3 for details) and periodicity (as is the case for both direction and season) is possible. The use of covariates also implies that the requirement of identical distribution only applies for random variables sharing the same covariates (as for instance waves from the same direction occurring during the same time of year). It is not recommended to apply the model across discontinuous (abrupt) covariate variations. Extreme value models incorporating covariates are called non-stationary extreme value model in the statistical literature.

The statistical uncertainty due to the typically limited sample size of historical extremes is estimated by the tool and may be propagated through to the end results. A Bayesian Markov Chain Monte Carlo (MCMC) technique is adopted (see Section 1.4 for details).

1.1 Model components

The J-EVA statistical model contains the following model components.

- Marginal models describing the marginal distribution of each parameter (i.e., the distribution of the parameter without considering the values of the remaining parameters)
- Rate of occurrence describing how often a parameter (event) occurs
- Conditional extremes model describing the distribution of other parameters conditional on a selected parameter being extreme

Each of the components is detailed below.

1.2 Marginal models

Marginal (univariate) distributions are fitted to each stochastic variable in turn. A combination of a gamma (Γ) distribution, modelling the bulk of the data, and Generalized Pareto (GP) tails modelling the distribution tails above a threshold is used for the marginal distributions. Whenever relevant, both the upper and lower tails are modelled with a GP distribution, the lower tail basically being a GP tail fitted to the reversed data below the low threshold.

$$P(x) = \begin{cases} P_\Gamma(u_1|\alpha,\mu)\left\{\left(1+\xi_1\frac{u_1-x}{\zeta_1}\right)^{-\frac{1}{\xi_1}}\right\} & ,x < u_1 \\ P_\Gamma(x|\alpha,\mu) & ,u_1 \le x \le u_2 \\ 1-\left(1-P_\Gamma(u_2|\alpha,\mu)\right)\left\{\left(1+\xi_2\frac{x-u_2}{\zeta_2}\right)^{-\frac{1}{\xi_2}}\right\} & ,x > u_2 \end{cases} \quad (1.1)$$

The gamma distribution is given by:

$$P_\Gamma(x|\alpha,\mu) = \frac{1}{\Gamma(\alpha)}\gamma\left(\alpha,\frac{\alpha}{\mu}x\right) \quad (1.2)$$

where $\Gamma(\alpha)$ is the complete gamma function and $\gamma\left(\alpha,\frac{\alpha}{\mu}x\right)$ is the lower incomplete gamma function.

The model parameters defining the marginal distributions are:

a	gamma distribution shape parameter
μ	gamma distribution mean parameter (gamma shape multiplied with gamma scale parameter)[1]
ξ_1	GP shape parameter for lower tail
ζ_1	GP scale parameter for lower tail[2]
ξ_2	GP shape parameter for upper tail
ζ_2	GP scale parameter for upper tail

The thresholds, at which the GP tails take over, are set as quantiles in the gamma distribution of the bulk data, i.e.

$$u_1 = P_\Gamma^{-1}(\kappa_1) \quad (1.3)$$

$$u_2 = P_\Gamma^{-1}(\kappa_2)$$

where κ is a constant (covariate-free) non-exceedance probability. Threshold uncertainty is included ensemble averaging results over a range of values for κ_1 and κ_2. These are sampled from a uniform distribution over a pre-set quantile interval.

The model parameters are estimated in a sequential way; first the gamma distribution is fitted to all data, then the threshold is calculated from the fitted gamma distribution and sampled threshold non-exceedance probability and finally the GP lower and upper tails fitted independently to the data sample below u_1/above u_2 respectively. The log-likelihood functions are:

$$\ell_{\Gamma,j}(\boldsymbol{z}|\boldsymbol{b}) = -\sum_{i=1}^{n}\left\{(\alpha-1)\ln z_{ij} - \frac{\alpha}{\mu}z_{ij} - \ln\Gamma(\alpha) - a(\ln\mu - \ln\alpha)\right\},$$

$$\ell_{GP_{LT},j}(\boldsymbol{z}|\boldsymbol{b}) = -\sum_{i:\, z_{ij}<u_1}\left\{\ln\zeta_1 + \left(1+\frac{1}{\xi_1}\right)\ln\left(1+\frac{\xi_1}{\zeta_1}(u_1 - z_{ij})\right)\right\} \quad (1.4)$$

$$\ell_{GP_{UT},j}(\boldsymbol{z}|\boldsymbol{b}) = -\sum_{i:\, z_{ij}>u_2}\left\{\ln\zeta_2 + \left(1+\frac{1}{\xi_2}\right)\ln\left(1+\frac{\xi_2}{\zeta_2}(z_{ij} - u_2)\right)\right\}$$

[1] The distribution parameters are practically uncorrelated with this formulation of the gamma distribution. This improves mixing of the MCMC chain

[2] As for the gamma distribution, an orthogonal parameterization has been used, where adjusted scale parameter, $\nu = \zeta(1+\xi)$, is sampled. For the ease of interpretation, the results are, however, presented for the scale parameter ζ.

1.3 Rate of occurrence

The occurrence of events is considered a Poisson process and the Poisson annual rate of occurrence ρ is required for estimation of annual non-exceedance probabilities. In the covariate-free case, ρ is simply estimated by the total number of historical events divided by the length of the historical data series in years. In the case of covariates, the covariate domain is divided into m bins of constant area, Δ, and the rate the log-likelihood function of ρ approximated by [2]

$$\ell_{\rho,j}(\boldsymbol{z}|\boldsymbol{b}) = \sum_{k=1}^{m} c_k \ln\big(\rho(k\Delta)\big) - \Delta \sum_{k=1}^{m} \rho(k\Delta) \tag{1.5}$$

where c_k is the number of threshold exceedances in bin k.

1.4 Conditional extremes

The conditional extremes model by Heffernan & Tawn (2004), model distributions of parameters conditional on one parameter being extreme. This is useful for modelling for instance the distribution of spectral peak period or wind speeds when the significant wave height is extreme.

The original conditional extremes model proposed by Heffernan & Tawn makes use of probability integral transform to marginal distributions with standard Gumbel distributions. This introduces asymmetry in the marginal distributions and makes modelling of negatively dependent variables somewhat more complicated than positively dependent variables. Keef, Papastathopoulos, & Tawn (2013) propose a modification of the model replacing the Gumbel margins by Laplace margins whereby both positive and negative tails become exponential. This modification to the original model is applied in J-EVA.

The marginal distributions are defined over the entire range from the 'lower' end-point of the lower tail to the upper end-point of the upper tail by the combined Gamma-GP model (Eq. (1.1)).

Probability integral transformation to Laplace margins is given by:

$$Y_j = \begin{cases} \ln\big(2\mathrm{P}\,(X_j)\big), & \mathrm{P}\big(X_j\big) < 0.5 \\ -\ln\Big(2\big(1-\mathrm{P}(X_j)\big)\Big) & \mathrm{P}\big(X_j\big) \geq 0.5 \end{cases} \tag{1.6}$$

The Heffernan & Tawn (2004) conditional distribution for a set of variables with Laplace margins simplifies into one function for both positive and negative dependence (Keef, Papastathopoulos, & Tawn, 2013):

$$\begin{gathered} \big(Y_{j^c}|Y_j = y\big) = a_j y + y^{b_j} W_j \\ j, j^c = 1,2, j^c \neq j \end{gathered} \tag{1.7}$$

with the random variable, Y_{j^c}, being conditioned on the random variable, Y_j. We use notation Y to indicate that these variables have Laplace margins. W_j is a random variable from an unknown distribution. We introduce the additional parameters, m and s and assume that $Z_j = \big(W_j - m_j\big)/s_j$ follows a common distribution independent of covariates. Hence Eq. (1.7) may be written as:

$$\begin{gathered} \big(Y_{j^c}|Y_j = y\big) = ay + y^{b_j}\big(m_j + s_j Z_j\big), \\ j, j^c = 1,2, j^c \neq j \end{gathered} \tag{1.8}$$

The negative log-likelihood for pairs of the sample $\{y_{i1}, y_{i2}\}$ is given by:

$$\ell_{CE,j} = \sum_{i, x_{ij} > \psi_{ij}(\theta_i, \phi_i \lambda_j)} \left\{ \ln s_j y_{ij}^{\beta_j} + \frac{\Big(y_{ij^c} - \big(a_j y_{ij} + m_j y_{ij}^{b_j}\big)\Big)^2}{2\left(s_j y_{ij}^{\beta_j}\right)^2} \right\}, \tag{1.9}$$

$$j, j^c = 1,2, j^c \neq j$$

$u_{CE,j}$ is the threshold with non-exceedance probability, λ_j, adopted for the conditional extremes model, meaning that the model is fitted to pairs of variables for which the non-exceedance probability of the conditioning variable exceeds λ_j. This threshold is set independently of the Generalized Pareto threshold u_2, and may be lower than that since the distribution below the GP threshold u_2 is defined by the gamma distribution.

Conditional extremes model threshold uncertainty is included by sampling λ_j from a uniform distribution over a pre-set quantile interval followed by ensemble averaging results over several different values of λ_j.

Residuals, r, are calculated from the estimated model parameters as:

$$r_{ij} = \frac{1}{\hat{s}_j}\left(\left(y_{ij^c} - \hat{a}_j y_{ij}\right) y_{ij}^{-\hat{b}_j} - \hat{m}_j\right) \tag{1.10}$$

Multidimensional dependencies are modelled through the residuals. For each parameter, $j = 2, \dots, n$, with n being the total number of variables modelled, the residual is calculated for each event i leading to a vector of residuals for each event $\boldsymbol{r}_i = [r_{i2}, \dots, r_{in}]$. These n vectors of residuals are later used for simulating data in the model.

It then follows that the Laplace marginal value of parameter j conditioned on parameter 1 is given by

$$\left(Y_j | Y_1 = y\right) = a_j y + y^{b_j}\left(m_j + s_j r_j\right) \tag{1.11}$$

The probability transform in Eq. (1.6) is inversed to get the non-exceedance probabilities of the associated parameters. The magnitude of each associated parameter is then calculated from its marginal distribution.

1.5 Covariates

Penalised B-splines are used to model the parameter variation with covariate. The basic idea of penalised B-splines, originally introduced by Eilers & Marx (1996), is to use B-splines with a moderately large number of evenly-spaced knots and control the parameter smoothness by a variance penalty factor, τ^2.

B-spline regression is started by dividing the domain over which to fit a curve into n' equal intervals by specifying the position of $n' + 1$ knots. B(asis)-splines are then constructed as sequences of polynomial functions of degree, q, connected the knots. Each B-spline is positive in a range spanning $q + 2$ knots, and zero elsewhere. Curve-fitting using B-splines consists in finding the coefficients, $\beta_{i=1:n'+q}$, with which to multiply the B-splines. The function value may be expressed as the linear combination of the spline basis, B, and the coefficients.

$$f(x) = \sum_{i=1}^{n'+q} \beta_i B_i(x) \tag{1.12}$$

Penalised B-splines (P-splines) are an extension of B-splines in which a penalty is put on the differences between adjacent β-coefficients. The degree of roughness is controlled by a variance parameter, τ^2, and the difference penalty matrix, $\mathbf{K}$. For first order differences, the difference matrix is given by:

$$\mathbf{K} = \begin{bmatrix} 1 & -1 & & & \\ -1 & 2 & -1 & & \\ & \ddots & \ddots & \ddots & \\ & & -1 & 2 & -1 \\ & & & -1 & 1 \end{bmatrix} \tag{1.13}$$

The basis of B-splines and the effect of roughness penalty, introduced through τ^2, is illustrated in Figure 1.1.

Both directional and seasonal variations are periodic. Periodic smoothing is introduced by 'wrapping' the spline at the ends. Specifically, the last q basis splines are merged with the first q splines and the total number of basis functions reduced by q. The difference penalty matrix is wrapped similarly, i.e., $\mathbf{K}$ is now:

$$\mathbf{K} = \begin{bmatrix} 2 & -1 & & & \dots & -1 \\ -1 & 2 & -1 & & & \\ & -1 & 2 & -1 & & \\ \vdots & & \ddots & \ddots & \ddots & \\ & & & -1 & 2 & -1 \\ -1 & & & & -1 & 2 \end{bmatrix} \tag{1.14}$$

B-splines are extendable to higher dimensions through tensor-product B-splines (see e.g. [3]). The multidimensional surface is now described by tensor-products of B-splines. The tensor-product B-splines in two dimensions are illustrated in Figure 1.2. The coloured shapes underlying the surface are the individual tensor-product B-splines scaled by the respective coefficients. The total number of β-coefficients to estimate is now $(n'_\theta + q) \times (n'_\phi + q)$. Different number of knots and different penalty factors may apply for each dimension. However, as Figure 1.2 also illustrates, large roughness penalty in one dimension may influence the smoothness in other dimensions. This indicates that roughness penalty should be determined for all dimensions simultaneously.

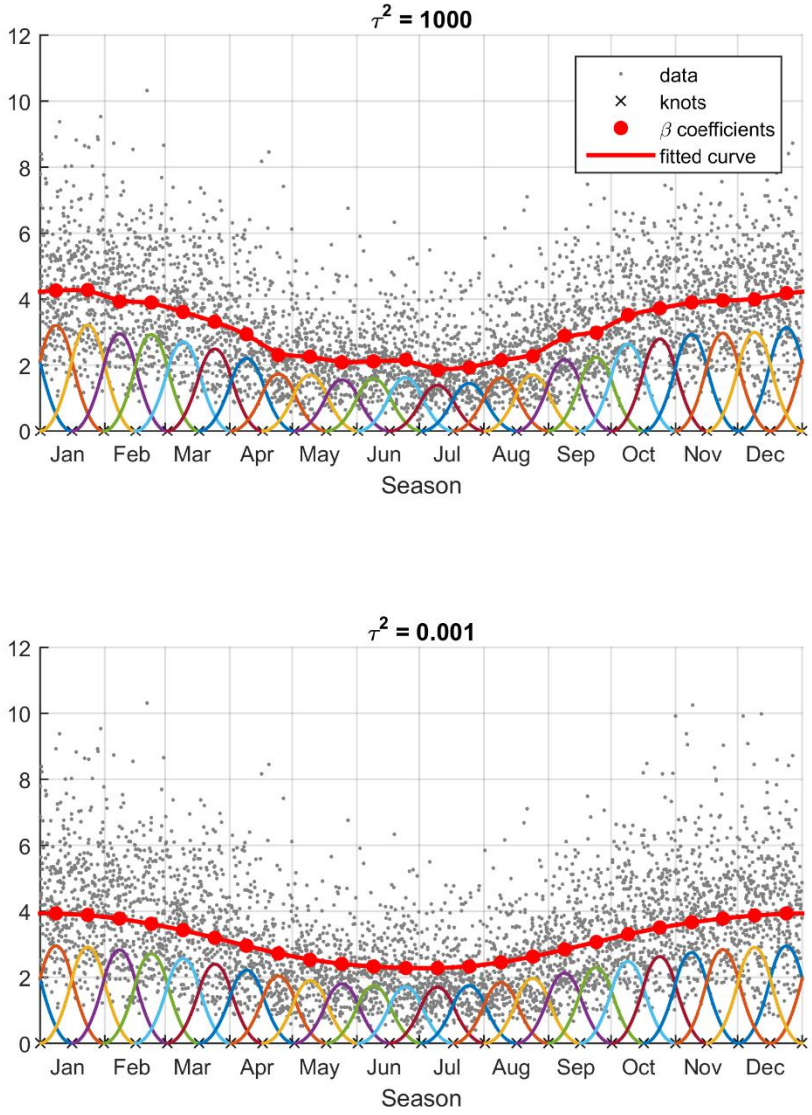

Figure 1.1 Quantile regression analysis for some fictive seasonally varying parameter, illustrating the components of P-splines

The coloured curves show the individual B-splines each multiplied by its respective b-coefficient. Quadratic B-splines (q=2) and first order penalty have been used.

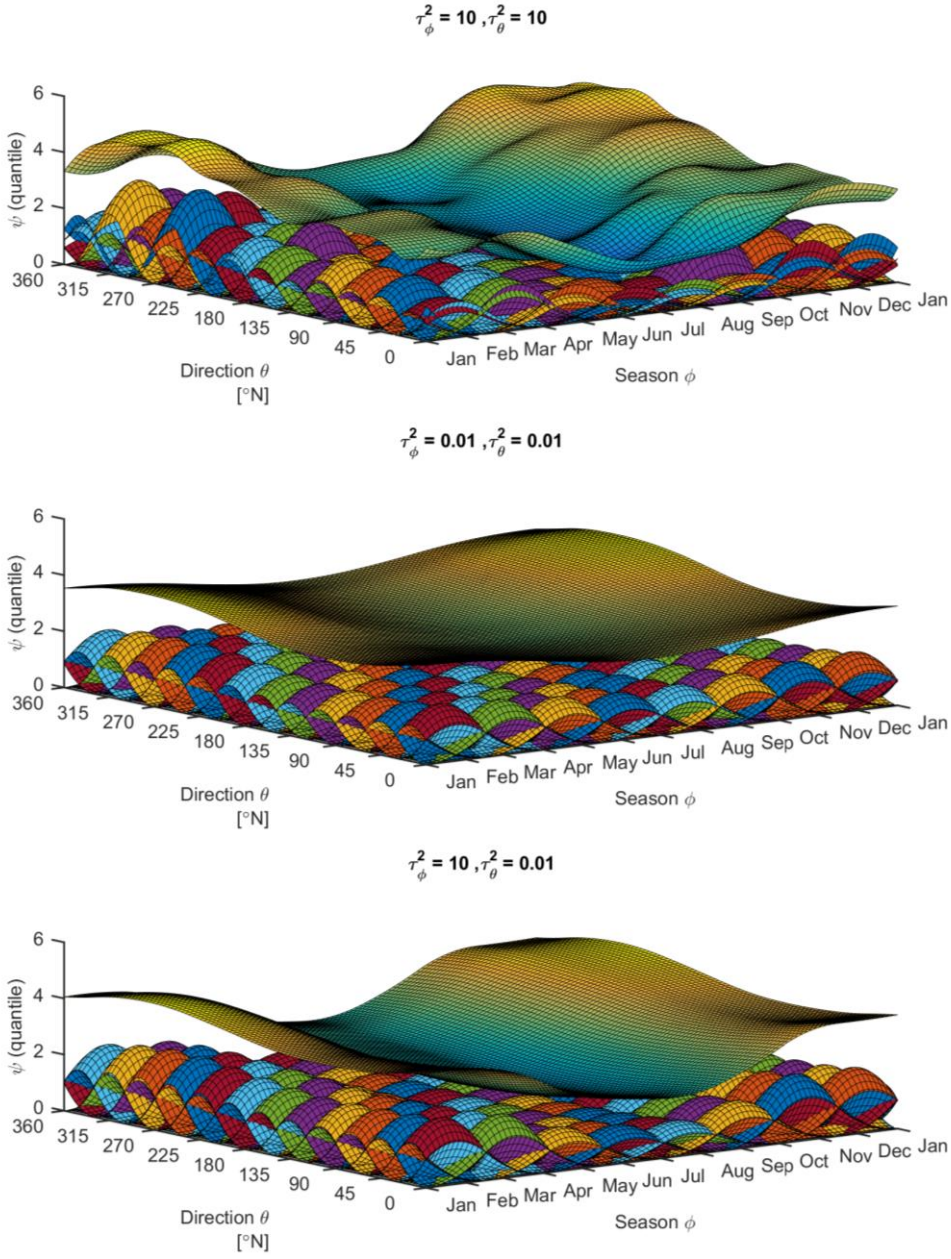

Figure 1.2 Quantile regression analysis, illustrating the components of tensor-product P-splines in two dimensions.

The coloured surfaces show the individual tensor-product B-splines each multiplied by its respective β -coefficient. Quadratic B-splines ($q = 2$) and first order penalty have been used.

Generalised linear array models

The penalised B-spline approach outlined above requires evaluation $\boldsymbol{x} = \boldsymbol{B}\boldsymbol{\beta}$**,** where $\boldsymbol{B}$ is a (sparse) $m \times n$ matrix where m is the total number of data points irregularly spaced within the covariate domain, and n the total number of knots $n = n_1 \times n_2$. $\boldsymbol{\beta}$ is a $n \times 1$ vector of spline coefficients.

However, if we can organise our irregularly spaced data onto a regular $m_1 \times m_2$ grid, we may reduce the problem size substantially using Generalized Linear Array Models (GLAM) ([4], [5])These provide a computationally and memory-efficient framework for combining tensor product B-splines with array data and have been used in a very similar application in the past ([2])

In fact, the problem now reduces to evaluation of $\boldsymbol{B}_1 \mathcal{M}(\boldsymbol{\beta}) \boldsymbol{B}_2'$, where $\mathcal{M}(\boldsymbol{\beta})$ is a $n_1 \times n_2$ reordering of $\boldsymbol{\beta}$. $\boldsymbol{B}_1$ and $\boldsymbol{B}_2$ are size $m_1 \times n_1$ and $m_2 \times n_2$ respectively.

1.6 Parameter estimation

Distribution parameters for the model components described in Section 1.1 are defined by the $\boldsymbol{\beta}$ spline coefficients and parameter estimations thus consists in estimating the appropriate values of $\boldsymbol{\beta}$.

A Bayesian approach is applied to estimate the β-coefficients. The approach builds on work in [6], [7] and [8]

Priors

Spline Model

The prior for β up to a constant of proportionality is given by ([8]

$$\pi(\boldsymbol{\beta}|\tau^2) \propto \frac{1}{(\tau^2)^{\frac{rk(\boldsymbol{K})}{2}}} \exp\left(-\frac{1}{2\tau^2}\boldsymbol{\beta}^T\boldsymbol{K}\boldsymbol{\beta}\right) \qquad (1.15)$$

where $rk(\boldsymbol{K})$ is the rank of the penalty matrix, $\boldsymbol{K}$.

The variance parameter τ^2 is estimated through 10-fold cross-validation. Cross-validation is a robust and simple technique to optimise the predictive performance of a model, i.e., its capability of predicting the likelihood of a data sample that was not used to estimate the model. In this way the right complexity of the model is achieved – it is neither too simple nor is it over-fitting to the data. In this case, too simple a model would be too smooth and thereby ignore covariate effects that were truly present while a too complicated model would be exaggerating covariate effects by trying to adopt to the individual extreme events.

The 10-fold cross-validation consists in, for a given choice of τ^2, to fit the model to 90% of the data (training) and then calculate the likelihood of the remaining 10% of the data(validation). This is repeated 10 times such that all data points have been used one time for validation and the 10 likelihoods are then summed. This whole procedure is then repeated for a new choice of τ^2. Estimation of all values of τ^2 at once is not feasible as the model has as many values of τ^2 as the number of model parameters times the number of covariates. Instead, a sequential procedure has been adopted:

1. Values of τ^2 for the Γ-distribution are estimated by:
   - Estimate an appropriate global value by varying all τ^2 at the same time
   - Estimate a ratio between the shape α and mean μ by varying these separately (but using same value for season and direction)
   - Estimate the ratio between season ϕ and direction θ, using the relative ratio between α and μ as above
   - Repeat first sub-step but now using the relative ratios between α, μ, ϕ and θ.
2. The Γ-distribution is now fitted using the most appropriate combination of τ^2 estimated above and together with appropriate quantile thresholds κ_1, κ_2 this provides the non-stationary threshold above which the GP tail is assumed. For each GP tail, the steps a-d are followed though now with the ratio of GP shape ξ to scale ζ estimated under second sub-step above.

Figure 1.3 show an example of the results of a cross-validation, in this case for the upper tail of the $H_{m0,p,eq}$ variable. The rows in the plot show results of cross-validation steps *a* to *d*. Upper and lower subplots show the summed log-likelihood score on the 10 validation sets as against the prescribed value of τ^2. Row 2 and 3 show colour-scaled plots of the summed log-likelihood score for the tested combinations of τ_x^2 (along x-axis) and τ_y^2 (along y-axis). Yellow indicates higher cross-validation score (better predictive performance). The right-hand plots show the same results as the left-hand plots but smoothing the results across neighbouring τ^2 combinations. Results in left hand plots are normally used. The black dots show random combinations sampled from the probability distribution that can be constructed from the summed log-likelihood score. The black crosses indicate the optimum point.

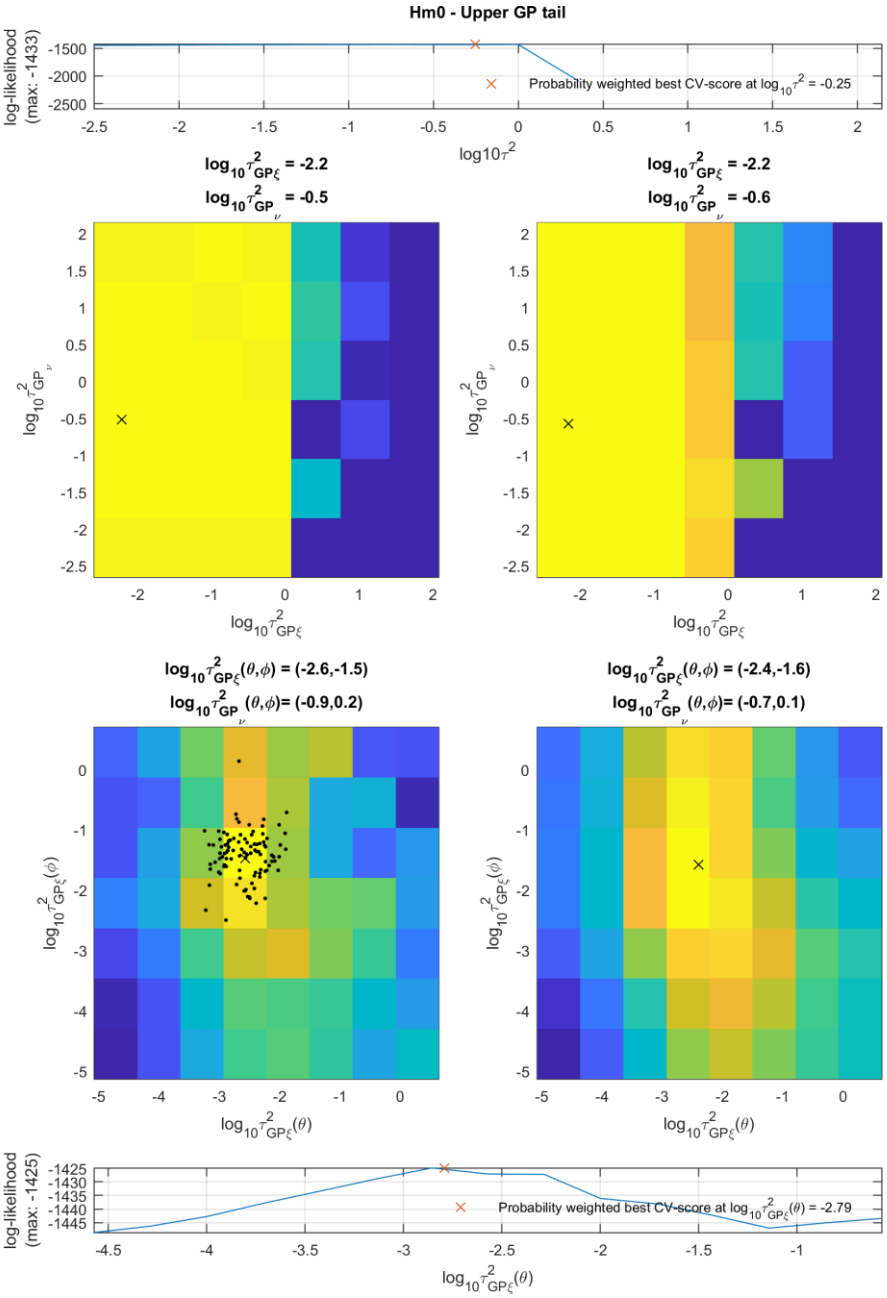

Figure 1.3 Example of cross-validation for the upper GP tail of the distribution of $H_{m0,p,eq}$.
See explanation in text for details

Marginal Distributions

In addition to the priors on the spline coefficients $\boldsymbol{\beta}$, we may also specify priors for the values of the actual distribution parameters or the support ranges. In the case of a negative GP shape parameter, the support range for the GP distribution has an upper end-point X_{max} given by (see Section 1.2 for definition of parameters)

$$X_{max} = -\frac{\zeta}{\xi} + u \qquad (1.16)$$

The distribution tail will asymptotically approach this limit. If a physical absolute upper limit of a parameter is known, it may be introduced in the extreme value analysis by setting the upper end-point of the GP support range to be this limit.

Proposal generation

The posterior distributions are approximated using Markov Chain Monte Carlo methods with a Metropolis-Hastings (MH) sampling scheme. The MH scheme progresses as follows (for one model component):

1. Define start values[3], $\boldsymbol{\beta}^{(0)}$ Set iteration number $i = 1$.

2. For each model parameter; Propose candidate coefficients, $\boldsymbol{\beta}^*$ from a multivariate normal distribution $MVN\left(\boldsymbol{\beta}^{(i-1)}, \mathbf{S}\right)$. Two approaches are followed to estimate the covariance matrix $\mathbf{S}$
   - Following the approach of Rue ([8])also adopted by Lang and Brezger (/13/), proposals are drawn from a MVN with covariance matrix $\mathbf{S} = \left(\mathbf{B}^T\mathbf{B} + \frac{1}{\tau^2}\mathbf{K}\right)^{-1}$
   - Following Roberts and Rosenthal ([9])the empirical covariance matrix is estimated, and proposals drawn from a MVN with covariance matrix

     $$\mathbf{S} = (1-\epsilon)^2 2.38^2 \frac{\Sigma_n}{d} + \epsilon^2 \times 0.01 \frac{I_d}{d} \qquad (1.17)$$

     where Σ_n is the empirical covariance matrix of size $d \times d$ estimated from the markov chain. The latter term $0.01 I_d/d$ is random noise and the small constant ϵ is used to control the degree of random noise in the proposal. Roberts and Rosenthal use $\epsilon = 0.05$ and we adopt the same value here.

   The latter approach requires an estimate of the covariance matrix, which can only be obtained from running the MCMC. Hence, approach a. is first run for a large number of iterations. As approach b. turns out to be computationally faster, the MCMC algorithm has been set to switch to this approach after a number of iterations. Multivariate normal random samples are generated from a Cholesky decomposition $\mathbf{L}$ of the covariance matrix $\mathbf{S}$. Hence

   $$\boldsymbol{\beta}^* = \boldsymbol{\beta}^{(i-1)} + \mathbf{L} \times \boldsymbol{u} \qquad (1.18)$$

   where $\boldsymbol{u}$ is a vector of standard normal random (uncorrelated) samples.

3. Accept $\boldsymbol{\beta}^*$ with probability:

   $$\mathcal{A}\left(\boldsymbol{\beta}^{(i-1)}, \boldsymbol{\beta}^*\right) = \min\left\{1, \frac{\mathcal{L}(\boldsymbol{z}|\boldsymbol{\beta}^*)\pi\left(\boldsymbol{\beta}^*|(\tau^2)^{(i-1)}\right)\pi\left((\tau^2)^{(i-1)}\right)}{\mathcal{L}(\boldsymbol{z}|\boldsymbol{\beta}^{(i-1)})\pi(\boldsymbol{\beta}^{(i-1)}|(\tau^2)^{(i-1)})\pi((\tau^2)^{(i-1)})}\right\} \qquad (1.19)$$

4. Steps 2-3 are repeated for each model parameter after which the iteration counter i is incremented by one

Full model inference

The procedure detailed above is valid for one single model component (gamma distribution bulk, GP tail, Conditional extremes model). However, the full model requires estimation of all components in a hierarchical order as follows:

Parameter 1: Gamma distribution bulk → GP tails
Parameter 2: Gamma distribution bulk → GP tails
…
Parameter n: Gamma distribution bulk → GP tails
} →Conditional Extremes Model

This is achieved as follows:

1. For each input variable (e.g., H_{m0}, T_p, ..., etc);
   - Fit the gamma distribution to all events and save several independent samples from the chain. Also fit the rate of occurrence model for the primary parameters of interest that are later used as conditioning parameters.

[3] Start values for spline coefficients are made by fitting constant models through (seasonally-directionally) binned data, followed by fitting a smoothing spline through the estimated parameter values

- At each stored sample of the gamma distribution of bulk data, sample a threshold non-exceedance probability, compute the threshold, run a GP chain, and save an appropriate number of samples of this after burn-in. Both high and low tail are estimated independently in this way.

This procedure results in n samples (*n = number of Gamma samples times number of GP samples*) of each marginal distribution.

2. Fit all conditional extremes models to the marginal distribution samples. The CE models are fitted simultaneously in order to achieve vectors of residuals emanating from the same historical events, whereby multidimensional dependencies can be carried over into storm simulations (see also Section 1.4). The conditional extremes model threshold ψ uncertainty is accounted for by updating the threshold non-exceedance probability λ for each update of the GP tail threshold in the marginal models. The iteration procedure for each λ update is as follows:
   - Sample a threshold non-exceedance probability and identify the events above this in the conditioning distribution.
   - Fit the CE model across all GP tail updates and to each variable in turn. The CE chain is run for several iterations for each GP tail update, but only the last iteration is stored. Also, the residuals are stored for the last iteration. By running this procedure over all variables in turn, a matrix of residuals is built for each stored CE iteration with size number of threshold exceeding events times number of variables.

The above procedure results in an equal number of samples of the marginal and conditional models, the latter with associated residuals. Several thresholds in both marginal tails and conditional extremes are incorporated in this sample, thus accounting for some of the threshold uncertainty. Equal weight is thereby given to all possible thresholds within the assumed plausible range. It is our experience with constant models that this is a reasonably good approximation for most data sets and superior to a constant threshold approach.

Proper implementation of the MCMC approach ensures that the final sample of model parameters thus obtained represents a sample from the posterior distribution of the model parameters. The uncertainty related to the extrapolation from a limited input data sample to events with a very low exceedance probability is reflected in this posterior distribution.

An overview of the different distribution parameters to be determined for each marginal and conditional extremes distribution is given in Table 1.1. The threshold quantiles are specified as constants and do therefore not vary with covariates. This means that a certain threshold for example for a GP tail model is taken as a constant (across covariate space) quantile in the underlying Gamma distribution. But as the Gamma distribution itself is non-stationary with respect to covariates, the actual threshold for the GP model will also vary with covariates. The quantiles are sampled uniformly from specified intervals.

Table 1.1 Overview of model parameters

Description	Symbol	Type[4]
Rate of occurrence	ρ	Tensor-Product B-spline
Γ distribution shape	α	Tensor-Product B-spline
Γ distribution mean	μ	Tensor-Product B-spline
GP low tail threshold quantile	κ_1	Constant
GP low tail shape parameter	ξ_1	Tensor-Product B-spline
GP low tail scale parameters	ζ_1	Tensor-Product B-spline
GP high tail threshold quantile	κ_2	Constant
GP high tail shape parameter	ξ_2	Tensor-Product B-spline
GP high tail scale parameters	ζ_2	Tensor-Product B-spline

[4] In the case of a constant (covariate-free) model, all parameters are constant.

Description	Symbol	Type[4]
CE threshold quantile	λ	Constant
CE a parameter	a	Tensor-Product B-spline
CE b parameter	b	Tensor-Product B-spline
CE mean parameter	m	Tensor-Product B-spline
CE standard deviation parameter	s	Tensor-Product B-spline

1.7 Simulation and return value estimation

Due to the complexity of the model and the need to ensemble average over the posterior distribution sample of the model parameters, return values are obtained by simulating events in the model. Popular speaking, such a simulation consists in sampling a very large number of events whereby the sought return value can be 'read off' as the i'th largest event in the simulated sample. The rank i depends on the simulation length (numbers of years simulated) and the return period in question.

Combined with an appropriate event (storm) model this procedure also allows for swift convolution of the long-term distribution of the slowly varying parameters with a short-term distribution of a certain type of response. The classical example in this respect is the convolution of the long-term distribution of sea states with the short-term distribution of maximum wave crest heights to obtain the long-term distribution of the maximum crest elevation.

The simulation procedure followed to simulate one year of events is detailed below.

1. Sample a particular iteration from the MCMC chain
2. Sample the number of events from a Poisson distribution with arrival rate corresponding to the average annual number of events in the input data set
3. Sample non-exceedance probability for all events
4. For a non-stationary model, assign covariates to each event through the fitted non-stationary rate function for the conditioning variable
5. Calculate the magnitude of the conditioning variable for all events from its marginal non-stationary distribution
6. Resample events from the data set for all events with non-exceedance probability below the conditional extreme model quantile threshold \lambda as the conditional extremes model is only applicable for conditioning events with non-exceedance probability above λ. In practice, the resampling is done by searching for the nearest event in the data set in terms of all covariates and magnitude
7. Magnitudes of conditioned parameters $\eta_2, \dots, \eta_n$ above the conditional extreme model quantile threshold λ are modelled through the conditional extremes model. A vector of residuals $\boldsymbol{r}_i = [r_{i2}, \dots, r_{in}]$ emanating from the same event in the data set is sampled for each event from the stored residuals for the particular MCMC iteration. The Laplace marginal values for all conditioned parameters calculated from eq. (1.11) and the marginal distributions applied to convert the Laplace marginal values to the physical values.

Return values with long recurrence period requires many years to be simulated. Denoting the number of years n and the required return period T_r, reasonably converged estimates of return values are obtained when $n \geq 100T_r$. In other words, a 100-year return value requires simulation of around 10,000 years.

Return values are usually reported as quantiles in the distribution of the annual maximum. The annual maximum distribution is constructed from the simulation by only retaining the largest simulated value per year and the relationship between quantile and return period given by:

$$q_r = \exp\left(-\frac{1}{T_r}\right) \quad (1.20)$$

The return values hereby obtained reflect the uncertainty in the extreme value distributions and larger uncertainty will inflate the return values especially for return periods longer than the duration of the historical input data sample. This is achieved by integrating across the posterior distribution of the model parameters (effectively achieved by sampling amongst the MCMC iterations when simulating events in step 1). This type of distribution is also known as the posterior predictive annual maximum distribution.

Conditional distributions of associated parameters are readily obtained from the simulation of conditioned parameters.

1.8 References

[1] P. Thompson, Y. Cai, R. Moyeeda, D. Reeve and J. Stander, “Bayesian nonparametric quantile regression using splines,” *Computational Statistics and Data Analysis,* vol. 54, pp. 1138-1150, 2010.

[2] P. Jonathan, D. Randell, Y. Wu and K. Ewans, “Return level estimation from non-stationary spatial data exhibing multidimensional covaiate effects,” *Ocean Engineering,* no. 88, pp. 520-532, 2014.

[3] P. Eilers and B. Marx, “Multivariate calibration with temperature interaction using two-dimensional penalised signal regression,” *Chemometrics and Intelligent Laboratory Systems,* vol. 66, no. 2, pp. 159-174, 2003.

[4] I. D. Currie, M. Durban and P. H. C. Eilers, “Generalised linear array models with applications to multidimensional smoothing,” *Journal of the Royal Statistical Society: Series B (Statistical Methodology),* vol. 68, no. 2, 2006.

[5] P. H. C. Eilers, I. D. Currie and M. Durban, “Fast and compact smoothing on large multidemsional grids,” *Computational Statistics & Data Analysis,* vol. 50, no. 1, pp. 61-76, January 2006.

[6] P. J. Green and B. W. Silverman, “Nonparametric Regression and Generalised Linear Models,” *Chapman & Hall,* 1994.

[7] S. Lang and A. Brezger, “A Bayesian P-Splines,” *Journal of Computational and Graphical Statistics,* no. 13, pp. 183-212, 2004.

[8] G. O. Roberts and J. S. Rosenthal, “Examples of Adaptive MCMC,” *Journal of Computational and Graphical Statistics,* vol. 18, pp. 349-367, 2009.

[9] H. Rue, “Fast Sampling of Gaussian Markov Random Fields with Applications,” *Journal of the Royal Statistical Society,* vol. Series B, 2001.

[10] P. Eilers and B. Marx, “Flexible smoothing using B-splines and penalised likelihood (with comments and rejoinder),” *Stat. Sci,* vol. 11, pp. 89-121, 1996.

[11] P. Eilers and B. Marx, “Splines, knots and penalties,” *Wiley Interdisciplinary Reviews: Computational Statistics:II,* vol. 6, pp. 637-653.

[12] G. Feld, D. Randell, Y. Wu, K. Ewans and P. Jonathan , “Estimation of Storm Peak and Intra-Storm Directional-Seasonal Design Conditions in the North Sea,” Vols. OMAE2014-23157, 2014.

[13] G. Feld, D. Randell, Y. Wu, K. Ewans and P. Jonathan, “Estimation of Storm Peak and Intra-Storm Directional-Seasonal Design Conditions in the North Sea,” *OMAE,* 2015.

[14] J. E. Heffernan and J. A. Tawn, “A conditional approach for multivariate extreme values,” *Journal of the Royal Statistical Society: Series B (Statistical Methodology),* no. 66, pp. 497-546, 2004.

[15] P. Jonathan, K. Ewans and D. Randell, “Joint modelling of extreme ocean environments incorporating covariate effects,” *Coastal Engineering,* no. 66, pp. 22-31, 2013.

[16] C. Keef, I. Papastathopoulos and A. J. Tawn, “Estimation of the conditional distribution of a multivariate variable given that one of its components is large. Addional constraints for the Heffernan and Tawn model.,” *Jounal of Multivariate Analysis,* pp. 396-404, 2013.

[17] D. Randell, K. Turnbull, K. Ewans and P. Jonathan, “Bayesian inference for nonstationary marginal extremes,” *Environmetrics,* vol. 27, no. 7, pp. 439-450, 2016.

[18] H. F. Hansen, D. Randell , A. R. Zeeberg and P. Jonathan, “Directional-seasonal extreme value analysis of North Sea storm conditions,” *Ocean Engineering,* p. 195, 2020.

Appendix G Validation of WRF wind storm peaks

Presented in this Appendix are the validation plots of the wind speed storm peaks between measurements and WRF model results. The joint peaks consider that the historical and model storm peak may not occur at the same time step. The joint peaks were conditioned sure that they occur within a window of +/- 18 hours. All validations are shown for the height of analysis, i.e., 160 mMSL.

Appendix G.1 Peak Wind Speed Validation at 160 mMSL

Appendix G.1.1 IJmuiden Ver (IJVA and IJVB)

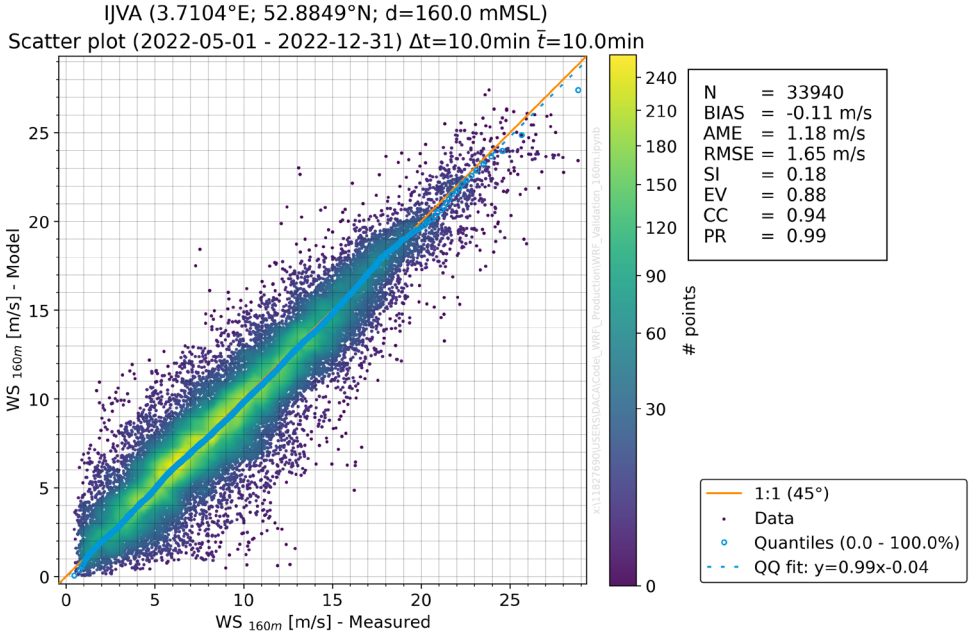

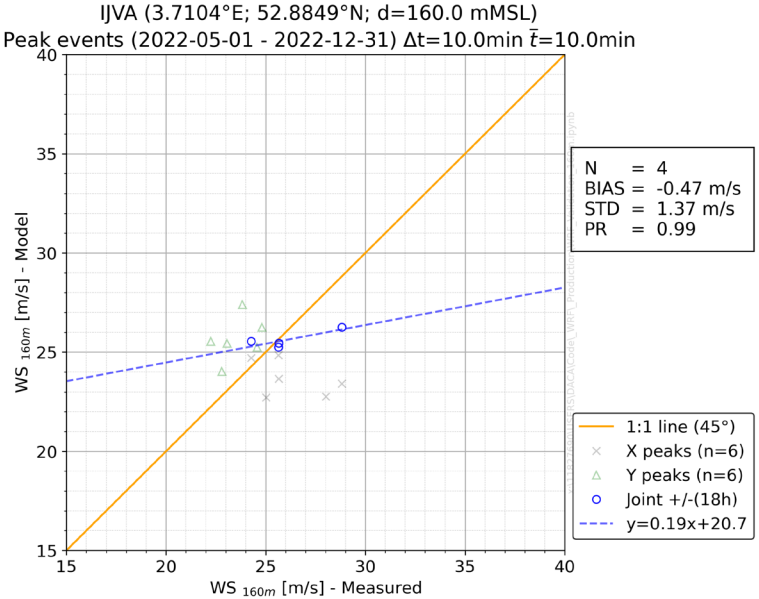

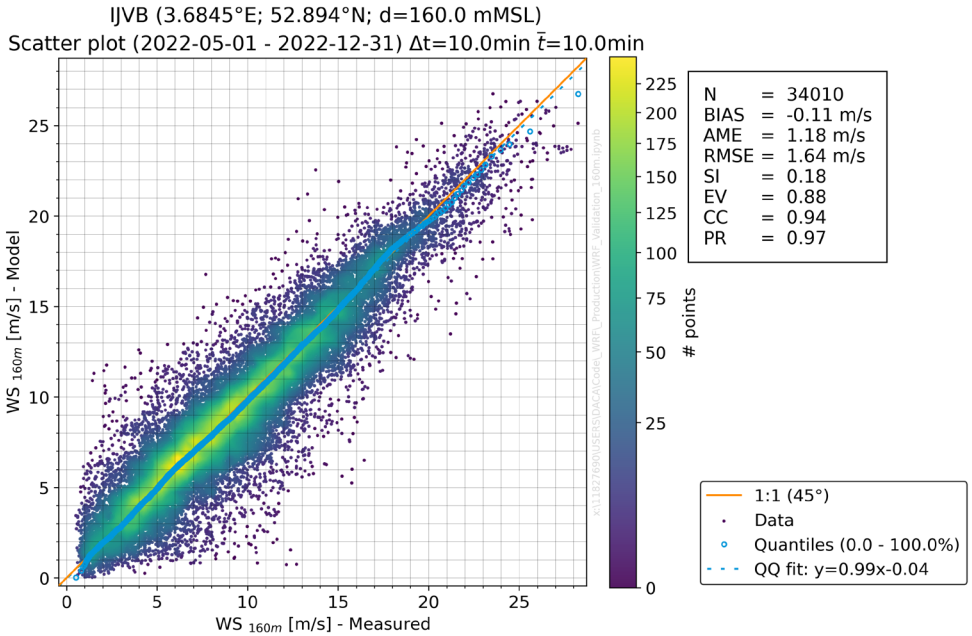
IJVB (3.6845°E; 52.894°N; d=160.0 mMSL)
Scatter plot (2022-05-01 - 2022-12-31) Δt=10.0min $\bar{t}$=10.0min
WS 160m [m/s] - Model
WS 160m [m/s] - Measured
# points
N = 34010
BIAS = -0.11 m/s
AME = 1.18 m/s
RMSE = 1.64 m/s
SI = 0.18
EV = 0.88
CC = 0.94
PR = 0.97
1:1 (45°)
Data
Quantiles (0.0 - 100.0%)
QQ fit: y=0.99x-0.04

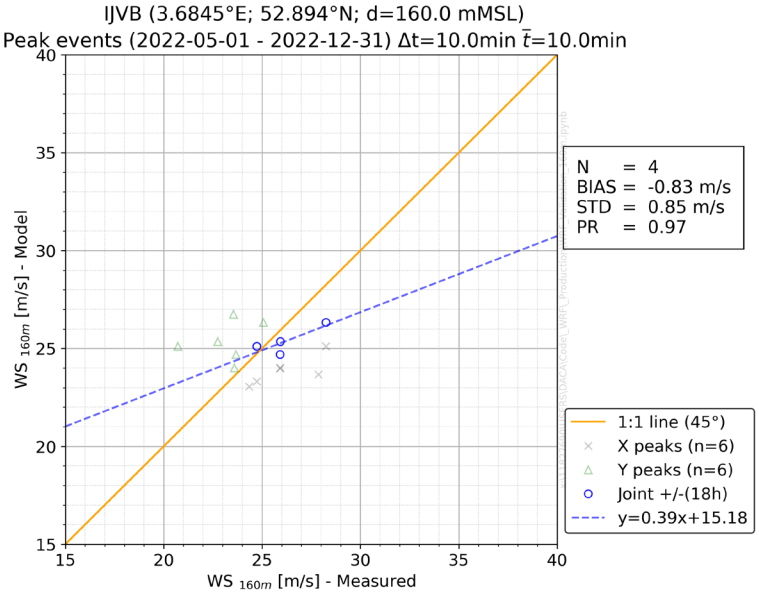
IJVB (3.6845°E; 52.894°N; d=160.0 mMSL)
Peak events (2022-05-01 - 2022-12-31) Δt=10.0min $\bar{t}$=10.0min
WS 160m [m/s] - Model
WS 160m [m/s] - Measured
N = 4
BIAS = -0.83 m/s
STD = 0.85 m/s
PR = 0.97
1:1 line (45°)
X peaks (n=6)
Y peaks (n=6)
Joint +/-(18h)
y=0.39x+15.18

Appendix G.1.2 Hollandse Kust West (HKW)

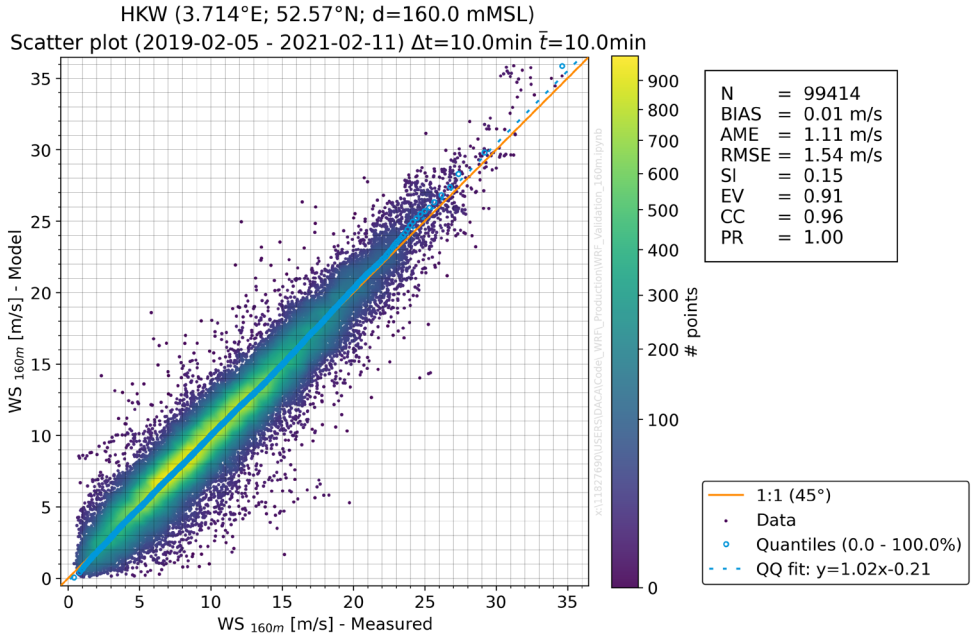

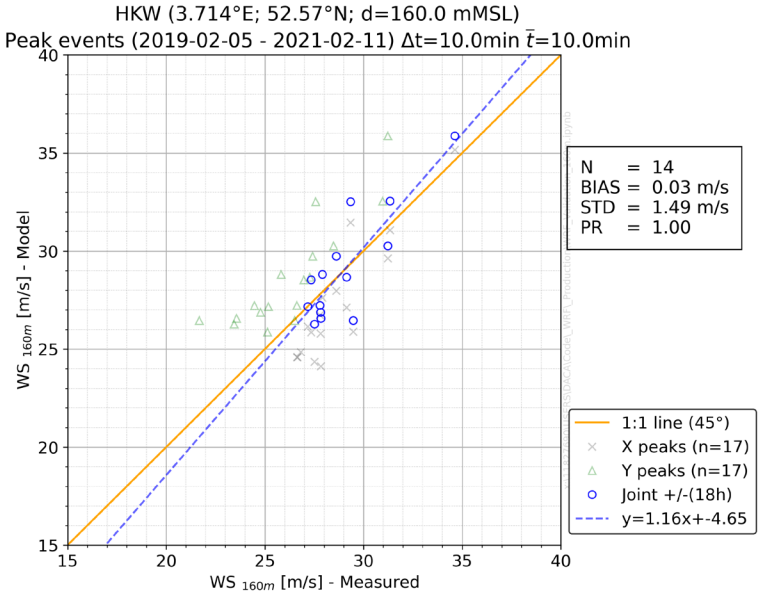

Appendix G.1.3 Hollandse Kust Zuid (HKZ)

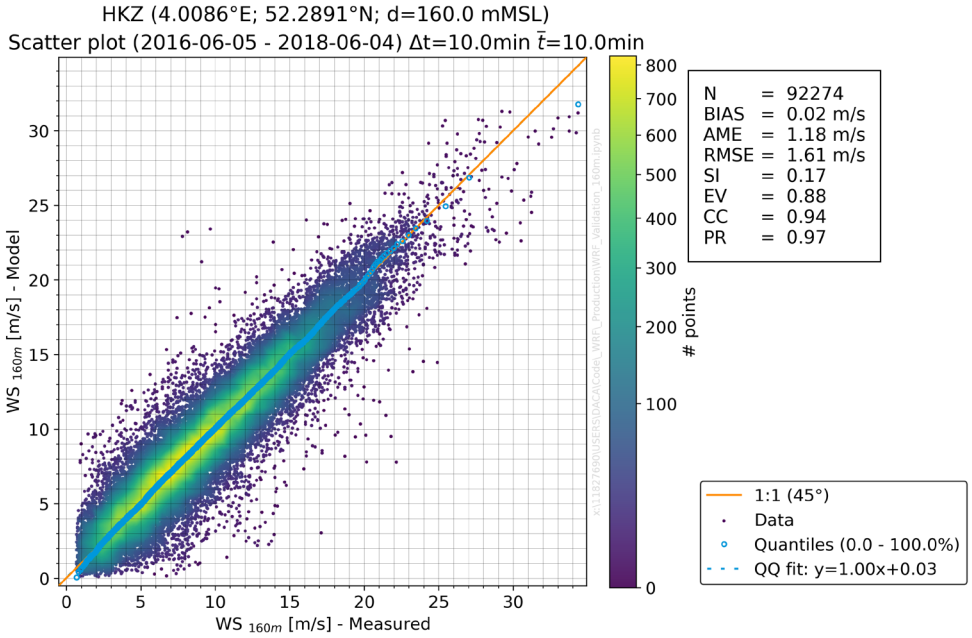

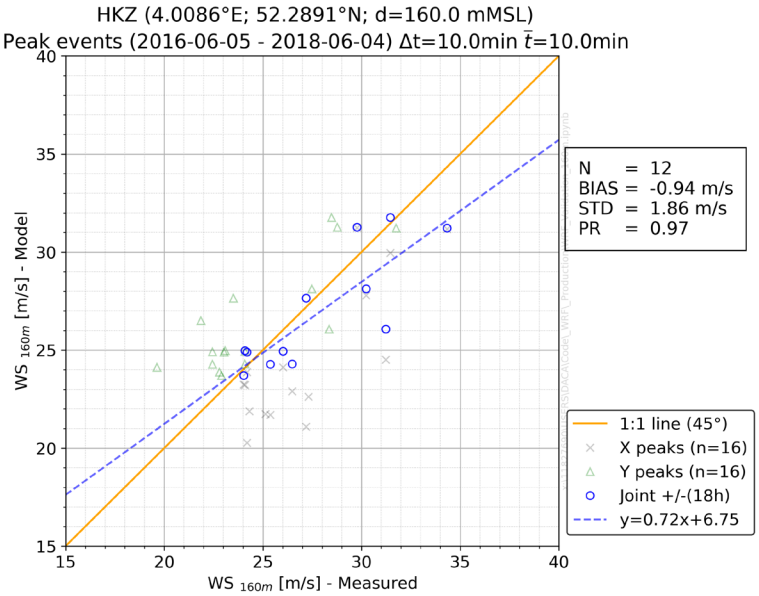

Appendix G.1.4 Hollandse Kust Nord (HKN)

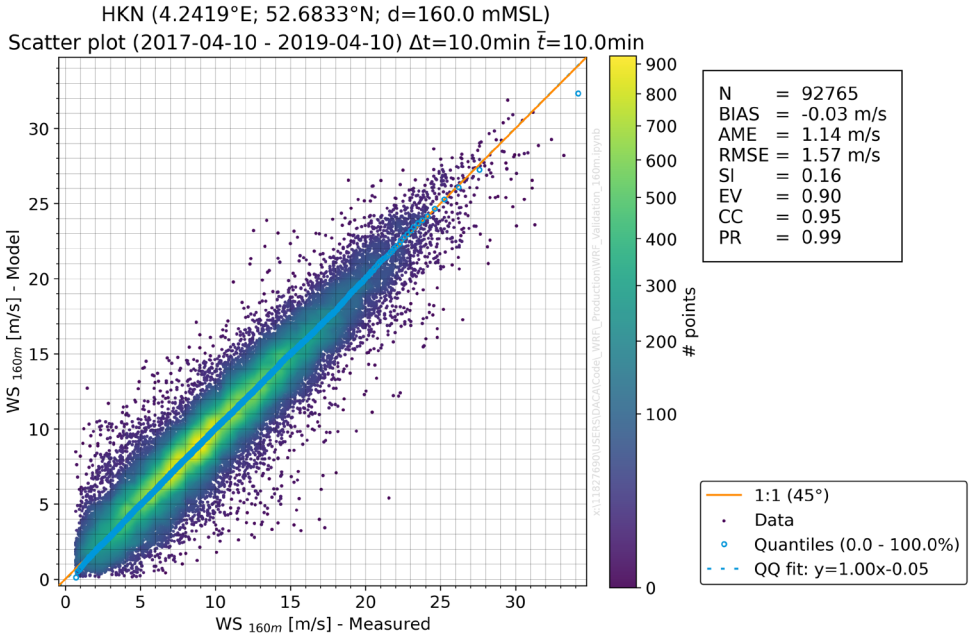

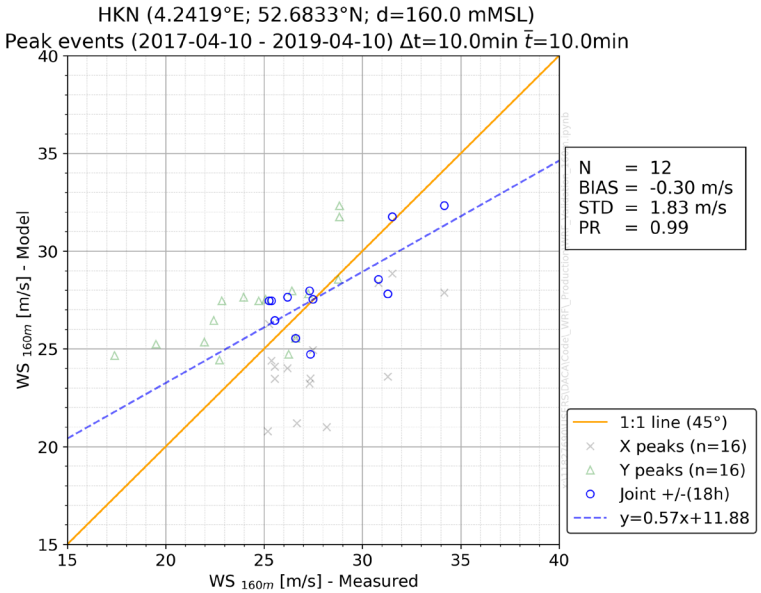

Appendix G.1.5 Ten Noorden van de Waddeneilanden (TNW)

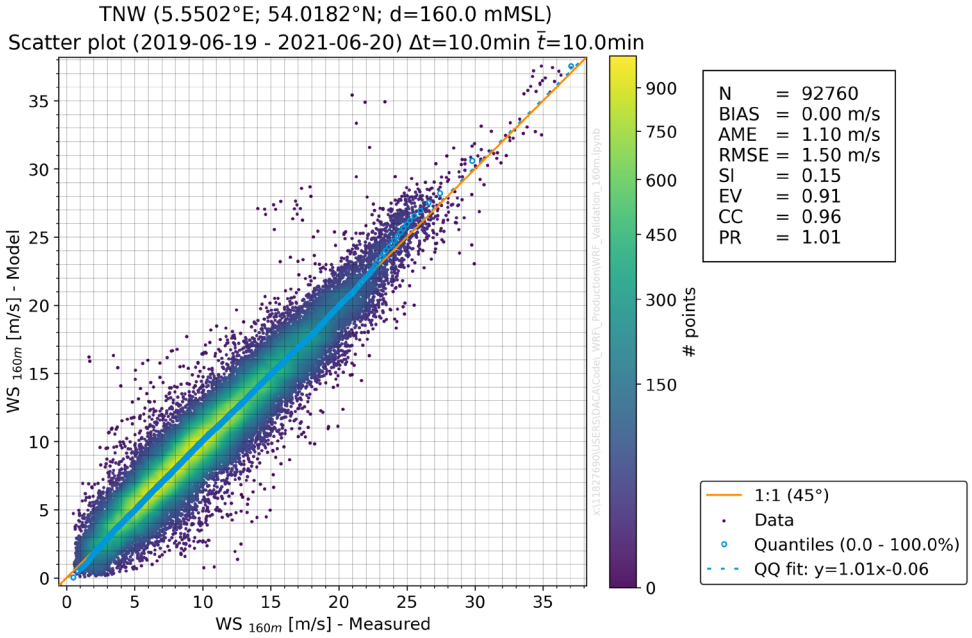

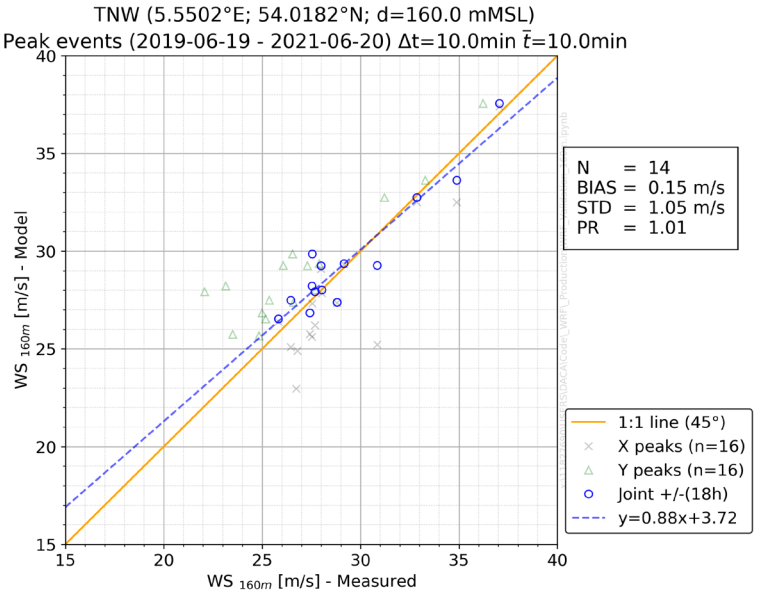

Appendix G.1.6 Meteomast Ijmuiden LiDAR (MMIJ-Lidar)

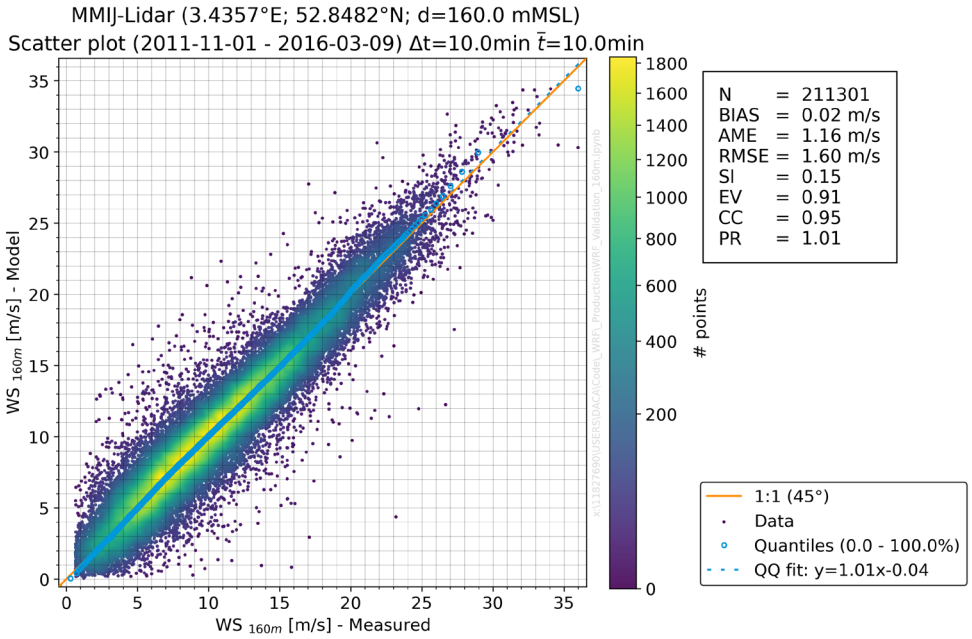

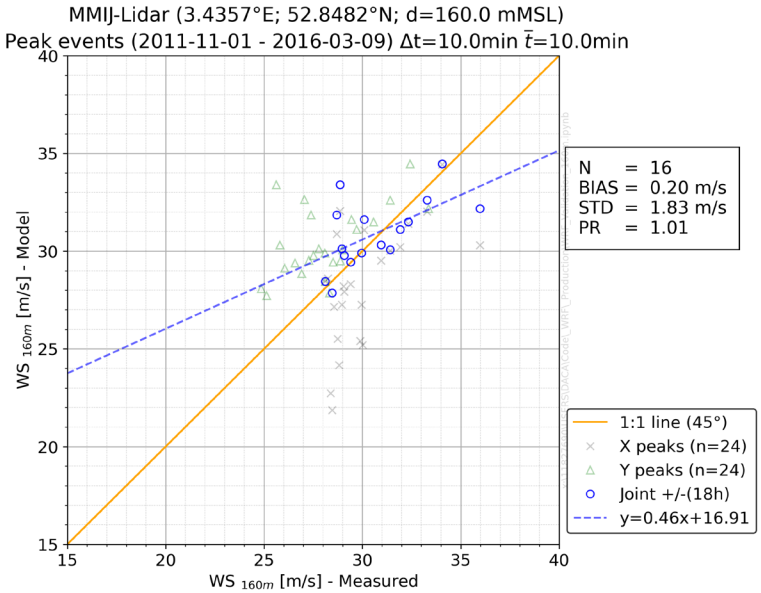

Appendix G.1.7 K13a Platform LiDAR

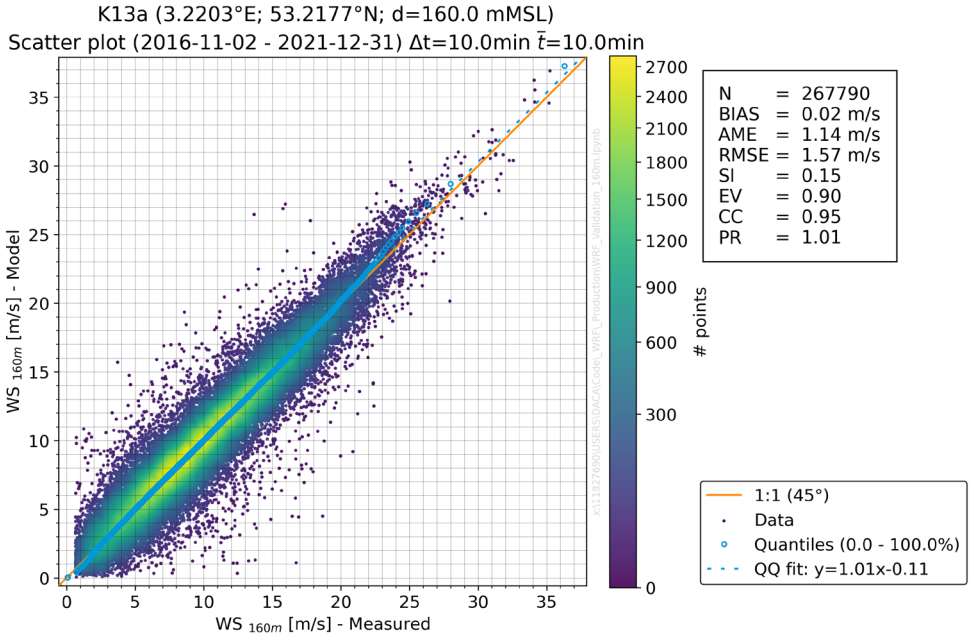

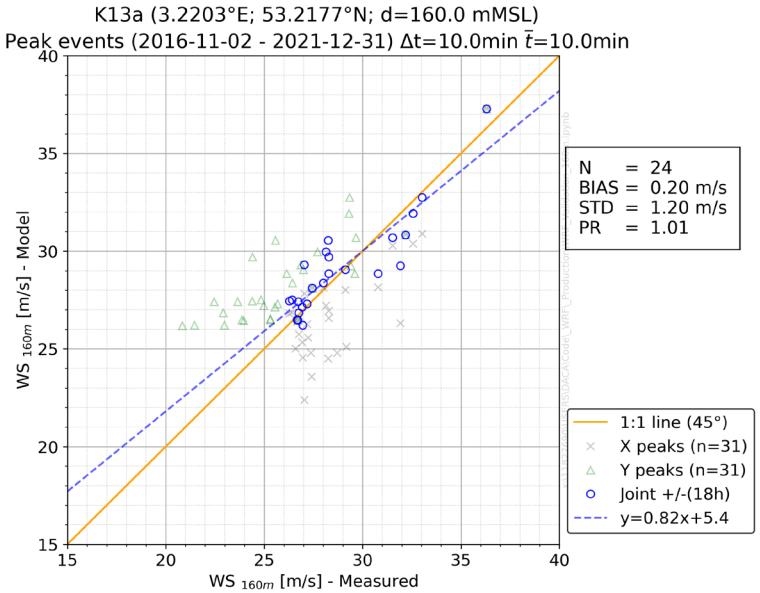

Appendix G.1.8 Euro Platform (EPL)

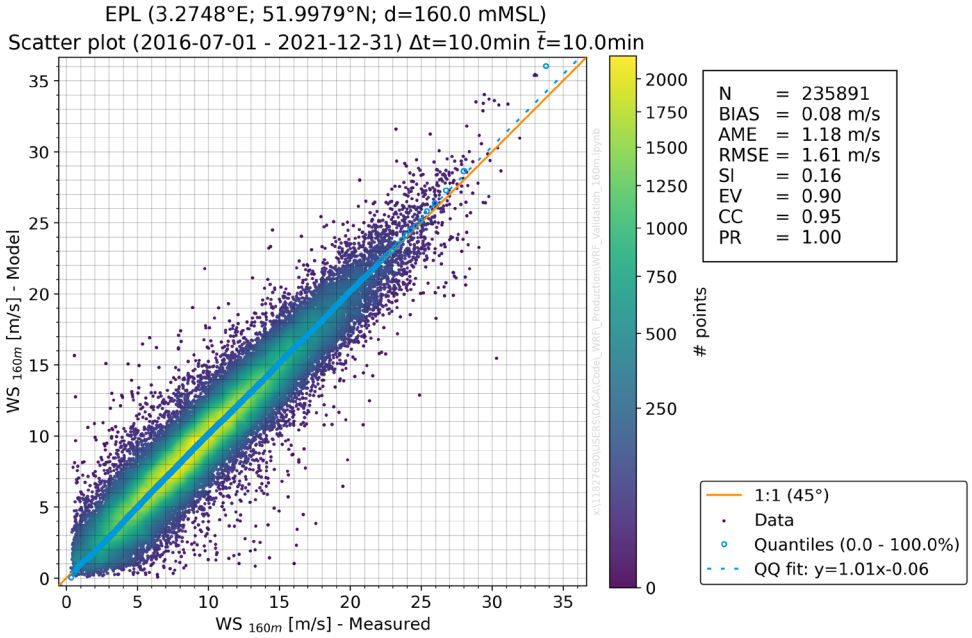

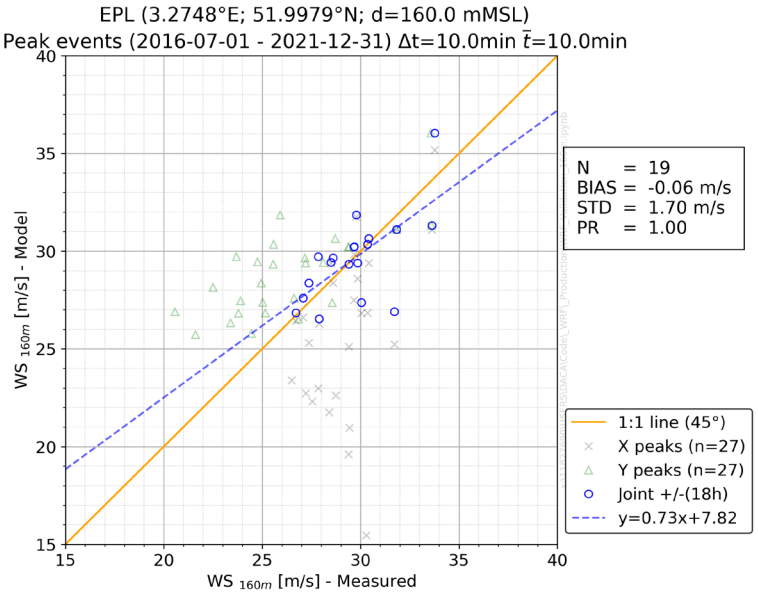

This investigation was carried out by DHI Consortium, commissioned by RVO, an agency of the Ministry of Economic Affairs and Climate Policy.

The information in this document is valid at the time of publishing (see month/year). Updates will be published on the website https://offshorewind.rvo.nl, at the relevant sitemap, General Information, submap Revision Log and Q&A. In the Revision Log is indicated which versions are the latest and what the changes are in relation to previous versions. The documents can be found at the relevant sites, indicated in the List of all reports and deliverables.

Contacts
Netherlands Enterprise Agency (RVO)
Graadt van Roggenweg 200 | 3531 AH | Utrecht
P.O. Box 8242 | 3503 RE | Utrecht
www.rvo.nl / https://english.rvo.nl

Netherlands Enterprise Agency (RVO) | December 2023